Deposition of ultra-thin metal oxide films for gas sensing applications

This thesis is submitted in partial fulfilment of the requirements for the Degree of Doctor of Philosophy (Chemistry)

Rachel Lyndsey Wilson

2017

Supervised by: Professor Claire J. Carmalt and

Dr Christopher S. Blackman

Declaration

I, Rachel L. Wilson confirm that the work presented in this thesis is my own. Where information has been derived from other sources, I confirm that this has been indicated in the thesis.

.....

Abstract

The aim of this research project was to investigate the use of Atomic Layer Deposition (ALD) and Chemical Vapour Deposition (CVD) to deposit *n*- and *p*-type metal oxide thin films for use in gas sensing applications, with the long term goal to identify the materials which provide maximum sensitivity and selectivity.

Two ALD reactors have been designed and constructed specifically for this project. *N*-type TiO_2 thin films have been deposited by ALD of titanium(IV) isopropoxide and water, where film growth was shown to proceed via a self-limiting mechanism. Films were characterised using AFM, XRD, XPS and Raman, which confirmed anatase phase on the film surfaces.

TiO_2 films of various thickness were deposited onto gas sensor substrates and exposed to a range of test gases in order to evaluate their gas sensitivity at operating temperatures of 350 °C and 480 °C at several different relative humidity's. Electrical resistance changes were observed for a 50 nm TiO_2-coated sensor in response to NH_3, where the sensor response was found to decrease with increasing relative humidity. However for a 10 nm film, whose thickness was most consistent with reported literature values of the Debye length for TiO_2 was the not the most sensitive.

Attempts to deposit *p*-type NiO films via ALD were less successful. However two novel nickel complexes were synthesised: $[Ni(dmamp)_2]$ and $[Ni\{(N^iPr_2)_2CNEt_2\}_2]$, whose volatility was greater than some of the other commonly used nickel precursors for ALD and CVD applications. These precursors, along with $[Ni(thd)_2]$ and $[Ni(Cp)_2]$, have been screened for their use in the deposition of NiO thin films via ALD with water. However, XPS analysis confirmed nickel metal and/or $Ni(OH)_2$ on the film surfaces, which has been attributed to both a lack of reactivity between the nickel precursors and water and issues with the reactor design. Separate CVD experiments performed with $[Ni(dmamp)_2]$ and $[Ni\{(N^iPr_2)_2CNEt_2\}_2]$ resulted in the deposition of NiO films, as confirmed by XRD and XPS. Under the CVD conditions used, film growth could be controlled relatively easily, as compared to other conventional CVD methods.

Acknowledgements

I would first like to thank both my supervisors, Professor Claire Carmalt and Dr Christopher Blackman who have provided continuous support and encouragement throughout my PhD. The Parkin/Carmalt group has been a great group to be a part of over the past 3 years and I have made some great friends. I would also like to thank the EPSRC for funding my PhD project.

For helping me learn various film characterisation and analytical techniques, I would like to thank Dr Steven Firth, Dr Michael Powell, Dr Francesco Di Maggio, Dr Caroline Knapp, Dr Joe Bear, Dr Nick Chadwick, Dr Sanjay Sathasivam, Dr Carlos Sotelo-Vazquez, Dr Kersti Karu, Miss Lilian Hayes, Dr Steve Hudziak and Mr Martin Vickers. Sincere thanks to Dr Alaric Taylor who has always been on hand to help out with AFM and ellipsometry measurements – even when overwhelmed with work himself. Thank you to Dr Cristian Simion at the National Institute of Materials Physics in Romania for carrying out all of the gas sensing measurements – without you these results would not have been possible. I would like to thank Mr Jim Percival who has always been on hand to help with the construction of the ALD reactors. Without your patience and kindness things would have taken a lot longer! Thank you to Mr Tom Bridges who has also provided considerable support with the many problems encountered with the ALD reactors.

Thank you to Miss Lilian Hayes and Mr Dominic Potter for your friendship throughout my time at UCL. We have been a great team in supporting each other and providing encouragement during the hard times.

Finally, thank you to my parents who have supported me throughout every stage of my life and without you I would not have achieved half of the things I have. And Billy - thank you for everything.

Table of Contents

List of Abbreviations

AACVD	Aerosol-assisted chemical vapour deposition
acac	Acetylacetonate
AFM	Atomic force microscopy
ALD	Atomic layer deposition
ALE	Atomic layer epitaxy
amd	Amidinate
APCVD	Atmospheric pressure chemical vapour deposition
APCI	Atmospheric pressure chemical ionisation
apo	2-amino-pent-2-en-4-onato
BE	Binding energy
CBE	Chemical beam epitaxy
CCDC	Cambridge crystallographic data centre
CI	Chemical ionisation
Cp	Cyclopentadienyl
Cp’	Monomethyl cyclopentadienyl
CVD	Chemical vapour deposition
CVI	Chemical vapour infiltration
deamp	1-diethylamino-2-methyl-2-propanoxide
DLI	Direct liquid injection
dmae	dimethylaminoethoxide
dmamb	1-dimethylamino-2-methyl-2-butanoxide
dmamp	2-dimethylamino-2-methylpropanoxide
dmg	dimethyl-glyoximato
DRAM	Dynamic random access memory
DSC	Differential scanning calorimetry
EA	Elemental analysis
EI	Electron ionisation
EL	Electroluminescent
emamp	1-ethylmethylamino-2-methyl-2-propanoxide
ESI	Electrospray ionisation
Et	Ethyl
EtCp	Ethyl cyclopentadienyl
FTO	Fluorine-doped tin oxide
FWHM	Full width half maximum
GMS	Gas mixing system
GPC	Growth per cycle
hfac	hexafluroacetylacetonate
^{i}Pr	Isopropyl
k	Extinction coefficient
I	Current
KE	Kinetic energy
LCVD	Laser chemical vapour deposition
LPCVD	Low pressure chemical vapour deposition
MALDI	Matrix assisted laser desorption ionisation
Me	Methyl
MEMS	Microelectromechanical systems
MFC	Mass Flow Controller
MOCVD	Metal-organic chemical vapour deposition
MOSFET	Metal-oxide semiconductor field-effect transistor
n	Refractive index

NMR	Nuclear magnetic resonance
NSP	Nebulised spray pyrolysis
OEt	Ethoxide
$O^{i}Pr$	Isopropoxide
$O^{n}Pr$	Propoxide
OLED	Organic light emitting diode
OMe	Methoxide
$O^{t}Bu$	tert-butoxide
ppm	Parts per million
PCVD	Photochemical chemical vapour deposition
PECVD	Plasma enhanced chemical vapour deposition
PTFE	Polytetrafluorethylene
QCM	Quartz crystal microbalance
R	Resistance
Ra	Roughness (average)
ReRAM	Resistive random access memory
RH	Relative humidity
RMS	Root mean squared roughness
^{s}Bu	sec-butyl
sccm	Standard cubic centimeters per minute
SEA	Spectroscopic ellipsometry analysis
SEM	Scanning electron microscopy
SMO	Semiconducting metal oxide
SOFC	Solid oxide fuel cell
SPM	Scanning probe microscopy
^{t}Bu	tert-Butyl
TCO	Transparent conducting oxide
TGA	Thermogravimetric analysis
thd	2,2,6,6-tetramethyl-3,5-heptanedionate
THF	Tetrahydrofuran
TTIP	Titanium(IV) isopropoxide
Vp	Vapour pressure
XRD	X-ray diffraction
XPS	X-ray photoelectron spectroscopy

List of Symbols

β	Additional broadening at half the maximum intensity
rp	Amplitude reflection coefficient of *p*-polarised light
rs	Amplitude reflection coefficient of *s*-polarised light
α, β, γ	Angles between crystal lattice parameters
Å	Angstrom
Ra	Average surface roughness
R_{air}	Baseline gas sensor resistance
BE	Binding energy
K_B	Boltzman constant
n_0	Charge carrier concentration
e	Charge of electron
a, b, c	Crystal lattice parameters
h, k, l	Crystal lattice planes
F	Crystal structure factor
L_d	Debye length
Δ	Delta
D_{calc}	Density of unit cell
k	Extinction coefficient
M	Formula weight
v	Frequency of incident radiation
F	Gas flow rate through bubbler
S	Gas sensor signal
GPC	Growth per cycle
d	Inter-planar spacing
K	Kelvin
kE	Kinetic energy
B	Mean crystallite size
I	Measured XPS peak area
R_{int}	Measure of the precision/reproducibility of crystal structure
R_{sigma}	Measure of the signal-to-noise ratio of crystal structure
µ	Micron
nm	Nanometres
Z	Number of repeating units in unit cell
ε_0	Permittivity of free space
h	Planck constant
Ψ	Psi
n	Refractive index
σ	Relative concentration of element in XPS spectrum
ε	Relative permittivity (dielectric constant)
R	Relative sensitivity factor
R_{NH3}	Resistance of gas sensor when exposed to NH_3 gas
Rq	Root mean square surface roughness
K	Scherrer constant
T	Temperature
θ	Theta
Vp	Vapour pressure
V	Volume of unit cell
λ	Wavelength of X-ray radiation

List of Figures

Chapter 1: Introduction

Chapter 2: Experimental

Chapter 3: ALD of Titanium Dioxide thin films

Chapter 4: ALD of Nickel Oxide thin films

Chapter 5: CVD of Nickel Oxide thin films

Chapter 6: Gas Sensor Testing

Chapter 7: Conclusions and future perspectives

Appendix A: SEM of TiO_2 thin films

Appendix B: Mass Spectra of synthesised precursors

List of Tables

Chapter 1: Introduction

Chapter 3: ALD of Titanium Dioxide thin films

Chapter 4: ALD of Nickel Oxide thin films

Chapter 5: CVD of Nickel Oxide thin films

Chapter 6: Gas Sensor Testing

Appendix C: Crystal data for synthesised precursors

List of Schemes

Chapter 4: ALD of Nickel Oxide thin films

Chapter 1
Introduction

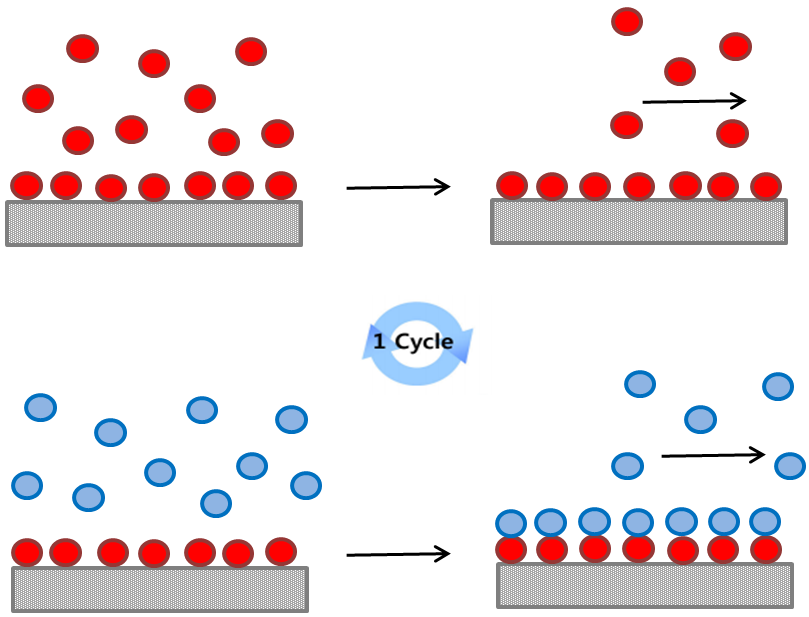

Chapter 1 Introduction

1.1 General Introduction and Aims

This thesis presents the results of an investigation into the use of atomic layer deposition (ALD) and chemical vapour deposition (CVD) of *n*- and *p*-type metal oxide thin films for use in gas sensing applications. Metal oxide gas sensors can be used for the detection of toxic, combustible and flammable gases and oxygen depletion.[1] Some examples of where such systems are utilised include process control industries, environmental monitoring, traffic safety, alcohol breath testing, boiler control and fire detection.[2] The target materials of interest were *n*-type TiO_2 and *p*-type NiO thin films, both of which have scope for use in gas sensing due to their favourable chemical and physical properties.

Chemoresistive gas sensors fabricated using *p*-type metal oxide semiconductors have received relatively little attention compared to their *n*-type congeners, which may be ascribed to their apparently low sensitivities. A major drawback of using *n*-type metal oxides for gas sensing is their sensitivity to moisture and humidity, which can affect the gas sensor response. *N*-type metal oxide gas sensors are capable of reacting with ambient moisture as well as the analyte gas; which can decrease the density of chemisorbed oxygen species within the electron-depletion layer.[3] It is therefore not possible to use *n*-type chemoresistive gas sensors without taking into account the humidity during the test procedure. *P*-type metal oxide gas sensing materials however, are believed to be less moisture sensitive due to the distinctive oxygen adsorption and interaction with moisture in the atmosphere, which plays a key role in the sensing mechanism.[3] *P*-type semiconducting metal oxides are therefore very attractive materials within the semiconductor industry.

ALD provides atomic level control of film growth, allowing fabrication of materials with defined thickness in the order of nanometres, making it an ideal tool for exploring the fundamental gas sensing properties of these materials. The relationship between film thickness and gas response will be investigated at film thicknesses on the order of the Debye length to try and determine the optimum film thickness which results in the greatest gas sensor response. Currently no systematic or comparative

study of exploiting nanoscaled *p*-type metal oxide materials for gas sensing exists. Decoration of *p*-type oxides with noble metal particles has been demonstrated to dramatically increase sensitivity[4,5] but as yet these studies are in their infancy. In addition, the major problem with chemoresistive gas sensors is their lack of selectivity.[6]

Two ALD reactors have been designed and constructed specifically for the purpose of this project. Initially, the deposition of *n*-type titanium dioxide (TiO_2) by ALD was demonstrated. There are many reports which demonstrate the use of ALD to deposit TiO_2 from a variety of different precursor materials. Starting with this already well known material would allow the ALD reactor and reaction parameters to be optimised before going on-to investigate alternative *p*-type materials (NiO). CVD techniques have been employed when ALD of certain precursors has proven to be unsuccessful. Performing CVD experiments on the ALD reactor would enable the precursors to be introduced into the reactor in a more controlled manner, with more control over the deposited film thickness as compared to conventional CVD techniques.

The long term goal of this research project is to identify the most promising new materials and provide key information regarding the optimisation of the materials synthesis to obtain materials with maximum sensitivity and selectivity.

It is important to note that ALD is a relatively new technique within the chemistry department at University College London; therefore little existing experimental expertise was available throughout these experiments.

1.2 Atomic Layer Deposition

1.2.1 The History of Atomic Layer Deposition

Atomic layer deposition (ALD) is a relatively new thin film deposition technique which first dates back to the 1960's, where it was known as "molecular layering" in the soviet union.[7] It was not until the early 1970's that it became known as atomic layer epitaxy (ALE) in Finland by Tuomo Suntola.[8] The first studies of ALE were focused on growing high-quality polycrystalline zinc sulfide (ZnS) films for use in electroluminescent (EL) display panels,[9] which were first publicly displayed at Helsinki airport from 1983 to 1998.[8]

Over the past 30 years the material selection for ALD has widened and its applications expanded to various areas including; semiconductor devices,[10] catalysis,[7] integrated circuits,[11] microelectromechanical systems (MEMS)[12] and photovoltaic applications.[13] Microelectronics is rapidly becoming one of the most important application areas for ALD research.[13] The continuous drive towards the miniaturisation of devices was first predicted in 1965 by Gordon Moore.[14] He stated that the number of transistors on a single device will double every 18 - 24 months, which became known as "Moore's Law".[15] His prediction has therefore put a greater demand on thin film deposition techniques; new designs require a higher complexity with excellent conformality and accurate control over film thickness.[16] The distinctive features of ALD make it an ideal method for meeting such requirements over other thin film deposition techniques (for example, CVD). Figure 1.1 shows the rapid increase in published articles on ALD (grey bars) over the past two decades. This shows promise to a bright future for research and development within the field of ALD for microelectronic applications.

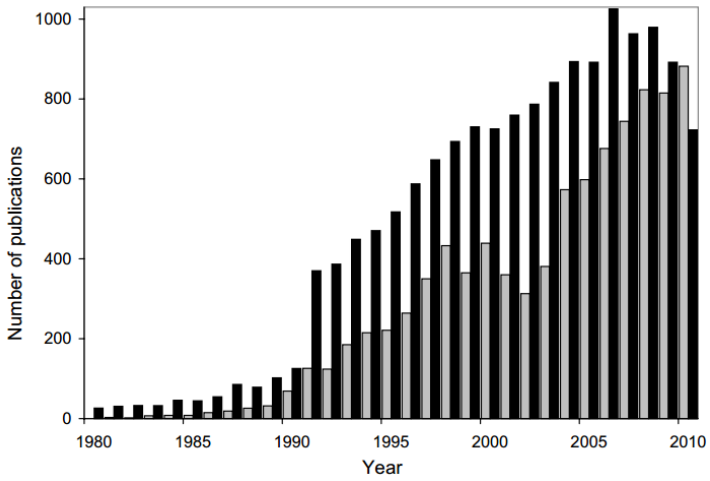

Figure 1.1 Number of articles published per year on ALD (grey bars) and number of articles published on CVD divided by five (black bars)[10]

1.2.2 Principles of ALD

ALD is a gas-phase thin film deposition technique which involves sequential, alternative dosing of chemical reactants (known as precursors) onto a substrate surface.[17] Reactive molecular precursors are volatile and contain the desired elements of the film to be grown. For example, equation 1.1 shows a compound with metal (M) and ligands (L) reacting with a co-reactant (A) with ligands (N) to produce the desired film (MA) and by-product ligands (NL) are omitted.

$$ML_2 + AN_2 \rightarrow MA\ (film) + 2\ NL\ (volatile\ by\text{-}product) \qquad (1.1)$$

ALD reactions can be separated into two half-cycles. The first half-cycle involves exposure of the metal precursor into the reactor in the form of vaporised molecules. The precursor then chemisorbs onto the substrate surface where self-limiting reactions between the precursor and surface atoms occurs,[18] introducing new functional groups for the following reaction to form a saturated layer. An inert gas (usually nitrogen or argon) is then purged into the reactor to remove volatile by-products and any excess unreacted precursor. The second half-cycle involves exposure of the co-reactant precursor vapour into the reactor which undergoes a self-limiting reaction with the new functional groups on the substrate surface, generating a film.[11] The second precursor restores the reactivity of the surface towards the first

precursor by eliminating ligands in the form of volatile by-products. A second gas purge step is then performed to remove the volatile by-products and any unreacted precursor. Factors which may prevent self-limiting growth include the deposition temperature, co-reactant still present in the gas phase after the purge step and surface reactions such as β-hydride elimination.

The sequential dosing and purging is important to prevent the two precursors coming into contact with each other and therefore resulting in CVD-like behaviour. This sequence of steps is referred to as one ALD reaction cycle, which may deposit anywhere between 0.1 Å and 3 Å of material,[12] depending on the precursors being used and the reaction conditions. Usually, the number of chemisorbed species on the substrate surface is too small for the formation of a complete monolayer in one ALD reaction cycle due to steric hindrance of the bulky reactant molecules.[19] Figure 1.2 shows a simplified diagram of the ALD growth mechanism (by-product ligands are not shown).

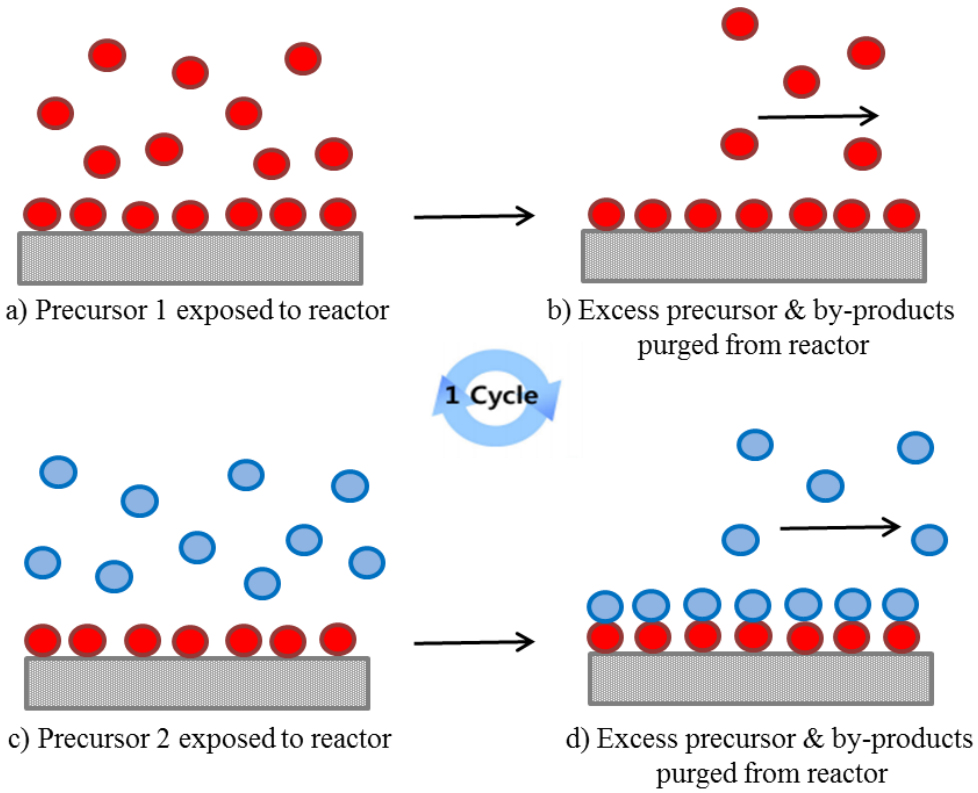

Figure 1.2 Simplified diagram to illustrate ALD growth mechanism

As described earlier, in order for "true" ALD growth to occur, there are two fundamental aspects which must be fulfilled:

1) **Surface reactions must be *complementary*** - each of the two half-cycle reactions must prepare the surface for its reaction with the other precursor, so that the deposition cycles can be repeated.[18]

2) **Surface reactions must be *self-limiting*** - the amount of precursor deposited in each of the half-cycle reactions is uniform across the surface, provided that the saturation level has been reached.[10]

It is important to note that the sequential dosing of precursors does not qualify ALD growth; it is the fact that the film growth is self-limiting. This self-limiting nature enables films to be deposited with exceptional uniformity in thickness, regardless of changes in the vapour flux across the substrate surface.[18] The high uniformity in film thickness which can be achieved means that not only flat surfaces can be coated; in fact excellent conformality can be achieved over rough topologies and in troughs and holes, avoiding film discontinuities.[10]

The characteristic feature of ALD is that films of almost any thickness can be deposited (from microns to monolayers),[20] where the film thickness depends solely on the number of reaction cycles. This allows precise control over the film thickness. Due to the self-limiting nature of ALD growth, the amount of material deposited in each reaction cycle should be constant; irrespective of the process parameter conditions.

Unlike CVD processes which are highly temperature dependent, ALD processes have a weak temperature dependency (Figure 1.3),[13] as the growth rate depends on the number of reaction cycles only. ALD processes display a temperature window, where film deposition occurs via a self-limiting mechanism. Within this temperature range, there is sufficient energy for chemical reactions to take place on the substrate surface and a constant growth rate is observed. This substrate temperature region is known as the "ALD process window",[21] where the half-cycle reactions result in the formation of fully saturated layers. For reproducibility in film thickness, ALD

experiments should be performed at growth temperatures within this process window. It is important to note that the ALD temperature window varies depending on which precursors are being used and on the target film material.

Typically, as the deposition temperature is reduced below the "ALD process window", the film thickness decreases. This is because precursor adsorption to the substrate surface is a thermally activated process.[21] Groner *et al*. showed that the growth rate of aluminium oxide (Al_2O_3) by ALD decreased at temperatures below 100 °C. Reinke *et al.* reported that the growth rate of TiO_2 by ALD of [$Ti(O^iPr)_4$] and water decreased below a growth temperature of 190°C.[22] Conversely, depositions performed at lower temperatures may also result in a higher growth rate. In this case the precursors condense onto the walls of the reactor and the substrate, as the temperature is insufficient for film growth to occur. As both precursors are present within the reactor at the same time, they can readily react with each other which results in a thicker film being produced. When the growth temperature is increased to that above the "ALD process window", the growth rate usually increases quite significantly due to thermal decomposition of the metal precursor, resulting in CVD-like growth.[21] Again, the decomposition temperature of the metal precursor will determine the upper limit of the "ALD process window", so it is different for each precursor.

Figure 1.3 illustrates the relationship between the ALD growth rate as a function of the deposition temperature.

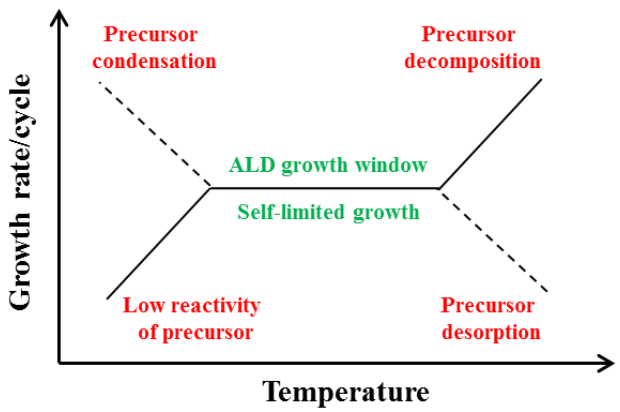

Figure 1.3 ALD growth rate as a function of deposition temperature

1.2.3 Advantages and Disadvantages of ALD

Atomic layer deposition has several advantages for deposition of thin films, as outlined below:

- Accurate thickness control at the monolayer level.[23]
- Film thickness depends only on the number of reaction cycles.
- Excellent conformality; which means that 3D structures can be easily coated.[24]
- High reproducibility.[25]
- Low deposition temperatures can be utilised (typically < 350 °C).[26]
- Low impurity levels within films.

The lower deposition temperatures which can be utilised make ALD an ideal technique for the deposition of thin films onto temperature-sensitive substrates such as polymeric or biological samples.[8] However, the main disadvantage of ALD is the slow growth rate, as usually only a few angstroms of material are deposited in each reaction cycle.[12] It can often be the case that sub-monolayer growth occurs rather than full monolayer growth. This can be due to several factors such as the deposition conditions and steric hindrance of bulky ligands on precursor molecules. The slow growth rate of ALD can often be alleviated by the ability to do large batch processing or role-to-role. However, the slow growth rate also makes ALD an economical industrial process for high value applications, for example solar cells,[26] high strength glass, optics[27] and semiconductor fabrication.[23] Nevertheless, ALD is also being considered for the coating of 'low value' products such as food packaging, either using role-to-role or batch processing.[28] The slow growth rate is mitigated by the techniques compatibility with large batch processing and insensitivity to process parameters such as temperature and dose.

1.3 Chemical Vapour Deposition

Chemical vapour deposition (CVD) has been used for many years as a central deposition technique for a variety of materials including metals, oxides, nitrides, sulfides, composites and powders.[29] In fact, the majority of the elements in the periodic table have been deposited via CVD in some way or another; either as the pure element or more commonly as a compound.[29] Films deposited by CVD cover a broad range of application areas, including semiconductors for microelectronics, ceramics for hard coatings, metallic films for protective coatings and fibre coating.[30]

There are several different types of CVD processes which include:[29,31]

- Conventional chemical vapour deposition (thermal CVD).
- Atmospheric pressure chemical vapour deposition (APCVD).
- Aerosol-assisted chemical vapour deposition (AACVD).
- Low pressure chemical vapour deposition (LPCVD).
- Metal-organic chemical vapour deposition (MOCVD).
- Plasma enhanced chemical vapour deposition (PECVD).
- Laser chemical vapour deposition (LCVD).
- Photochemical vapour deposition (PCVD).
- Chemical beam epitaxy (CBE).
- Chemical vapour infiltration (CVI).

CVD processes involve the introduction of gaseous precursors into a heated reaction chamber; where simultaneously, homogeneous reactions take place in the gas phase and heterogeneous reactions take place on or near the substrate surface, resulting in a film being deposited on the hot substrate (Figure 1.4).[32] Unlike ALD which involves sequential dosing and purging of precursors, CVD uses a continuous flow of a precursor(s).[17] CVD deposition rates are often much higher than that of ALD[33] and also require much higher temperatures (350 - 1200 °C)[30] which can limit their applications to deposit onto temperature-sensitive substrates.

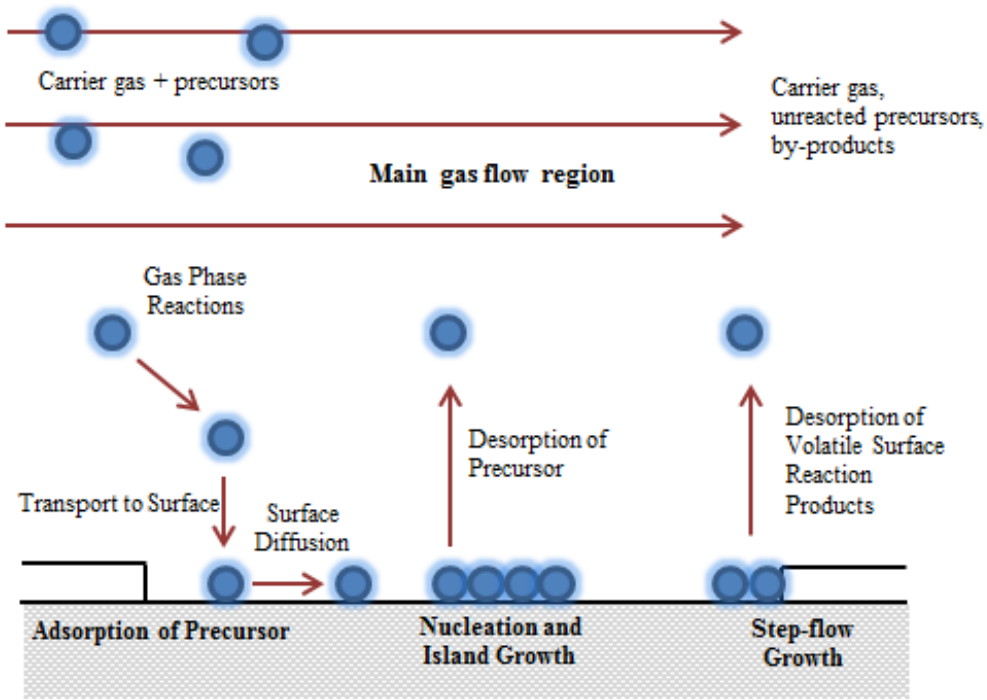

Figure 1.4 Chemical vapour deposition reaction mechanism

There are three different growth models which exist for CVD film deposition, which help describe some of the different morphologies observed (Figure 1.5).[34] Usually, the type of CVD growth taking place can be determined using scanning electron microscopy (SEM).

1) Island growth (or Volmer-Weber) – atoms in the deposited film are more strongly attracted to each other than the substrate.

2) Layer growth (or Frank-van der Merwe) – proceeds layer by layer, where the atoms in the film are attracted more strongly to the substrate than to each other.

3) Stranski-Krastanov – between the two extremes, by proceeding initially by a layered growth followed by island type growth afterwards.

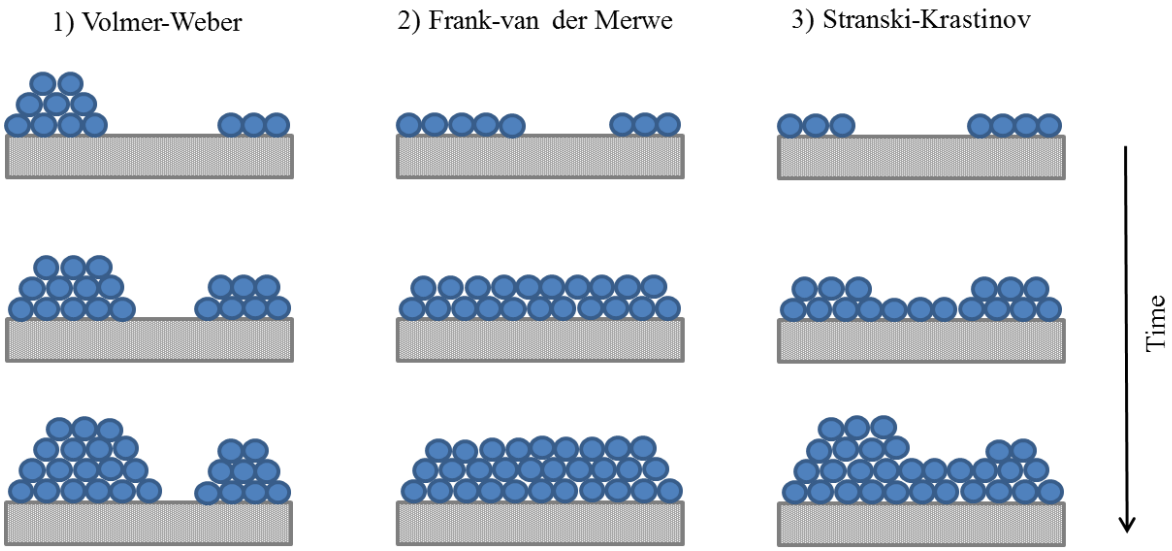

Figure 1.5 Basic models of CVD film growth

1.4 ALD vs CVD

Although ALD deposition rates are slower than CVD, the self-limiting nature of ALD enables a much greater control over the film thickness, in the order of angstroms.[8] ALD is capable of producing films of higher purity and uniformity, which makes it a much more attractive technique within the semiconductor industry.[17] 3D nanostructures and microstructures can be confidently coated with uniform and conformal thin films. Table 1.1 outlines the main advantages of ALD over CVD.

ALD	CVD
Low deposition temperature	High deposition temperature
Excellent control over film thickness	Good control over film thickness
Excellent uniformity	Good uniformity
Excellent conformality	Good conformality
Excellent reproducibility	Good reproducibility
Low impurity levels	Some impurity levels
High degree of control	Limited level of control
Slow deposition rate	Fast deposition rate

Table 1.1 ALD vs CVD main features

1.5 Chemistry of Precursors

1.5.1 General requirements of ALD precursors

Many thin film materials can be grown via ALD including oxides, sulfides, nitrides, fluorides and metals.[35] In the past 10 years or so, the interest in ALD of metal oxide and nitride films has increased due to their wide range of functional properties which make them promising materials for use in a range of technological applications.[36] Precursors used in atomic layer deposition can be gaseous, liquids or solids,[12] but it is highly important that they are volatile at a temperature lower than the ALD growth temperature.[13] With the exception of highly volatile precursors, it is often a requirement that they are heated to increase the vapour pressure and therefore facilitate transportation of the vaporised molecules into the reactor. It is also preferable that precursors react aggressively with sites on the substrate surface in an irreversible fashion and be thermally stable at the ALD growth temperature.[13] For industrial sized processes, the cost of precursors involved becomes an important factor.

1.5.2 General requirements of CVD precursors

Usually the same precursor requirements apply, regardless of the type of CVD taking place. "Ideal" CVD precursors should possess the following characteristics:[30,31]

- Sufficient volatility.
- Large temperature "window" between evaporation and decomposition.
- Stable during evaporation.
- High chemical purity.
- Decomposes cleanly with minimal incorporation of impurities in films.
- Compatible with co-reactant precursors.
- Stable when exposed to air or moisture (i.e. long shelf-life).
- Readily manufactured in high yields and low costs.
- Non-hazardous and low toxicity.

Precursors most commonly used in CVD processes are metals, metal hydrides, halides and metalorganic compounds.[30] Metal halides are typically more stable than metal hydrides, whereas metalorganic compounds can be deposited at lower temperatures. This gives rise to metalorganic precursors being increasingly used in semiconductor applications.[30]

CVD is generally considered as one precursor reacting with a secondary gas at a substrate surface to deposit the material of interest, however it is not uncommon for precursors to act as a "single-source" and deposit films without the need of the secondary gas. In this case a delicate balance must be achieved between the thermal stability of the precursor in the gas phase and the chemical reactivity at the substrate surface.[37]

Often the precise precursor requirements will differ depending on the type of CVD being used. It is advantageous that CVD precursors are air stable and not react with water. However, these are the opposite requirements for ALD precursors, where highly moisture and water sensitive precursors are sought for the deposition of metal oxide films with acceptable growth rates. Additionally, the ligand size of the precursors is important for both CVD and ALD precursors. ALD precursors require relatively small ligands with low steric hindrance around the metal centre; otherwise very low growth rates would be achieved. In contrast, CVD processes favour precursors with bulky ligands as this can increase the vapour pressure and thus make the precursor less air/moisture sensitive.[31] Figure 1.6 outlines the major precursor characteristics which must be fulfilled in order to achieve respectable CVD and ALD film growth.

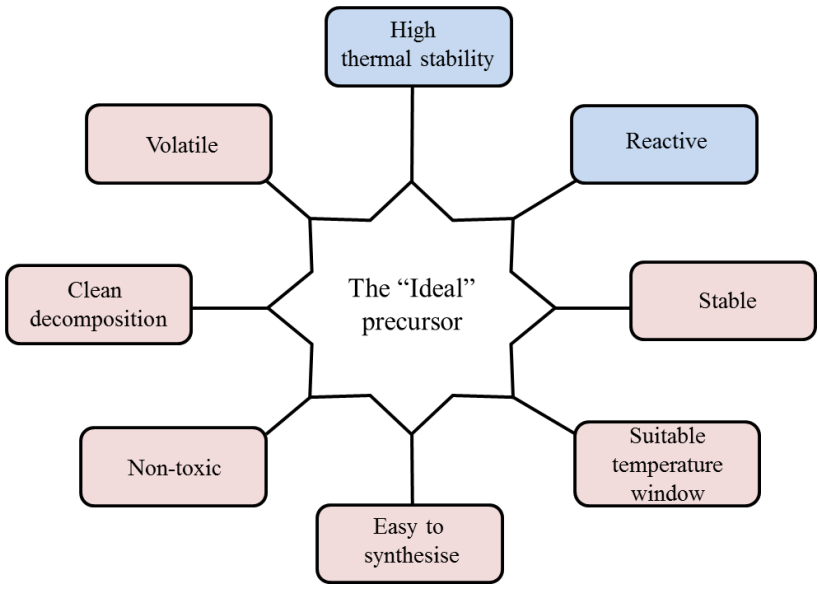

Figure 1.6 Summary of the most important characteristics for CVD precursors (red) and ALD precursors (red and blue)

1.5.3 Types of precursors

1.5.3.1 Metal precursors

ALD growth normally involves reaction of a metal precursor with a non-metal precursor (co-reactant, or oxidant). There are a variety of different compounds which can be used as metal precursors (Figure 1.7); the most commonly used are alkoxides, alkyls, halides, β-diketonates and cyclopentadienyls.[13] There are benefits and drawbacks to using each type of metal precursor for ALD. For example, metal alkyls are very reactive but stable alkyls are not available for many metals.[13] Metal chlorides (halides) are reactive and temperature stable, but leave chlorine impurities in the film, which is undesirable. Advantages of using β-diketonates are that they are normally thermal stable and can be easily synthesised, but they can have limited volatility.[38]

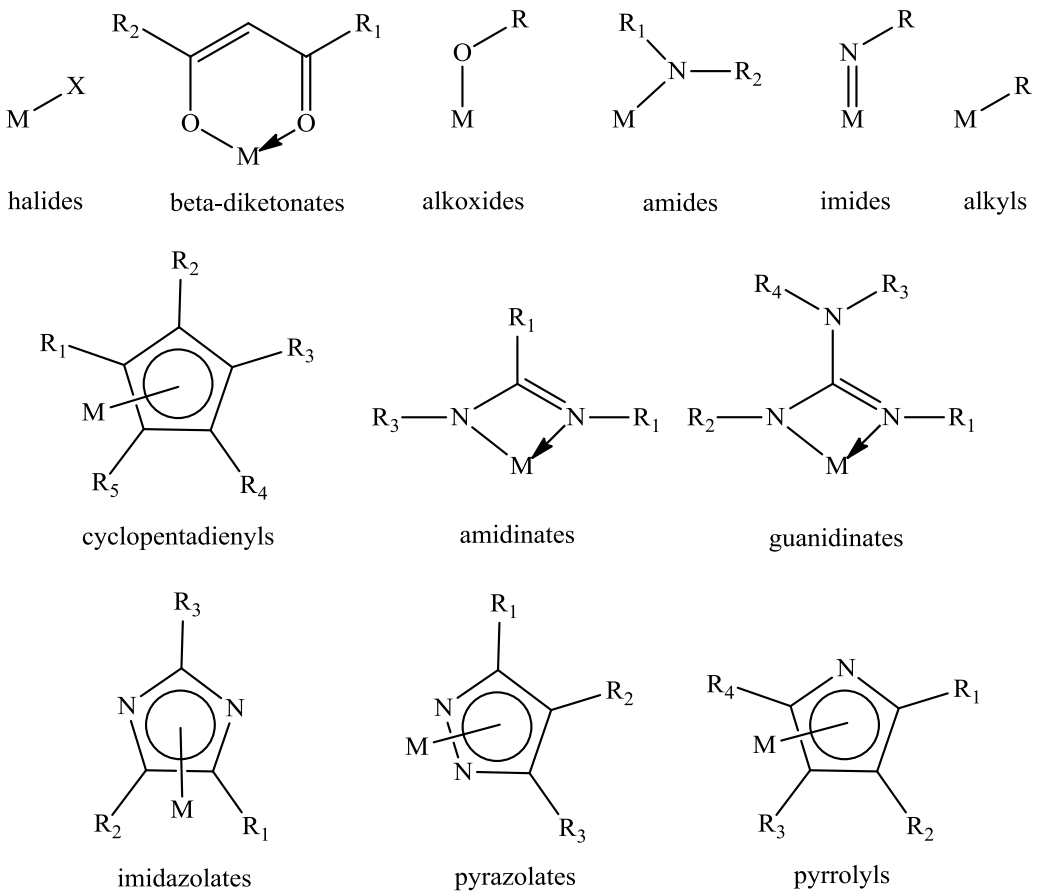

Figure 1.7 Classes of metal precursors used in ALD and CVD

Alkoxides

Metal alkoxides have been successfully employed in many oxide deposition processes. They are commonly used as oxide precursors to deposit early-transition metals.[39] However these precursors have been less studied for late-transition metals and alkaline earth metals, as they tend to have low solubility, stability and volatility.[11] Alkoxides contain metal-oxygen bonds which are strong and usually relatively short in length. This implies multiple-bond character due to the π-bonding of the oxygen *p*-orbital to the metal *d*-orbital.[40] ALD of titanium isopropoxide, $[Ti(O^iPr)_4]$ and water is a common example of the use of alkoxides in practise. Ritala *et al.* reported the deposition of TiO_2 from $[Ti(O^iPr)_4]$ and water where a temperature-independent growth rate of 0.3 Å/cycle was achieved between 250 - 325°C.[19] Aarik *et al.* have demonstrated the deposition of TiO_2 from $[Ti(O^iPr)_4]$ and water and also with H_2O_2 at substrate temperatures in the range of 100 - 250 °C.[41]

Aluminium alkoxides have also been widely used as ALD precursors. Aluminium alkoxides have a strong affinity for water so are valuable precursors for the deposition of aluminium oxide by ALD with water.[42] Aluminium ethoxide, $[Al(OEt)_3]$ and Aluminium propoxide, $[Al(O^nPr)_4]$ have both been used in combination with H_2O and O_2 to deposit Al_2O_3 thin fims.[13]

Thin films deposited from alkoxides and aminoalkoxides are mainly amorphous throughout, which may be a result of impurities within the films due to thermally unstable precursors.[13] Nickel(II) aminoalkoxides such as $[Ni(dmamp)_2]$ (dmamp = 2-dimethylamino-2-methyl-1-propanolate), $[Ni(deamp)_2]$ (deamp = 1-diethylamino-2-methyl-2-propanoxide), $[Ni(emamp)_2]$ (emamp = 1-ethylmethylamino-2-methyl-2-propanoxide) and $[Ni(dmamb)_2]$ (dmamb = 1-dimethylamino-2-methyl-2-butanoxide), have been employed as precursors for metal-organic chemical vapour deposition (MOCVD) of nickel metal thin films[43] and ALD of NiO thin films.[44] The volatile liquid precursor nickel bis(1-dimethylamino-2-methyl-2-butanolate), $[Ni(dmamb)_2]$ has been employed - as an MOCVD precursor[45] and an ALD precursor with water[44] for the deposition of NiO at temperatures in the range of 230 - 410 °C and 140 - 240 °C, respectively. The use of aminoalkoxides for ALD of ZrO_2 has also been investigated. Matero *et al.* demonstrated the use of $[Zr(dmae)_4]$, $[Zr(dmae)_2(O^tBu)_2]$ and $[Zr(dmae)_2(O^iPr)_2]$ (where dmae is dimethylaminoethoxide, $[OCH_2CH_2N(CH_3)_2]$), to deposit ZrO_2 by ALD with water at 190 - 340 °C.[46]

β-diketonates

β-diketonate precursors such as acetylacetonate (acac), 2,2,6,6-tetratmethyl-3,5-heptanedionate (thd) and hexafluroacetylacetonate (hfac) exist for a large variety of elements and have been employed for obtaining a variety of metal oxide films. β-diketonates are available for the following elements; Mg, Ca, V, Cr, Mn, Fe, Co, Ni, Cu, Zr and many more.[26] Although β-diketonate ligands can be easily synthesised and have reasonable thermal stability,[38] they are usually bulky and have low reactivity, which means that film growth rates are often low. In order to achieve their highest oxide growth rates, they require a more reactive co-reactant such as O_3.[26] The insufficient reactivity of β-diketonates is therefore the main limitation for their use in

ALD of metal oxide thin films.[38] Having said this, there are still reports in the literature of β-diketonates being used to deposit metal oxide films by ALD. Lindahl *et al.* presented the formation of NiO films via ALD of bis(2,2,6,6-tetramethylheptane-3,5-dionato) nickel(II), [Ni(thd)$_2$] and water.[47] The authors reported that a large excess of water was required in order to reach the saturation level at growth temperatures up to 275°C. In addition, copper(II) hexafluoroacetylacetonate, [Cu(hfac)$_2$], has been utilised as an ALD precursor to deposit copper oxide films with water.[48] Although the fluorinated ligand, hexafluoroacetylacetonate, exhibits a higher volatility as compared to their non-fluorinated counterparts, the fluorine residues present within the deposited films can create adhesion problems to the substrate.[48] Nickel(II) acetylacetonate, [Ni(acac)$_2$] and copper(II) acetylacetonate, [Cu(acac)$_2$] have been employed to deposit NiO[49] and CuO[50] films respectively by ALD with O_3.

Cyclopentadienyls

Metal cyclopentadienyl (Cp) complexes are attractive ALD and CVD precursors because they are usually volatile and reactive towards water. The impurity levels in the deposited films are normally minimal too.[51] In cyclopentadienyl compounds the metal is usually coordinated to all five carbon atoms in the Cp ring. This therefore enhances the stability and reactivity of the compounds whilst providing shielding effects.[38] The Cp rings, as well as the R groups on the rings can be substituted to increase or decrease the bulkiness of the compound. Cp complexes of Mg, Hf, Zr, Ni and Ca[38] have been used to deposit metal oxide films by ALD with water as the co-reactant. Metallocenes have also been used to form pure metal films of Cr, Mn, Co and Ni at high temperatures (> 500 °C).[51] Nickel cyclopentadienyls have been used to deposit nickel metal by CVD and nickel oxide by ALD. For nickel oxide growth, highly reactive co-reactants are usually required (e.g. O_3, O_2, H_2O_2) in order to achieve films of high purity.[52] On the other hand, CVD of cyclopentadienyl compounds often results in films with high levels of carbon contamination.[51] Nickel oxide thin films have been deposited by ALD of nickelocene, [Ni(Cp)$_2$] and water at 165 °C. A consecutive reduction step then reduced NiO to Ni metal using hydrogen radicals.[53] The use of bis-(ethylcyclopentadienyl) nickel, [Ni(EtCp)$_2$] as an ALD

precursor has also been demonstrated by Lu *et al.*, where NiO films were deposited at substrate temperatures between 150 - 250 °C using O_3 as the co-reactant.[54] However there are reports in the literature of NiO films being successfully deposited by ALD of $[Ni(Cp)_2]$ and water at a substrate temperature of 250 °C.[55]

Guanidinates

Guanidinate complexes are favourable ALD precursors, where the earliest report of their use for thin film deposition was reported by Carmalt *et al.* in 2005.[56] Since these precursors do not contain metal-carbon bonds, the amount of carbon contamination within the resulting films is minimal, which inevitably improves the ultimate purity and electrical characteristics of the films.[57] The R and R' groups on the ligand backbone can be easily tuned which enables a significant degree of electronic and steric stabilisation. It is expected that the bidentate chelating effect of these ligands enhances the thermal and chemical stability of the resulting metal complex, which makes them suitable precursors for ALD and CVD applications.[36] The presence of the NR_2 moiety in guanidinate compounds allows zwitterionic resonance structures to form[36] (Figure 1.8). Amidinates do not possess the NR_2 moiety and are incapable of forming such resonance structures because the π system is restricted to the coordinating nitrogen's.

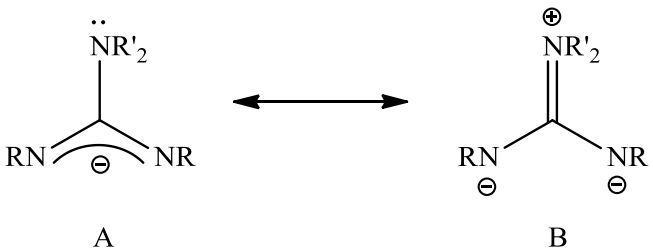

Figure 1.8 The resonance structures of guandinate ligands

The literature demonstrations that metal guanidinates have been utilised to deposit a range of carbonitride films. Zirconium guanidinates,[58] $[ZrCp'\{\eta^2\text{-}(^iPrN)_2CNMe_2\}_2Cl]$ and $[ZrCp'_2\{\eta^2\text{-}(^iPrN)_2CN\text{-}Me_2\}Cl]$ where Cp' = monomethylcyclopentadienyl and titanium guanidinates,[56] $[Ti(NMe_2)_2Cl\{^i\text{-}PrNC[N(SiMe_3)_2]N^iPr\}]$ have been used to deposit zirconium and titanium

carbonitrides respectively via LPCVD (low pressure chemical vapour deposition) at 600 °C. A variety of copper and silver guanidinate complexes have also been synthesised as potential ALD and CVD precursors by the Barry group.[59]

Consequently, decision of which is the most suitable precursor depends on several parameters, including the target film material to be deposited, growth temperature, and co-reactant etc. To date, very few nickel guanidinate complexes have been synthesised and their use in ALD/CVD applications evaluated. Those reports in the literature describe the synthesis and characterisation of bulky nickel(I) guanidinates, which gives scope for research into new precursors in this area.

1.5.3.2 Non-metal precursors

Non-metal precursors (oxidants or co-reactants) are normally hydrides; water (H_2O), hydrogen sulfide (H_2S) and ammonia (NH_3)[11] which are used to grow oxides, sulfides and nitrides respectively; all of which are volatile and thermally stable. Many ALD papers have reported that H_2O and H_2S form suitable surface species for the metal precursor to be anchored to.[11] Other commonly used oxidants are O_3, H_2, and H_2O_2.[26] Hydrogen plasmas have been used as co-reactants as a source of hydrogen radicals. However, the chemistry of plasmas is rather difficult to control, which may lead to additional side reactions.[60]

ALD precursors for oxygen sources include H_2O, hydrogen peroxide (H_2O_2), ozone (O_3), oxygen (O_2) and alcohols (such as methanol or ethanol). For the deposition of metal oxides via ALD, water has most commonly been used as the oxidant. Occasionally, water is not a desirable oxidant because it may be too reactive with the metal precursor. Therefore water-free ALD processes have been developed, where an alkoxide metal precursor acts as both the metal and oxygen source and a second metal precursor (typically a metal chloride) acts as a second metal source.[61] The metals in the two compounds may be the same (equation 1.2) or different (equation 1.3), where *a* and *b* are the oxidation states of the metals. If different metals are used, then mixed oxides are formed.

$$M(OR)_a + MX_a \rightarrow 2\,MO_{(a/2)} + aRX \qquad (1.2)$$

$$bM(OR)_a + aM'X_b \rightarrow M_bM'_aO_{(a+b)/2} + (a+b)RX \qquad (1.3)$$

Utilisation of two metal precursors and eliminating the use of a separate oxygen precursor means that the substrate surface is less susceptible to oxidation. This is highly important for when oxide thin films are being coated directly onto a silicon substrate, without creating an inter-facial silicon oxide layer.[11]

More reactive oxidising agents (O_3 for example) are normally used when the metal precursor is less reactive. However, this causes problems in some applications, for example gate oxide applications, where the strong oxidising character of O_3 can create SiO interfacial layers which are too thick.[11] There are also reports of O_2 being used as an oxidant for ALD processes. TiO_2 films have been deposited by ALD of titanium iodide and O_2 at substrate temperatures in the range of 200 - 350 °C.[62] It is likely that if the metal precursor is thermally unstable, then O_2 is reactive enough to form the oxide film at low growth temperatures.

1.6 ALD of metal oxide thin films

1.6.1 Introduction to metal oxide thin films

ALD has been used to deposit a variety of metal oxide thin films with various applications in industry, such as dielectrics in electroluminescent displays,[11] metal-oxide semiconductor field-effect transistors (MOSFET),[12] optics, electronics[27] and superconducting devices.[40] Many oxides are known for their chemical inertness, resistance to oxidation and good high temperature properties.[9] They can provide several advantages including high electrical conductivity (transparent conducting oxides, TCO's), optical transparency and chemical stability.[63] Yet there are still exceptions; some metal oxides are thermally (for example silver oxide) or chemically unstable and some readily undergo oxidation (FeO and MnO). Some of the most widely deposited metal oxide materials are zirconium dioxide, aluminium oxide, tin oxide and titanium dioxide.[26]

1.6.2 ALD of TiO_2 thin films

There are several different titanium-based precursors which have been employed in the ALD of titanium dioxide (TiO_2) thin films. Titanium tetrachloride [$TiCl_4$] and titanium isopropoxide [$Ti(O^iPr)_4$] are the most commonly used precursors, together with either water or hydrogen peroxide.[13,64] Reports have shown that high quality thin films have been produced at temperatures in the range of 100 - 500 °C.[65] Chlorides make good ALD precursors because they are stable, volatile, reactive and usually cheap. However, the main drawback of $TiCl_4$ is that it is highly corrosive to the system and reactions evolve HCl gases. Aarik *et al*. have observed significant chlorine contamination in TiO_2 thin films grown at 100 °C.[66] Figure 1.9 shows a schematic of an ALD deposition cycle for a titanium-based metal precursor and water as the oxidant.

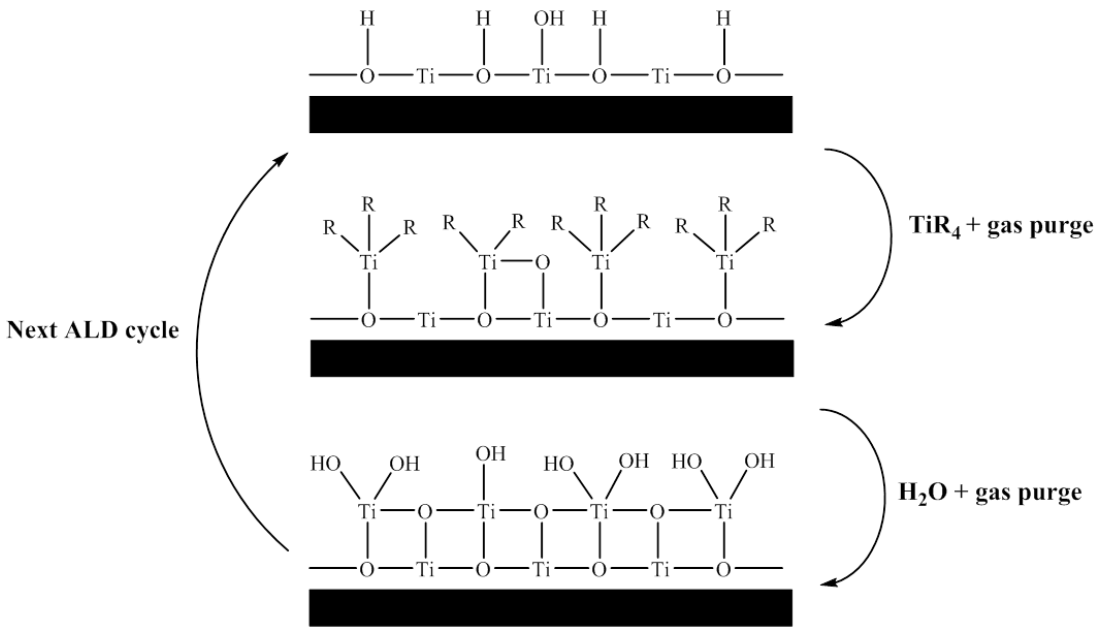

Figure 1.9 Schematic of ALD growth mechanism for titanium metal precursor and water[6]

Titanium alkoxides, such as titanium ethoxide [$Ti(OEt)_4$] and titanium isopropoxide [$Ti(O^iPr)_4$], are also widely used precursors for the growth of TiO_2 thin films because they are halide-free and non-corrosive.[67] Both the substrate temperature and dose times have been shown to influence the resultant growth rate of the films. Temperatures in the range of 50 - 350 °C and 200 - 400 °C have been used to grow

films using titanium isopropoxide and titanium ethoxide respectively.[64] It has been reported that when using titanium ethoxide as the metal precursor, lower growth rates are achieved at temperatures below 300 °C when compared to titanium isopropoxide.[64] Additional titanium alkoxides which can be used to grow TiO_2 films are shown below. The precursors are ordered by their decomposition temperatures.[67]

$$[Ti(O^tBu)_4] \leq [Ti(O^iPr)_4] \leq [Ti(OEt)_4] \leq [Ti(OMe)_4]$$

Titanium isopropoxide is an ideal precursor of choice for the deposition of TiO_2 by ALD, as although it is not as stable as titanium ethoxide, it is favoured due to its high vapour pressure. Titanium methoxide $[Ti(OMe)_4]$ can undergo oligomerisation, which is due to the tendency of the titanium to saturate its co-ordination number; which decreases the volatility relative to monomers. Oligomerisation can be prevented by using bulky alkyl groups, but if the alkyl chains are too long, the intermolecular forces between the alkyl groups increases, which lowers the volatility of the precursor.[19] Titanium tert-butoxide $[Ti(O^tBu)_4]$ was omitted as even though it has a high vapour pressure, it is believed to be facile to thermal decomposition.[19]

1.6.3 ALD of NiO thin films

ALD of nickel oxide (NiO) thin films is becoming increasingly more studied due to its wide-range of properties, making it an attractive material for various applications such as electrochromic devices and catalysts.[47] NiO films possess excellent chemical stability with very high resistivity and melting point (~ 2000 °C).[68] When heated, NiO behaves as a *p*-type semiconductor material due to the generation of Ni^{2+} vacancies in the NiO structure,[68] which means that it can be used in transparent electrodes and window coatings.[69] Recently, NiO films have drawn more attention due to their ability to reproducibly switch between high and low-conductivity states due to external currents or voltages,[70] which is applicable to resistive random access memories (ReRAMs). The antiferromagnetic properties of NiO also play an important role in magnetic recording and magnetic memories.[71]

NiO films have been prepared using several techniques including; metal-organic chemical vapour deposition (MOCVD),[43,45,72] nebulised spray pyrolysis (NSP),[68] electron-beam evaporation, sol-gel[73] and atomic layer deposition (ALD).[44,47, 49,52,54,55]

Reports show that there are a limited number of nickel precursors which have been used to produce NiO films via ALD. Precursors which have been closely examined are [Ni(acac)$_2$] (acac = acetylacetonato),[49,52] [Ni(thd)$_2$] (thd = 2,2,6,6-tetramethyl-3,5-heptanedionate),[47] [Ni(Cp)$_2$] (Cp = cyclopentadiene),[55,74] [Ni(dmamp)$_2$] (dmamp = 2-dimethylamino-2-methylpropanoxide),[13] [Ni(dmg)$_2$] (dmg = dimethyl-glyoximato)[13] and [Ni(apo)$_2$] (apo = 2-amino-pent-2-en-4-onato).[75] All of which have been used for ALD with various oxygen sources; O_2, H_2O, O_3.

Yang *et al.* reported that [Ni(acac)$_2$], [Ni(apo)$_2$] and [Ni(dmg)$_2$] (Figure 1.10) had poor vapour phase stabilities in the order [Ni(apo)$_2$] > [Ni(acac)$_2$] > [Ni(dmg)$_2$].[75] [Ni(acac)$_2$] has a low volatility because it is capable of forming trimers,[47] which makes it a less suitable precursor for ALD. [Ni(dmg)$_2$] has a chelate structure with polar O-H-O groups. The low volatility of this precursor is likely to be due to these polar groups. The [Ni(apo)$_2$] ligand belongs to the class of β-ketoiminates, where the oxygen and nitrogen atoms are coordinated to the nickel centre. As a result of this, its volatility is lower than that of [Ni(thd)$_2$].[72]

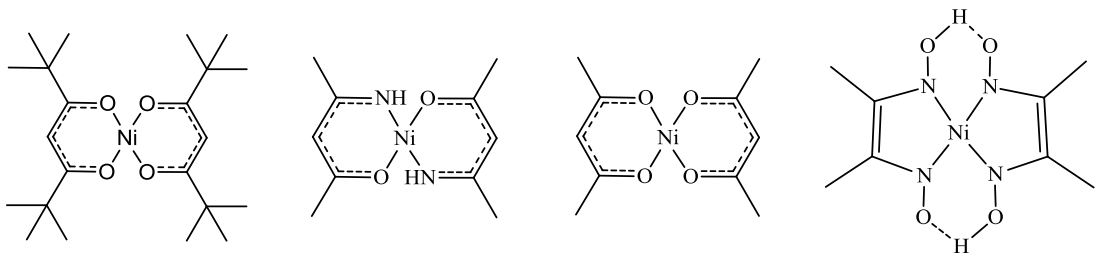

Figure 1.10 Structures of nickel-containing precursors

Several reports have shown the growth of NiO films using the $[Ni(thd)_2]$ and H_2O precursor combination.[47] Although the precursor is a solid, its "closed" structure formed by the large tert-butyl groups means that it has a reasonably high vapour pressure. Reports show that it can be deposited at temperatures below 300 °C[52] to give NiO growth rates in the region of 0.3 - 0.4 Å /cycle.[47]

$[Ni(dmamp)_2]$ and $[Ni(Cp)_2]$ are both solids at room temperature, with relatively high volatilities. They can be used to deposit NiO films at temperatures between 100 - 170°C[76] and 165 - 330 °C,[77,53,55] respectively. However, reports of ALD of $[Ni(Cp)_2]$ and water are more limited to porous materials than flat substrates. $[Ni(dmamp)_2]$ was originally synthesised as a CVD precursor for nickel metal, but has received more attention recently as a precursor for ALD of NiO.[44,75]

Guanidinates are relatively new precursors for thin film deposition, where their earliest reported use dates back to 2005. A variety of oxides (TiO_2, ZrO_2, HfO_2); nitrides (GdN, DyN) and metals (Cu) have since been deposited by CVD and ALD techniques using metal guanidinate precursors.[78] The majority of the metal oxide films deposited by ALD have used H_2O as the co-reactant precursor. Reports showing the use of nickel guanidinates to deposit NiO films are in their infancy, which gives scope for research in this area.

1.7 Applications of metal oxide films

Metal oxide films deposited by either ALD or CVD have applications across several different areas such as microelectronics,[36] photovoltaics,[26] optoelectronics,[79] anti-reflective coatings[80] and gas sensing.[81]

Microelectronics is probably one of the most studied and useful applications for ALD processing. The main driving force for the continued interest of ALD in microelectronics is the ability to create uniform step coverage over topographical structures.[21] ALD is becoming increasingly important since the industry transitioned to using high-k-dielectrics for the transistor gate stack in microelectronics.[26] In 2007, Intel introduced ALD to its production line in order to gain accurate control over gate oxide film thickness and conformaltiy to ultimately prevent leakage current through the gate oxide.[26] The conformality requirements are even higher for dynamic random access memories (DRAM's), so ALD is the only suitable technique for when feature sizes become smaller than 100 nm.[12]

The use of ALD for photovoltaic applications dates back to the early 1990's, where the application was reported in 1994 by Bedair and co-workers.[82] At that time, their research focused on the deposition of GaAs, AlGaAs and AlAs films for use in solar cells. Materials have since been fabricated by ALD to serve a range of purposes within the photovoltaics industry, such as passivation layers and electrodes.[48] ALD has also been used to produce transparent conducting oxides (TCO's) for solar cell technologies.[26]

Fuel cells are also becoming increasingly more important as alternative forms of energy supply. ALD is being explored as a method to create components for energy-efficient solid oxide fuel cells (SOFC), which are devices capable of converting chemical energy into electrical energy.[26] Such components include solid electrolytes, ion conductors and catalysts.[48] Other noteworthy applications of ALD include organic light emitting diodes (OLED's), semiconductor devices,[10] catalysis[7] and gas sensing.[83]

1.8 Metal oxide films for gas sensing

1.8.1 Gas sensor introduction

Semiconducting metal oxides (SMO's) have attracted a lot of attention in the field of gas sensing due to their low cost, compact size, simplicity in fabrication and use, versatility in detecting a wide variety of toxic/flammable gases and stability in harsh environments.[1] Semiconductors are arranged as lattice structures, and when heated 'free' electrons and 'holes' are generated, which thus affects the conductivity of the material. SMO's are electrically conductive sensors whose resistance changes when in contact with particular gases (reducing or oxidising gases). Although the fundamental mechanisms are still controversial, a gas response is essentially due to the chemisorbed gas species capturing or replenishing electrons from the thin film.[84] Ideally, the gases to be detected should react with the gas sensor surface in a reversible manner.

The performance of metal oxide gas sensors is strongly influenced by the film morphology and structure of the sensors,[84] which is a great problem when trying to achieve highly sensitive materials. Previously reported methods for depositing thin film gas sensing materials include magnetron sputtering,[2] sol-gel,[85] CVD,[83] ultrasonic spray pyrolysis[2] and more recently by ALD.[86] Improvements in sensor properties can be achieved using ALD, which can produce highly conformal metal oxide films with excellent thickness control. There are three main components which are typical of semiconductor gas sensors; gas sensing material (thin film), electrodes and a heater[87] (Figure 1.11).

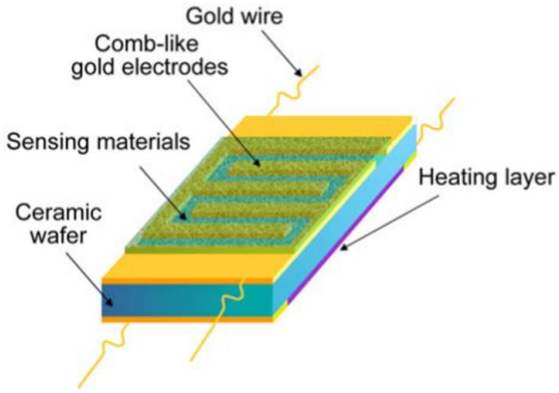

Figure 1.11 Gas sensor structure based on a ceramic wafer substrate[44]

An *n*-type SMO (TiO_2 for example) interacts with ambient oxygen, which can trap electron charge carriers from the bulk of the film, resulting in an electron-depleted layer at the film surface.[88] Therefore the material film thickness is an important factor for the gas sensing mechanism. As the film thickness decreases, the size of the electron-depleted layer makes up a greater proportion of the material (Figure 1.12), so theoretically the entire sensing element becomes electron-depleted, providing the least conducting state (i.e. the greatest change in electrical conductivity).[89]

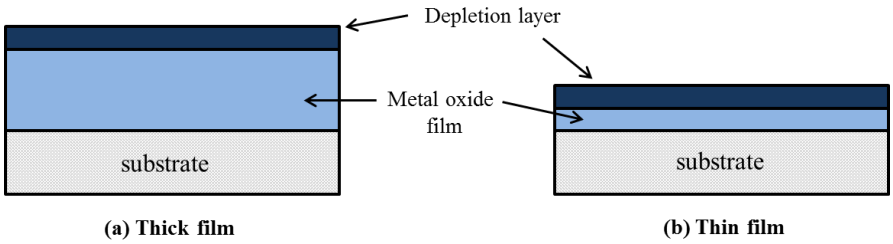

Figure 1.12 Effect of metal oxide film thickness on the proportional size of the electron depletion layer

The key factor defining the enhancement of the gas sensor response with film thickness is the Debye length.[90] This characterises the size of the space-charge region next to the surface where the free carrier concentration may be affected by the chemisorbed gas species.[90] Sysoev *et al.* reported the Debye length for TiO_2 to be ~0nm at 250 °C.[91] The resistance through this space-charge region will be different to that of the 'bulk' film. ALD is therefore an advantageous technique for semiconductor processing, as it is capable of depositing semiconductor metal oxide

films with thicknesses in the order of the Debye length.[90] The use of ALD for exploring the effect of *n*-type SnO_2 film thickness on the gas sensor response was reported by George *et al.* in 2008.[90] An optimum sensitivity towards CO gas was found at a film thickness of 3 nm, which correlates with the Debye length for SnO_2 under the conditions of test.

1.8.2 Gas sensing mechanism

Although the fundamental gas sensing mechanism is still controversial, a gas response is essentially due to a change in conductivity through the adsorption/desorption of gases at the material surface. An *n*-type metal oxide semiconductor is one where the majority of charge carriers are electrons. Upon interaction with a gas in ambient oxygen, a change in the electrical conductivity is observed. Interaction with a reducing gas (e.g. NH_3) sees an increase in the conductivity, whereas interaction with an oxidising gas (e.g. O_2) serves to deplete the sensing layer of charge carrying electrons and the film conductivity decreases.[83] A *p*-type metal oxide semiconductor has positively charged holes as the charge carriers, so the opposite effects are observed for *p*-type materials when exposed to either reducing or oxidising gases. Exposure to an oxidising gas sees an increase the film conductivity, as the gas increases the number of positively charge holes. Whereas exposure of the material to a reducing gas sees a decrease in the film conductivity, as the negative charge introduced into the material reduces the number of positively charged holes.[84] The table below summarises the gas response for *n*- and *p*-type materials.

Classification	Oxidising Gases	Reducing Gases
n-type	Resistance increase	Resistance decrease
p-type	Resistance decrease	Resistance increase

Table 1.2 Resistance changes of *n*- and *p*-type materials when exposed to different gases

When semiconducting metal oxides are exposed to air, oxygen molecules adsorb onto the film surface; where *n*-type materials can capture electrons from the bulk of the film to produce an electron-depletion layer at the film surface,[88] and *p*-type materials can form a hole-accumulation layer by the adsorption of negatively charge oxygen.[3] The creation of the depletion region results in an increase in the resistance of the oxide material.[92] A schematic representation of the gas sensing mechanism for an *n*-type metal oxide semiconductor is outlined in Figure 1.13. The target gas (reducing gas) reacts with the surface oxygen species, which releases electrons back into the conduction band of the material, resulting in an increase in conductivity.

When the sensor is exposed to a reducing gas, the electrons in the electron-depletion layer return to the bulk of the film, which results in an increase in the electrical conductivity (decrease in resistance).[90] The operational temperature can influence the types of oxygen species found on the film surface. Generally, molecular oxygen (O_2^-) is present at temperatures below 150 °C, whereas at higher temperatures atomic oxygen species are dominant (O^-, O^{2-}).[84] When the sensor is exposed to an oxidising gas, the gas molecules fill the oxygen vacancies within the electron-depletion layer and recapture electrons from the bulk of the film.[90] The recapture of electrons therefore decreases the electrical conductivity (increase in resistance).

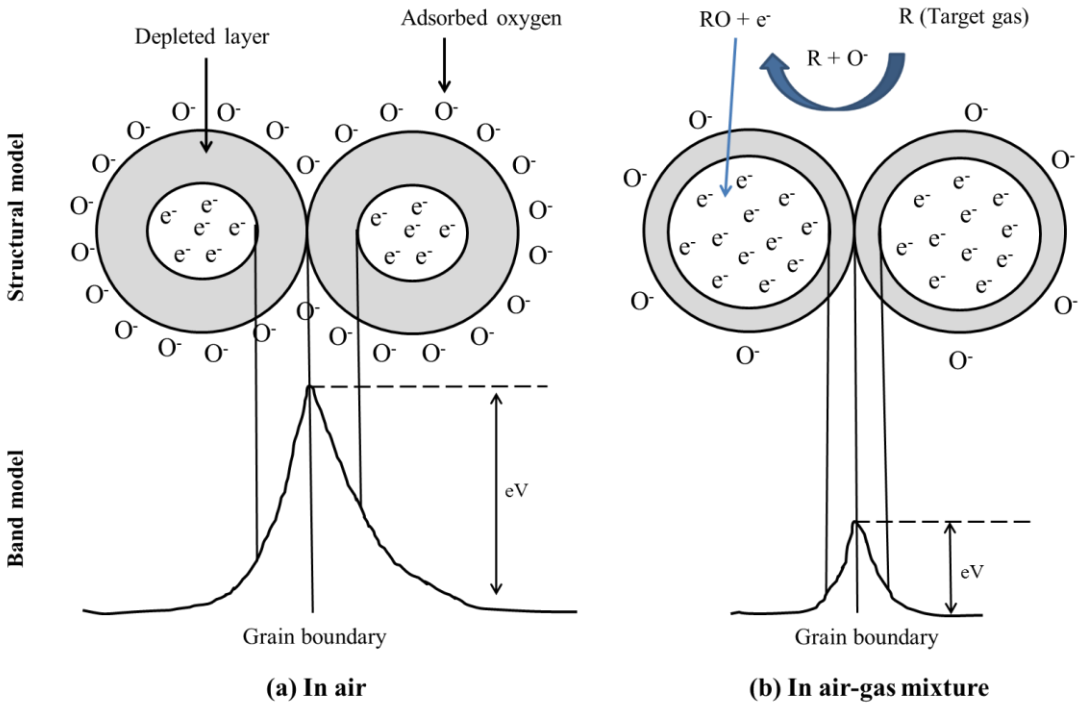

Figure 1.13 Schematic representation of the gas sensing mechanism for an *n*-type metal oxide semiconductor upon exposure to (a) air and (b) reducing gas

1.8.3 Metal oxide films for gas sensing

ALD of thin films is gradually becoming more prevalent in the semiconductor industry due to the continuous decreasing size of semiconductor devices. Therefore the need for ALD to produce highly conformal thin films has increased.[21]

As described earlier, TiO_2 is an *n*-type semiconducting material, which means that electrons act as the charge carriers. Although the gas sensing properties of TiO_2 have been widely investigated,[93,94,95] there is little knowledge about the effect of the TiO_2 film thickness on the gas sensing properties at thicknesses at the order of the Debye length.

TiO_2 films have been deposited onto a variety of gas sensing materials via several techniques such as ALD,[93] magnetron sputtering,[95] ultrasonic spray pyrolysis[2] and electric field assisted aerosol CVD.[2] The films have been tested for their sensitivity and selectivity towards a wide range of gases which includes H_2, NH_3, O_2, CO and NO_2. Marichy *et al.* deposited TiO_2 by ALD onto carbon nanotubes with varying

thicknesses, which were then tested for their sensitivity towards NO_2 and O_2 gases.[94] Unexpectedly, the TiO_2 films exhibited *p*-type behaviour towards NO_2 and O_2. Bittencourt *et al.* have previously reported that carbon nanotube/metal oxide films can behave as either *n*-type or *p*-type semiconductors, depending on the loading of the carbon nanotubes dispersed into the metal oxide matrix.[96]

NiO however, behaves as a *p*-type semiconductor because the majority of charge carriers which contribute to an electrical current are positively charged holes.[97] *P*-type metal oxides are interesting as gas sensing materials, as they have received very little attention compared to *n*-type metal oxides. *P*-type materials are highly advantageous gas sensing materials as they are believed to be moisture independent. This is in contrast to *n*-type gas sensing materials, which are very sensitive to moisture and humidity.

NiO films for gas sensing applications have primarily been deposited by magnetron sputtering.[81,98] The films have been screened for their gas sensitivity and selectivity towards a wide range of gases such as NO_2, CO, C_2H_5OH, H_2, CH_4, NH_3 and HCHO.[3,98] Zhou *et al.* reported that loading NiO nanotubes with platinum nanoparticles enhanced the sensitivity and selectivity towards ethanol gas.[99] *p*-NiO/*n*-ZnO heterostructues synthesised by Liu *et al.* showed an enhanced sensor performance for the detection of acetone as compared to pure NiO or ZnO alone.[100] NiO has also been used dope TiO_2 films; where ~ 10% wt. NiO was sufficient to convert the TiO_2 from an *n*-type material to a *p*-type material. [101]

There is currently no systematic/comparative study of *p*-type materials for gas sensing, and little knowledge about the effect of film thickness on the gas response.

1.9 Thesis outline

This thesis focusses on the synthesis of *n*-type TiO_2 and *p*-type NiO thin films by atomic layer deposition and chemical vapour deposition. The design of the ALD reactor will be introduced, which was designed and constructed specifically for the purpose of this research project.

The synthesis of *n*-type TiO_2 thin films by ALD will first be discussed, with a comprehensive review and discussion of the deposition process and film characterisation.

The development of new precursors for the deposition of *p*-type NiO thin films will then be introduced; with an in-depth discussion into the characterisation of such precursors. This will then lead onto the fabrication of NiO thin films using ALD and CVD techniques, with a comprehensive analysis of the films produced.

Finally, the gas sensitivity and selectivity of the *n*-type TiO_2 films synthesised by ALD will be examined to determine the effect of film thickness on the sensing properties at the order of the Debye length. The effects of humidity on the sensor performance will also be demonstrated.

In conclusion, the results presented in this thesis are summarised with potential future work from the results obtained.

Chapter 2
Experimental

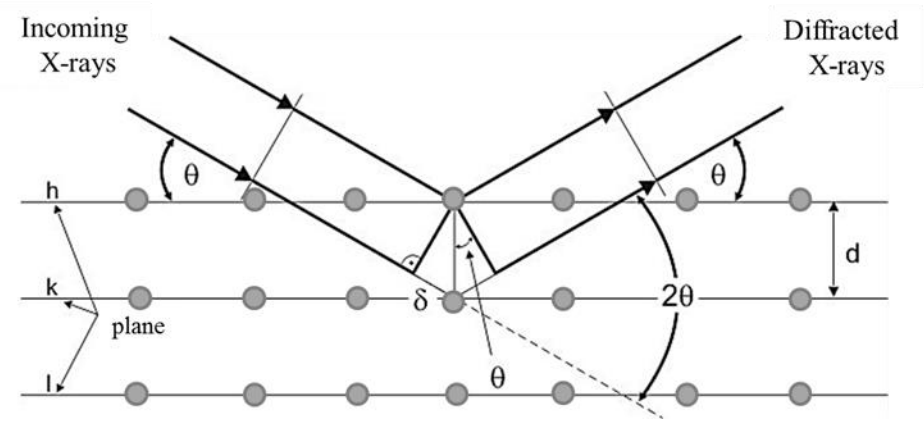

Chapter 2 Experimental

2.1 Introduction

This chapter describes the general experimental procedure used to deposit thin films via atomic layer deposition (ALD) and chemical vapour deposition (CVD) methods. More detailed descriptions of the deposition methods are given in chapters 3, 4 and 5. The analytical techniques used to characterise the films are also described, along with their theoretical basis.

2.2 ALD and CVD film deposition

ALD and CVD of metal oxide thin films were performed using two flow-type, cold-walled ALD reactors, which were both designed and constructed in house. A schematic of the reactors is outlined in Figure 2.1.

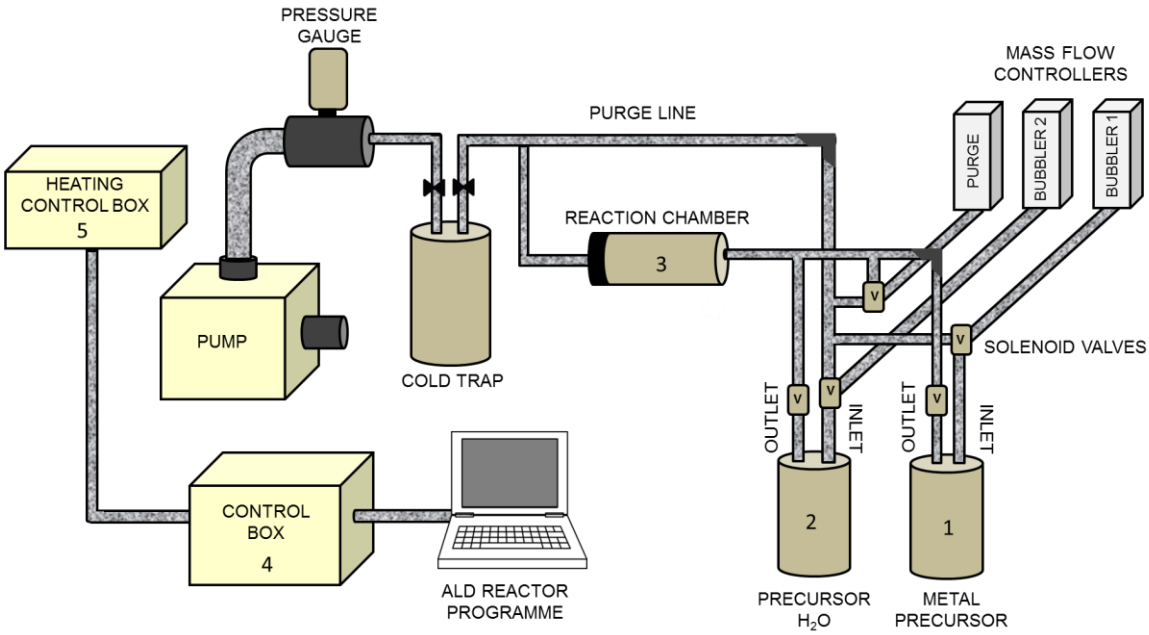

Figure 2.1 Schematic of ALD reactor

The majority of the components were constructed from stainless steel; one reactor was constructed from 1/8" diameter pipework, and the other in 1/4" pipework. Most of the tubing parts used to construct the reactor were purchased form Swagelock. KF flange/clamp fittings, vacuum fittings and pressure gauges were purchased from Oerlikon Leybold. The model number of the oil sealed vacuum pumps used was a TRIVAC D4B (4.2 - 5 m^3/h pumping speed), obtained from Oerlikon Leybold. Figure 2.2 shows a photograph of the reactor once construction was complete.

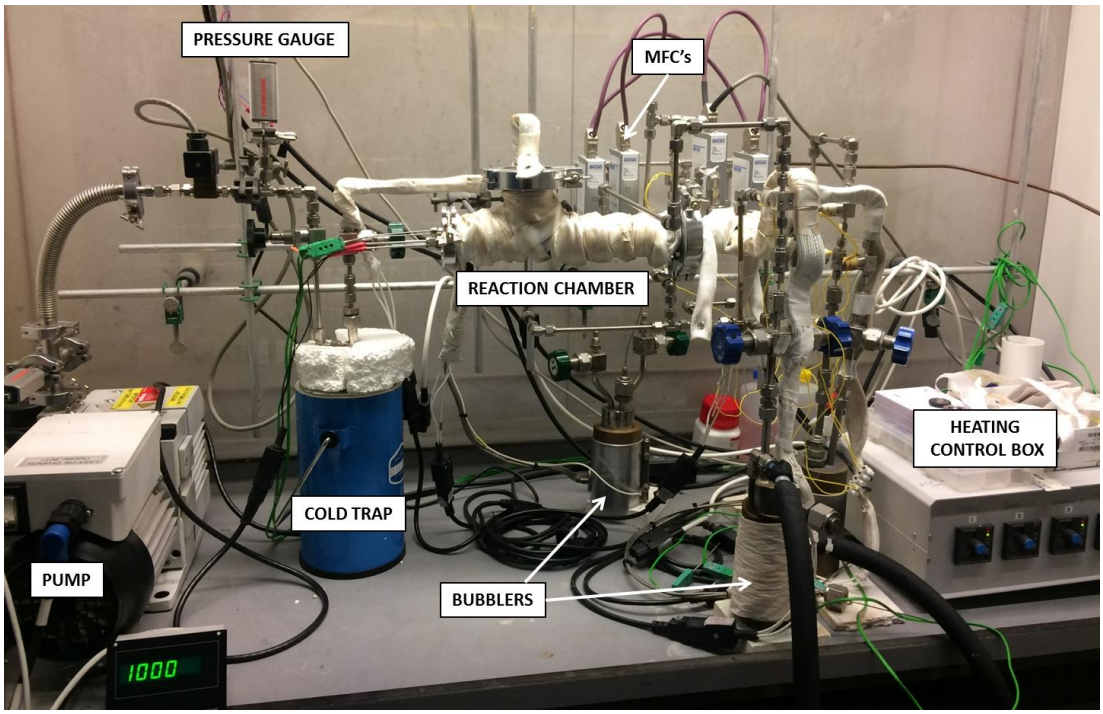

Figure 2.2 Photograph of ALD reactor

The majority of the depositions were performed on quartz glass (obtained from Wuxi Crystal and Optical Instrument Company Limited), with some depositions also performed on super premium microscope slides (VWR) and silicon (Si(100)) substrates obtained from the Eindhoven University of Technology (TU/e). Prior to deposition, substrates were cut into ~ 4.0 cm x 2.5 cm pieces, cleaned using iso-propanol (Sigma Aldrich, 99.5%) and left to air dry before loading into the reactor.

The substrate was loaded onto a substrate heating block (Figure 2.3) which sits inside the reaction chamber (**3**), as outlined in Figure 2.1.

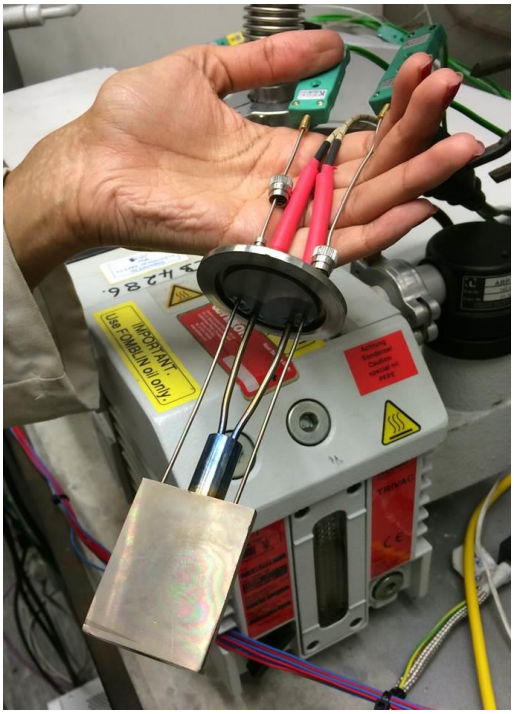

Figure 2.3 Substrate heating block sits inside the reaction chamber. Attached thermocouples were used to monitor and control the temperature of the substrate

A base pressure of 4 x 10^{-3} to 4 x 10^{-2} mbar was achieved when under vacuum (depending on which reactor was being used). The vapour pressure of the metal precursor was manipulated by varying the temperature of the bubbler (**1**). The bubbler was contained within a copper heating sleeve; the temperature of which was subsequently controlled using a k-type thermocouple which was positioned inside the bubbler so that the tip of the thermocouple was suspended in the precursor. The inlet pipe to the bubbler extended below the precursor level, so that when an argon gas (99.998%, obtained from BOC) feed was used, the vaporised molecules were forced into the outlet line and thus transported through the reactor (Figure 2.4). Water vapour was generated by holding bubbler (**2**) at 5 °C. The dosing and purging of precursors was controlled using series 9 solenoid valves (obtained from First Sensor). Vapour pressure curves for each precursor were used to estimate the precursor dose.

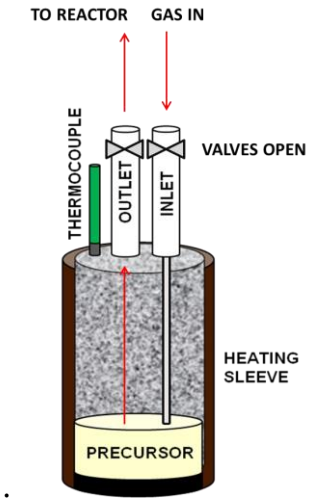

Figure 2.4 Schematic of precursor bubbler held within heating sleeve and attached thermocouple

The outlet lines from each of the bubblers to the reaction chamber were heated using tapes (Electrothermal 400 W, 230 V) to a temperature greater than that of bubbler (**1**), but lower than that of the substrate heating block to prevent precursors either condensing or reacting in the pipelines and causing blockages. In these experiments, metal oxide films were grown at substrate temperatures in the range of 150 - 450 °C. The control boxes (**4** and **5**) were used to monitor and maintain all temperatures and gas flows throughout. A cold trap was placed in between the reaction chamber outlet and the pump inlet in order to capture any residual precursor or by-products, with the purpose of protecting the pump from being damaged.

Pureshield argon gas (99.998%) supplied by BOC, was used as the carrier gas for all depositions. Gas flow rates were controlled using Mass Flow Controllers (MFC's) purchased from Brooks Instrument (GF40 model number), with flow rates varying from 20 - 700 sccm, depending on the precursor being used and reaction conditions. The reactor running pressures therefore varied in the range of ~ 1.0 - 7.0 mbar. The metal precursor was introduced into the reaction chamber by bubbling the carrier gas into the bubbler to assist the transportation of vaporised precursor molecules. Water was introduced into the reaction chamber by means of its own vapour pressure, without any bubbling. The reactor was programmed using a custom IGI Systems Lab Interface Input control box which automatically controls all temperatures and heating systems, gas flow rates and solenoid valves.

ALD of TiO_2 was carried out using titanium (IV) isopropoxide, $[Ti(O^iPr)_4]$ (Acros Organics, 98+%) and distilled water. ALD of NiO was carried out using Bis(cyclopentadienyl)nickel(II), $[Ni(Cp)_2]$ (Alfa Aesar, dry) and distilled water. All other nickel(II) precursors utilised in this work were synthesised in house (as described in chapter 4).

2.2.1 ALD film deposition

ALD films were deposited by alternately exposing the metal precursor and water precursor into the reaction chamber, with an inert gas purge step in between each dose. This was to prevent CVD-like growth mechanisms occurring. Therefore one complete ALD reaction cycle consists of; metal precursor dose, gas purge, water dose, gas purge. The dose and purge sequences were automatically controlled using solenoid valves (obtained from First Sensor).

Metal oxide film growth occurs via two self-limiting surface reactions as outlined in equations 2.1; where the asterisk indicates surface-bound species.

$$(1)\ OH^* + M(OR)_4 \rightarrow O\text{-}M(OR)_3^* + RH$$

$$(2)\ O\text{-}M(OR)_2^* + H_2O \rightarrow O\text{-}M\text{-}OH^* + 2RH \qquad (2.1)$$

The dosing and subsequent purging steps as described above were repeated to achieve the desired number of reaction cycles, and hence produce films of a particular thickness. Because each of these surface reactions were performed sequentially, this means that the two gas-phase precursors were never in contact with each other (provided that sufficient dose and purge times were employed), and hence gas-phase reactions cannot take place to allow CVD-like growth.

2.2.2 CVD film deposition

CVD films were deposited by continuously dosing the metal precursor into the reactor under a constant flow of inert gas until the desired reaction time/film thickness had been reached. No water precursor was utilised during the CVD experiments. A key difference between the CVD and ALD processes is that during CVD, the substrate holder was maintained at a temperature at or above the decomposition temperature of the metal precursor to ensure that the precursor decomposed onto the substrate to form a metal oxide film.

2.3 Analytical techniques

2.3.1 Filmetrics

A Filmetrics F20 Thin Film Analyser was used to measure the film thickness of the TiO_2 films deposited by ALD. This is an optical measurement instrument which uses spectral reflectance to measure the amount of light reflected from a thin film over a range of wavelengths (380 – 1050 nm), with the incident light perpendicular to the sample surface.[102] Light is partially reflected when it encounters an interface between two materials (Figure 2.5). The amount of reflected light is determined by the discontinuity in the refractive index (n) and the extinction coefficient (k). Reflections from multiple interfaces interfere with each other, causing oscillations in the wavelength spectrum.[103] It is the frequency of these oscillations which determines the distance between the interfaces and hence the thickness of the film. So a thicker film will exhibit a greater number of oscillations over a given wavelength range, and thinner films will exhibit fewer oscillations.

Before conducting any measurements, a baseline was first performed using a silicon reference sample. Sample measurements were taken at numerous points across the substrate from the inlet end of the substrate to the outlet end of the substrate. Values were averaged to determine the average film thickness, which was used to calculate the growth per cycle for the film deposited. The accuracy of the equipment is reported as the greater of 0.4% or 2 nm.[102]

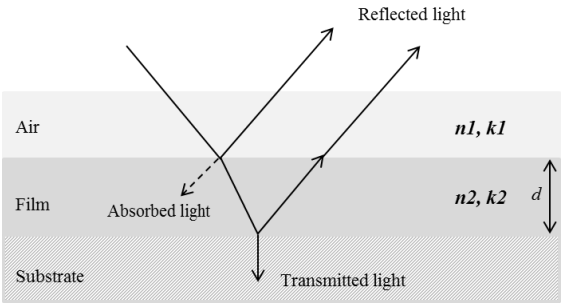

Figure 2.5 Spectral reflection of light from multiple interfaces in order to determine the film thickness

2.3.2 Ellipsometry

Ellipsometry is an optical measurement technique, which performs non-contact and non-destructive measurements on thin films and multilayer samples to achieve film thickness and optical properties. This technique was used to measure the thickness of the films deposited by ALD and CVD of the nickel(II) precursors. Unlike filmetrics, it measures the reflectance of light at non-normal incidence and at two different polarisations. The technique provides a very accurate determination of film thickness by measuring the phase between *p*- and *s*-polarised reflection beams, where the ratio of the amplitude reflection coefficients (*rp* and *rs*) is defined by $\rho = rp/rs$.[76] This ratio is expressed as two parameters; **Ψ** (Psi) and **Δ** (Delta), where **Ψ** is the amplitude ratio and **Δ** is the phase difference between the reflected p and s wave components.[76] These can be used to determine the film thickness along with the refractive index and extinction coefficient of the film.

Because ellipsometry is an indirect technique, it means that a model based analysis must be performed in order to get the actual values of the model parameters.[104] In order to perform the analysis procedure, dispersion law parameters are fitted to the model, which are characteristic for certain materials.[105]

Measurements were performed using a Semilab SE-2000 ellipsometer, equipped with Semilab Sam suite measurement software. A continuous spectrum of light is generated from a 75 W xenon lamp ranging from ultraviolet through to visible to infrared (185 – 2000 nm). The light then enters a polariser which controls the intensity of light beam. This resulted in a standard beam diameter of 3.5 mm for a 75° angle of incidence. The beam hits the sample and is reflected off into an analyser and compensator equipped with 2 detectors. The machine has independent arm angle selection, so is capable of performing measurements with detection angles in the range of 12 - 90°. For these experiments, data was recorded at angles of incidence of 60, 65, 70 and 75°.

Standard spectral range was 245 - 990 nm. The data was modelled using Spectroscopic Ellipsometry Analysis (SEA) software. Figure 2.6 shows a schematic of an ellipsometer.

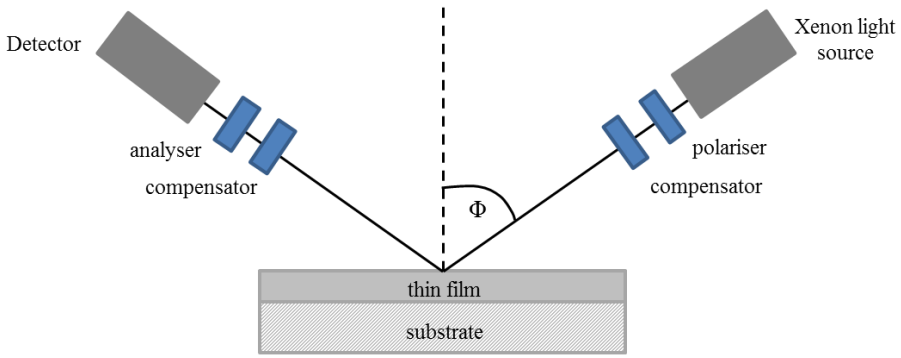

Figure 2.6 Schematic optical configuration of an ellipsometer

2.3.3 Atomic Force Microscopy (AFM)

Atomic force microscopy (AFM) is a form of scanning probe microscopy (SPM) which can image the 3D topography and surface properties of a sample. Images are generated as a small probe with a sharp tip (or cantilever) is scanned along a sample surface and the force between the probe and the sample is measured on the atomic level. Topographical images are assembled by scanning the cantilever across the surface line by line. A laser beams onto the top of the cantilever, which is then reflected onto sensitive photodiodes. As the cantilever interacts with the films topographical features, it affects the reflection of the beam. The signal from the photodiodes are sent to a piezo actuator which moves the cantilever up or down, and it is the deflection of the cantilever which was used to assemble topographical images. AFM can determine surface roughness which is an indicator of film quality. Figure 2.7 shows a schematic of a non-contact mode AFM.

AFM measurements were obtained using a Nanosurf Easy Scan Atomic Force Microscope, with a 10 μm head in non-contact mode with oscillating probe. Scan areas were 5 x 5 μm, with measurements recorded at 250 points/line with 1 sec/line scan time. So measurements were effectively recorded every 20 nm across the sample. Data recorded were the average roughness (*Ra*) and the root mean square roughness (*Rq* or RMS). The RMS is defined as the standard deviation of the elevation within the z axis, within a given scan area. This was calculated automatically in the AFM software using equation 2.2, where *zav* is the average of the z values within the scan area; *zi* is the z value for a given point; N is the number of points within the scan area and *Rq* is the root mean square roughness.[106] Images of the deposited metal oxide films were obtained at 3 different locations across the film and the average RMS was determined.

$$Rq = \frac{\sqrt{\sum(zi - zav)^2}}{N} \qquad (2.2)$$

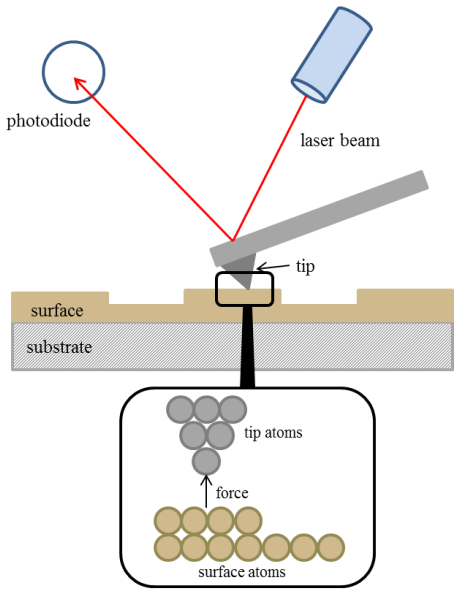

Figure 2.7 Schematic of non-contact mode atomic force microscope (AFM)

2.3.4 X-Ray Diffraction (XRD)

The structure and physical properties of thin films and multi-layers can be studied using X-ray diffraction (XRD). This includes film morphology, crystallographic orientation, lattice parameters and d-spacings.[107] When X-rays interact with a crystalline material a diffraction pattern is produced, which is characteristic for that material; almost like a fingerprint of the substance.[108] Light is diffracted when the incident beam of X-rays interfere with each other and interact with the crystal planes of the material. However diffraction only occurs when Bragg's law is satisfied, as shown in equation 2.3, where n is a positive integer, λ is the wavelength of the incident beam, d is the inter-planar spacing and θ is the angle between the incident (or diffracted) beam and the lattice planes. The incident beam interacts with a set of crystal planes at certain angles (θ), which is then reflected, or diffracted at a beam angle of 2θ from the incident beam.

$$n\lambda = 2d\sin\theta \qquad (2.3)$$

XRD measurements were performed using a Bruker-Axs D8 (GaDDS) diffractometer which operates with a Cu X-ray source, monochromated ($K\alpha_1$ and $K\alpha_2$) and a 2D area X-ray detector with a resolution of 0.01°. The diffraction patterns obtained were compared with database standards from the Inorganic Crystal Structure Database (ICSD), Karlsruhe, Germany. The beam spot is approximately $5mm^2$, which means that several areas of the sample can be analysed separately. For all thin films analysed an incident angle of 0.5 - 1° was used, and the diffracted X-rays were detected at angles from 10 - 66°. Figure 2.8 shows a schematic of how X-rays are diffracted from a sample.

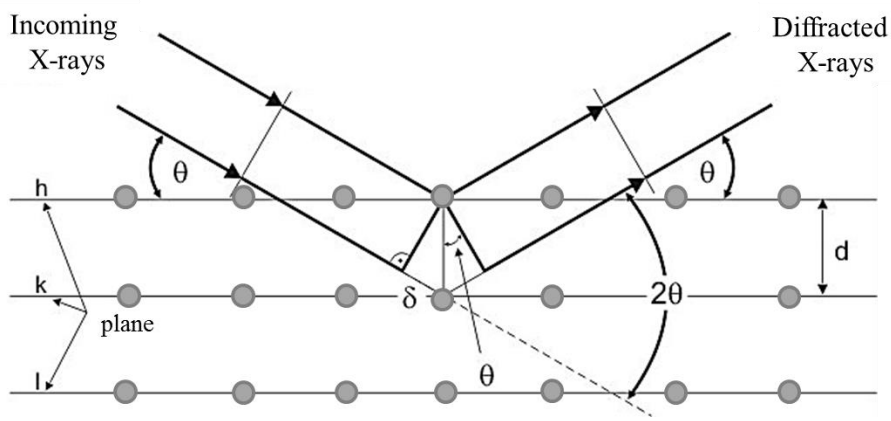

Figure 2.8 Diffraction of X-rays from lattice planes (hkl) exhibit constructive interference effects leading to specific angles where reflections are observed

2.3.5 Raman Spectroscopy

Raman spectroscopy provides information on the molecular vibrations of materials when exposed to a laser beam. Chemical and structural information can therefore be determined for a material, as well as material identification and quantitation. The technique involves shinning a laser beam onto a sample and detection of the scattered light.

There are two resultant effects from the interaction of the material with the laser beam. The first is Rayleigh scattering, where the scattered light is of the same frequency as the incident light. The second effect is where the scattered light has a different frequency to the incident light; this is known as Raman scattering.[109] This shift in frequency is due to interactions between the incident light and the vibrational energy levels of the molecules in the material. The 'shifted' frequencies are known as Raman lines, which together constitute a Raman spectrum. However, it is the intensity of the 'shifted' light which is plotted against the frequency in a Raman spectrum.

Raman spectroscopy was performed using a Renishaw 1000 spectrometer equipped with a 633 nm wavelength laser. A laser beam (~ 2 - 3 μm in diameter) with variable laser power was exposed to the thin film and scattered light was detected at frequencies in the range 100 - 1500 cm^{-1}. The instrument was calibrated using silicon at a wavelength of 520.5 cm^{-1} prior to measurements being taken. A minimum scan time of 120 seconds was used and typically a minimum of 1 accumulations (number of scans). The technique is non-destructive and requires no sample preparation. Figure 2.9 illustrates the energy changes between Rayleigh and Raman scattering.

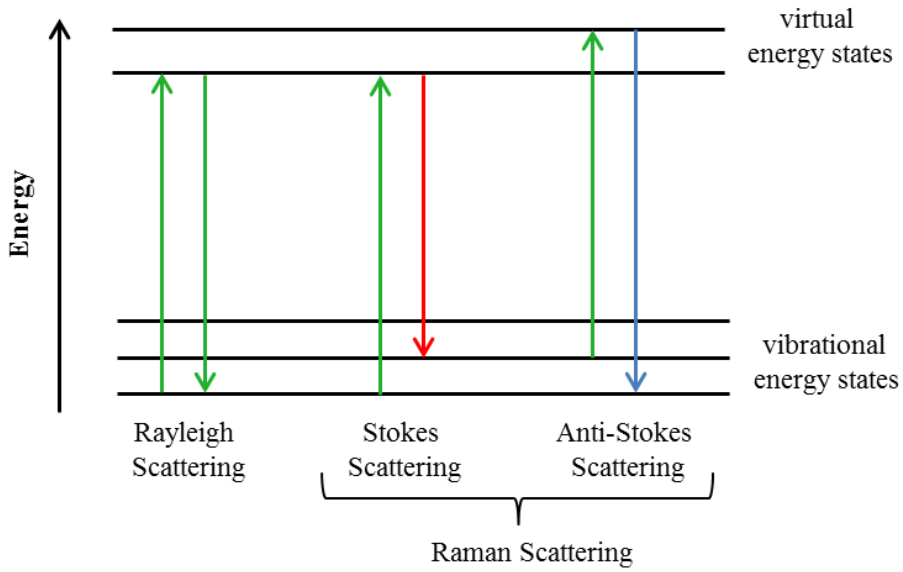

Figure 2.9 Jablonski diagram illustrating Rayleigh and Raman scattering

2.3.6 X-Ray Photoelectron Spectroscopy (XPS)

X-ray photoelectron spectroscopy (XPS) is a highly sensitive surface analysis technique which can provide valuable quantitative and chemical state information from the surface of a material. The technique involves irradiating X-rays on to the sample surface, which excites electrons. If the binding energy of the electrons is lower than the energy of the X-ray, the electrons at the surface can be emitted as photoelectrons. The kinetic energy of the photoelectrons emitted helps to identify the elements present in the sample. In the Einstein photoelectric law (equation 2.4),[110] BE denotes the binding energy of the photoelectron to the atom concerned.

$$KE = hv - BE \qquad (2.4)$$

The binding energy is determined by measurement of the kinetic energy (KE), as *hv* is already known. Small variations in the kinetic energy enable the chemical states of the elements to be determined. From the binding energies and peak intensities, the chemical state concentration of the elements present can be determined.

XPS analysis was performed using a Thermo Scientific K-Alpha X-ray photoelectron spectrometer with monochromated Al K alpha radiation, a dual beam charge compensation system and constant pass energy of 50 eV. Survey scans were collected in the range 0 - 1200 eV. XPS data was fitted using CasaXPS software. The principal peaks of interest were Ti2p, Ni2p O1s, Si2p and C1s. The escape depth in this system was in the range of 1 - 10 nm. Depth profiling was carried out via argon ion sputtering.

2.3.7 Scanning Electron Microscopy (SEM)

Scanning electron microscopy (SEM) is a powerful technique used to image the morphology of sample surfaces. A focussed beam of electrons is scanned over the surface to create an image of the surface. The electrons interact with the sample to produce signals which reveal information about the morphology, chemical composition and crystalline structure. The types of signals produced include secondary electrons, backscattered electrons, auger electrons, X-rays and photons of various energies.[111] Secondary electrons are most commonly used for imaging purposes.

SEM analysis was performed using a JEOL JSM 6700F Field Emission Scanning Electron Microscope equipped with the JEOLPC-SEM software. Typically, a working distance of 8 mm was used with an accelerating voltage of 5.0 kV. Prior to analysis, samples were carbon coated to enhance conductivity and reduce the accumulation of electrostatic charge at the surface which can cause image distortion. Samples were electrically grounded to a sample stage using carbon tape and silver paint. Images were taken at several points across the substrate to observe any changes in the morphology from the inlet end of the substrate to the outlet end.

2.3.8 Nuclear Magnetic Resonance Spectroscopy (NMR)

Nuclear magnetic resonance (NMR) is a powerful technique used to determine the structure of compounds, as well as their purity. NMR is related to the magnetic properties of the nuclei; many nuclei have spin and are electrically charged. When an external magnetic field is applied, this affects the alignment of the nuclei. Nuclei which are aligned opposed to a magnetic field are less stable than those aligned with the magnetic field. It is therefore possible to make the nuclei flip to the more stable alignment when the right amount of energy is supplied (this produces a peak in an NMR spectrum). This is known as resonance, and occurs in both proton and carbon NMR spectroscopy.

NMR spectroscopy analyses were performed using a Bruker AMX 300 MHz spectrometer and Bruker Avance III 600 MHz spectrometer equipped with a four nucleus gradient probe for $^{1}H/^{13}C/^{31}P/^{19}F$ experiments. A small amount of the sample to be analysed was dissolved in either deuterated chloroform, $CDCl_3$ or deuterated benzene, C_6D_6 and transferred into an NMR sample tube. Proton and carbon NMR measurements were performed on all synthesised compounds. The spectra produced were analysed using an ACD/NMR processor program.

2.3.9 Elemental Analysis

Quantitative elemental analysis (EA) was performed at University College London (UCL). It is a technique used to determine the structure and purity of a synthesised compound. The data was obtained through combustion analysis. This involves burning a small amount of the synthesised compound in an excess of oxygen and various traps collect the combustion products (CO_2, H_2O and NO). The masses of these combustion products are then used to calculate the mass fractions of carbon, hydrogen and nitrogen (CHN) atoms of the synthesised compound. Although not a primary technique for structural determination, EA can provide very useful complementary information and is the fastest and most inexpensive way of doing so.

2.3.10 Mass Spectrometry

Mass spectrometry is a powerful technique used to determine the structure of compounds. A mass spectrometer converts individual molecules into charged particles (ions) so that they can be manipulated by external electric and magnetic fields. A mass spectrometer is composed of three main components;

1. Source – enables ionisation of the molecule(s) of interest. This can be achieved using a variety of techniques such as electron ionisation (EI), chemical ionisation (CI), electrospray (ESI), matrix assisted laser desorption (MALDI) and atmospheric pressure chemical ionisation (APCI).

2. Analyser – accelerates and deflects the charged ions using either a magnetic or electric field depending on the m/z ratio (mass-to-charge ratio).

3. Detector – detects the ions from the analyser.

Ions are separated according to their momentum (mass multiplied by velocity) by a magnetic field. EI and CI are the most common forms of ionisation for relatively low molecular weight, thermally stable and volatile compounds.

EI is the classical ionisation method in mass spectrometry. Sample molecules are vaporised and introduced into the EI source using a heated-insertion probe. These then interact with electrons at an energy of 70 eV in the ion source. Some of the molecules are ionised by removal of an electron, which are then extracted from the source by a high voltage and separated in the mass analyser. The ions formed are radical cations in the form of M^+. The internal energy of the ions created is relatively high so some compounds may not yield molecular ion information under these conditions. If a molecular ion peak is not observed using EI, then CI is normally used which is described as a “soft” ionisation technique.

With the CI technique, a reagent gas (methane or ammonia) is introduced into the ion source and ionised by an electron beam. This results in various reagent gas ions being formed in the source. The sample is then introduced into the source in the same way as for EI and undergoes ion-molecule reactions with the reagent gas ions. The most common ionisation mechanisms which occur are proton transfer, in which a compound with a proton affinity greater than that of the reagent gas is ionised to form a $[M+H]^+$ ion and electrophilic addition, in which a cation produced by the ionisation of the reagent gas is attached to the sample molecule, which can produce $[M+NH_4]^+$ ions from many compounds when ammonia is used as the reagent gas. Both these mechanisms create ions with less internal energy than is the case for EI, resulting in less fragmentation and hence a more intense molecular ion peak.

In ESI a fine spray of charged droplets is created by the application of a high voltage (typically 1 - 3 kV) to a capillary containing a stream of solvent (the mobile phase). The mobile phase is usually 50:50 water (0.1% formic acid): methanol. The process is assisted by use of a heated co-axial nebuliser gas such as nitrogen. The charged particles are expelled from the tip of the capillary which evaporate to form de-solvated ions. Evaporation of the solvent results in the generation of isolated gas-phase ions. ESI occurs at atmospheric pressure and the ions formed in positive mode are in the form of $[M+H]^+$. Dimers can also form as $[2M+H]^+$. Solvent adducts can be formed with acetonitrile: $[M+H+MeCN]^+$ and with methanol: $[M+H+MeOH]^+$. If the compound can lose a proton more easily that gain a proton (e.g. acidic molecules), negative ions can form. Ions formed in the negative phase are most commonly in the form of $[M-H]^-$. In general, compounds containing amino, amide, ester, aldehyde/keto or hydroxyl functional groups are suitable for positive ion ESI and compounds containing carboxylate, hydroxyl/phenol or imide functional groups are suitable for negative ion ESI.

Mass spectra were recorded using Thermo MAT900 (EI and CI ion sources) and Micromass LCT Premier (ESI ion source) spectrometers. Figure 2.10 shows a schematic of the main components of a mass spectrometer.

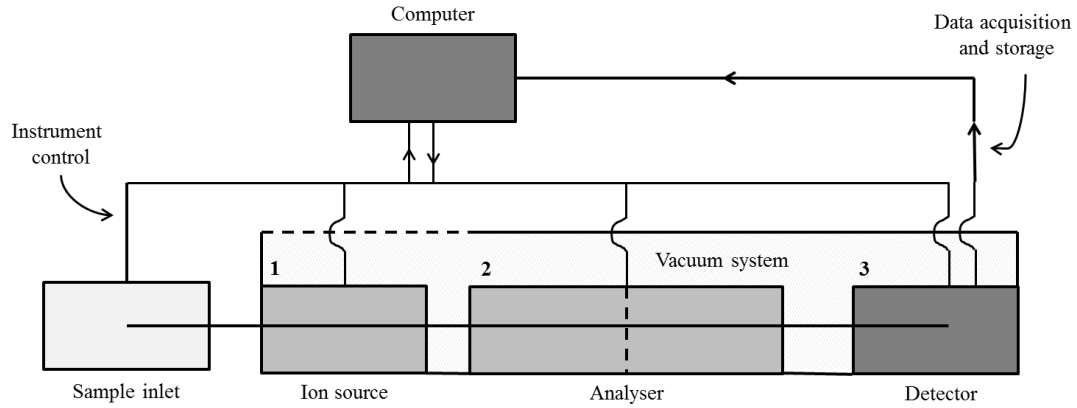

Figure 2.10 Schematic of the main components of a mass spectrometer

2.3.11 Thermogravimetric Analysis (TGA)

Thermogravimetric analysis (TGA) is a technique which monitors the mass of a sample as a function of temperature or time, as the sample is exposed to a controlled temperature program under a controlled atmosphere. The sample (~ 10 - 15 mg) is placed in a sample pan atop of a precision balance inside a furnace. The sample is then heated from 25 - 600 °C at a ramp rate of 10 K/min. During the experiment the mass of the sample is monitored, which allows the determination of several parameters, which include (but are not limited to); sample decomposition temperature, evaporation rates, purity and presence of any residual solvent. Helium was used as the purge gas which flows over the sample and exits via the exhaust; this controls the sample environment during the experiment. TGA experiments were performed using a Netsch simultaneous TG-DTA/DSC apparatus equipped with Proteus software.

2.3.12 X-Ray Crystallography

Crystals were placed in Fomblin, and a suitable single crystal was selected and mounted on a nylon loop. X-ray diffraction data were recorded on an Agilent Super Nova Dual Diffractometer (Agilent Technologies Inc, Santa Clara CA) with Cu-Kα radiation (λ = 1.5418 Å) at 150 K. Unit cell determination, data reduction and absorption corrections were carried out using CrysAlisPro.[112] The structure was solved with the SIR2004[113] structure solution program using Direct Methods and refined by full matrix least squares on the basis of F^2 using SHELX 2013[114] within the OLEX2 GUI.[115] Non-hydrogen atoms were refined anisotropically and hydrogen atoms were included using a riding model.

Chapter 3

ALD of titanium dioxide thin films

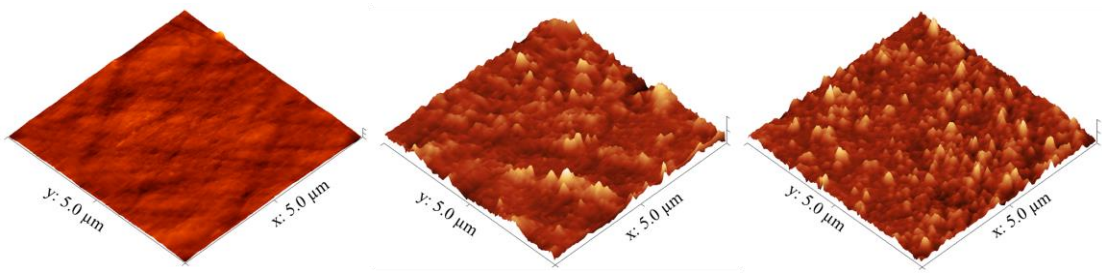

Chapter 3 ALD of Titanium Dioxide thin films

3.1 Introduction

This chapter describes the atomic layer deposition (ALD) of *n*-type titanium dioxide (TiO_2) thin films. Films were deposited using titanium tetraisopropoxide [$Ti(O^iPr)_4$] as the metal precursor and water as the co-reactant. The films were analysed using various techniques to determine the film quality and conformality.

One of the characteristics of ALD is that there are several reaction parameters which can be varied to enable 'true' ALD growth to occur; that is that reactions are complementary and self-limiting. Throughout these experiments, the reaction parameters investigated (but not limited to) included; precursor dose times, precursor purge times, precursor vapour pressures and substrate growth temperature.

3.2 Depositions using [$Ti(O^iPr)_4$]

3.2.1 [$Ti(O^iPr)_4$] precursor for ALD

Titanium(IV) tetraisopropoxide, [$Ti(O^iPr)_4$] (TTIP), is an orange liquid which was obtained from Acros Organics, (98+%) and was used as purchased. It is a volatile precursor and there are numerous publications outlining its use as a precursor for ALD.[22] TTIP decomposes on heating at 275 °C[41] according to equation 3.1:

$$Ti(OC_3H_7)_4 \rightarrow TiO_2 + 4\ C_3H_6 + 2\ H_2O \qquad (3.1)$$

However, decomposition of the metal precursor is not desirable as this would result in CVD-like behaviour. To prevent thermal decomposition occurring, the growth temperature was kept at a temperature below the decomposition temperature of the precursor.

The vapour pressure of TTIP can be manipulated by varying the temperature of the bubbler in which it is contained. Manipulation of the vapour pressure means that the volume of precursor released into the reaction chamber during each dose sequence can be easily controlled. Again, to prevent precursor decomposition, the temperature of the bubbler was held at a temperature lower than the decomposition temperature of the precursor. The vapour pressure equation for TTIP is shown in equation 3.2, where the temperature, T is in kelvin and the vapour pressure, Vp is in Torr.[116] Figure 3.1 shows the vapour pressure curve for TTIP plotted in mbar. A bubbler temperature of 25 °C created sufficient vapour pressure (0.176 mbar) to dose TTIP through the reactor.

$$log(Vp) = 9.837 - \left(\frac{3193.7}{T}\right) \qquad (3.2)$$

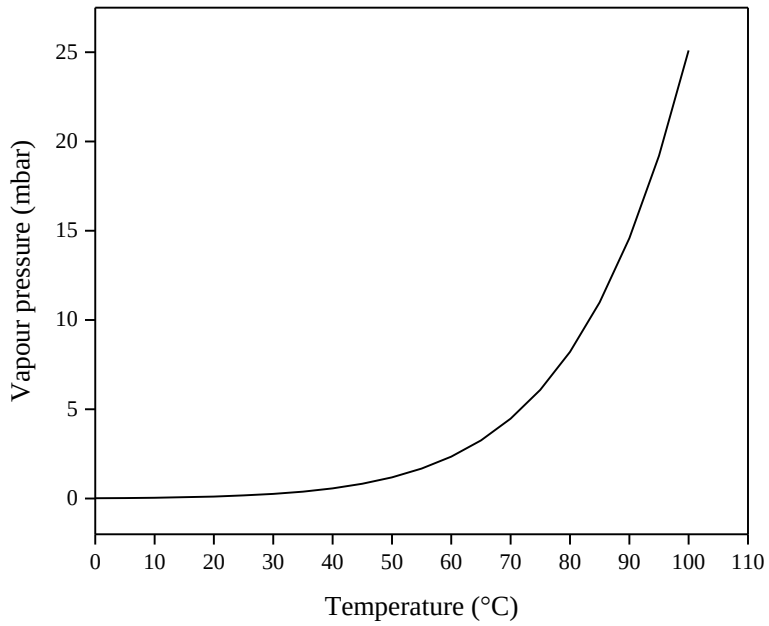

Figure 3.1 Vapour pressure curve for TTIP

3.2.2 ALD of $[Ti(O^iPr)_4]$ and water

ALD depositions were carried out using titanium(IV) isopropoxide, $[Ti(O^iPr)_4]$ (Acros Organics, 98+%) and distilled water. Pureshield argon (99.998%) obtained from BOC, was used as the inert carrier gas. Quartz glass (obtained from Wuxi Crystal and Optical Instrument Company Limited) and super-premium microscope slides (obtained from VWR) were used as the substrate materials. Prior to deposition, substrates were cut into ~ 4.0 cm x 2.5cm pieces, cleaned using iso-propanol (Sigma Aldrich, 99.5%) and air dried before loading into the reactor. Whilst the substrate holder was being heated to the required temperature, the reactor was pumped down under vacuum to achieve a base pressure of ~ 4 x 10^{-2} mbar. Gas flows were then turned on, where the running pressure was recorded. As described in Chapter 2, TTIP was introduced into the reaction chamber by bubbling the carrier gas into the bubbler to assist the transportation of vaporised precursor molecules. Water was introduced into the reaction chamber by means of its own vapour pressure, without any bubbling systems.

Standard TiO_2 depositions were carried out at a deposition temperature of 200 °C under the conditions outlined in Table 3.1. A growth rate of ~ 0.30 - 0.50 Å/cycle was achieved, depending on the number of cycles (film thickness measured by filmetrics).

	Time	**Purge flow (sccm)**	**TTIP bubbler flow (sccm)**	**Water bubbler flow (sccm)**	**Growth temp (°C)**
TTIP dose	2.5 sec	100	100	0	200
TTIP purge	1 min	100	100	0	200
H_2O dose	2.0 sec	100	100	0	200
H_2O purge	3 min	100	100	0	200

Table 3.1 Reaction conditions used to deposit TiO_2 films via ALD of TTIP and water

Following an induction period, the film thickness increased with the number of reaction cycles in a relatively linear fashion; the data has been fitted using two discrete trend lines (Figure 3.2). This is as expected for ALD growth, where the amount of material deposited in each reaction cycle should be constant. An induction period was present between 50 and 400 cycles, which is related to the time taken to establish ideal ALD growth of TiO_2. It is widely believed (although not fully proven) that the hydroxyl sites on the substrate surface act as nucleation sites, which initiate TiO_2 growth (see Figure 1.9 in chapter 1). These sites can aid in the adsorption and desorption of the precursor and hence govern the nature of the films grown.[60] Once stable nuclei are formed; these will grow together, coalesce and form a continuous film.[52] When a continuous layer of TiO_2 has been formed on the substrate, the ALD growth kinetics and behaviour change, as they now become controlled by the chemistry of the precursor being deposited on the 'new' surface.[60] It is then after this point that the ALD growth becomes more linear with the number of reaction cycles.

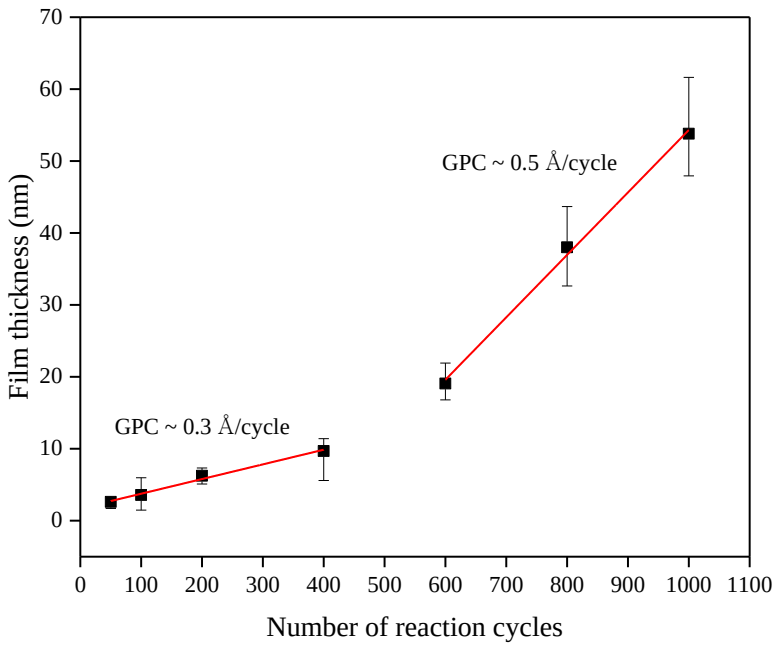

Figure 3.2 Increase in TiO_2 film thickness and growth rate with number of reaction cycles at a deposition temperature of 200 °C (measured by filmetrics)

The ALD growth rate observed was 0.3 - 0.5 Å/cycle, which is comparable to the growth rate achieved using similar TiO_2 systems. For the $[Ti(O^iPr)_4]$ and water precursor combination, Ritala and Leskelä reported a growth rate of 0.3 Å/cycle at a deposition temperature of 250 - 325 °C[19] and Matero *et al*. reported a growth rate of 0.33 - 0.60 Å/cycle at 300 °C.[117] Typical Ti-O bond lengths in TiO_2 are 1.96 Å,[118] so one monolayer of TiO_2 should theoretically be 3.92 Å thick. But due to the steric hindrance of the bulky $[Ti(O^iPr)_4]$ molecules, the number of chemisorbed species on the surface is not high enough to form a complete monolayer of TiO_2 during one reaction cycle. This is why a growth rate less than 1 Å/cycle was observed.

The refractive indices (*n*) of the deposited films were obtained by ellipsometry at two different wavelengths using Tauc-Lorentz/Lorentz dispersion function modelling (Table 3.2). The angles of incident used to obtain such values were 65°, 70° and 75°; which are close to the Brewster angle for TiO_2, which is ~ 67 - 68°.[119] The most accurate ellipsometry measurements are achieved at a polarising angle (also known as the Brewster angle) for which an unpolarised plane wave is reflected as a linearly-polarised plane wave.[120] At this angle, the ratio of reflection coefficients for p and s polarised light (*rp*, *rs*) is maximised and therefore the measurement sensitivity is at its maximum also.[76] The refractive index values for the TiO_2 films are in line with those reported in the literature, which range from 1.9 to 2.6 depending on the deposition temperature and titanium precursor.[19,121,122] The refractive index increases with film thickness, which suggests that the density and crystallinity of the films increases. This is consistent with the above explanation regarding initial nucleation growth leading to formation of a continuous film.

# cycles	Film thickness (nm)	GPC (Å/cycle)	*n* @ 560 nm	*n* @ 632.8 nm
50	3	0.5	1.8	1.8
100	4	0.4	1.8	1.8
200	6	0.3	2.1	2.1
400	10	0.2	2.1	2.1
600	19	0.3	2.1	2.1
800	38	0.5	2.2	2.1
1000	53	0.5	2.3	2.3

Table 3.2 Film thickness and refractive indices of TiO_2 films deposited by ALD with different number of reaction cycles at 200 °C

3.2.3 Characterisation of TiO_2 films

The surface morphology of the TiO_2 films deposited by ALD was studied using non-contact mode atomic force microscopy (AFM). All films showed good thickness uniformity across the substrate; with film thickness varying by ~ 1 - 3 nm from the inlet end of the substrate to the outlet end. The outlet end of the substrate tended to be slightly thicker than the inlet end for most samples. This is believed to be due to the reactor design, where the outlet end of the substrate sits close to the exhaust of the reaction chamber. Therefore the laminar flow of precursor/purge gas across the outlet end of the substrate was reduced slightly, so some of the unreacted precursor may not have been sufficiently purged out and therefore the film thickness is slightly thicker.

The AFM images in Figure 3.3 show that as the number of reaction cycles increases, the surface roughness of the TiO_2 films also increases. It was observable that initially film growth occurs via small nucleation sites, which then coalesce into a denser and less porous film. Some larger particulates were observed on the film surface as the number of reaction cycles exceeds 800; however the surface roughness remained relatively low at 3.7 nm for the 1000 cycle film and 5.2 nm for the 1500 cycle film.

This presence of larger particulates at greater film thicknesses suggests a higher probability for scattering of X-rays. The root mean square (RMS) roughness values measured for these films are shown in Table 3.3.

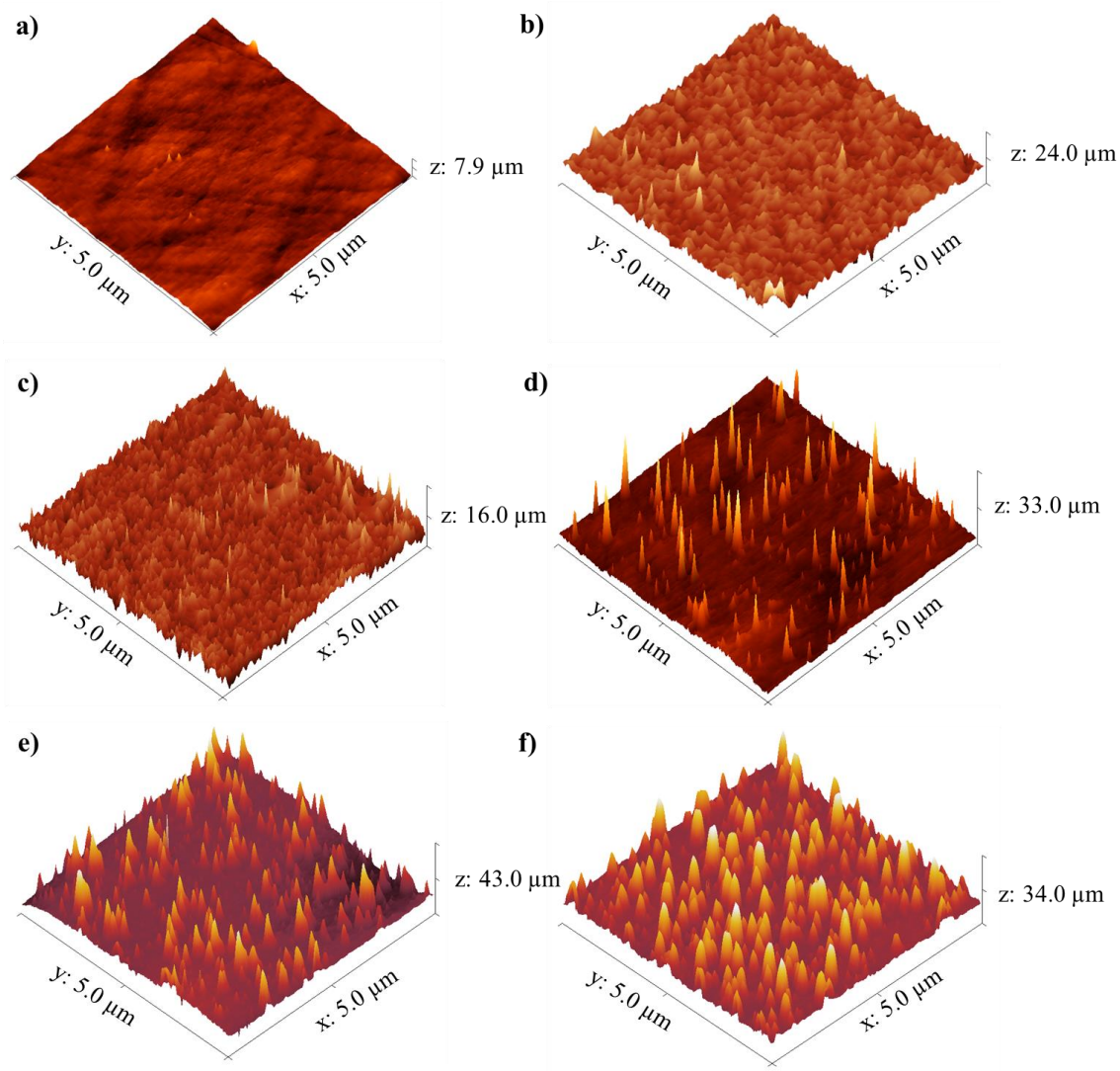

Figure 3.3 AFM images of TiO_2 films deposited at 200 °C with a) 100 cycles, b) 400 cycles, c) 600 cycles, d) 800 cycles, e) 1200 cycles and f) 1500 cycles. Images set to a physical scale factor of 50 in the z axis.

# cycles	Film thickness (nm)	RMS (nm)
100	4	0.6
200	6	0.6
400	10	1.7
600	19	2.4
800	38	2.2
1000	53	3.7
1200	66	3.9
1500	80	5.2

Table 3.3 Film thickness and roughness measurements of TiO_2 films grown at different number of reaction cycles

X-ray diffraction (XRD) measurements show that films deposited below 800 reaction cycles (~ 40 nm thick) appear amorphous. It is likely that this is because the films are too thin to produce significant diffraction, which is consistent with the appearance of a broad background peak attributed to breakthrough to the glass substrate. For films deposited at 800 cycles anatase peaks start to become visible, with the (101) reflection the most intense (Figure 3.4) but the (004), (105) and (211) anatase reflections were not distinguishable (anatase PDF reference number PDF 01-071-1166). As the number of reaction cycles increases further to 1500 cycles, the intensity of the anatase peaks increases as compared to the film deposited at 800 cycles. The relative peak intensity ratio between the (101) and (200) reflections was 3:1 for the 1500 cycle film, whereas a 2.5:1 ratio was observed for the film deposited at 800 cycles; this is the same as the peak ratio for the anatase reference pattern. The 1500 cycle film however, exhibits a more intense (101) peak than the reference pattern which indicates preferential film growth along the (101) crystal plane as the film thickness increases. As the film thickness increases, the (004), (105) and (211) reflections start to become more observable, which suggests that the film crystallinity increases with film thickness.

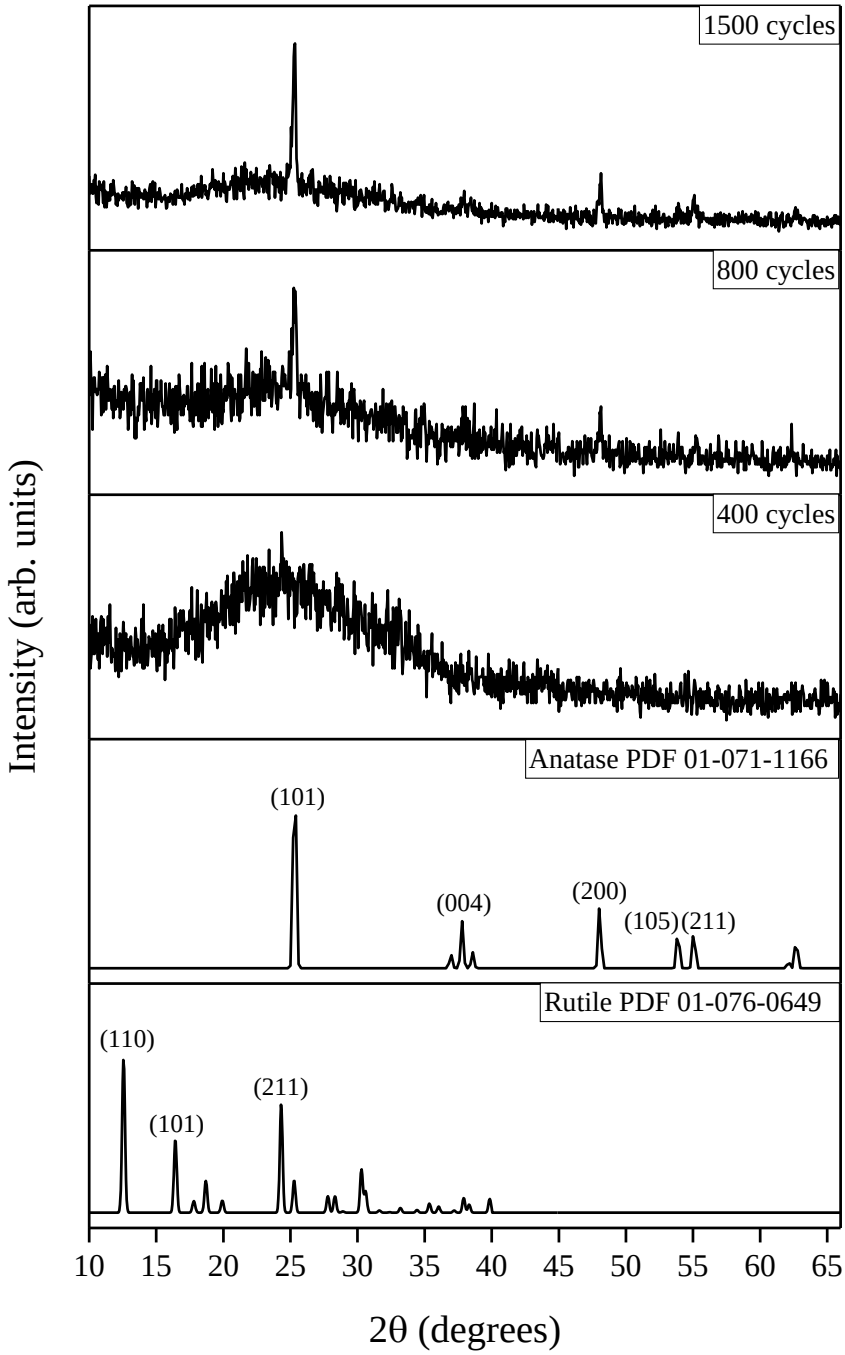

Figure 3.4 Typical XRD pattern for TiO_2 films deposited by ALD at 200 °C for 400, 800 and 1500 cycles at 200 °C. Typical anatase and rutile reference patterns for ALD films are included

It has been reported that the crystalline outcome of certain oxide films depends on several factors including the substrate material, film thickness, precursors and growth temperature. Leskela and Ritala have reported that the substrate material significantly affects the crystallinity of TiO_2 films grown using $TiCl_4$ and water as precursors.[11] Thin films (< 200 nm) grown on amorphous substrates (i.e glass) were amorphous in nature, whereas films grown on crystalline substrates tended to be crystalline. However, when the film thickness was increased, it was found that the films grown on glass had an increasing tendency towards crystallisation.[9] This idea can be related to these results seen for TiO_2 deposited on quartz and microscope slides.

Together with the weakness of the diffraction patterns and the AFM images, it can be suggested that initially when the film thickness is low, the films consisted of mixtures of amorphous and anatase phases, where the fraction of anatase phase increased with increasing film thickness.[19] It is believed that this can be attributed to the oligomerisation of the alkoxides at the surface; where they may create a transition between an amorphous layer and crystalline film.[9] This is consistent with the findings from ellipsometry where the measured refractive indices increased with film thickness. For these depositions there was no rutile phase present because the growth temperature of 200 °C was not high enough. It is widely considered that bulk anatase converts irreversibly to rutile in air at temperatures in the range 400 - 1200°C.[123]

Utilisation of the Scherrer equation allows an approximate calculation of the mean crystallite size for these TiO_2 films. This was calculated by measuring the broadening of the X-ray reflections from the (101) crystallographic plane. If the crystallite sizes are small, this creates a broadening of the diffraction pattern maxima by an amount which is inversely proportional to the crystallite size.[124]

Through measurement of this additional peak broadening, the crystallite size can be approximately measured using equation 3.3, where B is the mean size of the crystallites (nm), K is a dimensionless number known as the Scherrer constant (this depends on how the peak width is determined, the shape of the crystallites and size distribution. K can vary between 0.62 and 2.08 but a value of 0.90 was used in this case), λ is the wavelength of X-ray radiation (nm), β is the additional broadening at half the maximum intensity (FWHM) after subtracting the instrumental line broadening (in radians) and θ is the Bragg angle (in degrees).

$$B = \frac{K\lambda}{\beta cos\theta} \qquad (3.3)$$

Table 3.4 shows the approximate crystallite sizes calculated using the Scherrer equation for TiO_2 films deposited at different thicknesses'.

# cycles	Film thickness (nm)	Approximate crystallite size (nm)
800	46	40
1500	115	50

Table 3.4 Approximate crystallite sizes of TiO_2 films deposited at different thicknesses'

It is important to note that the Scherrer equation normally works on the requirements that the material being analysed is of cubic phase with round particles. TiO_2 anatase is tetragonal phase and so the absolute values that the Scherrer equation produces are to be taken with some scepticism. Comparison of the relative values gives an indication of the film crystallinity and structure. Here, it is advocated that the film deposited at 800 cycles consists of a single layer of separated crystallites as the crystallite size is similar to the measured film thickness and the grain size observed using AFM. The film thickness of the 1500 cycle film however is approximately twice that of the crystallite size which implies that the film consists of a bi-layer of crystallites. This supports the XRD data in Figure 3.4, which shows that the film crystallinity increases with film thickness.

Similarly, Raman spectroscopy measurements confirm the presence of TiO_2 anatase peaks for films deposited at thicknesses of ~ 100 nm and above. Raman spectroscopy is capable of unambiguously distinguishing between the three polymorphic forms of TiO_2 (anatase, rutile and brookite). Figure 3.5 shows a dominant anatase band at 141cm^{-1} with additional bands at lower intensity observed at 195 cm^{-1}, 396 cm^{-1}, 518 cm^{-1} and 638 cm^{-1}.[125,122] Rutile phase displays its most intense and characteristic bands at 446 cm^{-1} and 610 cm^{-1},[122] which were not observed. For films deposited at thicknesses below 100 nm, the Raman spectra were very close to that of the bare substrate, so no anatase bands were detected.

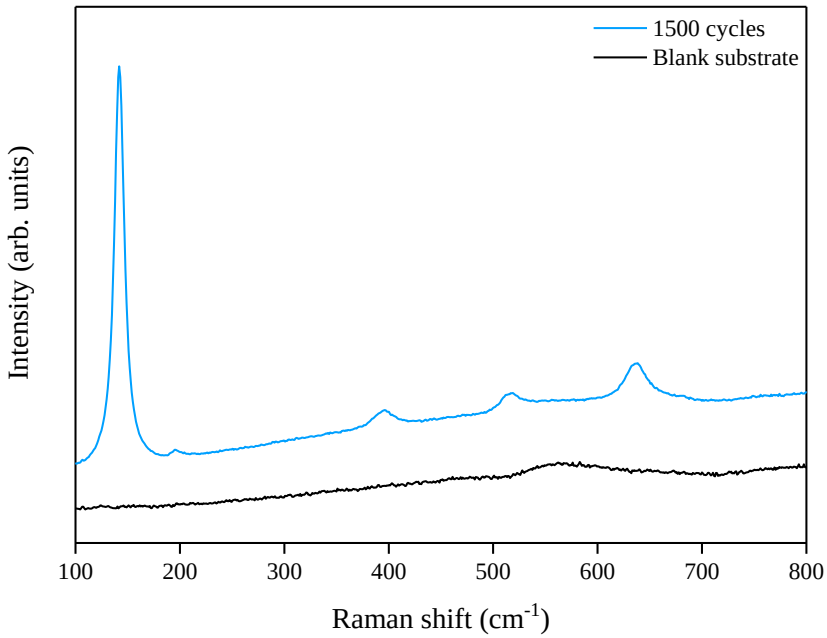

Figure 3.5 Typical Raman spectrum of TiO_2 anatse films deposited by ALD at thicknesses > 100 nm

Scanning electron microscopy (SEM) was used to image the surface of the TiO_2 films, but as the films were very thin (< 120 nm), this technique revealed no further information about the morphology of the films. See appendix A for a selection of the SEM images.

To determine the elemental composition and electronic state of the elements within the TiO_2 films, X-ray photoelectron spectroscopy (XPS) was performed. The data reveals the presence of Ti and O elements on the film surface with minimal contaminants present, as shown by the survey spectrum (Figure 3.6). A small peak was observed at 347 eV which was attributed to Ca2p ions in the glass leaching through into the TiO_2 film.

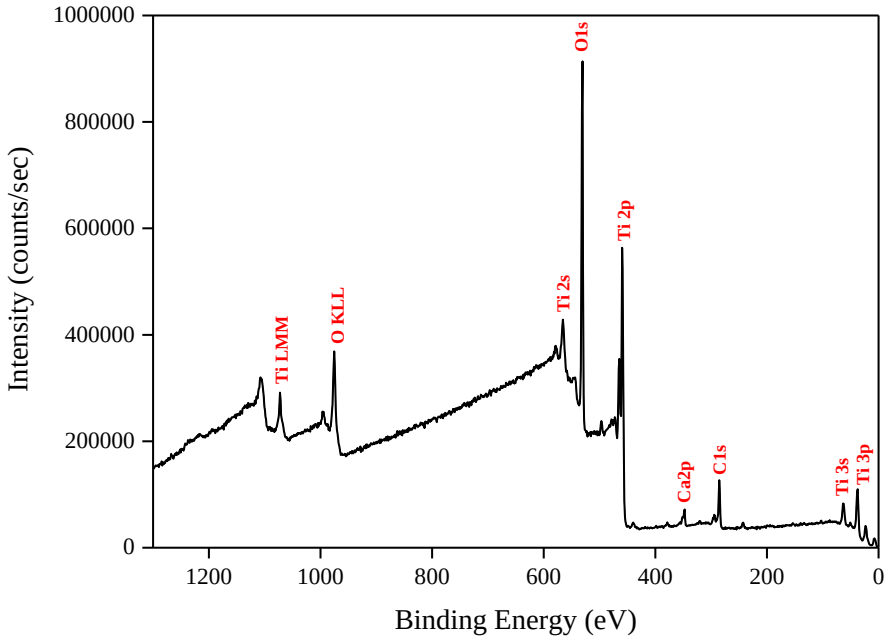

Figure 3.6 Typical XPS survey of TiO_2 films deposited by ALD of TTIP and water at 200 °C

High resolution surface scans of the Ti2p peak (Figure 3.7a) confirm the presence of Ti^{4+}, with $2p_{3/2}$ and $2p_{1/2}$ peak binding energies of 458.0 eV and 464.0 eV respectively, with a peak separation of 5.7 eV. These values are within ± 0.2 eV of literature values.[126,127] De-convolution of the O1s peak reveals 2 peaks. The peak at the highest binding energy (531.7 ± 0.2 eV) can be attributed to surface adsorbed water and the peak with the lowest binding energy (529.5 ± 0.2 eV) is ascribed to the O1s core peak of O^{2-} bound to Ti^{4+} (Figure 3.7b). Again, these peaks are consistent with literature values for these peak environments.

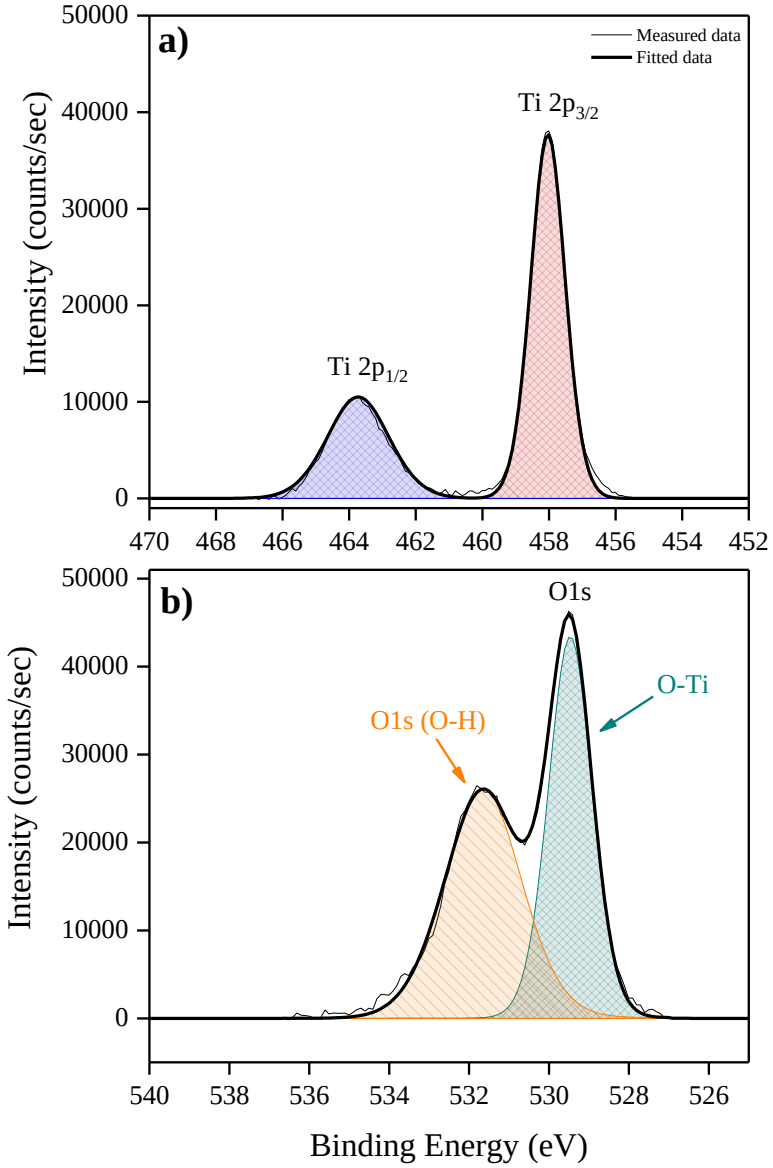

Figure 3.7 Typical high resolution XPS spectra of a) Ti2p peak and b) de-convoluted O1s peak for TiO_2 films

The areas of the Ti2p and O1s peaks in the XPS spectrum are proportional to the amount of element present, so the Ti:O elemental ratio can be determined using equation 3.4, where σ is the relative concentration of the element, I is the measured peak area and R is the relative sensitivity factor which is specific to each element and each orbital.

$$\sigma = I/R \qquad (3.4)$$

The relative sensitivity factor of O1s is listed as 0.66 and the relative sensitivity factor of Ti2p is listed as 1.80 (NIST X-ray photoelectron spectroscopy standard reference database). The elemental ratio of Ti:O was 1:2.4 which confirms the empirical formula of TiO_2. An argon ion etching gun was used to penetrate into the film (50 - 400 second etch time), allowing depth profile analysis. Upon etching, it was observed that different Ti2p peak environments (**B** and **C**) were present; with more environments becoming visible as the film was etched deeper (Figure 3.8).

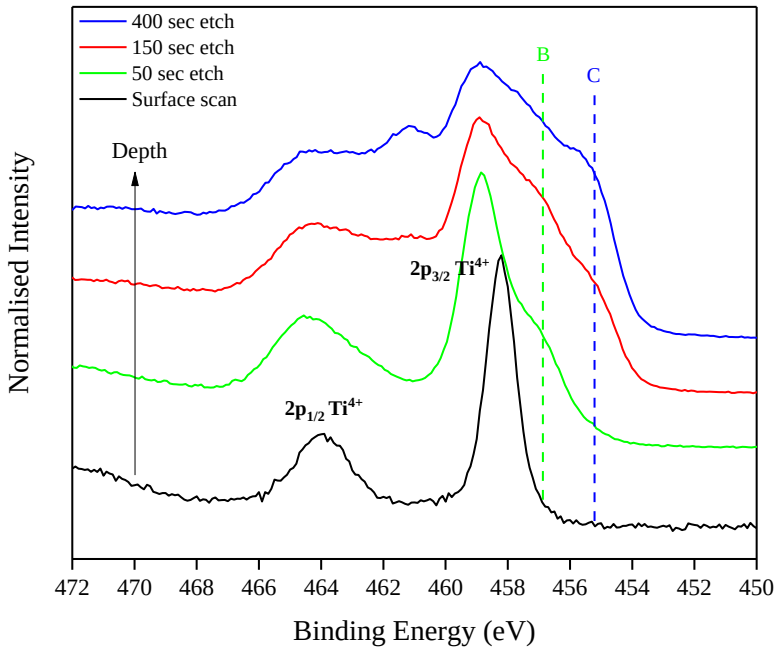

Figure 3.8 XPS depth profile analysis of high resolution Ti2p peak. Band **C** indicates the presence of additional peak environments due to the etch process

Figure 3.9 shows that along with the core TiO_2 peaks (**A**), there are two more species in the Ti2p spectra of the sputtered samples: component **B** at a binding energy of 457.3 ± 0.2 eV which can be associated to Ti-OH bonds because it is closely correlated to the second component **B** of the O1s peak at a binding energy of 530.9 ± 0.2 eV, which is attributed to the hydroxides.[125] The fact that the binding energy of peak **B** (457.3 ± 0.2 eV) is in between the binding energies of Ti^{4+} (458.9 ± 0.2 eV) and Ti^{3+} eliminates the possibility of it being due to Ti^{2+} (typical Ti^{2+} binding energy is ~ 455 eV). This suggests that peak **B** originates from core level Ti^{4+} bound to an

oxygen vacancy.[128] A slight shift to a lower binding energy was observed for peak **B**, as the removal of oxygen leads to a higher electron density than the ones corresponding to Ti^{4+} in TiO_2 (peak A).[128] This therefore rules out the possibility of peaks **B** and **B'** being due to the formation of Ti^{3+} or Ti^{2+}. So from the core level peaks of O1s and Ti2p, there is strong evidence of the existence of oxygen vacancies within the films, which have formed due to the etching process.

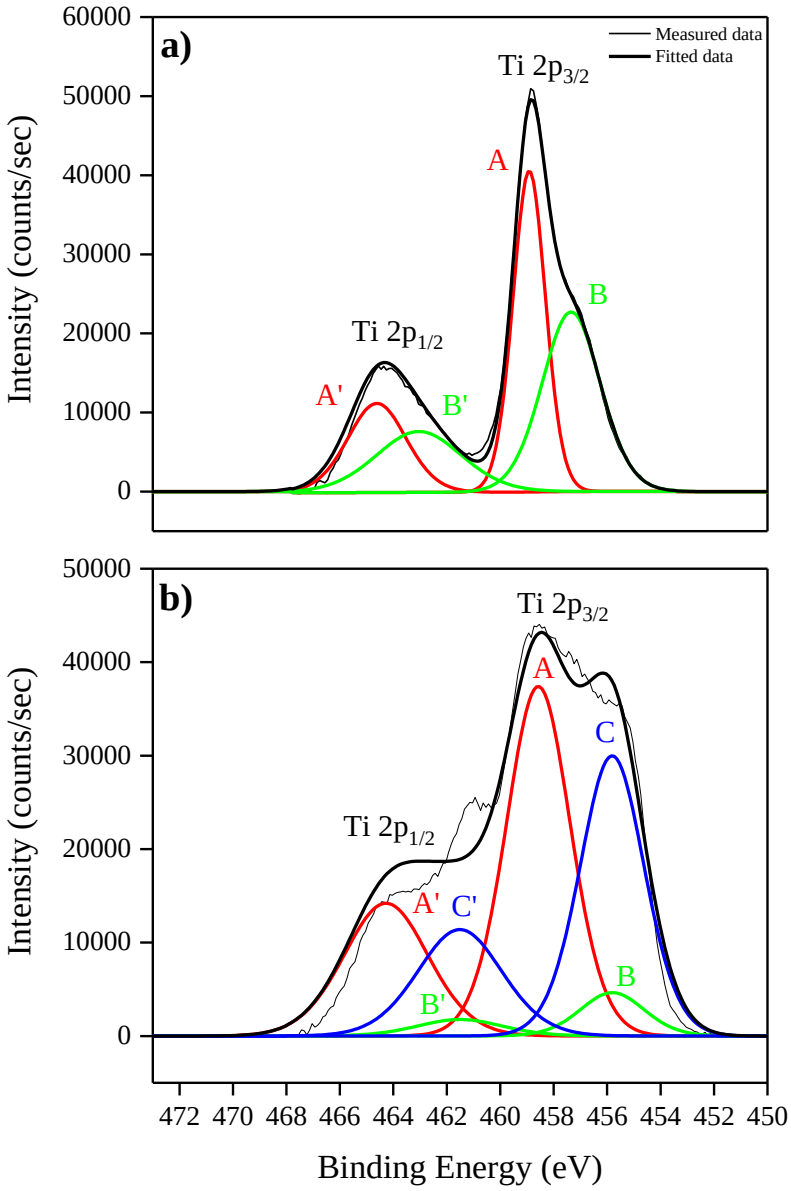

Figure 3.9 High resolution Ti2p spectra of the TiO_2 films: a) sputtered for 50 sec; b) sputtered for 400 secs. The labels at the curves indicate the component of the spin-orbit splitting peaks: **A**, **B** and **C** – Ti $2p_{3/2}$ and **A'**, **B'** and **C'** – Ti$2p_{1/2}$

The third component Ti2p - **C** at a binding energy of 455.2 eV can be attributed to the presence of the lower oxidation state of titanium (Ti^{3+}), Ti_2O_3.[128,125] This species is present due to the reduction of Ti^{4+} to Ti^{3+}. It cannot be definitively determined whether the Ti^{3+} species are coming from the bulk TiO_2 film or whether they form due to reduction of Ti^{4+} from the ion etching gun; however due to the presence of Ti^{4+} on the film surface, the latter is more likely. From the O1s peak it is clear that during etching, the amount of oxygen bound in the film as O^{2-} to Ti^{4+} increases and surface adsorbed oxygen species are no longer detected.

Depth profile analysis of the Si2p peak shown in Figure 3.10 confirmed that the films were pin-hole free as no SiO_2 was detected from beam breakthrough to the substrate (XPS escape depth is in the range 1 - 10 nm).

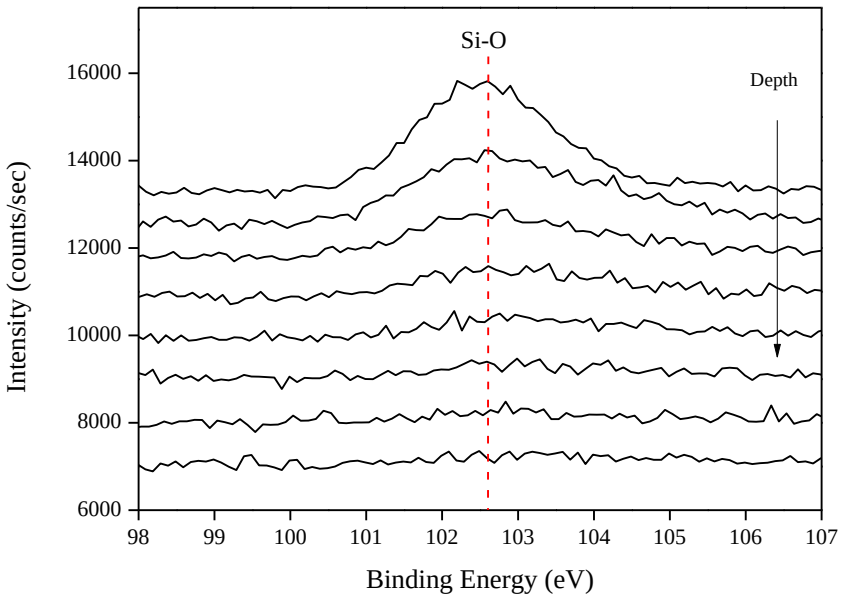

Figure 3.10 High resolution Si2p spectra of the TiO_2 films sputtered at 50 second intervals. The amount of SiO_2 detected decreases with depth confirming films are pinhole free

3.2.4 Effect of dose and purge times on growth rate

For true ALD growth to occur, it is important that the growth conditions are optimised in order to produce high quality and highly conformal films. The most important parameters to be investigated are the dose times, purge times and the growth temperature.

To verify that the film growth proceeds in a self-limiting manner, rather than mass transport limited decomposition of the TTIP, ALD depositions were performed at 200 °C and the dose time of each precursor was independently varied (keeping all other parameters fixed: purge times, temperature and number of reaction cycles). When investigating the effect of precursor dose times on the film growth rate, a 1 minute purge was used for TTIP and a 3 minute purge time was used for water (same as conditions outlined in Table 3.1). When investigating the effect of precursor purge times on the film growth, a 2.5 second dose was used for TTIP and a 2.0 second dose was used for water.

In Figure 3.11a, it can be seen that as the TTIP dose time was increased from 2.5 seconds to 5.5 seconds, the growth per cycle (GPC) remained fairly constant. This suggests that the TTIP has fully saturated the substrate surface (i.e. there are no more free hydroxyl groups on the surface for the TTIP to react with), which confirms that the film growth is self-limiting.[67] However, as the TTIP dose time is increased further, to more than 5.5 seconds the TiO_2 growth rate increases. This is believed to be because the 1 minute TTIP purge time is not sufficient to remove all of the unreacted TTIP within the reaction chamber, so when the water is then dosed both precursors were present in the reactor simultaneously, leading to CVD-like growth occurring.

Through variation of the water dose time (Figure 3.11b), both low and high water doses were capable of saturating the surface, indicating that changing the water dose time had less of an influence on the growth rate as compared to TTIP. Figure 3.11b suggests that the water dose is tending towards saturation beyond a 5 second dose time, but it is likely that insufficient purge times are responsible for the slope above 5 seconds.

The level of saturation was slightly higher at higher water dose times than lower water dose times (~ 0.45 Å/cycle compared to ~ 0.20 Å/cycle) and this increase is attributed to a greater hydroxyl group density on the film surface after the higher water dose; hence more TTIP could react with these sites on the surface to form TiO_2. A similar pattern of results were observed by Matero *et al.*, where a higher water dose resulted in a growth rate of ~ 0.6 Å/cycle and a lower water dose resulted in a growth rate of ~ 0.3Å/cycle.[117]

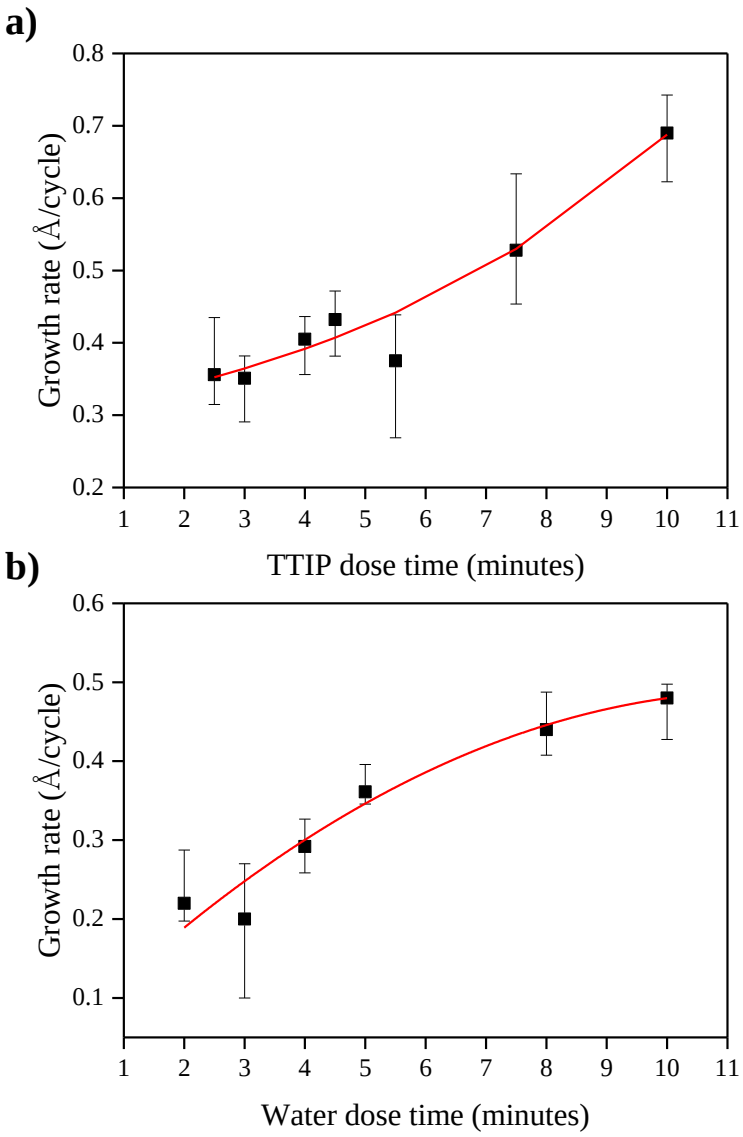

Figure 3.11 Effect of independently varying the dose time of each precursor on the growth rate of TiO_2 films deposited at 200 °C with 100 cycles

It is possible to determine whether the chemisorbed species are stable on the surface by independently varying the precursor purge times. Once the surface is fully saturated with precursor, the layers should be stable enough to resist changes in its film thickness when the purge time is varied. Figure 3.12a shows that a 5 minute or greater water purge time resulted in a fairly constant growth rate (~ 0.3 Å/cycle). This verifies that the chemisorbed layers are stable on the substrate surface, so any further purging will not affect the film thickness. At water purge times below 5 minutes, there is still unreacted precursor in the reactor; in which a purge time of < 5 minutes is insufficient to remove all of the water. This is why a higher growth rate was observed. These findings suggest that a 5 minute water purge time should be used rather than a 3 minute purge time. By changing the TTIP purge time, minimal changes were observed in the TiO_2 growth rate (Figure 3.12b). This behaviour has also been reported elsewhere: Aarik *et al*. have shown that mass changes recorded using *in-situ* QCM (quartz crystal microbalance) during ALD of TiO_2 do not depend on the purge time for TTIP.[41] A possible explanation is that TTIP may readily react with the surface hydroxyl groups and with the short TTIP dose time used (2.5 seconds); any unreacted precursor is easily purged from the reactor in as little as 30 seconds.

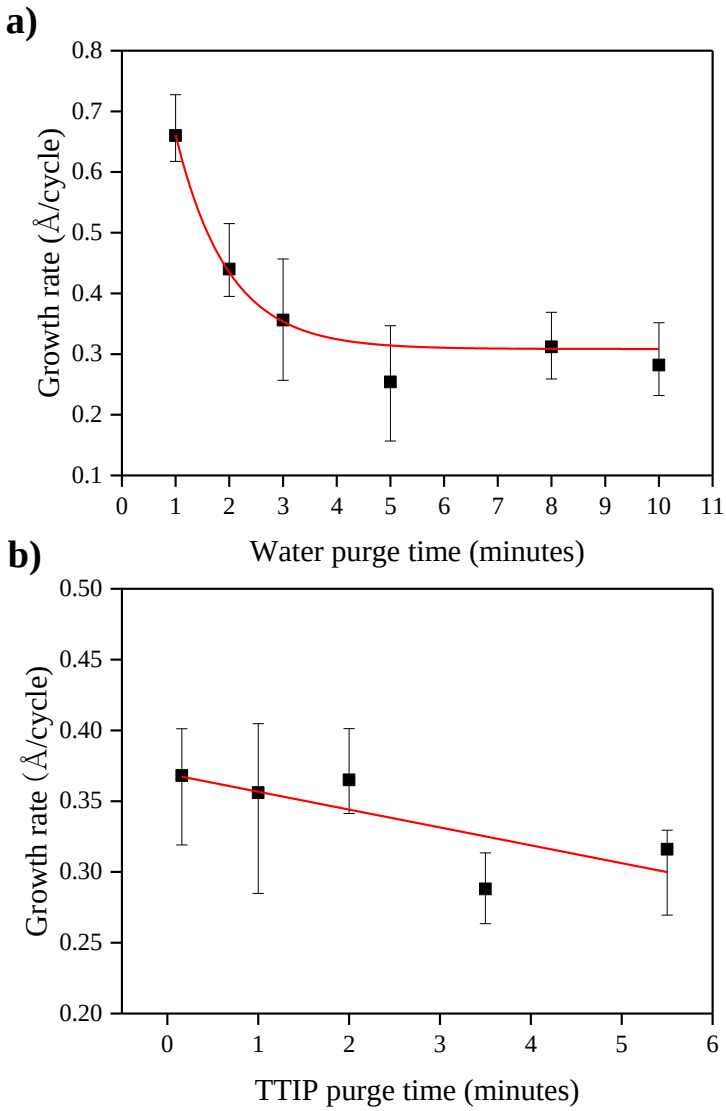

Figure 3.12 Effect of independently varying the purge time of each precursor on the growth rate of TiO_2 films deposited at 200 °C with 100 cycles

3.2.5 Effect of temperature on growth rate

The ALD growth temperature strongly determines the amount of material which chemisorbs to the substrate surface in a saturating manner. Figure 3.13 depicts the growth rate for TiO_2 films deposited at 100 cycles from TTIP and water as a function of temperature (2.5 second TTIP dose, 1 minute purge, 2.0 second water dose, 3 minute purge sequences). It can be seen that a temperature-independent growth rate of ~ 0.5 Å/cycle was obtained between 225 °C and 275 °C, where there is sufficient thermal energy for reactions to take place. This temperature region is known as the "ALD process window"; where the film is fully saturated.[8] When the growth temperature was increased to 400 °C, the film thickness increased rapidly due to thermal decomposition of the TTIP becoming dominant, resulting in CVD-like behaviour. These results are consistent with the reported decomposition temperature of TTIP of 275 °C.[41] It is also believed that the surface of the growing TiO_2 may catalyse the decomposition of TTIP more effectively than the glass substrate.[19] At growth temperatures below 225 °C the growth rate decreases due to low reactivity of precursors, as there is insufficient thermal energy for chemical reactions to take place. Consequently there may be porous areas of coverage across the surface.

For reproducibility in film thickness ALD depositions should be performed within the "ALD process window". Ritala and Leskelä have previously reported a temperature-independent growth rate of 0.30 Å/cycle for TiO_2 grown at temperatures between 250 - 325 °C.[19]

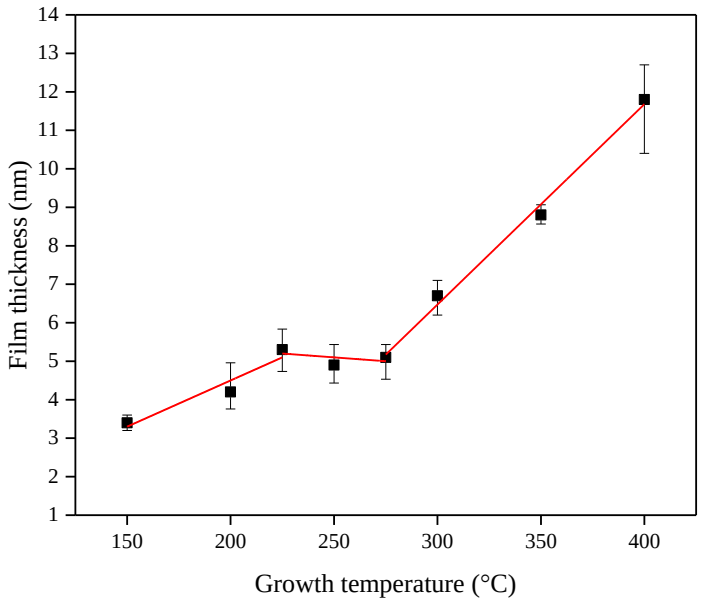

Figure 3.13 Temperature dependence on the growth rate of TiO_2 films grown at 100 cycles using 2.5 second TTIP dose, 1 minute purge, 2.0 second water dose, 3 minute purge sequences

AFM analysis of TiO_2 films deposited with 100 cycles at different growth temperatures illustrate that the surface roughness increases with growth temperature (Figure 3.14). Films were deposited using the dose/purge conditions outlined above. A possible explanation could be due to the precursor decomposing at high temperatures (TTIP decomposition temperature 275 °C),[41] which can lead to uncontrolled growth with reduced uniformity and therefore higher surface roughness. Changes in crystallinity, improved crystal growth, or a higher degree in the preferential growth direction can also affect the surface roughness.[50] The AFM images suggest that the crystallinity of the films increases with growth temperature. The root mean square (RMS) roughness values measured for these films are shown in Table 3.5.

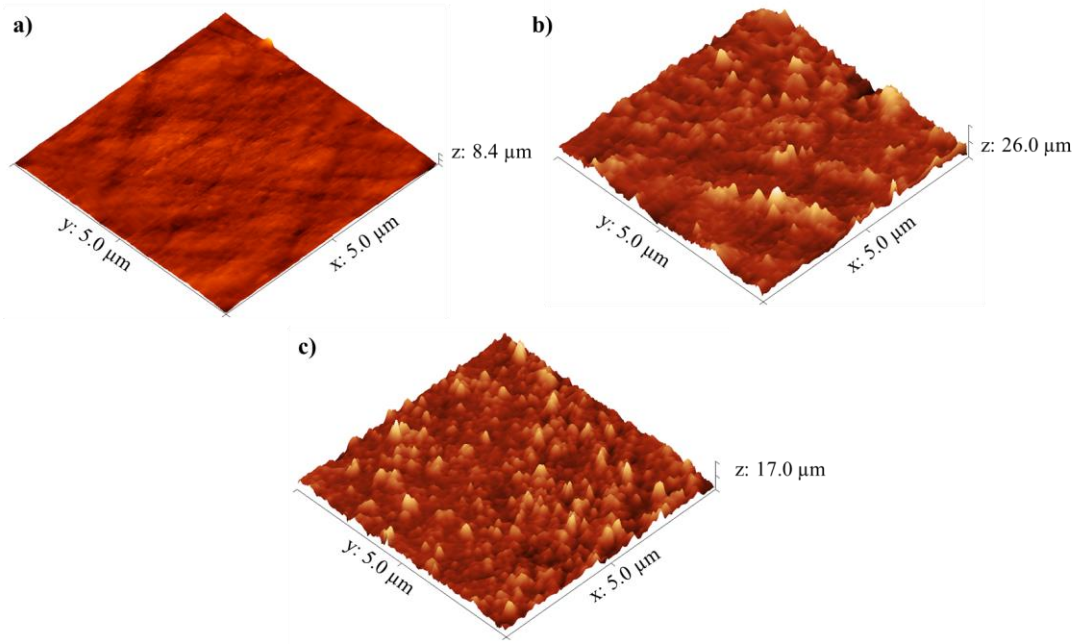

Figure 3.14 AFM images of 100 cycle TiO_2 films deposited at a) 200 °C, b) 300 °C and c) 400 °C. Images set to a physical scale factor of 30 in the z axis

Growth temperature (°C)	Film thickness (nm)	RMS (nm)
200	5	1.1
300	7	1.5
400	12	4.0

Table 3.5 Film thickness and roughness measurements for 100 cycle TiO_2 films deposited at different substrate temperatures

Due to these materials being 'ultra-thin', no further information about the morphology/structure of the TiO_2 films could be obtained using X-ray diffraction or Raman spectroscopy techniques. However, XPS analysis of the core level peaks of Ti2p and O1s confirm the presence of Ti^{4+} and oxygen vacancies respectively as described earlier in section 3.2.3.

3.3 Overall Conclusions

Atomic layer deposition of TiO_2 thin films has been demonstrated using titanium isopropoxide and water as precursors. Through manipulation of the precursor vapour pressures, dose/purge times, gas flow rates and substrate temperatures, the optimum growth conditions for TiO_2 have been established. ALD reaction cycles were carried out using a 2.5 second TTIP dose, 1 minute purge, 2.0 second water dose followed by a 3 minute purge to achieve a TiO_2 growth rate in the range of 0.3 - 0.6 Å/cycle. Under these conditions, growth occurred in a self-limiting manner to produce fully saturated TiO_2 films which were highly uniform.

An induction period was observed between 50 and 400 cycles, which was related to the time taken to establish ideal ALD growth. The importance of the surface hydroxyl groups has been emphasised, as these initiate TiO_2 growth by aiding in the adsorption and desorption of the precursor and hence govern the nature of the films grown. It has been suggested that growth occurs initially via stable nucleation sites on the surface, which then grow and coalesce to form a continuous film. This idea is supported by AFM analysis of the films, where the surface roughness of the films increased with film thickness and also with temperature. The "ALD process window", where growth was fully saturated was established at growth temperatures between 225 - 275 °C.

The TiO_2 films were also analysed using XRD, XPS and Raman spectroscopy. XRD has shown that films < 40 nm in thickness appear amorphous because the films are too thin to produce significant diffraction. Diffraction patterns for films > 40 nm thick confirm the presence of anatase phase, where the intensity of the diffraction pattern increases with film thickness. Refractive index values obtained through ellipsometry confirm that the films become more dense and crystalline with film thickness. Raman spectroscopy measurements were also conclusive with the presence of anatase phase.

XPS analysis confirmed Ti^{4+} oxidation state on the film surfaces with the core level Ti2p binding energies in line with those reported in the literature. De-convolution of the O1s peak showed 2 peaks which can be attributed to surface adsorbed water and the O1s core peak of O^{2-} bound to Ti^{4+}. Upon argon ion etching, additional peak environments became visible within the Ti2p and O1s spectra which were attributed to the existence of oxygen vacancies and Ti^{3+} species through the reduction of Ti^{4+}. Depth profile analysis also confirmed that the films were pin-hole free.

Chapter 4

ALD of nickel oxide thin films

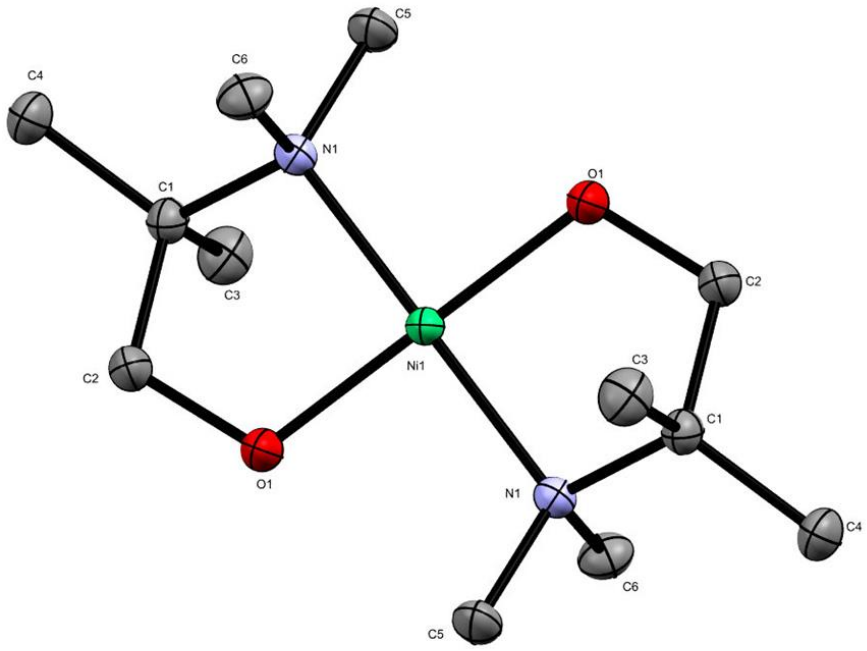

Chapter 4 ALD of nickel oxide thin films

4.1 Introduction

This chapter describes the atomic layer deposition of *p*-type nickel oxide (NiO) thin films. Depositions were performed using four different metal precursors as listed below.

- Nickel(II) bis(2,2,6,6-tetramethyl-3,5-heptanedionate), $[Ni(thd)_2]$
- Bis(cyclopentadienyl)nickel(II), $[Ni(Cp)_2]$
- $[Ni(dmamp)_2]$, (dmamp = 2-dimethylamino-2-methyl-1-propanolate)
- Nickel guanidinate, $[Ni\{(N^iPr_2)_2CNEt_2\}_2]$

The first two precursors have been reported in the literature previously for use in ALD with water as the co-reactant. However the latter two were novel precursors synthesised specifically for this work and therefore their application as potential ALD precursors was investigated. The films were analysed using various techniques to determine film quality and conformality.

One of the characteristics of ALD is that there are several reaction parameters which can be varied to enable 'true' ALD growth to occur; that is that reactions are complementary and self-limiting. Throughout these experiments, the reaction parameters investigated (but not limited to) included; precursor dose times, precursor purge times, precursor vapour pressures, gas flow rates and substrate growth temperature.

4.2 Experimental

4.2.1 General procedures

The majority of manipulations were performed under nitrogen using standard Schlenk tubes and a Unilab MBraun glove box. Oxygen-free nitrogen (99.9% purity) was obtained from BOC and used as supplied. All solvents were purified by standard methods with respect to oxygen and water and then stored over activated 3 Å molecular sieves until used. Anhydrous nickel(II) chloride hexahydrate (98+%) was obtained from Acros Organics and used as supplied. *N,N'*-diisopropylcarbodiimide (99%), was obtained from Acros Organics and purified with respect to oxygen and water using the freeze-pump-thaw technique and then stored over 3 Å molecular sieves until used. Nickel(II) acetate tetrahydrate, 2,2,6,6-tetramethyl-3,5-heptanedione, lithium diethylamide (≥ 95%), anhydrous sodium hydride (dry, 95%) and sodium acetate (> 99%) were obtained from Sigma Aldrich and used as supplied. Nickel(II) chloride anhydrous (98%) was obtained from VWR and used as supplied. Dmamp (2-dimethylamino-2-methyl-1-propanol) was obtained from MP Biomedicals and purified by standard methods with respect to oxygen and water using the freeze-pump-thaw technique and then stored over 3 Å molecular sieves until used. Methanol (99.8%), ethanol (95%) and petroleum ether (bp 40 - 60 °C) were purchased from Sigma Aldrich and used as supplied. Tetrahydrofuran (THF) and hexane were obtained from a dry solvent system within the chemistry department at UCL.

4.2.2 Physical measurements

^{1}H NMR and ^{13}C{^{1}H} NMR spectra were recorded using Bruker AMX 300 MHz and Bruker Avance III 600 MHz spectrometers and were referenced to the residual proton and ^{13}C resonances of the solvent. Microanalytical data and mass spectrometry data were obtained at University College London (UCL). Mass spectra were recorded using Thermo MAT900 and Micromass LCT Premier Spectrometers. Thermogravimetric analysis (TGA) was performed using a Netsch simultaneous TG-DTA/DSC apparatus equipped with Proteus software at atmospheric pressure, using aluminum pans under a constant flow of helium gas. The heating rate was 10 K/min. X-ray crystallography diffraction data were recorded on an Agilent Super Nova Dual Diffractometer with Cu-Kα radiation (λ = 1.5418 Å) at 150 K.

4.2.3 Precursor synthesis

4.2.3.1 Synthesis of $[Ni(thd)_2]$ (4.1)

(4.1a) A solution of nickel chloride hexahydrate, $NiCl_2.6H_2O$ (7.25 g, 30.5 mmol) in 100 cm^3 of distilled water was made and buffered with sodium acetate (10.11 g). This solution was then added slowly with continuous stirring to 15 cm^3 of ethanol containing a slight excess of 2,2,6,6-tetramethyl-3,5-heptanedione (9.82 g, 53.2 mmol). The precipitate was filtered using vacuum filtration, washed with water and dried in air. The green precipitate was re-crystallised from petroleum ether (bp 40 - 60 °C) and dried in a tube furnace (Carbolite 3-zone wire wound TZF 12) at 200 °C over 3 Å molecular sieves for 1 hour. The colour changed from green to purple, corresponding to the conversion of the dihydrate to the anhydrous form. The product was stored in a fume cupboard. Yield = 1.717 g, 13.2%. Mass spectra (ES+) m/z: 425.21 $[M]^+$. **^{1}H NMR [300 MHz, $CDCl_3$]** δ 0.98 [singlet, 36H, C-C$\underline{H}_3$], δ 5.51 [singlet, 2H, C-C$\underline{H}$-C]. **$^{13}C\{^1H\}$ NMR [75 MHz, $CDCl_3$]:** δ 28.2 [C-$\underline{C}H_3$], δ 39.7 [$\underline{C}$-$(CH_3)_3$], δ 92.0 [C-$\underline{C}$H-C], δ 196.4 [$\underline{C}$-C$(CH_3)_3$]. See appendix C for mass spectra.

(4.1b) Nickel acetate tetrahydrate (1.50 g, 6.02 mmol) was dissolved in warm methanol (10 cm^3) to form a green solution. This solution was added slowly to methanol (5 cm^3) containing a slight excess of 2,2,6,6-tetramethyl-3,5-heptanedione (1.67 g, 9.06 mmol). Distilled water (5cm^3) was then added to complete precipitation of a light green solid. The mixture was left to stir for 3 days at room temperature. The precipitate was filtered using vacuum filtration, washed with water and dried in air, before drying in a tube furnace (Carbolite 3-zone wire wound TZF 12) at 200 °C over 3 Å molecular sieves for 1 hour. The colour changed from green to purple, corresponding to the conversion of the dihydrate to the anhydrous form. The product was stored in a fume cupboard. Yield = 0.70 g, 27.3%. Mass spectra (ES+) m/z: 425.21 $[M]^+$. **^{1}H NMR [300 MHz, $CDCl_3$]** δ 0.98 [singlet, 36H, C-C$\underline{H}_3$], δ 5.51 [singlet, 2H, C-C$\underline{H}$-C]. **$^{13}C\{^1H\}$ NMR [75 MHz, $CDCl_3$]:** δ 28.2 [C-$\underline{C}H_3$], δ 39.7 [$\underline{C}$-$(CH_3)_3$], δ 92.0 [C-$\underline{C}$H-C], δ 196.4 [$\underline{C}$-C$(CH_3)_3$].

4.2.3.2 Synthesis of [Ni(dmamp)$_2$] (4.2)

Sodium hydride (1.745 g, 72.73 mmol) was dissolved in ~ 100 ml THF and stirred in an ice bath for 2 hours which formed a milky grey slurry. Dmamp (2-dimethylamino-2-methyl-1-propanol) (10.63 ml, 86.17 mmol) was added and the solution was refluxed overnight resulting in a clear orange/brown solution. The solvent was removed under vacuum to isolate the intermediate salt as a pale yellow solid. The sodium salt was added to a slurry of $NiCl_2$ (5.30 g, 40.89 mmol) in ~ 50 ml THF at 0°C and then warmed to room temperature. The solution was then refluxed for 2 days, forming a dark purple/black solution. The solution was filtered and the volume of solvent was reduced by approximately half and left in the freezer overnight. After filtering and removing the solvent under vacuum, a light brown solid was formed. The product was stored under an inert atmosphere. Yield = 10.2 g, 85.9%. Anal. calcd for $C_{12}H_{28}N_2NiO_2$ (291.06): C, 49.52; H, 9.70; N, 9.62. Found: C, 49.42; H, 9.92; N, 9.36. Mass spectra (CI) m/z: 291.2 $[M]^+$. **^{1}H NMR [600 MHz, C_6D_6]** δ 1.19 [singlet, 12H, C-(C$\underline{H}_3$)$_2$], δ 2.20 [singlet, 12H, N-(C$\underline{H}_3$)$_2$], δ 2.97 [singlet, 4H, O-C$\underline{H}_2$]. **^{13}C{^{1}H} NMR [150.90 MHz, C_6D_6]** δ 19.7 [C-(C$\underline{H}_3$)$_2$], δ 40.6 [N-(C$\underline{H}_3$)$_2$], δ 67.9 [N-$\underline{C}$-(CH$_3$)$_2$], δ 75.8 [O-(C$\underline{H}_2$)]. See appendix C for mass spectra.

X-Ray crystallography

Experimental: Single crystals of $C_6H_{14}NNi_{0.5}O$ (complex **4.2**) were recrystallised from THF. A suitable crystal was selected and mounted on a nylon loop on a SuperNova, Dual, Cu at zero, Atlas diffractometer. The crystal was kept at 161(14) K during data collection. Using Olex2,[115] the structure was solved with the SIR2004[113] structure solution program using Direct Methods and refined with the ShelXL[114] refinement package using Least Squares minimisation.

Crystal Data for $C_6H_{14}NNi_{0.5}O$ (*M*=145.54 g/mol): orthorhombic, space group Pbca, *a*=7.29116(10) Å, *b*=10.68510(13) Å, *c*=17.7933(2) Å, *V*=1386.22(3) Å^3, *Z*=8, *T*=150.5(7) K, μ(CuKα)=1.965 mm^{-1}, *Dcalc*=1.395 g/cm^3, 19533 reflections measured (15.714° ≤ 2θ ≤ 148.974°), 1412 unique (R_{int}=0.0229, R_{sigma}=0.0081)

which were used in all calculations. The final R_1 was 0.0217 ($I > 2\sigma(I)$) and wR_2 was 0.0610 (all data).

4.2.3.3 Synthesis of [Ni{(N^iPr_2)$_2$CNEt$_2$}$_2$] (4.3)

Lithium diethylamide (0.60 g, 7.58 mmol) was dissolved in 50 ml THF and stirred at room temperature for 30 minutes to form a pale yellow solution. Diisopropylcarbodiimide (1.2 ml, 7.75 mmol) was diluted in 10 ml THF and then added dropwise to the lithiated amine solution. The solution was stirred at room temperature for 3 hours, forming a pale orange solution. The solvent was then removed under vacuum to isolate the off-white powdery lithiated intermediate. Yield = 1.41 g, 90%.

The lithiated intermediate was dissolved in THF and stirred for 15 minutes at room temperature before adding nickel(II) chloride (0.527 g, 4.0 mmol) and then refluxing the solution for 18 hours. The solution went from pale orange to dark purple. The solution was then filtered to remove LiCl salt and evacuated to dryness, before extracting from hexane, filtering and removing the solvent under vacuum to afford a dark purple solid. The product was stored under an inert atmosphere. Yield = 1.31 g, 70.5%. Anal. calcd for $C_{22}H_{50}N_6Ni$ (457.38): C, 57.77; H, 11.02; N, 18.37. Found: C, 54.78; H, 10.40; N, 16.46. Mass spectra (ES+) m/z: 489.00 $[M+CH_3OH+H]^+$. **^{1}H NMR [600 MHz, C_6D_6]** δ 0.78 [triplet, 12H, C$\underline{H}_3$-CH$_2$], δ 1.54 [doublet, 24H, CH-(C$\underline{H}_3$)$_2$], δ 2.72 [quartet, 8H, CH$_3$-C$\underline{H}_2$], δ 3.15 [sept, 4H, C$\underline{H}$-(CH$_3$)$_2$]. **^{13}C{^{1}H} NMR [150.90 MHz, C_6D_6]** δ 13.8 [$\underline{C}$H$_3$-CH$_2$], δ 26.0 [CH-($\underline{C}$H$_3$)$_2$], δ 42.2 [CH$_3$-$\underline{C}$H$_2$], δ 48.5 [$\underline{C}$H-(CH$_3$)$_2$], δ 171.9 [N-$\underline{C}$-N]. See appendix C for mass spectra.

X-Ray Crystallography

Experimental: Single crystals of $C_{11}H_{24}N_3Ni_{0.5}$ (complexes **4.3a** and **4.3b**) were recrystallised from hexane. A suitable crystal was selected and mounted on a nylon loop on a SuperNova, Dual, Cu at zero, Atlas diffractometer. The crystal was kept at 161(14) K during data collection. Using Olex2,[115] the structure was solved with the SIR2004[113] structure solution program using Direct Methods and refined with the ShelXL[114] refinement package using Least Squares minimisation.

Crystal Data for complex (4.3a) $C_{11}H_{24}N_3Ni_{0.5}$ (*M*=227.69 g/mol): orthorhombic, space group Pbcn (no.60), *a*=10.61412(10) Å, *b*=20.7302(2) Å, *c*=12.10691(16) Å, *V*=2663.92(5) Å^3, *Z* =8, *T*=161(14) K, μ(CuKα)=1.172 mm^{-1}, *Dcalc*=1.135 g/cm^3, 41302 reflections measured (8.53° ≤ 2θ ≤ 147.41°), 2675 unique (R_{int}=0.0501, R_{sigma}=0.0161) which were used in all calculations. The final R_1 was 0.0351 (I > 2σ(I)) and wR_2 was 0.1009 (all data).

Crystal Data for complex (4.3b) $C_{11}H_{24}N_3Ni_{0.5}$ (*M*=227.69 g/mol): triclinic, space group P-1 (no.2), *a*=8.8931(3) Å, *b*=8.9707(3) Å, *c*=9.4611(3) Å, *α* =63.244(3)°, *β*=79.809(3)°, *γ*=85.968(3)°, *V*=663.30(4) Å^3, *Z*=2, *T*=155(7) K, μ(CuKα)=1.177 mm^{-1}, *Dcalc*=1.140 g/cm^3, 9393 reflections measured (10.614° ≤ 2θ ≤ 134.998°), 2391 unique (R_{int}=0.0461, R_{sigma}=0.0352) which were used in all calculations. The final R_1 was 0.0562 (I > 2σ(I)) and wR_2 was 0.1539 (all data).

4.2.4 Thin film deposition

ALD depositions were carried out using a nickel(II) precursor and distilled water. Pureshield argon (99.998%) obtained from BOC, was used as the inert carrier gas. Super premium microscope slides (from VWR), and quartz glass (obtained from Wuxi Crystal and Optical Instrument Company Limited) sides were used as the substrate materials. Prior to deposition, substrates were cut into ~ 4.0 cm x 2.5 cm pieces, cleaned using iso-propanol (Sigma Aldrich, 99.5%) and air dried before loading into the reactor. Whilst the substrate holder was being heated to the required temperature, the reactor was pumped down under vacuum to achieve a base pressure of ~ 4 x 10^{-2} mbar. Gas flows were then turned on, where the running pressure was recorded. As described in Chapter 2, the nickel precursor was introduced into the reaction chamber by bubbling the carrier gas into the bubbler to assist the transportation of vaporised precursor molecules. Water was introduced into the reaction chamber by means of its own vapour pressure, without any bubbling. To prevent the precursor condensing and reacting in the pipework, the bubbler outlet lines were held at a temperature higher than the bubbler temperature but lower than the substrate temperature.

The nickel(II) precursors were all solids at room temperature and were therefore sublimed at a certain temperature within the bubbler in order to generate sufficient gaseous molecules to be dosed into the reactor. Throughout these experiments, the reaction parameters investigated (but not limited to) included; precursor dose times, precursor purge times, precursor vapour pressures and substrate growth temperature.

4.3 Results and Discussion

4.3.1 Precursor synthesis

4.3.1.1 [Ni(thd)$_2$] (4.1)

[Ni(thd)$_2$] was synthesised via two different methods (Scheme 4.1 and Scheme 4.2) as outlined below.[129,130]

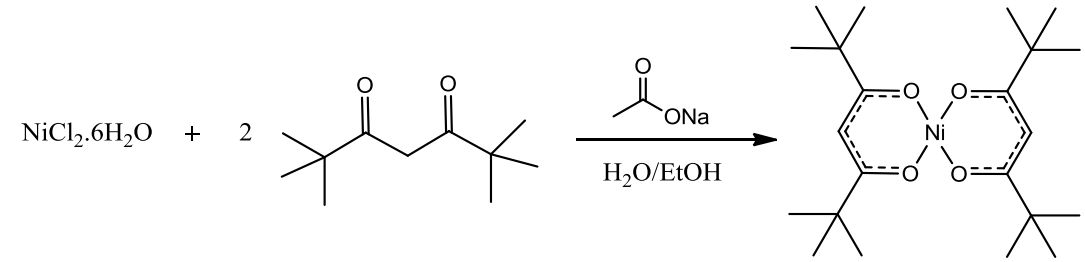

Scheme 4.1 Synthesis of compound (**4.1a**) [Ni(thd)$_2$]

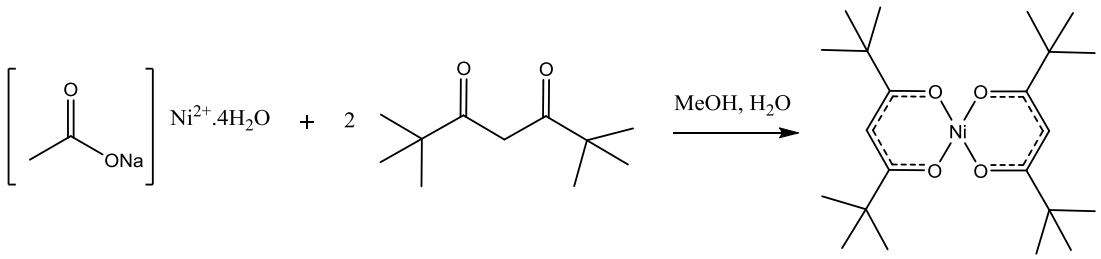

Scheme 4.2 Synthesis of compound (**4.1b**) [Ni(thd)$_2$]

^{1}H NMR and ^{13}C{^{1}H} NMR spectra for compound (**4.1**) are shown in Figure 4.1 and Figure 4.2 respectively. For [Ni(thd)$_2$] synthesised via both methods, the ^{1}H NMR spectrum shows peaks for two single proton environments; a singlet at 0.98 ppm for the 12 methyl groups (Ha) and a slightly broader singlet at 5.51 ppm for the two protons on the ligand backbone (Hb). The carbon NMR spectrum shows 4 different peak environments at 28.2, 39.7, 92.0 and 196.4 ppm, which are associated with the carbon environments C1, C2, C3 and C4, respectively as shown in Figure 4.2.

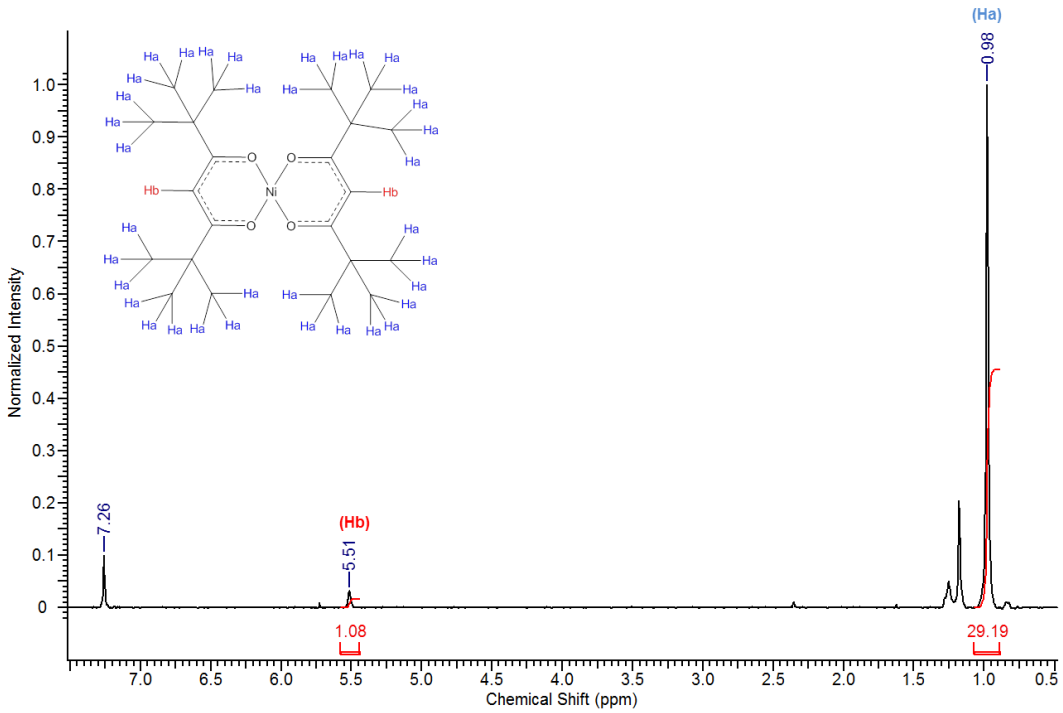

Figure 4.1 ^{1}H NMR spectrum of compounds (**4.1a**) and (**4.1b**) [Ni(thd)$_2$]

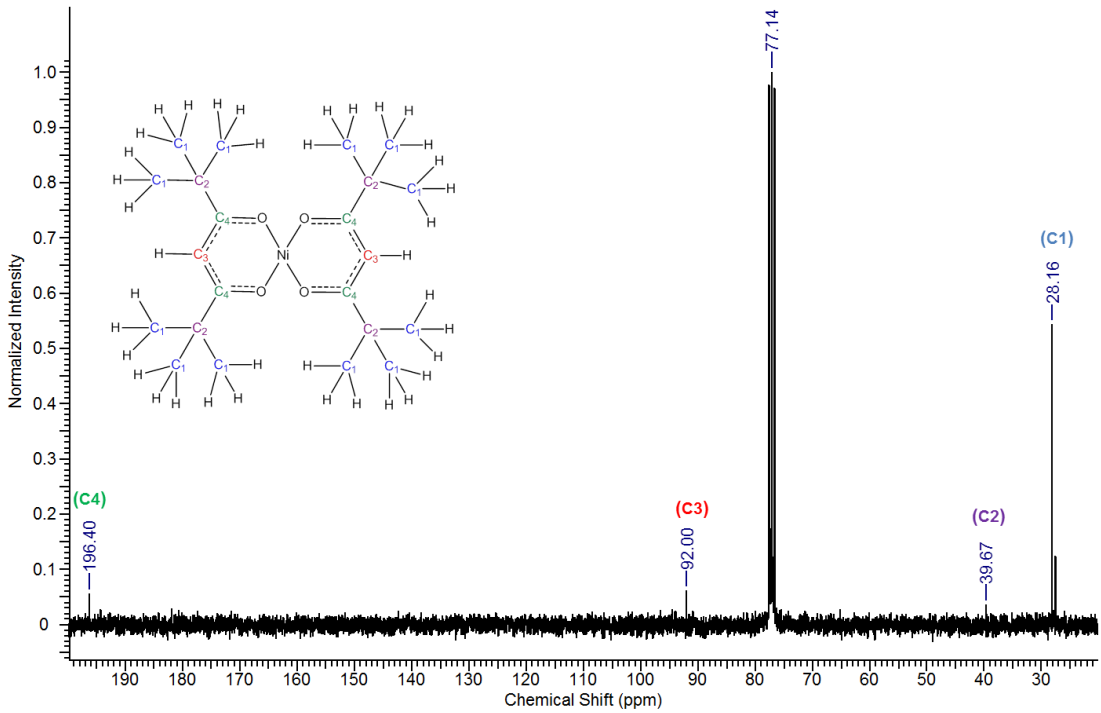

Figure 4.2 ^{13}C{^{1}H} NMR spectrum of compounds (**4.1a**) and (**4.1b**) [Ni(thd)$_2$]

4.3.1.2 [Ni(dmamp)$_2$] (4.2)

The novel precursor [Ni(dmamp)$_2$] was synthesised following adaptations from two different literature reports.[131,43] [Ni(dmamp)$_2$] synthesised in this work is different to those reported in the literature[132] because the two methyl groups on the dmamp ligand backbone are positioned on a different carbon atom (Figure 4.3). This structural change may slightly impact the volatility and thermal stability of the complex, but it is believed that unsymmetrically substituted ligands would significantly increase the volatility of the complex.[70] The two methyl groups on the ligand backbone are electron donating groups, so in complex **b)** these groups stabilise the dative-covalent bonding of nitrogen to the nickel centre, thus creating a more stable complex. The synthesis of the novel [Ni(dmamp)$_2$] complex is outlined in Scheme 4.3.

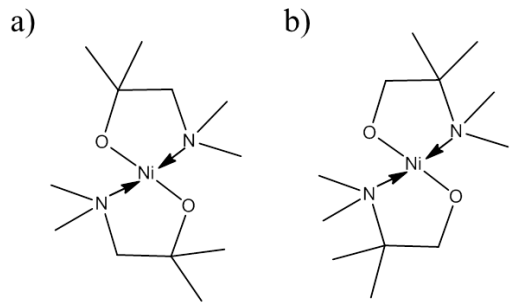

Figure 4.3 Structure of [Ni(dmamp)$_2$] synthesised in a) literature[131] and b) this work

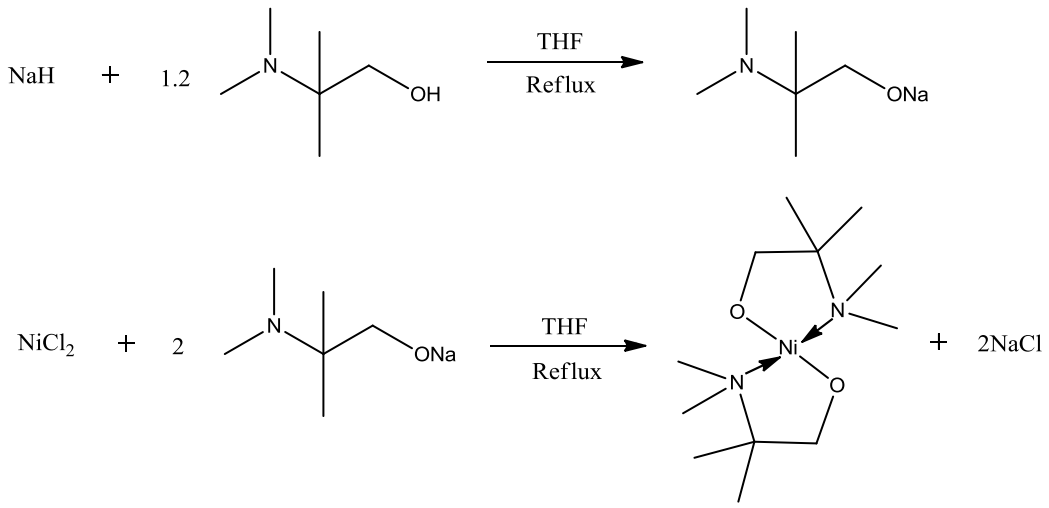

Scheme 4.3 Synthesis of compound (**4.2**) [Ni(dmamp)$_2$]

^{1}H NMR and ^{13}C{^{1}H} NMR spectra for compound (**4.2**) are shown in Figure 4.4 and Figure 4.5 respectively. The ^{1}H NMR spectrum shows 3 singlet proton environments at 1.19 ppm, 2.20 ppm and 2.97 ppm, corresponding to 4 methyl groups on the ligand backbone (Ha), 4 methyl groups on the nitrogen atoms (Hb) and 2 ethyl groups on the ligand backbone (Hc), respectively. The carbon NMR spectrum again shows 4 different peak environments at 19.7, 40.6, 67.9 and 75.8 ppm, which are associated to the carbon environments C1, C2, C3 and C4, respectively as shown in Figure 4.5.

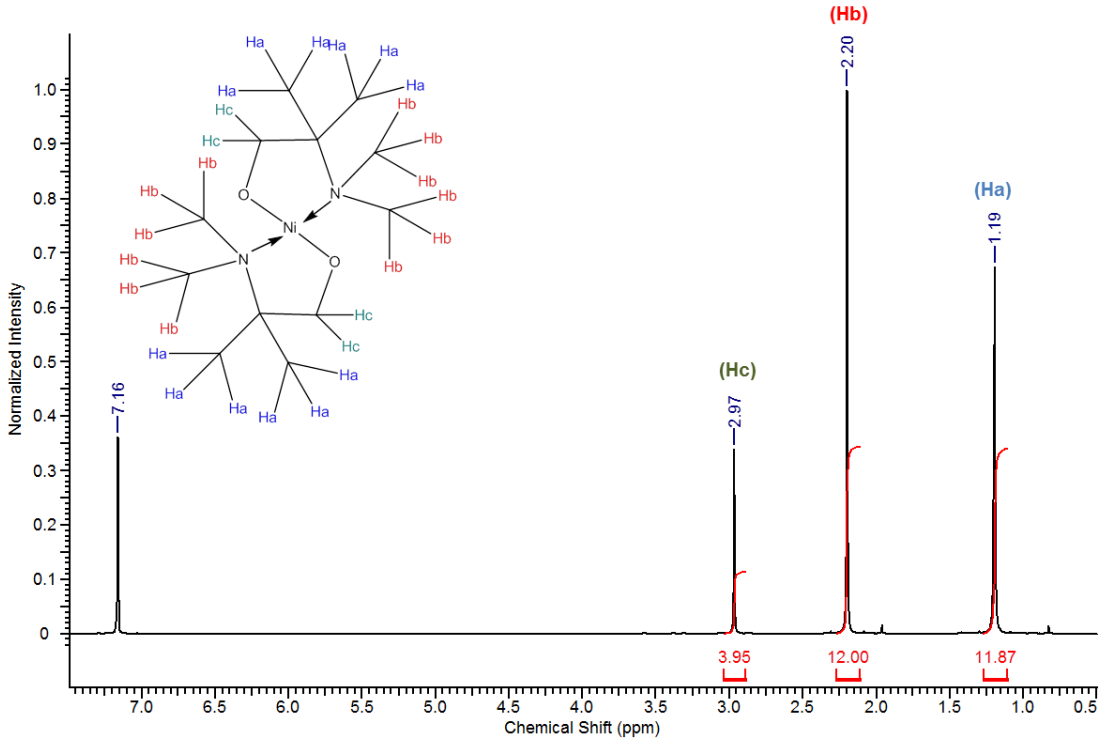

Figure 4.4 ^{1}H NMR spectrum of compound (**4.2**) [Ni(dmamp)$_2$]

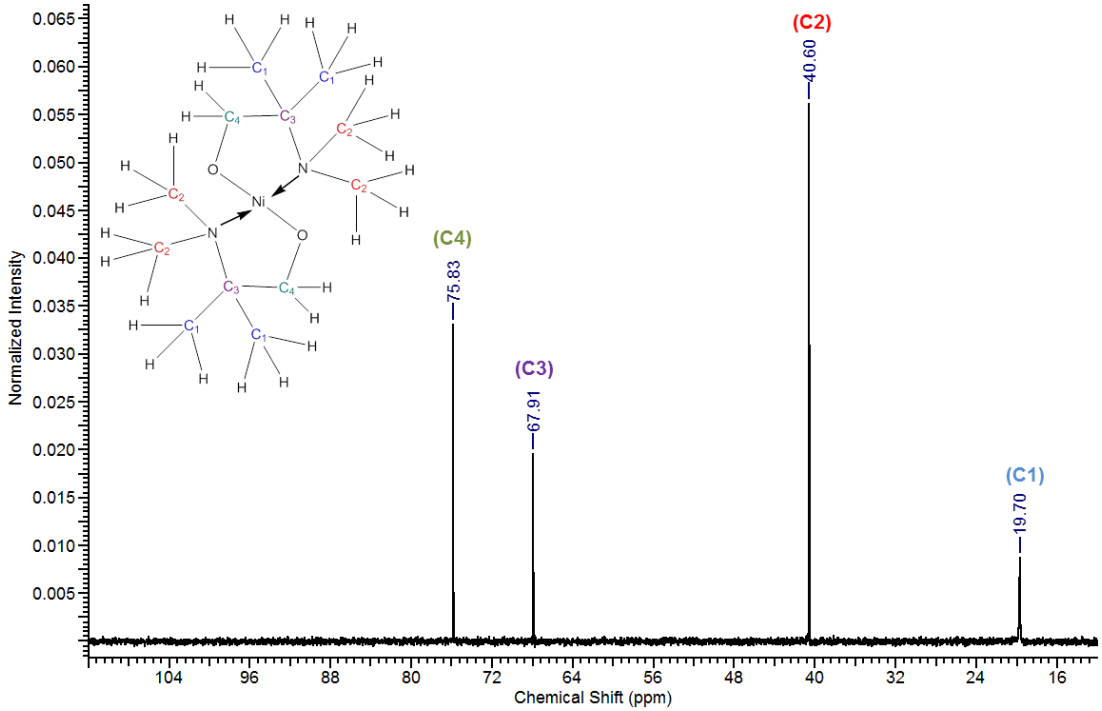

Figure 4.5 $^{13}C\{^{1}H\}$ NMR spectrum of compound (**4.2**) $[Ni(dmamp)_2]$

X-Ray crystallography

Figure 4.6 shows a single crystal of complex (**4.2**) mounted on the nylon loop prior to crystallographic analysis.

Figure 4.6 $[Ni(dmamp)_2]$ single-crystal mounted on nylon loop

A single-crystal structure determination showed the complex to have square planar geometry at the nickel centre, where the structure was consistent with the ^{1}H and ^{13}C NMR spectra. The complex possessed an orthorhombic space group.

The molecular structure of complex (**4.2**) (Figure 4.7) shows a nickel centre bound to 2 oxygen atoms and 2 nitrogen atoms. The O(1)-Ni(1)-O(1)^{1} and N(1)-Ni(1)-N(1)^{1} bond angles were both 180° which confirms the square planar geometry of the nickel centre. Both of the Ni-O and Ni-N bond lengths were 1.84 Å and 1.95 Å, respectively which are comparable with data reported in the literature.[133]

Bond angles for similar tetra-coordinated nickel complexes have been reported. Hubert-pfalzgraf *et al.* reported bond lengths of 1.93Å and 2.10 Å for Ni-O and Ni-N respectively,[131] and Yoo *et al.* reported values of 1.83 Å and 1.93 Å for Ni-O and Ni-N respectively.[43] Similarly, the C-N and C-C bond lengths within the dmamp ligands are also comparable to those outlined in these papers.

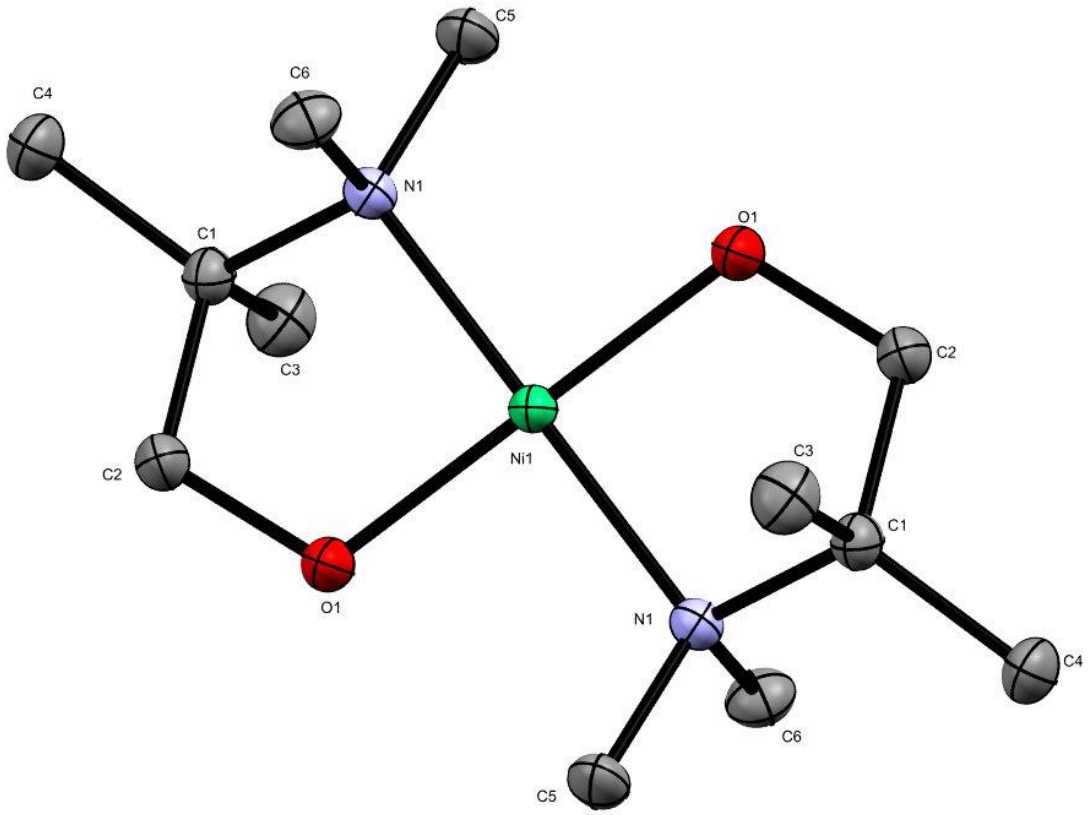

Figure 4.7 Crystal structure of complex (**4.2**). Atoms shown as thermal ellipsoids; carbon in grey, nitrogen in blue, oxygen in red and nickel in green. Hydrogen atoms omitted for clarity. CCDC deposition number 155335

Table 4.1 outlines selected bond lengths and bond angles for compound (**4.2**). See appendix C for full crystal data and structure refinement.

Atom - Atom	**Length (Å)**	**Atom - Atom**	**Length (Å)**
Ni(1) – O(1)	1.8426(7)	**N(1) – C(1)**	1.5224(13)
Ni(1) – O(1)^1	1.8426(7)	**N(1) – C(5)**	1.4787(14)
Ni(1) – N(1)^1	1.9544(8)	**C(3) – C(1)**	1.5321(15)
Ni(1) – N(1)	1.9544(8)	**C(4) – C(1)**	1.5321(14)
O(1) – C(2)	1.3996(13)	**C(1) – C(2)**	1.5307(14)
N(1) – C(6)	1.4899(14)		
Atom – Atom - Atom	**Angle (°)**	**Atom – Atom - Atom**	**Angle (°)**
O(1) – Ni(1) – O(1)^1	180.00(5)	**C(5) – N(1) – Ni(1)**	113.88(7)
O(1)^1 – Ni(1) – N(1)^1	88.41(4)	**C(5) – N(1) – C(6)**	106.90(8)
O(1) – Ni(1) – N(1)	88.41(4)	**C(5) – N(1) – C(1)**	112.95(8)
O(1)^1 – Ni(1) – N(1)	91.59(4)	**N(1) – C(1) – C(3)**	108.96(8)
O(1) – Ni(1) – N(1)^1	91.59(4)	**N(1) – C(1) – C(4)**	113.15(9)
N(1) – Ni(1) – N(1)^1	180.0	**N(1) – C(1) – C(2)**	104.18(8)
C(2) – O(1) – Ni(1)	112.10(6)	**C(3) – C(1) – C(4)**	110.31(9)
C(6) – N(1) – Ni(1)	105.95(6)	**C(2) – C(1) – C(3)**	108.80(9)
C(6) – N(1) – C(1)	112.61(8)	**C(2) – C(1) – C(4)**	111.19(9)
C(1) – N(1) – Ni(1)	104.46(6)	**O(1) – C(2) – C(1)**	110.12(8)

Table 4.1 Selected bond lengths and bond angles for compound **(4.2)** [Ni(dmamp)$_2$]

4.3.1.3 $[Ni\{(N^iPr_2)_2CNEt_2\}_2]$ (4.3)

The novel precursor $[Ni\{(N^iPr_2)_2CNEt_2\}_2]$ was synthesised following adaptations from two different literature reports which show the synthesis of copper bis-guanidinate complexes.[134,59] The novel complex should possess ideal properties for use as an ALD precursor in that it has relatively non-bulky ligands which should prevent steric hindrance around the nickel centre and therefore increase the volatility of the complex. The chelating effect of the guanidinate ligands is also expected to enhance the thermal and chemical stability of the nickel metal complex.[36]

^1H NMR and $^{13}C\{^1H\}$ NMR spectra for compound (**4.3**) are shown in Figure 4.8 and Figure 4.9 respectively. The ^1H NMR spectrum shows 4 proton environments at 0.78, 1.54, 2.72 and 3.15 ppm, corresponding to 4 methyl groups on the diethylamide ligand (Ha), 8 methyl groups on the diisopropylcarbodiimide ligand (Hb), 4 ethyl groups on the diethylamide ligand (Hc) and 4 CH groups on the diisopropylcarbodiimide ligand (Hd) respectively. The carbon NMR spectrum also shows 4 different peak environments at 13.8, 26.0, 42.2, 48.47 and 171.9 ppm, which are associated to the carbon environments C1, C2, C3, C4 and C5, respectively as shown in Figure 4.9.

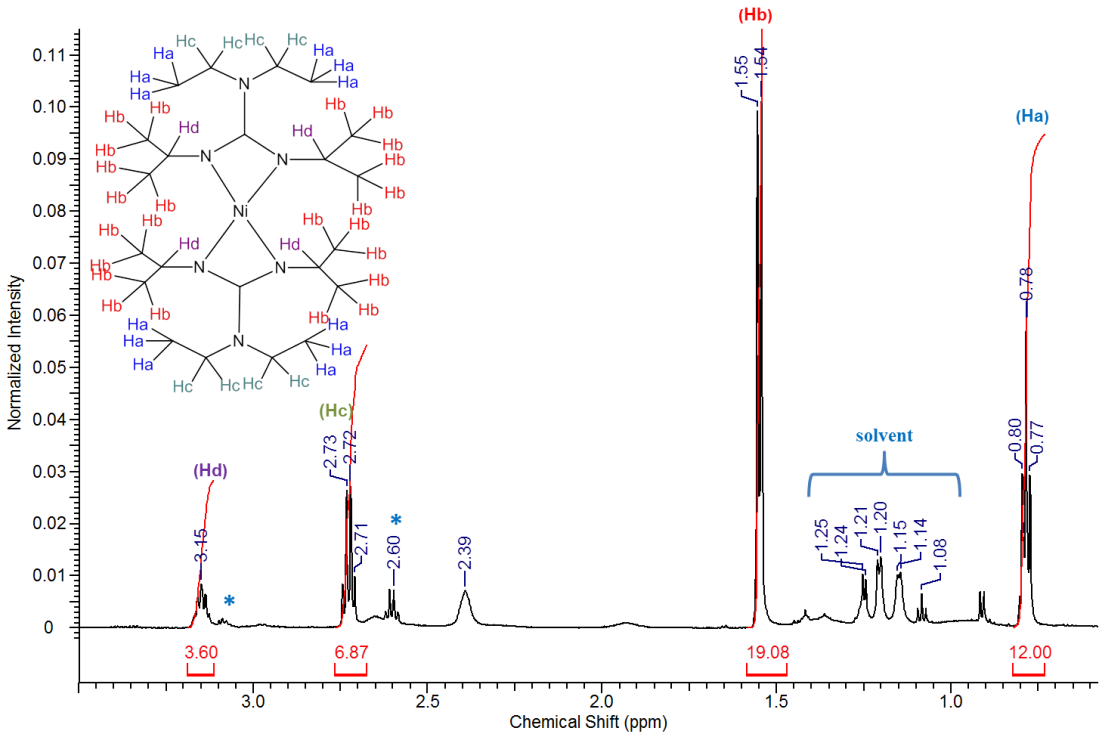

Figure 4.8 ^{1}H NMR spectrum of compound (**4.3**) [Ni{(N^{i}Pr$_2$)$_2$CNEt$_2$}$_2$]

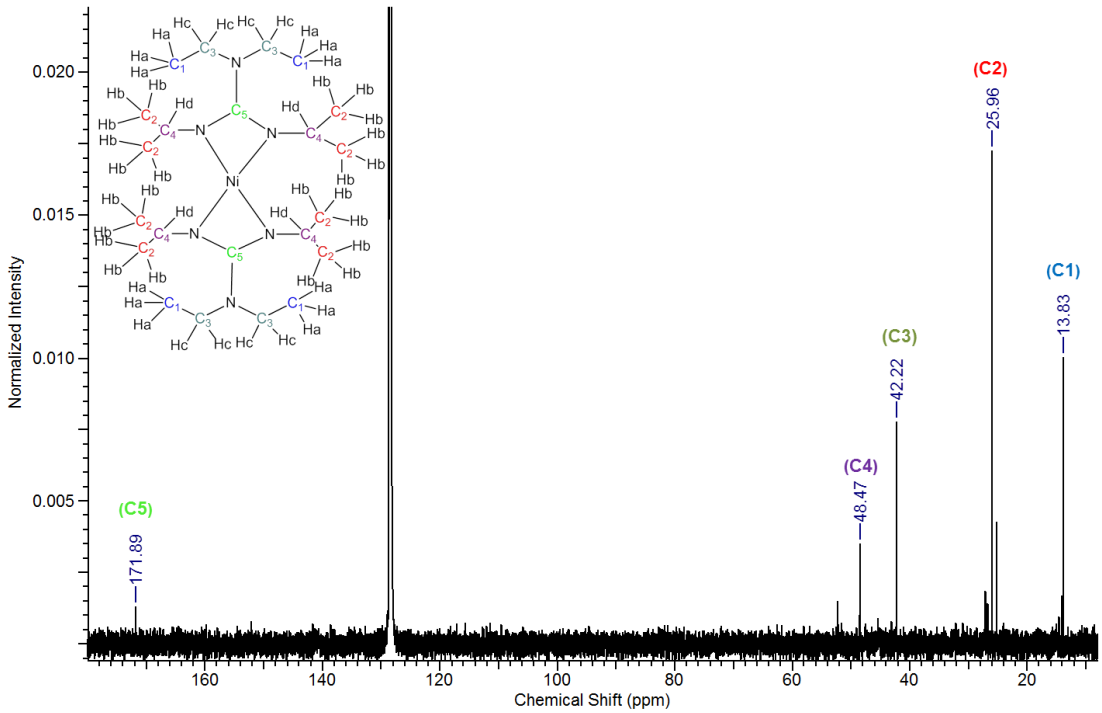

Figure 4.9 ^{13}C{^{1}H} NMR spectrum of compound (**4.3**) [Ni{(N^{i}Pr$_2$)$_2$CNEt$_2$}$_2$]

However, the ^{1}H NMR spectrum suggests the formation of two complexes (Scheme 4.4) as there were a number of overlapping multiplets corresponding to the iso-propyl and ethyl groups. The bisguanidinate complex [Ni{($N^{i}Pr_2$)$_2$CNEt_2}$_2$] was the expected product (**4.3a**), which was the major product formed in this case as a purple solid. Closer inspection revealed a minor product in the form of a green solid (**4.3b**), which was the result of the extra peak environments observed in the ^{1}H NMR spectrum (annotated by the asterisk, Figure 4.8).

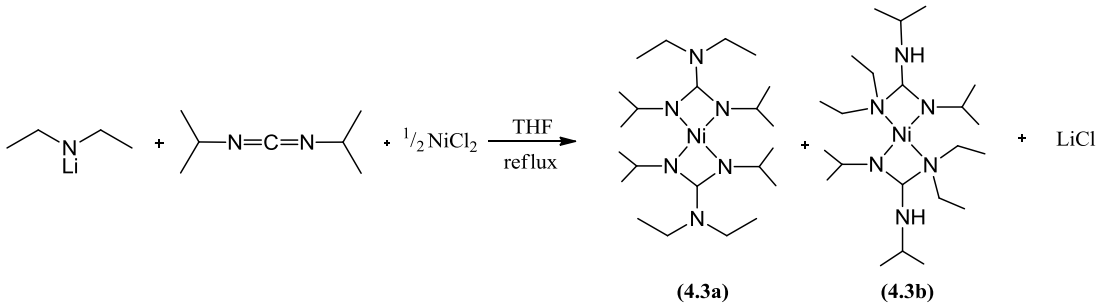

Scheme 4.4 Synthesis of compound (**4.3**) [Ni{($N^{i}Pr_2$)$_2$CNEt_2}$_2$]

The mechanism for the formation of (**4.3a**) and (**4.3b**) was not investigated; however this behaviour has been reported elsewhere in the synthesis of guanidinate complexes. Titanium guanidinate complexes synthesised by Carmalt *et al.* reported the formation of a mixture of complexes in a 70:30 ratio.[56] The formation of two complexes has been ascribed to partial hydrolysis and/or oxidation of the guanidinate ligand. Other reports have demonstrated that guanidinate ligands can undergo ligand transformations,[135] which has been described as a transamination reaction with exchange of a diethylamine group within the guanidinate ligand, for a dimethylaline group.[135] Therefore the formation of product (**4.3b**) could be due to a similar transamination reaction where the bis(diethylamine) group is exchanged for an isopropylamine group, resulting from the hydrolysis of $^{i}PrN=C=N^{i}Pr$. This may consequently be the cause of the broad peak present in the ^{1}H NMR spectrum at 2.39ppm, corresponding to an NH due to hydrolysis.

X-Ray crystallography

Figure 4.10 shows single crystals of complexes (**4.3a**) and (**4.3b**) mounted on the nylon loop prior to crystallographic analysis.

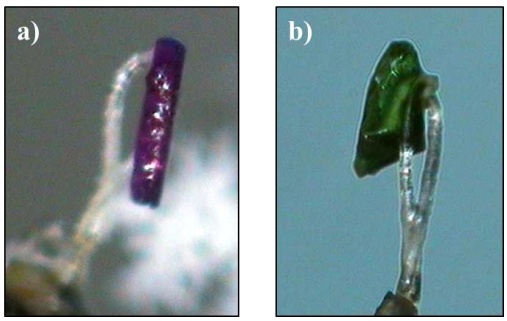

Figure 4.10 Ni(guanidinate)$_2$ single-crystals; a) complex (**4.3a**) and b) complex (**4.3b**) mounted on nylon loop

A mixture of purple rods and green hexagonal crystals were formed; both of which displayed photochromic behaviour. A single-crystal structure determination showed both complexes (Figure 4.11 and Figure 4.12) to have square planar geometry at the nickel centre, where the structures were consistent with the ^{1}H and ^{13}C NMR spectra. However, the complexes had different space groups; complex (**4.3a**) was orthorhombic whereas complex (**4.3b**) was triclinic. The molecular structure of complex (**4.3a**) (Figure 4.11) shows it to be dimeric with a symmetrically bridging Ni atom. The metallocyclic N-C-N angle of the ligand was close to 120°, which is characteristic for guanidinate ligands.[59] The C(2)–Ni(1)–C(1) and N(4)-C(2)-Ni(1) bond angles were both 180° which confirms the square planar geometry of the nickel centre. All 4 of the Ni-N (guanidinate bound) bond lengths were 1.93 Å, which are comparable to Ni-N bond lengths reported elsewhere in the literature. A similar nickel(II) bis-guanidinate complex synthesised by Ramos *et al.* exhibited Ni-N bond lengths in the range of 1.96 - 2.04 Å.[136] Likewise, bulky guanidinato nickel(I) complexes synthesised by Jones *et al.* had Ni-N bond lengths of 1.90 Å.[137] Similarly the C-N bond lengths within the guanidinate ligands (which are in the range of 1.32 - 1.38 Å), are also comparable to those observed in these related complexes.[137]

The molecular structure of complex (**4.3b**) (Figure 4.12) shows it to be dimeric with a bridging Ni atom. However as predicted by NMR, it can be observed that a transamination reaction has occurred due to partial hydrolysis/oxidation, where a diethylamine group has been exchanged for an isopropylamine group, resulting from the hydrolysis of $^{i}PrN=C=N^{i}Pr$. This has caused the metallocyclic N-C-N angle of the ligand to be reduced from the expected 120° to 115°. The $N(1)^{1}$-Ni(1)-N(1), N(2)-Ni(1)-$N(2)^{1}$ and $C(1)^{1}$-Ni(1)-C(1) bond angles were all 180° indicating square planar geometry at the nickel centre. The Ni-N (guanidinate bound) bond lengths were different in this case; Ni(1)-N(1) and Ni(1)-$N(1)^{1}$ bond lengths were both 1.94Å, whereas Ni(1)-N(2) and Ni(1)-$N(2)^{1}$ bond lengths were both 1.89 Å which are ~ 0.04 Å shorter than in complex (**4.3a**). Interestingly, the C-C bond lengths have been reduced (by ~ 0.04 Å) on the isopropylamine groups, but those on the diethylamine groups remain close to the values reported in the literature for guanidinate complexes.[134] In complex (**4.3b**) the ethyl groups are orientated to point "towards" the Ni metal centre rather than away from it as observed in complex (**4.3a**). This therefore has somewhat increased the steric bulk around the metal centre, which may be why some of the Ni(1)-N(1) and Ni(1)-$N(1)^{1}$ bond lengths are slightly greater in complex (**4.3b**) than (**4.3a**). See appendix C for full crystal data and structure refinement for complexes (**4.3a**) and (**4.3b**).

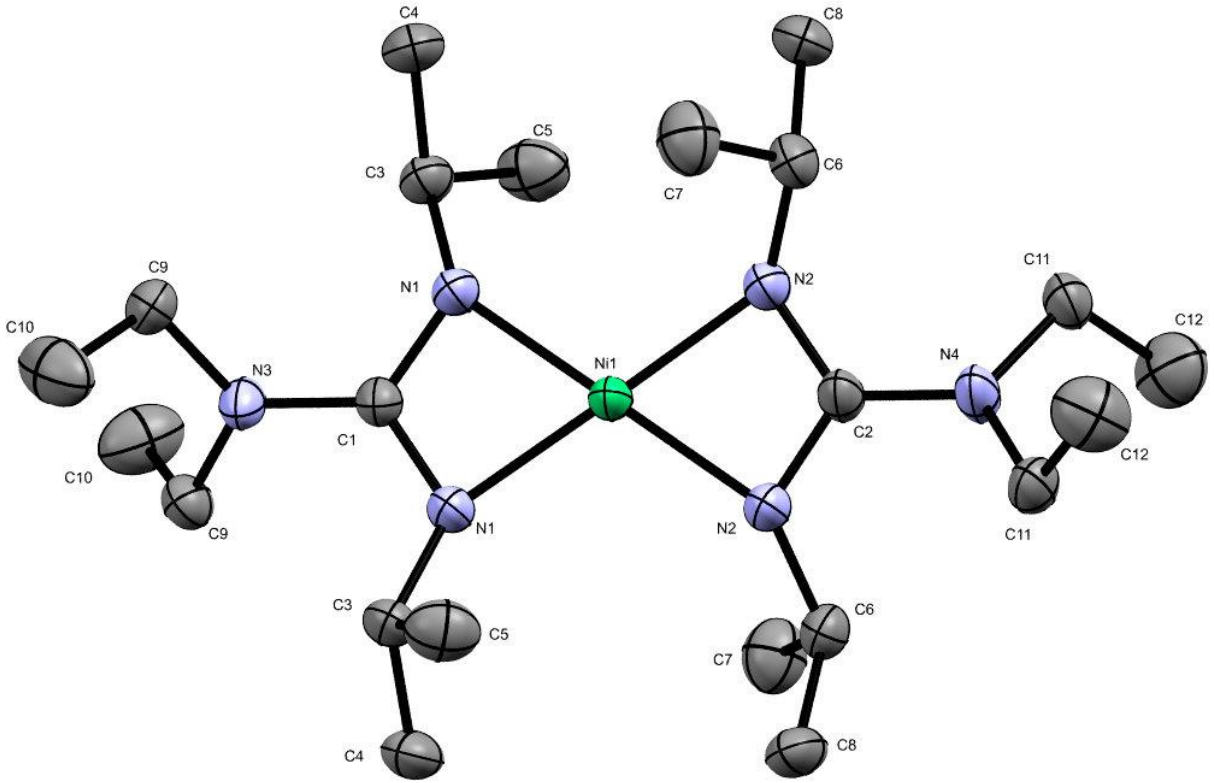

Figure 4.11 Crystal structure of complex (**4.3a**). Atoms shown as thermal ellipsoids; carbon in grey, nitrogen in blue and nickel in green. Hydrogen atoms omitted for clarity. CCDC deposition number 1553349

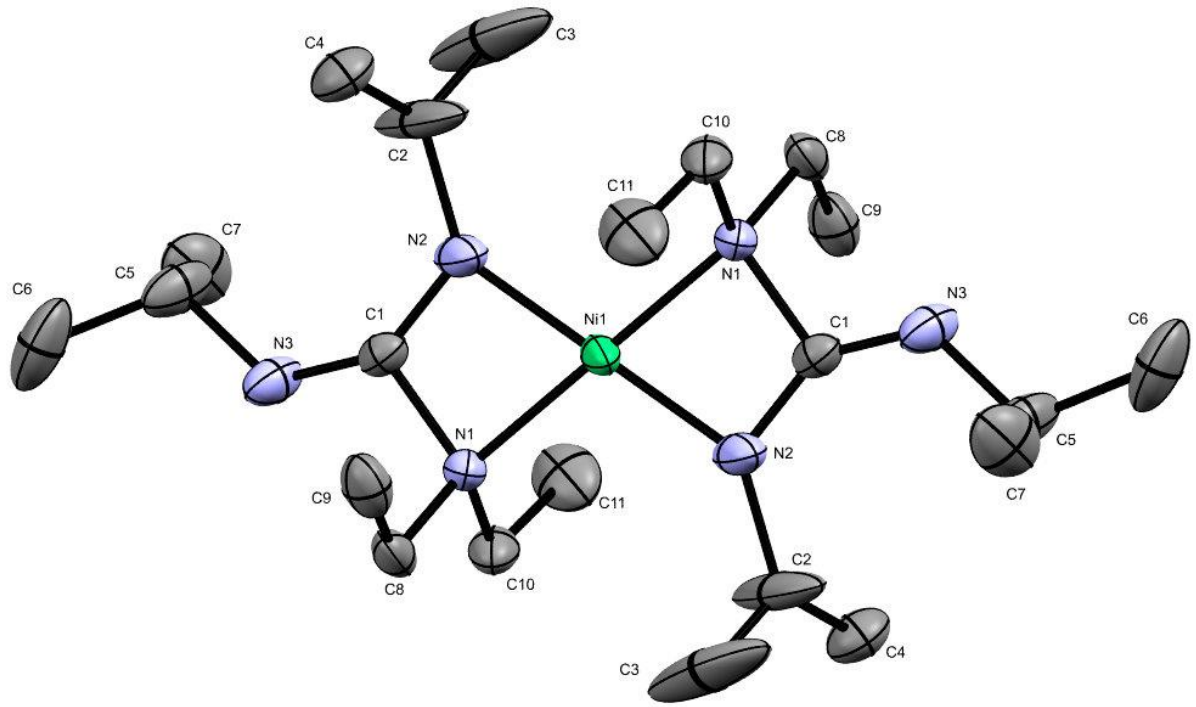

Figure 4.12 Crystal structure of complex (**4.3b**). Atoms shown as thermal ellipsoids; carbon in grey, nitrogen in blue and nickel in green. Hydrogen atoms omitted for clarity. CCDC deposition number 1553350

4.3.1.4 Summary

Three precursors have been synthesised; Nickel(II) bis(2,2,6,6-tetramethyl-3,5-heptanedionate), $[Ni(thd)_2]$; $[Ni(dmamp)_2]$, (dmamp = 2-dimethylamino-2-methyl-1-propanolate) and nickel guanidinate, $[Ni\{(N^iPr_2)_2CNEt_2\}_2]$, where the latter two were novel precursors synthesised for the purpose of this work. Complexes were analysed using $^1H/^{13}C$ NMR, mass spectrometry, elemental analysis and single crystal X-ray crystallography.

$[Ni(thd)_2]$, complex (**4.1**) was synthesised via two different synthetic routes in relatively low yields (13 - 28%). Analytical techniques confirmed the structure of complex (**4.1**), which were analogous to those reported in the literature.

The novel precursor $[Ni(dmamp)_2]$ (complex **4.2**) was synthesised following adaptations from two different literature reports. The $[Ni(dmamp)_2]$ synthesised in this work was different to those reported in the literature because the two methyl groups on the dmamp ligand are positioned on a different carbon atom. $[Ni(dmamp)_2]$ was synthesised in relatively high yields (~ 86%); recrystallisation in THF produced orange crystals of the orthorhombic space group with square planar geometry at the nickel centre, as confirmed by single crystal X-ray crystallography. The structure was consistent with the ^1H and ^{13}C NMR spectra.

The novel precursor $[Ni\{(N^iPr_2)_2CNEt_2\}_2]$ was synthesised following adaptations from two different literature reports which outline the synthesis of copper bis-guanidinate complexes. $[Ni\{(N^iPr_2)_2CNEt_2\}_2]$ was synthesised in relatively high yields (~ 70%); where NMR analysis confirmed the formation of two products – complexes (**4.3a**) and (**4.3b**). It is suggested that the formation of two products can be ascribed to partial hydrolysis and/or oxidation of the guanidinate ligand. The formation of complex (**4.3b**) is thought to be due to a transamination reaction where the bis(diethylamine) group is exchanged for an isopropylamine group, resulting from the hydrolysis of $^iPrN{=}C{=}N^iPr$. Single crystal X-ray crystallography showed purple (**4.3a**) and green (**4.3b**) crystals of the orthorhombic and triclinic space groups respectively, with both complexes showing square planar geometry at the nickel centre.

4.3.2 Decomposition Studies

Decomposition studies on compounds (**4.1**) - (**4.3**) were performed using thermogravimetric analysis (TGA).

The decomposition profile of [Ni(thd)$_2$] (**4.1**) shows that the precursor starts to sublime at around 180 °C. Subsequently after sublimation, precursor decomposition occurred in a rapid single step in the range of ~ 250 - 300 °C with an overall mass loss of ~ 85% (Figure 4.13). This mass loss was associated with the loss of both thd ligands to leave elemental Ni behind (red line). The differential scanning calorimetry (DSC) curve suggests a melting point of 230 °C (blue line) which is analogous with the reported literature value for the melting point of [Ni(thd)$_2$].[129] According to Lindahl *et al*., [Ni(thd)$_2$] starts to decompose at 275 °C,[47] which is comparable to the results obtained here.

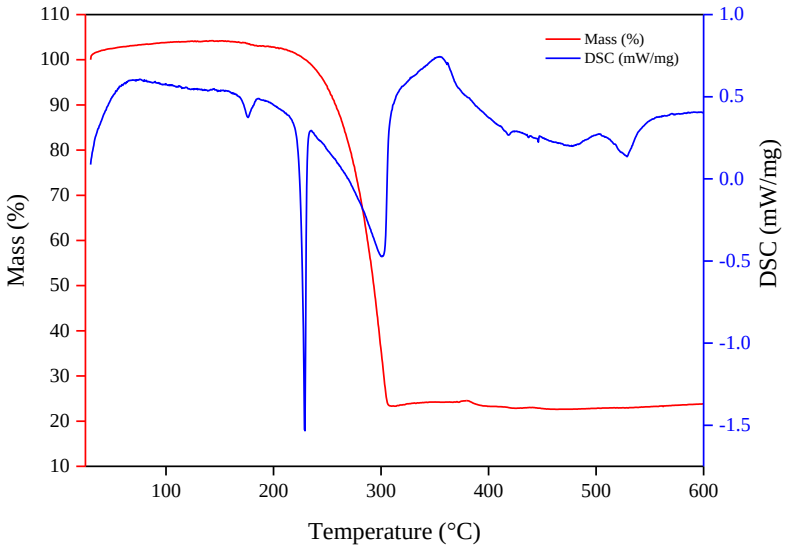

Figure 4.13 TGA/DSC curves for compound (**4.1**) [Ni(thd)$_2$]

The decomposition profile of the novel precursor [Ni(dmamp)$_2$] (**4.2**) shows that the precursor starts to sublime at around 90 °C. Subsequently after sublimation, precursor decomposition occurred in a rapid single step in the range of ~ 200 - 250°C, with an overall mass loss of ~ 75% (Figure 4.14). This mass loss is associated to the loss of both dmamp ligands to leave elemental Ni behind (red line). The differential scanning calorimetry (DSC) curve suggests a melting point of 180 °C (blue line). The data correlated well with that reported in the literature for similar dmamp-type structures.[138] The temperature range of weight loss for the novel [Ni(dmamp)$_2$] complex is similar to that for [Ni(acac)$_2$].[43]

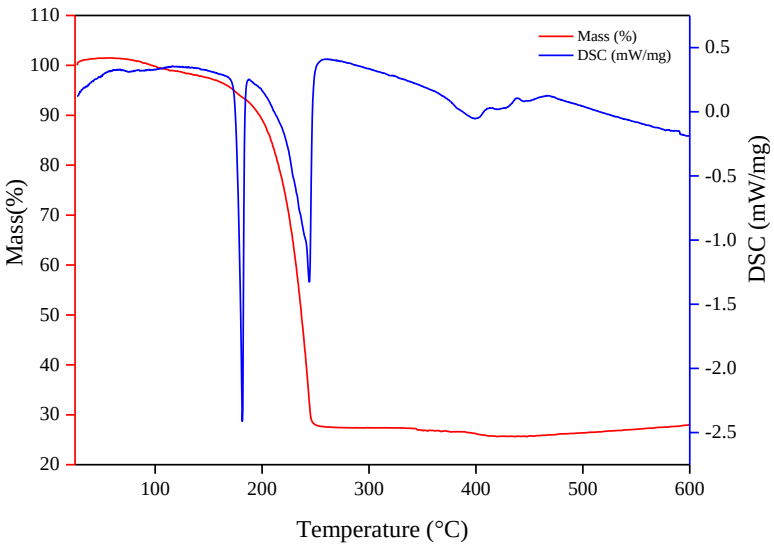

Figure 4.14 TGA/DSC curves for compound (**4.2**) [Ni(dmamp)$_2$]

Thermogravimetric analysis (TGA) of the novel crude product [Ni{(N^iPr_2)$_2$CNEt$_2$}$_2$] (**4.3**) shows that the precursor starts to sublime at around 110 °C. Subsequently after sublimation, precursor decomposition occurred in a rapid two step mass loss in the range of ~ 130 - 340 °C with an overall mass loss of ~ 65% (Figure 4.15). This mass loss is associated to the loss of both guanidinate ligands to leave elemental Ni behind (red line). The differential scanning calorimetry (DSC) curve suggests a melting point of 100 °C (blue line). TGA/DSC of the isolated major product (**4.3a**) was almost identical to that of the crude product, so for deposition purposes the crude product was used. The decomposition profile of the novel [Ni{(N^iPr_2)$_2$CNEt$_2$}$_2$] precursor is comparable to those reported in the literature for simialr nickel amidinate complexes[139] and copper guanidinate complexes.[134]

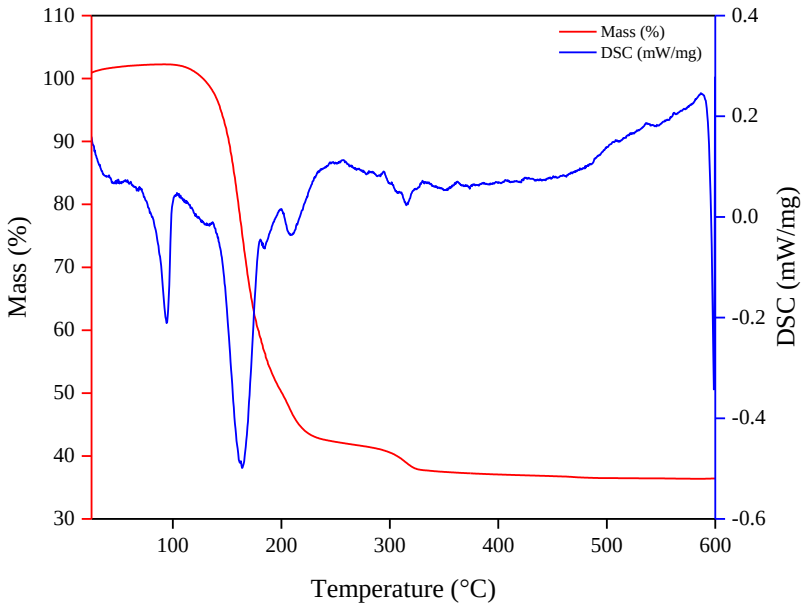

Figure 4.15 TGA/DSC curves for compound (**4.3**) [Ni{(N^iPr_2)$_2$CNEt$_2$}$_2$]

For ease of comparison, the TGA results for all three compounds are summarised in Figure 4.16. It is observable that [Ni{(N^iPr_2)$_2$CNEt$_2$}$_2$] has around the same volatility as [Ni(dmamp)$_2$], but a greater volatility than [Ni(thd)$_2$]. [Ni{(N^iPr_2)$_2$CNEt$_2$}$_2$] is however less thermally stabile due to the larger percentage of residual mass after decomposition (~ 36%).

Table 4.2 outlines the calculated mass loss of NiO for compounds (**4.1**) and (**4.2**) and Ni_3N for compound (**4.3**) at 600 °C. The observed mass loss during the TGA experiments for each of these compounds is also presented.

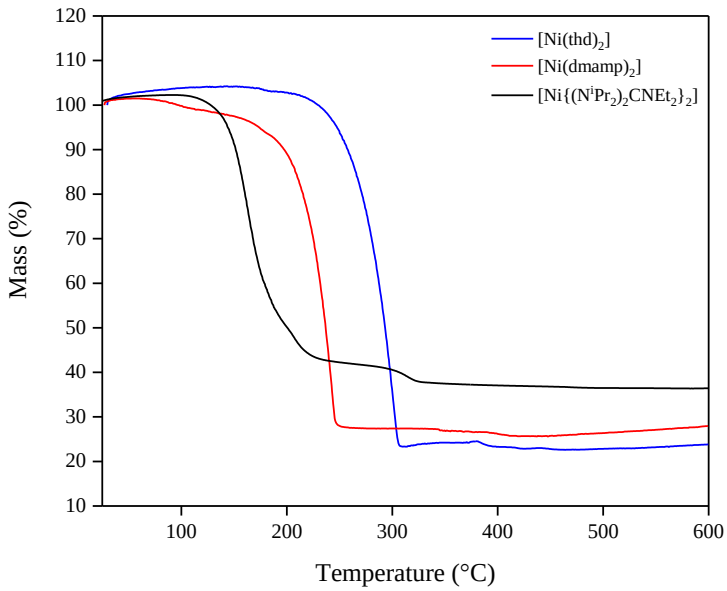

Figure 4.16 TGA curves for compounds (**4.1**), (**4.2**) and (**4.3**)

Compound	**Calculated mass loss for NiO (4.1 and 4.2) or Ni_3N (4.3) (%)**	**Observed mass loss at 600 °C (%)**
$[Ni(thd)_2]$ **(4.1)**	82	80
$[Ni(dmamp)_2]$ **(4.2)**	74	73
$[Ni\{(N^iPr_2)_2CNEt_2\}_2]$ **(4.3)**	61	64

Table 4.2 Calculated and observed mass losses for compounds **(4.1), (4.2)** and **(4.3)** during TGA experiments at 600 °C under a constant flow of helium

4.3.3 ALD with nickel precursors

4.3.3.1 ALD of [Ni(thd)$_2$]

4.3.3.1.1 [Ni(thd)$_2$] precursor for ALD

Nickel(II) bis(2,2,6,6-tetramethyl-3,5-heptanedionate), [Ni(thd)$_2$] is a purple powder which was synthesised in house as described in section 4.2.3.1. It has a reasonably high vapour pressure (0.1 Pa at 100 °C) and is reported to be stable on heating up to 350 °C.[47] There are several publications outlining its use as a precursor for ALD in combination with water[47,71] or ammonia[76,52] as co-reactants to deposit nickel oxide and nickel nitride films respectively. To prevent thermal decomposition occurring, the substrate temperature was kept at a temperature below the decomposition temperature of the precursor (300 °C) to prevent undesirable CVD-like growth occurring.

The vapour pressure of [Ni(thd)$_2$] can be manipulated by varying the temperature of the bubbler in which it is contained. Manipulation of the vapour pressure means that the amount of precursor released into the reaction chamber during each dose sequence can be easily controlled. Again, to prevent precursor decomposition, the temperature of the bubbler was held at a temperature lower than the decomposition temperature of the precursor. The vapour pressure equation for [Ni(thd)$_2$] is shown in equation 4.1, where the temperature, T is in kelvin and the vapour pressure, Vp is in kPa.[140] Figure 4.17 shows the vapour pressure curve for [Ni(thd)$_2$] plotted in mbar.

$$log(Vp) = 15.30 - \left(\frac{7200}{T}\right) \qquad (4.1)$$

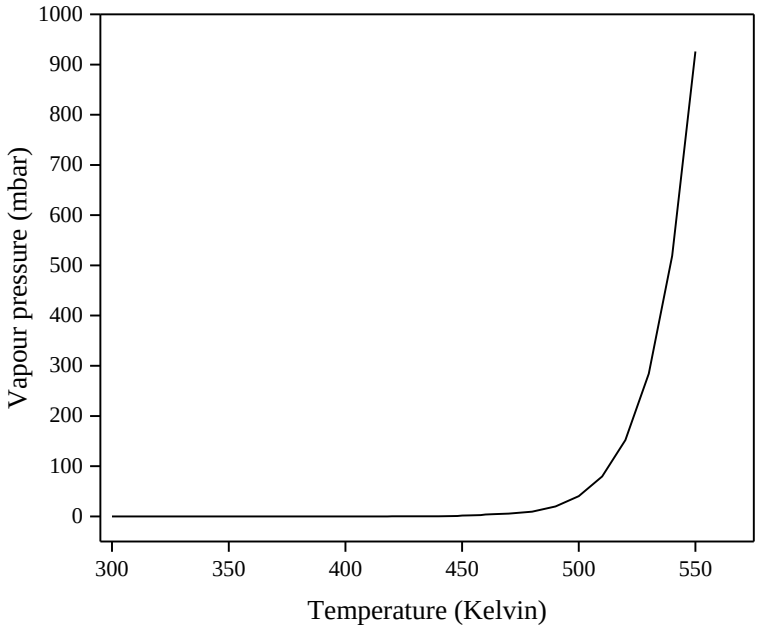

Figure 4.17 Vapour pressure curve for [Ni(thd)$_2$]

4.3.3.1.2 ALD of [Ni(thd)$_2$] and water

ALD depositions were carried out using nickel(II) bis(2,2,6,6-tetramethyl-3,5-heptanedionate), [Ni(thd)2], and distilled water. [Ni(thd)$_2$] is a solid at room temperature and must therefore be sublimed at a certain temperature within the bubbler in order to generate sufficient gaseous molecules to be dosed into the reactor. Initially the conditions used to deposit TiO_2 using TTIP and water (as described in chapter 3) were employed for [Ni(thd)$_2$] and water. The TiO_2 depositions worked effectively with a TTIP bubbler temperature of 25 °C, as this temperature was able to generate sufficient vapour pressure to dose the precursor into the reactor. Consequently, in order to produce the same vapour pressure as TTIP at 25 °C, [Ni(thd)$_2$] was heated to 145 °C (vapour pressure of 0.12 mbar).

A growth temperature of 230 °C was employed as this has previously been used in the literature for the deposition of NiO using [$Ni(thd)_2$] and water.[47] Table 4.3 outlines the initial deposition conditions.

	Time	**Purge flow (sccm)**	**[$Ni(thd)_2$] bubbler flow (sccm)**	**Water bubbler flow (sccm)**	**Growth temp (°C)**
[$Ni(thd)_2$] dose	2.5 sec	100	100	0	230
[$Ni(thd)_2$] purge	1 min	100	100	0	230
H_2O dose	2.0 sec	100	100	0	230
H_2O purge	3 min	100	100	0	230

Table 4.3 Initial reaction conditions used to deposit NiO films via ALD of [$Ni(thd)_2$] and water

However, upon analysing the substrates no NiO had been deposited, even upon increasing the number of reaction cycles.

Variation of [$Ni(thd)_2$] vapour pressure

As no NiO films were deposited using the conditions outlined in Table 4.3, this suggested that there could potentially be issues with the vapour transport of [$Ni(thd)_2$] into the reactor. In order to increase the vapour transport of [$Ni(thd)_2$], the gas flow rate for the purge line and the gas assist flow rate into the bubbler were each increased from 100 sccm to 140 sccm. Depositions were then repeated using the conditions in Table 4.3 but still no NiO films were deposited.

Variation of [$Ni(thd)_2$] dose conditions

As [$Ni(thd)_2$] is a solid precursor, it was likely that these ALD deposition conditions were not optimised for the [$Ni(thd)_2$]/water precursor combination. It was likely that not enough precursor was being dosed into the reactor to be able generate sufficient growth of NiO. Rather than directly increasing the [$Ni(thd)_2$] dose time, it can instead be manipulated through changing the gas flow rates and bubbler temperature.

Depositions were performed following a paper published by Lindahl *et al*. in 2009, where the authors demonstrate successful NiO depositions using [Ni(thd)$_2$] and water using a five-zone hot-wall ALD reactor[38,47] to achieve a growth rate of ~ 0.3 Å/cycle. The authors report their optimised ALD sequence as a 1.5 second [Ni(thd)$_2$] dose, 8 second purge, 4.5 second H_2O dose followed by an 8 second purge, where the precursor dose times were also reported as 3 x 10^{-6} and 3 x 10^{-4} moles per dose respectively. With regards to the moles per dose, it was established that the [Ni(thd)$_2$] dose used in the paper was around 10 times greater than the [Ni(thd)$_2$] dose utilised under the conditions outlined in Table 4.3.

The moles of precursor dosed per minute were calculated using equation 4.2 shown below;

$$\frac{Vp(mm.Hg)\ x\ F(L/min)}{(760-Vp)\ x\ 2.24} \qquad (4.2)$$

Where Vp is the vapour pressure at the temperature of sublimation and F is the gas flow rate through the bubbler upon the dose step. The moles dosed per minute can then be converted into the moles dosed per pulse.

Table 4.4 shows a comparison of the sublimation and dose conditions for [Ni(thd)$_2$] as outlined in the Lindahl paper and in this work as described above.

	Sublimation temp (°C)	**F(L/min)**	**Vp(mm.Hg)**	**[Ni(thd)$_2$] dose (sec)**	**[Ni(thd)$_2$] moles/pulse**
Lindahl paper[47]	165	0.37	0.545	1.5	3.0 x 10^{-6}
This work (Table 4.3)	145	0.14	0.089	2.5	3.0 x 10^{-7}

Table 4.4 Comparison of reaction conditions used in Lindahl paper and in this work

In order to simulate the conditions used in the paper and to achieve a greater moles per pulse during the [Ni(thd)$_2$] dose step, the sublimation temperature for [Ni(thd)$_2$] was increased to 180 °C (equates to a vapour pressure, Vp of ~ 1.5 mm.Hg) and the

gas flow rates were increased from 140 sccm to 700 sccm. Whilst keeping the precursor dose time at 2.5 seconds, under these new conditions the number of moles per pulse was increased to 2.5 x 10^{-5} moles/pulse - now around 8 times greater than that used in the Lindahl paper.

Depositions were then repeated under these new conditions (Table 4.5) to see whether increasing the precursor sublimation temperature and gas flow rates had an impact on the NiO film growth. Nevertheless, implementation of these conditions resulted in no NiO deposition.

	Time	**Bubbler temp (°C)**	**Purge flow (sccm)**	**[Ni(thd)$_2$] bubbler flow (sccm)**	**Growth temp (°C)**
[Ni(thd)$_2$] dose	2.5 sec	180	700	700	230
[Ni(thd)$_2$] purge	1 min	180	700	700	230
H_2O dose	2.0 sec	5	700	700	230
H_2O purge	3 min	5	700	700	230

Table 4.5 Conditions used to deposit NiO with increased vapour pressure of [Ni(thd)$_2$]

Variation of water dose time

One possible explanation as to why no NiO deposition occurred is that the water dose time was insufficient to completely saturate the substrate surface during the water dose. There are several reports in the literature which suggest that water saturates the substrate much slower than [Ni(thd)$_2$] does. Lindahl has reported that a water excess of around 100 times the amount of [Ni(thd)$_2$] was required for complete saturation.[52,47] The large water excess can most likely be attributed to a low reactivity of the adsorbed nickel species towards water.

To ensure that both precursors were completely saturating the substrate surface during each dose sequence, depositions were repeated using the conditions outlined in Table 4.5, but the water dose time was increased from 2.0 seconds to 4.5 seconds. However, this resulted in no NiO film deposition.

4.3.3.1.3 Characterisation of films

X-ray photoelectron spectroscopy (XPS) of the substrate revealed the presence of small amounts nickel on the substrate surface, as well as carbon, nitrogen and oxygen as expected. Figure 4.18 shows the survey spectrum.

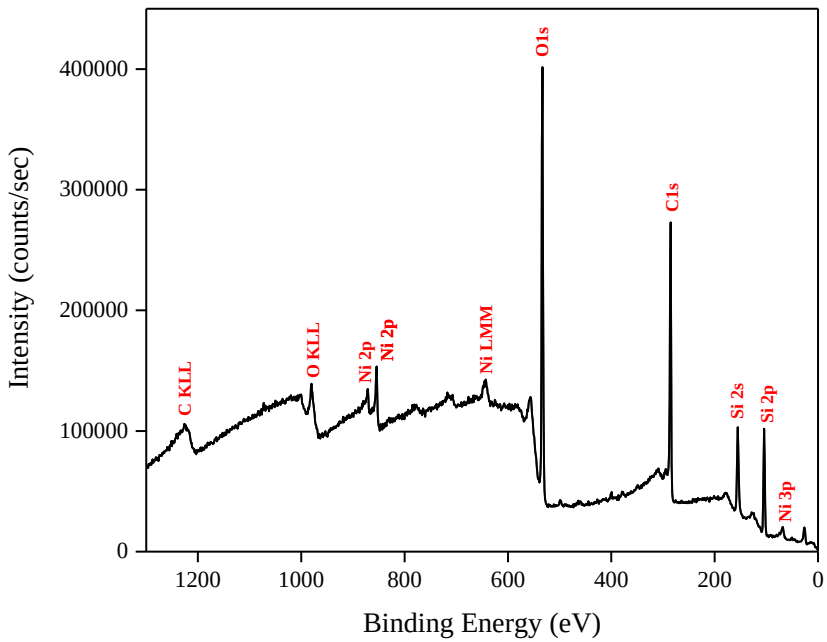

Figure 4.18 Typical XPS survey of films deposited by ALD of [$Ni(thd)_2$] and water

High resolution surface scans (Figure 4.19) of the Ni2p peak suggests the presence of Ni metal, with $2p_{3/2}$ and $2p_{1/2}$ peak binding energies of 853.5 eV and 870.9 eV respectively, with a peak separation of 17.1 eV. These values are within ± 0.2 eV of literature values.[142,143] The binding energies of these peaks are very similar to the $2p_{3/2}$ and $2p_{1/2}$ peaks for NiO which are in the region of 853.4 - 857.2 eV and 871.8 - 873.8 eV respectively. The doublet separation for NiO is 17.8 - 18.4 eV.[144,143] $Ni(OH)_2$ $2p_{3/2}$ and $2p_{1/2}$ peaks are also within the same region – $2p_{3/2}$ peaks are observed in the range of 855.3 - 856.6 ± 0.2 eV and $2p_{1/2}$ peaks are observed at 873.7 ± 0.2 eV. The doublet separation for $Ni(OH)_2$ is 17.7 - 17.8 eV.[145] The binding energies and doublet separation of the peaks observed in Figure 4.19 are therefore closely related to those reported for Ni metal. Small satellite peaks were observed

(donated by asterisk), with the $2p_{3/2}$ satellite feature at + 6 eV above the principal $2p_{3/2}$ peak. This was attributed to a predominant surface plasmon loss and a contribution from interband transitions.[146]

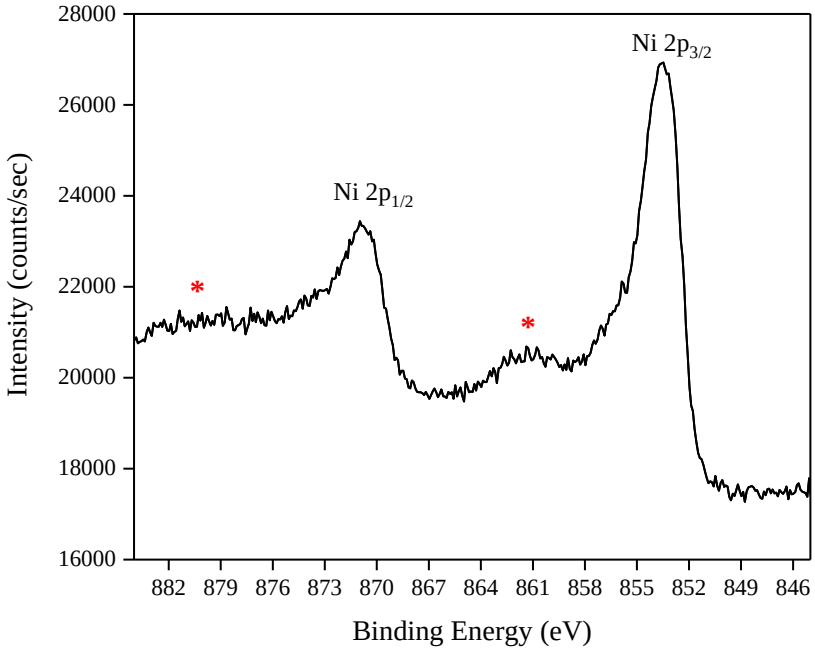

Figure 4.19 High resolution Ni2p spectrum of the films deposited using [Ni(thd)$_2$] and water. Asterisk denotes satellite features

However, deconvolution of the Ni2p$_{3/2}$ peak reveals the presence of an additional peak environment at 856.1 ± 0.2 eV corresponding to a $2p_{3/2}$ peak of NiO (Figure 4.20). The peaks were fitted with a FWHM value of 2.4 eV for both the Ni^0 and Ni^{2+} species. It can be concluded that the majority of species on the surface was Ni metal, with some NiO present too. However multiplet peak splitting was not observed, which is unique to NiO.

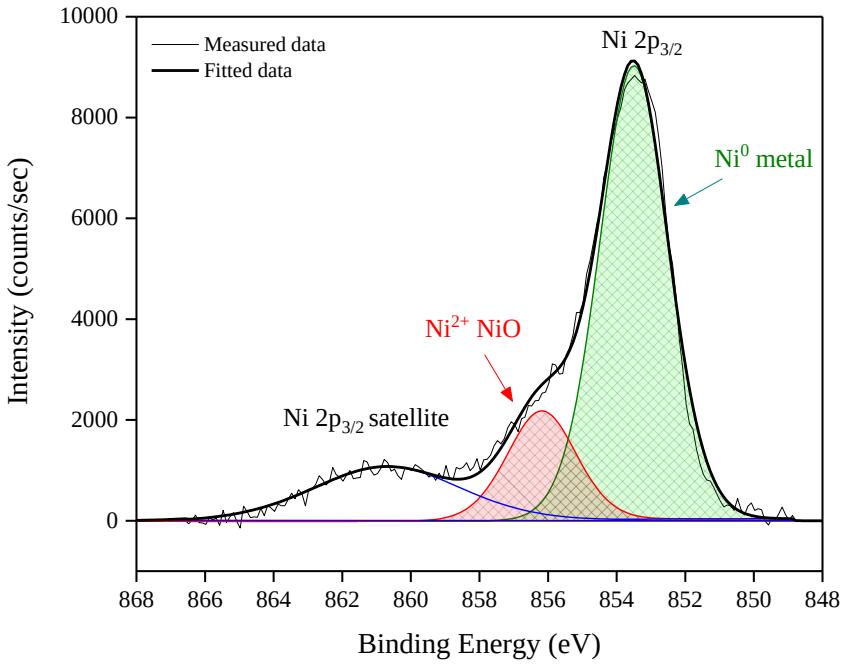

Figure 4.20 High resolution surface scan of Ni2p$_{3/2}$ peak. Peaks fitted with a FWHM of 2.4 eV

These results suggest that [Ni(thd)$_2$] was reacting with the hydroxyl groups on the substrate surface, but the surface adsorbed nickel species were inactive towards water. Therefore NiO growth was not initiated.

Variation of growth temperature

If the growth temperature was not high enough, this could have caused issues with precursor kinetics, where the precursors had insufficient energy to react with the substrate and/or each other. Increasing the growth temperature of those experiments performed in Table 4.3 and Table 4.5 from 230 °C to 275 °C and then to 350 °C was found to have no impact on the film growth. XPS showed similar results to those shown in Figure 4.19, where nickel metal was predominantly detected on the substrate surface. So increasing the growth temperature was incapable of initiating NiO film growth.

Piranha cleaning of substrates

NiO depositions had so far been unsuccessful, so it was important to think about the reactivity of the precursors with the substrate. The issue may have been partly due to the substrate itself, in the fact that it is not 'active' enough towards [$Ni(thd)_2$] to initiate film growth i.e. insufficient hydroxyl groups (although this was not a problem for TiO_2 growth).

Several ALD papers report the use of vigorous substrate cleaning protocols before conducting depositions, for example ultrasonic baths,[47] ozone treatment[71] and piranha cleaning.[69]

In order to enhance the substrate 'reactivity', a selection of microscope slides and quartz slides were cleaned using a piranha cleaning protocol.[147] The piranha cleaning solution was a mixture of sulfuric acid (H_2SO_4) and hydrogen peroxide (H_2O_2). As the mixture is a strong oxidising agent, it removes organic residues off the substrates. It also hydroxylates most surfaces (add OH groups), which makes them more hydrophilic (water-compatible). It was thought that if the density of hydroxyl groups on the surface was increased, then this could create more 'reaction sites' for [$Ni(thd)_2$] and thus possibly increase the chance of nucleation occurring. All depositions described previously were repeated, but again similar results were obtained, with primarily elemental Ni on the substrate surface and a very minimal amount of NiO.

4.3.3.1.4 Summary

$[Ni(thd)_2]$ was successfully synthesised via two synthetic routes (although with slightly low yields). It is a solid precursor and was therefore sublimed inside the bubbler at temperatures in the range of 145 - 180 °C.

Atomic layer deposition of NiO thin films using $[Ni(thd)_2]$ and water as precursors was shown to be unsuccessful. Although the precursor vapour pressure and gas flow rates could be easily manipulated using equation 4.2, this had no effect on the deposition outcome. Manipulation of the growth temperature and introduction of a piranha substrate cleaning protocol was found to have no impact on the film growth.

Nonetheless it was discovered that a large excess of water was required in order to achieve complete saturation of the substrate surface due to low reactivity of the adsorbed nickel species towards water. After implementation of these changes, nickel metal and nickel oxide were detected on the substrate surface following XPS analysis. High resolution spectra of the $Ni2p_{3/2}$ peak suggest the majority of the nickel species present were due to nickel metal, as binding energies and spin-orbit coupling values were comparable to those of nickel metal as reported in the literature, rather than NiO or $Ni(OH)_2$. Deconvolution of the $Ni2p_{3/2}$ peak revealed a small amount of NiO, however no multiplet peak splitting was observed that is typical of NiO.

It is thought that there were several possible reasons as to why NiO did not grow by ALD of $[Ni(thd)_2]$ and water. The fact that ALD growth of $[Ni(thd)_2]$ and water has been successfully reported in the literature suggests that in this case, the reactor design may not have been optimised to establish sufficient NiO growth under the conditions used. It is well known that the vapour pressure of solid precursors depletes as it is consumed; therefore due to the design or the reactor, the potentially minimal amount of $[Ni(thd)_2]$ dosed may have condensed or adsorbed onto the walls within the pipelines, thus reducing the amount of precursor chemisorbing onto the substrate. The same may have occurred with the water being dosed into the reactor; even though a large excess of water was used. It may perhaps be that an even larger excess of water was required to completely saturate the substrate surface. The fact

that piranha cleaning of the substrates failed to achieve sufficient NiO growth suggests that the substrates used were not a concern. In conclusion, the reason as to why NiO growth did not successfully occur can be explained by reactor issues.

4.3.3.2 ALD of $[Ni(Cp)_2]$

4.3.3.2.1 $[Ni(Cp)_2]$ precursor for ALD

Bis(cyclopentadienyl)nickel(II), $[Ni(Cp)_2]$ is a dark green powder which was purchased from Alfa Aesar and used as supplied. ALD depositions were performed at substrate temperatures in the range of 165 - 350 °C. ALD depositions using $[Ni(Cp)_2]$ are typically performed using either O_3, O_2 or H_2 as the co-reactant.[76] However there are a couple of reports showing the use of $[Ni(Cp)_2]$ and water to deposit NiO via ALD.[77,55,53]Although $[Ni(Cp)_2]$ is less volatile than some of the other nickel-containing organometallic compounds, $[Ni(Cp)_2]$ is far less toxic[148] and is commercially available. It is suggested that the decomposition temperature is 186 °C; however this has been disputed elsewhere.[148]

Kang and Rhee reported that by holding $[Ni(Cp)_2]$ isothermally in a sublimator and examining its gas phase infra-red spectra using a heated gas cell, that no substantial decomposition was observed at 120 °C. However a time factor was not taken into account with these studies. As decomposition is a time-dependent process, further studies[149] were performed with an isothermal 'wait' for a longer period of time after which it can be confirmed whether prolonged heating caused further thermal decomposition or not.[149] It was found that $[Ni(Cp)_2]$ decomposition was detected at a temperature as low as 77 °C and after prolonged heating (77 °C for 15 hours) the mass loss became constant. Decomposition studies performed in shorter timeframes may therefore not give an accurate representation of the decomposition profile.

To prevent thermal decomposition occurring, the substrate temperature was kept at a temperature below the decomposition temperature of the precursor to prevent undesirable CVD-like growth occurring. The vapour pressure of $[Ni(Cp)_2]$ can be manipulated by varying the sublimation temperature of the bubbler in which it is contained. Manipulation of the vapour pressure means that the amount of precursor released into the reaction chamber during each dose sequence can be more easily controlled. Again, to prevent precursor decomposition, the temperature of the bubbler was held at a temperature lower than the decomposition temperature of the precursor.

The vapour pressure equation for $[Ni(Cp)_2]$ is shown in equation 4.3, where the temperature, T is in kelvin and the vapour pressure Vp is in Pa.[150] Figure 4.21 shows the vapour pressure curve for $[Ni(Cp)_2]$ plotted in mbar.

$$ln(Vp) = 28.5 - 8402.4\ x\left(\frac{1}{T}\right) \qquad (4.3)$$

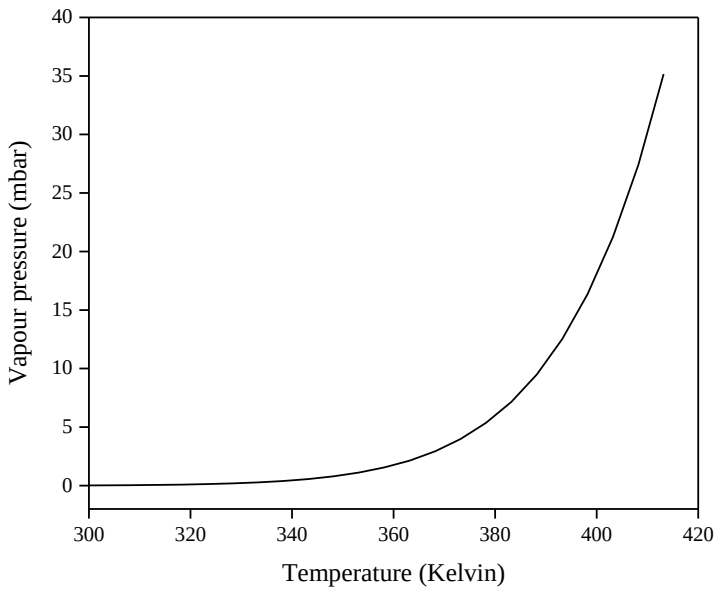

Figure 4.21 Vapour pressure curve for $[Ni(Cp)_2]$

4.3.3.2.2 ALD of [Ni(Cp)$_2$] and water

ALD depositions were carried out using Bis(cyclopentadienyl)nickel(II), [Ni(Cp)$_2$] (Alfa Aesar) and distilled water. [Ni(Cp)$_2$] is a solid at room temperature and must therefore be sublimed at a certain temperature within the bubbler in order to generate sufficient gaseous molecules to be dosed into the reactor. Initially the conditions used to deposit TiO_2 using TTIP and water (as described in chapter 3) were employed for [Ni(Cp)$_2$] and water.

For the initial depositions, [Ni(Cp)$_2$] was sublimed inside the bubbler at a temperature of 50 °C and dosed into the reactor with a gas assist. At this temperature, the vapour pressure of the precursor was 0.122 mbar (as calculated using equation 4.3), which is slightly lower than that of TTIP at 25 °C (0.176 mbar) and that of [Ni(thd)$_2$] at 165 °C (0.86 mbar) and 180 °C (2.54 mbar).

This is in line with a paper produced by Chae *et al.*,[53] where the [Ni(Cp)$_2$] bubbler was held at 50 °C for the deposition of NiO onto TiN/SiO_2 substrates by ALD. Similar papers also use bubbler temperatures within the range of 40 - 80 °C, with the most common bubbler temperature being 60 °C.[76] A growth temperature of 165 °C was employed as this relates to what has previously been reported in the literature.[76] Table 4.6 outlines the initial deposition conditions.

	Time	**Bubbler temp (°C)**	**Purge flow (sccm)**	**[Ni(Cp)$_2$] bubbler flow (sccm)**	**Water bubbler flow (sccm)**	**Growth temp (°C)**
[Ni(Cp)$_2$] dose	2.5 sec	50	100	100	0	165
[Ni(Cp)$_2$] purge	1 min	50	100	100	0	165
H_2O dose	2.0 sec	5	100	100	0	165
H_2O purge	3 min	5	100	100	0	165

Table 4.6 Initial reaction conditions used to deposit NiO films via ALD of [Ni(Cp)$_2$] and water

However, upon analysing the substrates no NiO had been deposited, even upon increasing the number of reaction cycles.

Variation of [Ni(Cp)$_2$] vapour pressure

As no NiO deposition occurred using the conditions outlined in Table 4.6, this suggested that there could be potential issues with the vapour transport of [Ni(Cp)$_2$] into the reactor. [Ni(Cp)$_2$] has a lower volatility than TTIP (Vp of TTIP and [Ni(Cp)$_2$] at 50 °C is 1.187 and 0.122 mbar respectively). In order to increase the volatility, and hence the vapour transport of [Ni(Cp)$_2$] into the reactor, the sublimation temperature of [Ni(Cp)$_2$] was increased from 50 °C to 100 °C. Depositions were then repeated using the conditions in Table 4.6 but no NiO deposition occurred. Repeats of the depositions with higher dose times for both precursors also resulted in no film growth.

[Ni(Cp)$_2$] mass transport effects

As increasing the vapour transport of [Ni(Cp)$_2$] into the reaction chamber appeared to have no effect on the film growth, it was possible that mass transport of the precursor was the issue and not vapour transport. In order to implement changes in the mass transport of precursors, [Ni(Cp)$_2$] was dosed under its own vapour pressure (with no gas assist) at a bubbler temperature of 100 °C. The purge flow rate was also decreased from 100 sccm to 20 sccm (Table 4.7). These changes were made to effectively 'slow down' the movement of the precursor through the reactor, and to therefore allow more time for it to react with the surface hydroxyl sites on the substrate. A few papers report the use of an 'exposure step' after dosing [Ni(Cp)$_2$] and before the water dose to allow time for the precursor to infiltrate the substrate materials.[55,77] However, implementation of these conditions resulted in no NiO deposition.

	Time	**Bubbler temp (°C)**	**Purge flow (sccm)**	**[Ni(Cp)$_2$] bubbler flow (sccm)**	**Water bubbler flow (sccm)**	**Growth temp (°C)**
[Ni(Cp)$_2$] dose	2.5 sec	100	20	0	0	165
[Ni(Cp)$_2$] purge	1 min	100	20	0	0	165
H$_2$O dose	2.0 sec	5	20	0	0	165
H$_2$O purge	3 min	5	20	0	0	165

Table 4.7 Conditions used to deposit NiO with implementation of mass transport effects for [Ni(Cp)$_2$]

Variation of growth temperature

If the growth temperature was not high enough, this could have caused issues with precursor kinetics, where the precursors had insufficient energy to react with the substrate and/or each other. Increasing the growth temperature of those experiments performed in Table 4.6 from 165 °C to 300 and 350 °C resulted in a selection of greyish tinted films at different number of reaction cycles (Table 4.8). These higher temperatures have been employed for ALD of [Ni(Cp)$_2$] elsewhere.[69] The deposition conditions used were as before: 2.5 second [Ni(Cp)$_2$] dose, 1 minute purge, 2.0 second water dose, 3 minute purge.

It is likely that a growth temperature of 165 °C is below the "ALD process window" for the [Ni(Cp)$_2$]/water precursor combination. Film growth is not initiated at this temperature as precursor adsorption to the substrate surface is a thermally activated process,[21] so [Ni(Cp)$_2$] has insufficient energy to react with the hydroxyl species on the substrate surface. Temperatures of 300/350 °C are within (or close to) the "ALD process window", where film deposition occurs via a self-limiting mechanism. Within this temperature range, there is sufficient energy for chemical reactions to take place on the substrate surface.

Bubbler temp (°C)		**Bubbler gas flow rates (sccm)**			**Deposition temp (°C)**	**# cycles**
H_2O	**$[Ni(Cp)_2]$**	**purge**	**$[Ni(Cp)_2]$**	**H_2O**		
5	100	100	100	0	300	250
5	100	100	100	0	300	250
5	100	100	100	0	300	350
5	100	100	100	0	300	600
5	100	100	100	0	350	250
5	100	100	100	0	350	1000
5	100	20	0	0	350	250
25	100	100	100	50	350	250

Table 4.8 Summary of conditions used to deposit NiO via ALD of $[Ni(Cp)_2]$ and water at higher substrate temperatures

4.3.3.2.3 Characterisation of films

The surface morphology of the films deposited by ALD was studied using non-contact mode atomic force microscopy (AFM) (Figure 4.22). Unlike the TiO_2 films, the surface roughness of these films was more variable with the number of reaction cycles. At 250 cycles a surface roughness of around 18 nm was observed, and the film appeared flat with some granular areas. By increasing the number of ALD cycles to 350, the roughness increased to around 45 nm. It is believed that this is due to secondary nucleation.[52] When the number of reaction cycles was increased from 350 to 600, the roughness deceased to 38 nm and then to 25 nm for 1000 cycles.

It is not definitively clear what growth mechanism is occurring - the AFM images appear to look fairly similar as the film thickness increases, with no obvious signs of nucleation sites coalescing to form a denser and less porous film (and hence more crystalline). The root mean square (RMS) roughness values (Table 4.9) also do not seem to show a significant relationship with the surface morphology of the films, as it is normally expected that the surface roughness would increase with the number of reaction cycles.

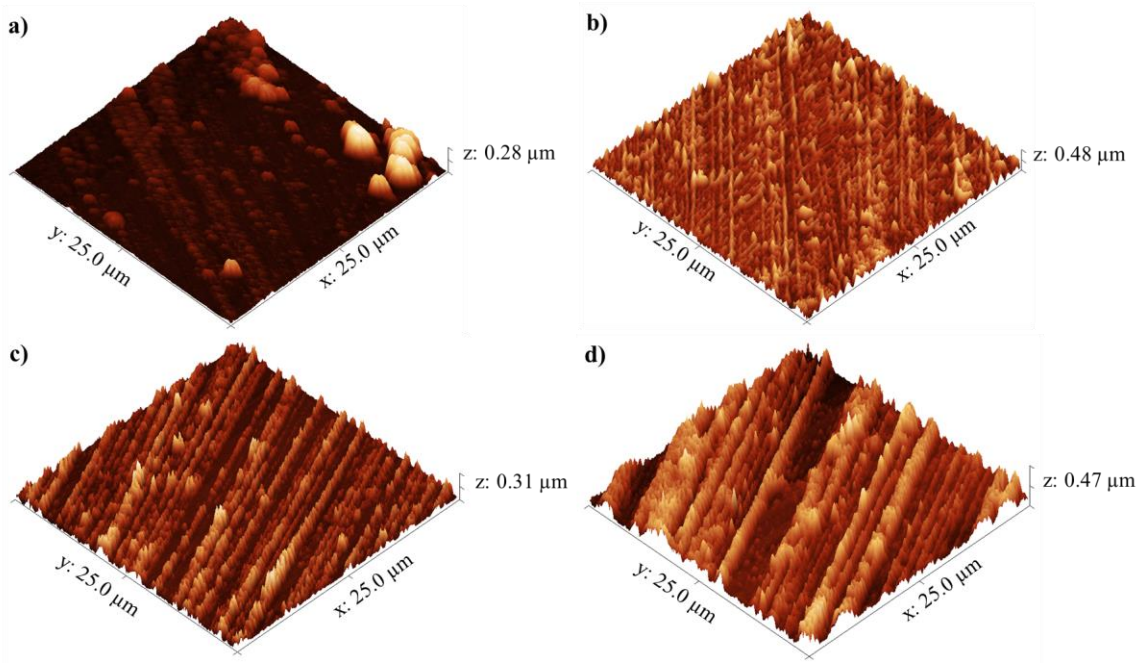

Figure 4.22 AFM images of films deposited using [$Ni(Cp)_2$] and water at 300 °C with a) 250 cycles, b) 350 cycles, c) 600 cycles and d) 1000 cycles. Images set to a physical scale factor of 10 in the z axis

# cycles	RMS (nm)
250	18
350	45
600	39
1000	25

Table 4.9 Roughness measurements on films deposited using [$Ni(Cp)_2$] and water via ALD at 300 °C with different number of reaction cycles

In order to characterise the materials and determine the elemental composition of the films described in Table 4.8, X-ray photoelectron spectroscopy (XPS) was performed on the as-deposited films at 300 °C. The data revealed the presence of Ni and O elements on the film surfaces with some carbon contamination present, as shown by the survey spectrum (Figure 4.23). Five seconds of argon ion sputtering saw an increase in the concentration of nickel. However, the carbon peak was still intense after sputtering which suggests there was carbon contamination within the films, which is not uncommon for cyclopentadienyl precursors.[51]

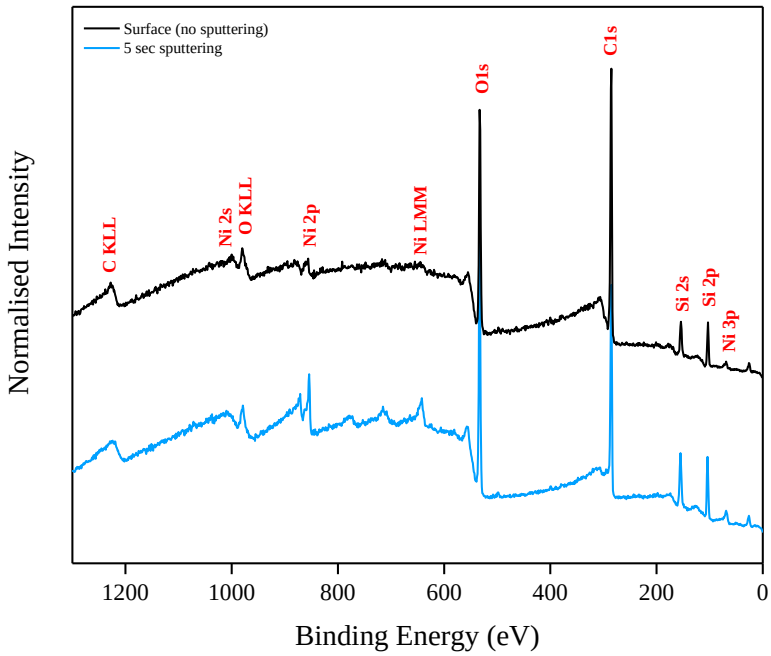

Figure 4.23 Typical XPS survey spectrum of films deposited by ALD of $[Ni(Cp)_2]$ and water at 300°C

Figure 4.24 shows a typical high resolution spectrum of the Ni2p core level peaks for the films deposited via ALD of $[Ni(Cp)_2]$ and water at 300 °C with 600 cycles. The spectrum shows evidence of Ni^{2+} as illustrated by the presence of Ni satellite peak ionisations[151] at 861.4 ± 0.2 eV and 880.7 ± 0.2 eV (denoted by asterisk). This strongly indicates that the surface of the film contains either NiO or $Ni(OH)_2$.

Upon 5 seconds of argon ion sputtering, it appears that Ni^{2+} was reduced to Ni^0. The binding energies and shape of the peaks are consistent with those of typical Ni^0 species.[152] The $2p_{3/2}$ and $2p_{1/2}$ peaks were primarily observed at 853.1 and 870.6 ± 0.2 eV of binding energy respectively. It is not unusual for metal ions to be reduced during argon ion sputtering.

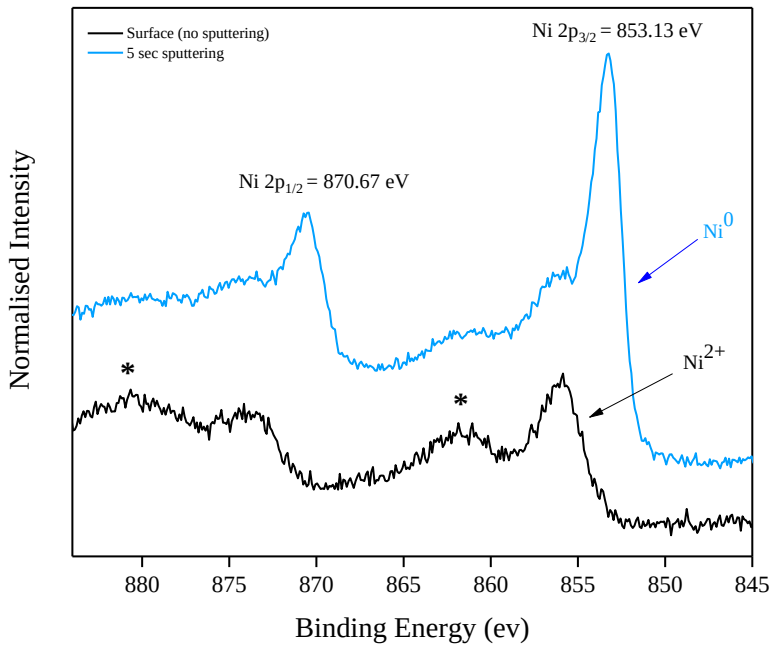

Figure 4.24 High resolution XPS spectrum of Ni2p peak for a 600 cycle film deposited at 300 °C with $[Ni(Cp)_2]$ and water. Five seconds of sputtering has reduced the Ni^{2+} species to Ni^0. Asterisk denotes satellite peaks

Following the convention by Frost[153] *et al.*, the satellite peaks can be classified into different types. The surface scan of the Ni2p peaks suggests 'type C', where there is one satellite peak to each Ni2p signal and is the pattern typically observed for Ni^{2+} species. Satellite peaks for Ni^{2+} species have been ascribed to charge transfer multi-electron transitions.[154]

For NiO species, multiplet-splitting is normally observed for the $Ni2p_{3/2}$ peak, with a prominent satellite shoulder ~ 1.8 eV above the principal peak, which is unique to NiO.[154,155] As this was not visible in these samples, it can be concluded that the surface species was $Ni(OH)_2$. Deconvolution of the surface $Ni2p_{3/2}$ peak (Figure 4.25) showed two obvious satellite intensities, fit by broad peaks (FWHM 3.5 eV) with binding energies at 5.4 eV and 7.2 eV above the principal peak at 856.1 ± 0.2 eV (peak A). The $2p_{3/2}$ peak was not accompanied by a satellite shoulder as in the case of NiO. The higher energy satellite peak (blue peak), again due to multi-electron excitation,[154] was shifted to a lower energy than the equivalent NiO peak (which has binding energies of 6.6 eV and 7.2 eV above the principal peak). The binding energies of the $Ni2p_{3/2}$ and $Ni2p_{1/2}$ surface scan peaks were 856.1 ± 0.2 eV and 873.9 ± 0.2 eV respectively, with a peak separation of 17.8 eV. These values are in agreement with reported values for $Ni(OH)_2$.[143,155]

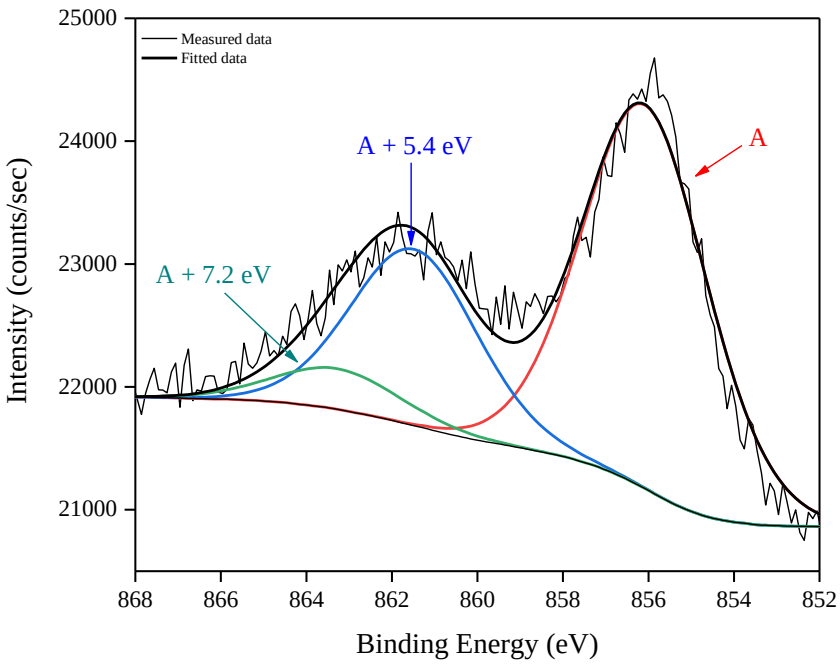

Figure 4.25 High resolution $Ni2p_{3/2}$ spectrum of $Ni(OH)_2$ with two obvious satellite intensities fit by broad peaks (FWHM 3.5 eV) with binding energies at 5.4 eV and 7.2 eV above the principal peak at 856.1 eV

The fact that Ni^{2+} present on the film surfaces is in the form of $Ni(OH)_2$ and not NiO suggests that growth was not occurring under 'true' ALD growth conditions. It is believed that [$Ni(Cp)_2$] reacted with the hydroxyl groups on the substrate surface to form surface-adsorbed Ni species. Upon the introduction of water into the reactor, it is thought that there were a limited number of reactive functional groups available for the water to react with, and thus restore the reactivity of the substrate towards [$Ni(Cp)_2$] again. It is therefore suggested that growth did not proceed in a self-limited manner to form conformal layers of material. This idea can be supported by the fact that; a) film thickness does not appear to increase after visual inspection of the substrates - all films, regardless of the number of cycles look the same. Under ALD conditions film thickness should increase linearly with the number of cycles; and b) the AFM and surface roughness profiles do not appear to show any relationship as the number of cycles is increased. The surface roughness of the films is relatively high (18 - 45 nm), which may suggest that films are porous in nature with no defined structural growth.

Due to the films being relatively thin, X-ray diffraction (XRD) and Raman spectroscopy techniques were unable to reveal any further information regarding the structural and physical properties of the films; including the crystallographic orientation and film morphology. The films appeared amorphous by XRD, which is likely due to the films being too thin to produce significant diffraction, which was consistent with the appearance of a broad background peak attributed to breakthrough to the glass substrate.

Scanning electron microscopy (SEM) analysis was performed on the $Ni(OH)_2$ films to image the morphology of the sample surfaces and to see if any further information could be obtained regarding the crystallinity or chemical composition (Figure 4.26). Samples were electrically grounded to a sample stage using carbon tape and silver paint.

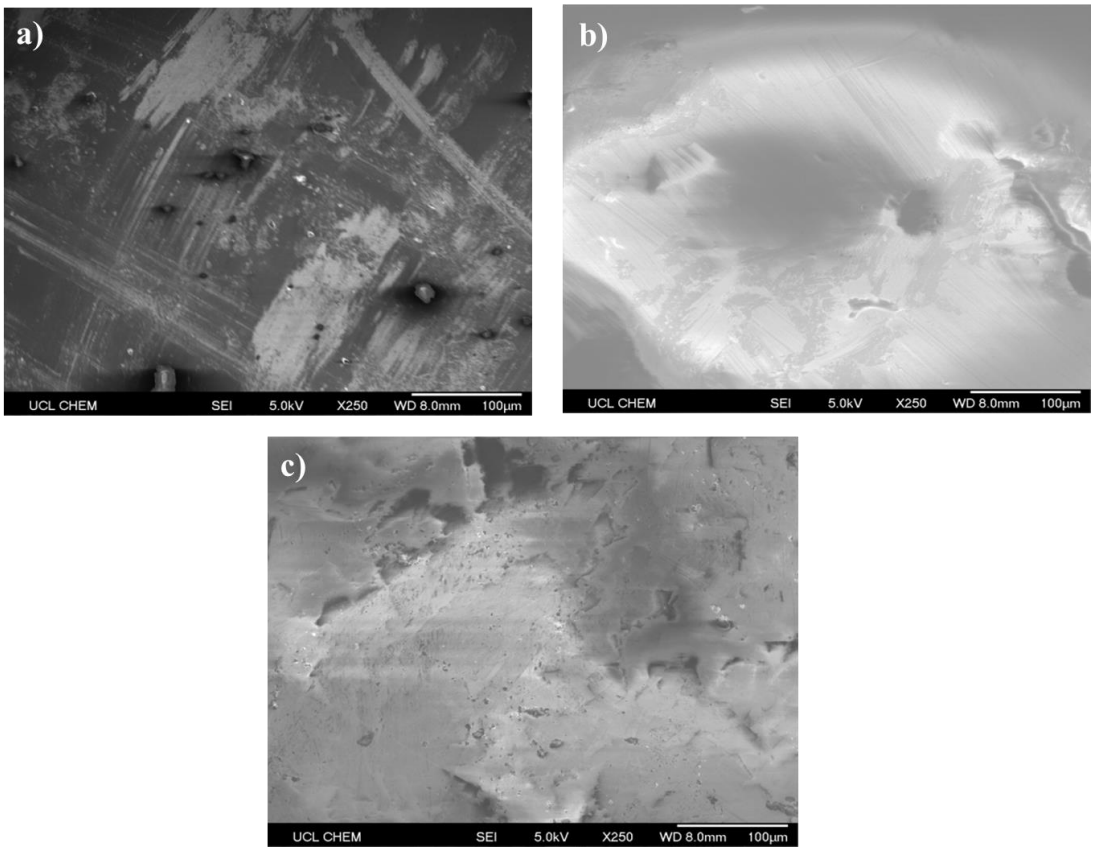

Figure 4.26 SEM images of films deposited from $[Ni(Cp)_2]$ and water at 300 °C, where a) is a blank quartz substrate, b) 600 cycle film and c) 1000 cycle film

The SEM images of the as-deposited films show comparatively little difference as compared to the blank substrate. In the image of the blank substrate, defects are visible which were characteristic of the substrates used throughout. The films show very little microstructure/crystallinity with increasing number of cycles. Sample **c)** (1000 cycles) shows some structural differences, but it is visible that the film is not very uniform, which supports the earlier explanations of poor ALD growth and insufficient reactivity of precursors.

Annealing of films

In order to investigate the effects of annealing on the chemical and physical properties of the films, samples (from Table 4.8) were annealed at 700 °C for 1 hour.[156] However, XPS analysis revealed that there were no Ni^{2+} species present on the surface after annealing. This suggested that the adsorption of precursors to the substrate surface was through physisorption[157] (weak van der Waals interactions) rather than chemisorption. Clearly, the deposited films were not very stable, as this would not have occurred if the precursors were deposited in a self-limiting and complementary manner. It is possible that the $Ni(OH)_2$ films were primarily in the form of α-$Ni(OH)_2$, which is reported to be more unstable than β-$Ni(OH)_2$.[158] It can therefore be concluded that there were severe issues regarding the reactivity of the precursors with each other and the substrate.

4.3.3.2.4 Summary

Atomic layer deposition of NiO thin films using $[Ni(Cp)_2]$ and water as precursors was shown to be unsuccessful at a growth temperature of 165 °C, where the $[Ni(Cp)_2]$ precursor was held at a temperature of 50 °C which was consistent with temperatures reported in the literature. The precursor vapour pressure and gas flow rates were manipulated though utilisation of equation 4.3, but this had no effect on the deposition outcome. It is believed that a growth temperature of 165 °C was below the "ALD process window", where there was insufficient thermal energy to initiate the growth kinetics.

Increasing the growth temperature in the range of 300 - 350 °C resulted in the deposition of thin grey films, which is in good resemblance with literature which reports that nickel oxide/hydroxide films produced via ALD are black in colour.[72,73] However, the colour may also be influenced by carbon contamination in the films due to partial thermal decomposition of $[Ni(Cp)_2]$[148] which is not uncommon for cyclopentadienyls. Deposition temperatures in this range are suspected to be within (or close to) the "ALD process window", where film deposition should occur via a self-limiting mechanism and there is sufficient energy for chemical reactions to take place.

AFM measurements show that the surface roughness of the films was rather variable with the number of reaction cycles. It is not definitively clear what growth mechanism was occurring, as the AFM images appear to look fairly similar as the film thickness increases, with no obvious signs of nucleation sites coalescing to form a denser and less porous film. Roughness measurements do not seem to show a significant relationship with the surface morphology of the films. As the film thickness doesn't appear to increase with the number of reaction cycles and the surface roughness of the films was relatively high (18 - 45 nm), this may suggest that the films were porous with no defined structural growth.

XPS analysis confirmed the presence of Ni^{2+} on the substrate, as illustrated by the presence of Ni satellite peak ionisations. Although high resolution spectra of the Ni2p peak strongly suggested the Ni^{2+} species was in the form of $Ni(OH)_2$ rather than NiO. No multiplet peak splitting was observed that is typical of NiO and binding energies and spin-orbit coupling values were comparable to those of $Ni(OH)_2$ as reported in the literature.

As the films were composed of $Ni(OH)_2$ rather than NiO, this suggested that the precursor dose and purge times may not have been optimised in order to form completely saturated layers. The fact that $Ni(OH)_2$ was present on the film surfaces rather than NiO suggests that the $[Ni(Cp)_2]$ dose time may not have been sufficient enough to react with all the functional groups on the surface. In addition, the surface-adsorbed Ni species may not have been very reactive towards water under the conditions used and with the reactor design used. Most reports showing the ALD of NiO from $[Ni(Cp)_2]$ have utilised either O_3, O_2 or H_2 as the co-reactant, so it may be that $[Ni(Cp)_2]$ was not particularly reactive with water under these test conditions.

SEM analysis revealed no further information about the morphology of the films, as the films show comparatively little difference as compared to a blank substrate. No increase crystallinity was observed with increasing number of reaction cycles and films appeared non-uniform, which supports previous explanations of poor ALD growth under the reaction conditions and reactor design used. Conversely, upon annealing the films no Ni^{2+} was detected on the substrate surfaces (as quantified by

XPS). This emphasised that the films were not stable and may be composed of the more unstable structure of α-$Ni(OH)_2$.

ALD of $[Ni(Cp)_2]$ and water to grow NiO was shown to be unsuccessful, even though there are reports in the literature suggesting that NiO can be grown by ALD using this precursor combination. It is therefore likely that there were problems with the precursor delivery and also holdups of water in the system. One way to investigate whether the delivery of $[Ni(Cp)_2]$ into the reactor was a problem would be to conduct CVD experiments at a higher substrate temperature. With controlled dosing of the precursor at a higher temperature, this should result in precursor decomposition on the substrate to form NiO. If this could be achieved then this would rule out any issues with precursor delivery into the reactor.

4.3.3.3 ALD of $[Ni(dmamp)_2]$

4.3.3.3.1 $[Ni(dmamp)_2]$ precursor for ALD

The novel precursor $[Ni(dmamp)_2]$, (dmamp = 2-dimethylamino-2-methyl-1-propanolate) is a brown solid which was synthesised in house as described in section 4.2.3.2. The TGA/DSC (Figure 4.14) shows that the onset of precursor vaporisation occurred at around 80 °C, with complete decomposition at ~ 240 °C.

There are several publications outlining the use of similar $[Ni(dmamp)_2]$-type structures for use in ALD with both H_2O[138] and O_2[45] as co-reactants to deposit NiO thin films. Although solids at room temperature, these nickel dialkylamino alkoxide complexes ($[Ni(dmamp)_2]$, $[Ni(emamp)_2]$, and $[Ni(deamp)_2]$) are volatile and thermally stable. As described earlier in section 4.3.1.2, the $[Ni(dmamp)_2]$ synthesised and utilised in this work was a novel precursor in that the 2 methyl groups on the dmamp ligand are positioned on a different carbon atom to those structures reported in the literature.[70] Although the temperature range of decomposition for this novel precursor is comparable to those reported in the literature for similar $[Ni(dmamp)_2]$-type structures, it is believed that the novel precursor has a higher thermal stability as its end decomposition temperature is

greater (240 °C compared to 174 °C in literature).[138] This means that it may have a wider scope for use in thin film deposition applications.

The vapour pressure of [Ni(dmamp)$_2$] could be manipulated by varying the temperature of the bubbler in which it was contained. Manipulation of the vapour pressure means that the amount of precursor released into the reaction chamber during each dose sequence can be more easily controlled. Again, to prevent precursor decomposition, the temperature of the bubbler was held at a temperature lower than the decomposition temperature of the precursor (240 °C) and to prevent CVD-like growth occurring, the substrate temperature was kept below 240 °C.

4.3.3.3.2 ALD of [Ni(dmamp)$_2$] and water

ALD depositions were carried out using [Ni(dmamp)$_2$], (dmamp = 2-dimethylamino-2-methyl-1-propanolate) and distilled water. [Ni(dmamp)$_2$] is a solid at room temperature and was therefore sublimed at a certain temperature within the bubbler in order to generate sufficient gaseous molecules to be dosed into the reactor. Initially, the conditions used to deposit TiO_2 using TTIP and water (as described in chapter 3) were employed for [Ni(dmamp)$_2$] and water.

For the initial depositions, [Ni(dmamp)$_2$] was sublimed inside the bubbler at a temperature of 80 °C, as the TGA shows that the onset of vaporisation occurs at this temperature (Figure 4.14). The precursor was dosed into the reactor using a gas assist. Following a paper by Yang[138] *et al.*, a growth temperature of 120 °C was employed, where the authors report ALD of NiO onto Si(001) substrates using an alternative [Ni(dmamap)$_2$] precursor (structure **a** in Figure 4.3) and water.

Similar papers also used growth temperatures within the range of 100 - 200 °C, with the most commonly used temperature being 100 - 140 °C.[70,44] Table 4.10 outlines the initial deposition conditions used at a growth temperature of 120 °C. Depositions were performed with varying number of reaction cycles. See Table 4.11 for a summary of all ALD depositions carried out using [Ni(dmamp)$_2$] and water.

	Time	**Bubbler temp (°C)**	**Purge flow (sccm)**	**[Ni(dmamp)$_2$] bubbler flow (sccm)**	**Water bubbler flow (sccm)**	**Growth temp (°C)**
[Ni(dmamp)$_2$] dose	2.5 sec	80	100	100	0	120
[Ni(dmamp)$_2$] purge	1 min	80	100	100	0	120
H_2O dose	2.0 sec	5	100	100	0	120
H_2O purge	3 min	5	100	100	0	120

Table 4.10 Initial reaction conditions used to deposit NiO films via ALD of [Ni(dmamp)$_2$] and water

However, upon analysing the substrates no NiO had been deposited, even upon increasing the number of reaction cycles. To increase the movement of precursor through the reactor, the depositions were repeated with higher gas flow rates of 600sccm (sample 4.5b, Table 4.11) for both the purge flow and the [Ni(dmamp)$_2$] bubbler flow, but this had no impact on the deposition outcome.

There were 4 possible explanations which were thought to be the root of no NiO film deposition occurring:

- Vapour pressure of [Ni(dmamp)$_2$] was not optimised.
- Precursor dose/purge times insufficient/not optimised.
- Reactivity issues between [Ni(dmamp)$_2$] and water.
- [Ni(dmamp)$_2$] precursor was insufficiently reactive towards substrate surface.

Variation of [Ni(dmamp)$_2$] vapour pressure

As no NiO deposition occurred using the conditions outlined in Table 4.10, this suggested that there could be potential issues with the vapour transport of [Ni(dmamp)$_2$] and thus it was not being efficiently transported into the reactor. In order to increase the volatility, and hence the vapour transport of [Ni(dmamp)$_2$] into the reactor, the sublimation temperature of [Ni(dmamp)$_2$] was increased from 80 °C to 120 °C and then to 150 °C. Depositions were then repeated using the conditions in Table 4.10 but this still resulted in no NiO deposition. ^{1}H NMR analysis of the precursor after being held in the bubbler at 120 °C confirmed that the precursor had decomposed (Figure 4.27). Figure 4.27a shows 3 singlet proton environments at 1.19 ppm, 2.20 ppm and 2.97 ppm, corresponding to 4 methyl groups on the ligand backbone, 4 methyl groups on the nitrogen atoms and 2 ethyl groups on the dmamp ligand backbone, respectively. However from Figure 4.27b, it is clear that after heating the precursor to 120 °C the peaks have shifted and split, indicating a change in the proton environments and hence a change in the precursor structure. This indicated that raising the sublimation temperature of the precursor higher than 80 °C resulted in significant precursor decomposition.

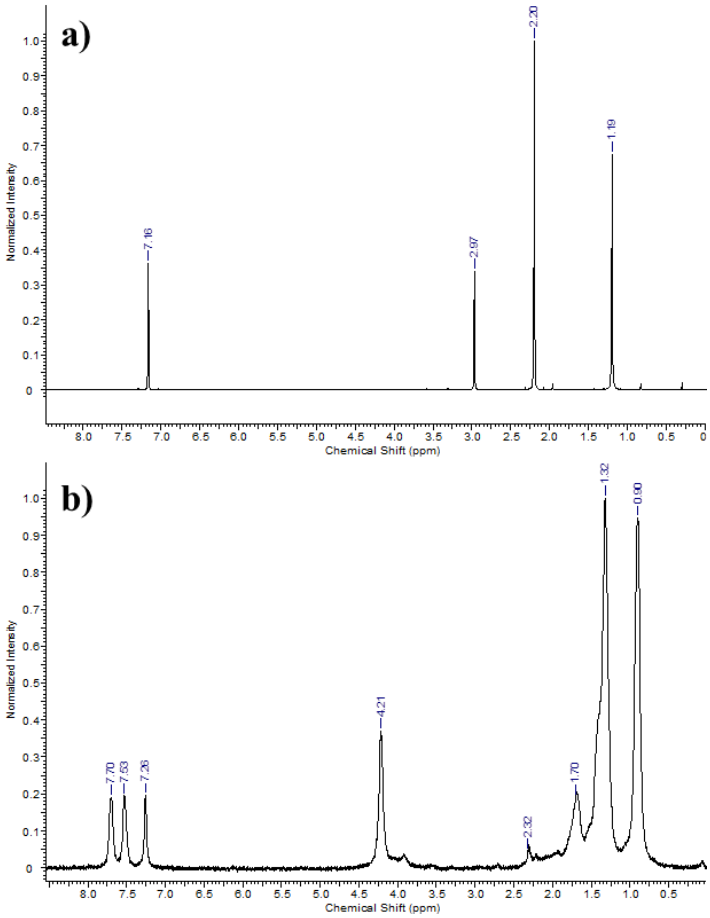

Figure 4.27 ^{1}H NMR spectra of [Ni(dmamp)$_2$]; a) as synthesised, and b) decomposed after heating in bubbler at 120 °C

Variation of precursor dose and purge conditions

As [Ni(dmamp)$_2$] is a solid precursor, it was possible that not enough gaseous molecules were being exposed into the reactor during the dose cycles. In order to overcome this problem, both the precursor dose times were increased. The [Ni(dmamp)$_2$] dose time was increased from 2.5 seconds to 8 seconds then 2 minutes and the water dose time was increased from 2 seconds to 3 seconds (samples 4.5c - 4.5f and 4.5h, Table 4.11). The bubbler temperatures and growth temperature remained unchanged to those described above (water bubbler 5 °C, [Ni(dmamp)$_2$] bubbler 80 °C, growth temperature 120 °C). However, after repeating the depositions using the higher precursor dose times, no NiO deposition occurred.

The gas flow rates for the purge line and the [Ni(dmamp)$_2$] bubbler assist were varied between 20 - 400 sccm, as it was not known how effectively or efficiently the precursor was moving through the reactor. Flow rates as low as 20 sccm (sample 4.5c, Table 4.11) were used to effectively 'slow down' the movement of the precursor through the reactor, and to therefore allow more time for it to react with the surface hydroxyl sites on the substrate. Conversely, higher flow rates (sample 4.5f, Table 4.11) were employed in case the precursor was not so volatile and therefore required a greater gas assist through the bubbler to assist its movement into the reactor. However, implementation of both these conditions resulted in no NiO deposition.

A possible thought as to why no deposition was occurring was that [Ni(dmamp)$_2$] may have been 'too reactive' with water. With a 3 minute gas purge, not all of the water may have been purged out of the reactor after the water dose. So when [Ni(dmamp)$_2$] was then dosed into the reactor a pre-reaction may have occurred, where the precursor might have reacted with residual water molecules prior to reaching the substrate, consequently depleting the very small amount of [Ni(dmamp)$_2$] dosed. In order to combat this, the water purge time was increased from 3 minutes to 10 minutes (sample 4.5g, Table 4.11). One can therefore be fairly confident that [Ni(dmamp)$_2$] was being dosed reasonably well (8 second dose) and water was being purged sufficiently also (10 minutes). However, depositions performed under these conditions resulted in no NiO deposition.

Variation of growth temperature

The growth temperature may not have been high enough to initiate ALD growth, and was therefore increased from 120 °C to 160 °C and a selection of the depositions which previously failed were repeated (samples 4.5i - 4.5l, Table 4.11). Similarly, depositions were performed with various precursor dose and purge times and with different gas flow rates through the [Ni(dmamp)$_2$] bubbler and the purge line. But a growth temperature of 160 °C resulted in no NiO film deposition.

If a growth temperature of 160 °C was not high enough, this may have caused issues with precursor kinetics at the substrate, where precursors had insufficient energy to react with the substrate and/or each other. This is because the precursor adsorption to the surface is a thermally activated process,[21] so [Ni(dmamp)$_2$] may have had inadequate energy to react with the surface hydroxyl groups on the substrate. One would expect that increasing the growth temperature from 160 °C to 250 °C (samples 4.5m - 4.5p, Table 4.11) would result in more favourable reaction kinetics, where growth is likely to be at the upper end of the "ALD process window", as the precursor completely decomposes at 240 °C, as shown by the TGA (Figure 4.14). At these higher temperatures there should be sufficient thermal energy for chemical reactions to take place on the substrate. These higher temperatures have been employed for ALD of other [Ni(dmamp)$_2$]-type structures elsewhere.[138] Nevertheless, after performing numerous depositions at growth temperatures of 200 - 250 °C, with various dose/purge times and flow rates, still no NiO deposition was observed.

ALD depositions were carried out at an even higher temperature of 450 °C (sample 4.5r, Table 4.11). XPS analysis confirmed the presence of small amounts of nickel metal as well as oxidised nickel on the substrate surface, but it was unclear as to whether it was NiO or Ni(OH)$_2$ due to the overlapping peak binding energies (Figure 4.28). At 450 °C, which is much higher than the decomposition temperature of [Ni(dmamp)$_2$] (~ 240 °C), it is apparent that the precursor thermally decomposed onto the substrate to form an oxidised nickel species. It has been reported by Min *et al.* that sometimes the growth rate of NiO decreases at higher temperatures, due to the formation of NiO in the vapour phase rather than depositing on the substrate,[45] which could be why the nickel species detected on the substrate was minimal. As no nickel was detected on the substrate surface at temperatures below the precursor decomposition temperature (< 250 °C), this suggested that there were underlying precursor reactivity issues.

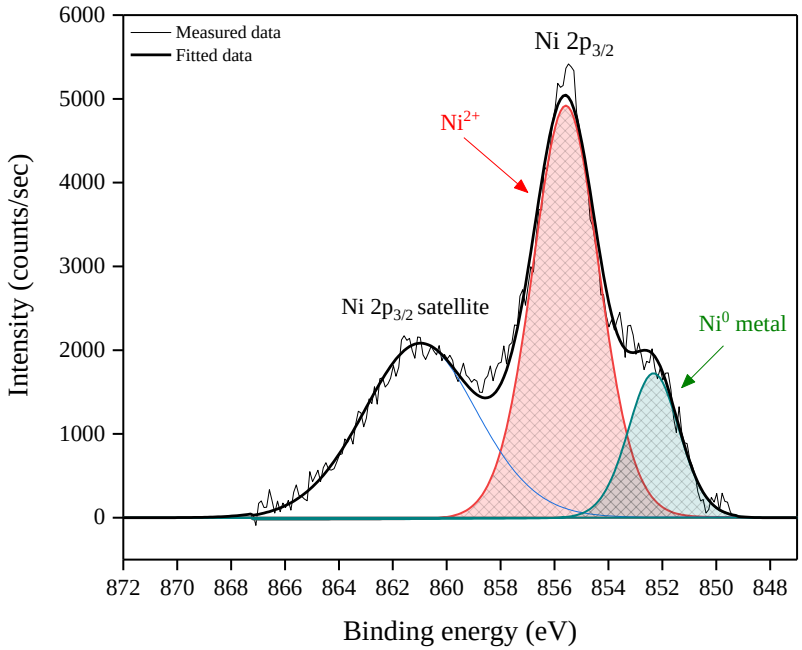

Figure 4.28 High resolution surface scan of the Ni2p$_{3/2}$ peak for films deposited by ALD of [Ni(dmamp)$_2$] and water at 450 °C. Ni^{2+} and Ni^0 peaks were fitted (FWHM 2.8 eV) with binding energies of 855.6 and 852.4 ± 0.2 eV respectively

Effect of substrate material on film growth

As depositions had so far been unsuccessful, it was important to think about the reactivity of the precursors with the substrate. The issue may have been partly due to the substrate itself, in the fact that it was not 'active' enough towards [Ni(dmamp)$_2$] to initiate film growth, i.e. insufficient hydroxyl groups. Therefore a variety of different substrate materials were acquired and a selection of the depositions outlined in Table 4.11 were repeated. Substrate materials tested included silicon, alumina, FTO (fluorine-doped tin oxide), float glass, $SrTiO_3$, and O_2 plasma treated quartz and silicon. Nevertheless, changing the substrate material was found to have no impact on the deposition outcome.

Sample ID	[Ni(dmamp)$_2$] dose	[Ni(dmamp)$_2$] purge	H_2O dose	H_2O purge	Ni Bubbler gas assist	Growth temp (°C)	Result
4.5a	2.5 sec	1 min	2 sec	3 min	100 sccm	120	No film
4.5b	2.5 sec	1 min	2 sec	3 min	600 sccm	120	No film
4.5c	8 sec	1 min	3 sec	3 min	20 sccm	120	No film
4.5d	8 sec	1 min	3 sec	3 min	100 sccm	120	No film
4.5e	8 sec	1 min	3 sec	3 min	200 sccm	120	No film
4.5f	8 sec	1 min	3 sec	3 min	400 sccm	120	No film
4.5g	8 sec	1 min	2 sec	10 min	20 sccm	120	No film
4.5h	2 min	30 sec	2 sec	3 min	20 sccm	120	No film
4.5i	2.5 sec	1 min	2 sec	3 min	100 sccm	160	No film
4.5j	2.5 sec	1 min	2 sec	3 min	600 sccm	160	No film
4.5k	5 sec	1 min	4 sec	3 min	100 sccm	160	No film
4.5l	3 min	1 min	2 sec	10 min	20 sccm	160	No film
4.5m	5 sec	1 min	3 sec	3 min	100 sccm	200	No film
4.5n	8 sec	1 min	2 sec	10 min	20 sccm	200	No film
4.5o	1 min	10 min	2 sec	10 min	20 sccm	200	No film
4.5p	8 sec	1 min	3 sec	3 min	100 sccm	250	No film
4.5q	8 sec	1 min	3 sec	3 min	20sccm	400	No film
4.5r	8 sec	1 min	3 sec	3 min	20sccm	450	**NiO film**

Table 4.11 Summary of ALD reactions using [Ni(dmamp)$_2$] and water. The [Ni(dmamp)$_2$] bubbler temperature was maintained at 80 °C

CVD of [Ni(dmamp)$_2$]

To determine whether vaporised [Ni(dmamp)$_2$] molecules could actually be transported into the reactor, depositions were performed in "CVD mode". This was achieved by simply opening the inlet and outlet valves of the bubbler and continuously dosing [Ni(dmamp)$_2$] into the reactor under a constant gas flow. The bubbler temperature was maintained at 80 °C, but the growth temperature was raised to 400 °C to ensure that the precursor decomposed onto the substrate. Table 4.12 outlines the depositions performed in CVD mode.

Sample ID	Purge flow (sccm)	[Ni(dmamp)$_2$] bubbler flow (sccm)	Deposition time (hrs)	Growth temp (°C)	Result
4.5s	20	20	20	400	Grey film
4.5t	20	20	50	400	Grey film
4.5u	20	20	66	400	Grey film

Table 4.12 Reaction conditions used to deposit [Ni(dmamp)$_2$] in CVD mode at 400 °C

The results show that [Ni(dmamp)$_2$] was successfully deposited onto the substrate via CVD, resulting in grey/black films where the thickness of the films increased with deposition time. It was apparent that utilisation of lower gas flow rates (20 sccm) was sufficient to generate enough precursor transport into the reactor. XRD data shown in Figure 4.29 confirmed that the deposited films were NiO with the (200) reflection the most intense. As the deposition time was increased, the intensity of the diffraction peaks increased, indicating an increase in film crystallinity. A broad background peak was observed for sample 4.5s (20 hours CVD) which is attributed to breakthrough to the glass substrate. XPS also confirmed the presence of NiO at the film surface as shown in Figure 4.30. The principal Ni^{2+} peak was observed at 855.0 ± 0.2 eV with 3 characteristic satellite peaks 1.6, 5.8 and 8.1 eV above the principal peak.

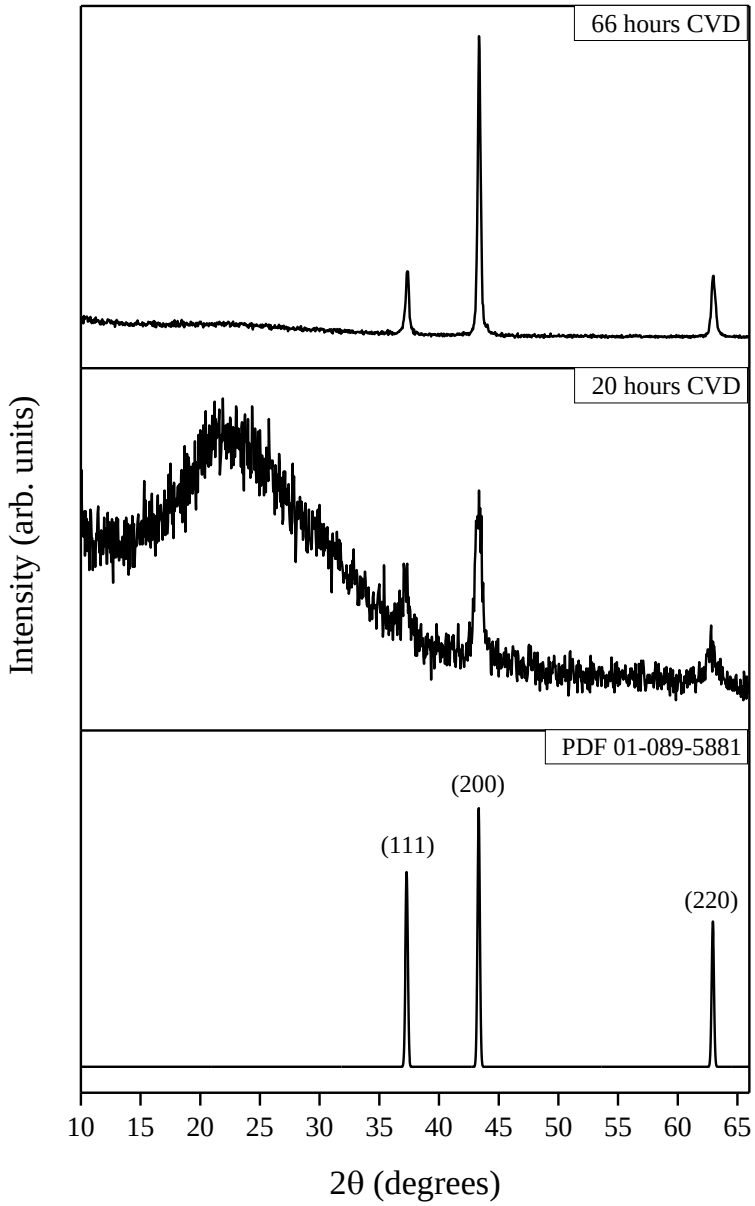

Figure 4.29 XRD patterns for NiO films deposited by CVD of [Ni(dmamp)$_2$] at 400 °C. Typical NiO reference pattern included (PDF 01-089-5881)

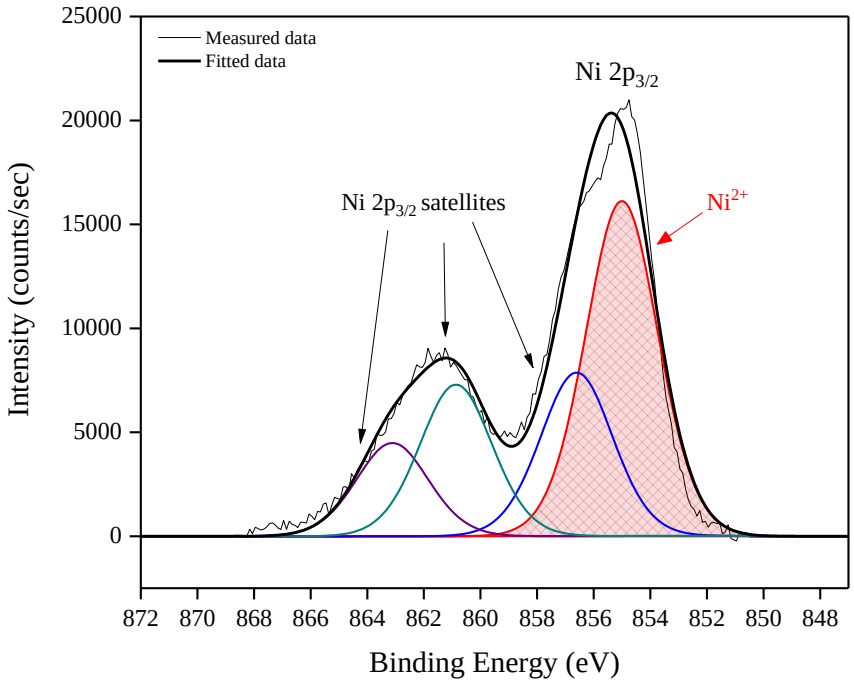

Figure 4.30 High resolution surface scan of $Ni2p_{3/2}$ peak with 3 observable satellite intensities fit by broad peaks (FWHM 3.0 eV) with binding energies at 1.6, 5.8 and 8.1 eV above the principal peak at 855.0 eV

Performing these depositions in CVD mode confirmed that $[Ni(dmamp)_2]$ was suitably volatile and could be easily transported into the reactor. The fact that CVD depositions at 400 °C worked but ALD depositions at 400 °C did not work, advocates that $[Ni(dmamp)_2]$ is insufficiently sensitive with water to react in an ALD scheme.

Pulsed-CVD of $[Ni(dmamp)_2]$

As CVD of $[Ni(dmamp)_2]$ resulted in the deposition of NiO, pulsed-CVD was carried out to see if the precursor could still be deposited. Pulsed-CVD involved dosing $[Ni(dmamp)_2]$ for 1 minute, followed by a 3 minute gas purge, which was repeated for 1000 cycles. The $[Ni(dmamp)_2]$ bubbler temperature was maintained at 80 °C and the growth temperature was 400 °C. Under these conditions, deposition was taken closer to those conditions used for ALD and theoretically, dosing the precursor into

the reactor in this way should still result in NiO deposition. Depositions carried out under pulsed-CVD conditions are outlined in Table 4.13.

	Time	**Purge flow (sccm)**	**[Ni(dmamp)$_2$] bubbler flow (sccm)**	**Growth temp (°C)**
[Ni(dmamp)$_2$] dose	1 min	20	20	400
purge	3 min	20	20	400

Table 4.13 Reaction conditions used to deposit [Ni(dmamp)$_2$] in pulsed-CVD mode for 1000 cycles at 400 °C

Pulsed-CVD with a 1 minute [Ni(dmamp)$_2$] dose time resulted in a grey NiO film. However when the dose time was reduced to 2.5 seconds, in order to bring the conditions closer to those used for ALD of TiO_2 (see chapter 3) no NiO film was deposited. It can therefore be concluded that pulsed-CVD of [Ni(dmamp)$_2$] starts to occur somewhere between 2.5 seconds and 1 minute. However it has been shown in Table 4.11 that when long [Ni(dmamp)$_2$] dose times (1, 2, and 3 minutes) were applied in ALD mode with water, no NiO deposition occurred.

4.3.3.3.3 Summary

Atomic layer deposition of NiO thin films using [Ni(dmamp)$_2$] and water as precursors was shown to be unsuccessful. The [Ni(dmamp)$_2$] bubbler was maintained at a temperature of 80 °C as TGA/DSC showed that the onset of precursor vaporisation occurred at 80 °C, with complete decomposition at ~ 240 °C. ^{1}H NMR analysis of the precursor after heating to temperatures above 80 °C confirmed that the precursor had decomposed. Depositions performed on various substrate materials were found to have no impact on the deposition outcome.

Although the precursor dose/purge times and gas flow rates could be easily manipulated, this had no effect on the deposition outcome. Variation of the growth temperature in the range of 120 - 250 °C had no effect on the film growth, however increasing the substrate temperature to 450 °C resulted in small amounts of nickel metal and Ni^{2+} species on the substrate surface due to thermal decomposition of the

precursor. However, it was unclear as to whether the Ni^{2+} species was NiO or $Ni(OH)_2$ due to the overlapping peak binding energies. It has previously been suggested that NiO may have formed in the gas phase rather than depositing on the substrate, which may explain the little amount of nickel detected on the substrate.

CVD of [$Ni(dmamp)_2$] was conducted to clarify whether the precursor was suitably volatile and could be easily transported into the reactor. The results confirm that NiO was deposited on the substrate at a growth temperature of 400 °C, which was established by XRD. The fact that CVD depositions at 400 °C worked but ALD depositions at 400 °C did not work, advocates that [$Ni(dmamp)_2$] is insufficiently sensitive with water to react in an ALD scheme under the reaction conditions used and with the reactor design used.

Pulsed-CVD experiments were performed to see whether [$Ni(dmamp)_2$] could still be deposited under conditions used closer to those used in ALD mode. 1 minute pulsed-CVD experiments resulted in NiO deposition, whereas 2.5 second pulsed-CVD experiments did not. These results suggest that during a 2.5 second dose time, an insufficient amount of precursor was released in to the reaction chamber to be able to saturate the substrate surface. It is well known that the volatility of solid precursors decreases as the precursor is depleted.

In conclusion, the results advocate that although a volatile enough precursor for ALD, [$Ni(dmamp)_2$] was unable to form NiO with water due to issues with precursor delivery and with the reactor itself.

4.3.3.4 ALD of [Ni{(N^iPr_2)$_2$CNEt$_2$}$_2$]

4.3.3.4.1 [Ni{(N^iPr_2)$_2$CNEt$_2$}$_2$] precursor for ALD

The novel precursor [Ni{(N^iPr_2)$_2$CNEt$_2$}$_2$] is a purple solid which was synthesised in house as described in section 4.2.3.3. The TGA/DSC (Figure 4.15) shows that the onset of precursor vaporisation occurred at around 110 °C, with complete decomposition at ~ 160 °C. The decomposition profile for the novel [Ni{(N^iPr_2)$_2$CNEt$_2$}$_2$] precursor is comparable to those reported in the literature for simialr nickel amidinate complexes[139] and copper guanidinate complexes.[134]

Metal guanidinate complexes are relatively new precursors for thin film deposition methods, with the first reported use being in 2005 by Carmalt *et al.* employing the use of titanium guanidinates to deposit titanium carbonitride films under low-pressure CVD conditions.[78] Guanidinate complexes are versatile N-N'-donor ligands due to the large range of derivatives available through substitution at the terminal nitrogen atoms.[159] The bidentate chelating effect of the ligand is also capable of increasing the thermal and chemical stability[36] at the metal centre due to their electronic flexibility,[58] which makes them appropriate precursors for CVD and ALD of various materials.

Copper guanidinate complexes have previously been reported as potential precursors for ALD and CVD applications,[159] however there are no reported studies on nickel guanidinate complexes for such techniques. The first synthesis and structural characterisation of a nickel(I) guanidinate was reported in 2011[137] by Jones *et al.*, which gives scope for research into nickel guanidinate complexes.

As described earlier in section 4.3.1.3, the [Ni{(N^iPr_2)$_2$CNEt$_2$}$_2$] synthesised and utilised in this work was a novel precursor synthesised following adaptations from two different literature reports which show the synthesis of copper guanidinate complexes.[134,59] The properties of the novel [Ni{(N^iPr_2)$_2$CNEt$_2$}$_2$] precursor cannot be directly compared to other nickel guanidinate complexes reported in the literature as the structures are very different and often consist of large, bulky ligands. However, the TGA shown in Figure 4.16 shows that the volatility of

$[Ni\{(N^iPr_2)_2CNEt_2\}_2]$ is on a par with the synthesised $[Ni(dmamp)_2]$, but it is more volatile than $[Ni(thd)_2]$, as well as $[Ni(Cp)_2]$ as reported in the literature.[148] This gives huge scope for the use of $[Ni\{(N^iPr_2)_2CNEt_2\}_2]$ as a precursor for use in ALD applications over some of the other nickel precursors widely used.

The vapour pressure of $[Ni\{(N^iPr_2)_2CNEt_2\}_2]$ could be manipulated by varying the temperature of the bubbler in which it was contained. Manipulation of the vapour pressure means that the amount of precursor released into the reaction chamber during each dose sequence can be more easily controlled. Again, to prevent thermal decomposition of the precursor occurring, the temperature of the bubbler and the growth temperature were kept at a temperature lower than the decomposition temperature of the precursor (160 °C) to prevent undesirable CVD-like growth occurring.

4.3.3.4.2 ALD of $[Ni\{(N^iPr_2)_2CNEt_2\}_2]$ and water

ALD depositions were carried out using $[Ni\{(N^iPr_2)_2CNEt_2\}_2]$ and distilled water. $[Ni\{(N^iPr_2)_2CNEt_2\}_2]$ is a solid at room temperature and was therefore sublimed at a certain temperature within the bubbler in order to generate sufficient gaseous molecules to be dosed into the reactor. Initially the conditions used to deposit TiO_2 using TTIP and water (as described in chapter 3) were employed for $[Ni\{(N^iPr_2)_2CNEt_2\}_2]$ and water.

For the initial depositions, $[Ni\{(N^iPr_2)_2CNEt_2\}_2]$ was sublimed inside the bubbler at a temperature of 110 °C, as the TGA shows that the onset of vaporisation occurs at this temperature (Figure 4.15). The precursor was dosed into the reactor using a gas assist. ALD has been used to deposit a range of metal oxide and metal nitride thin films using guanidinate precursors at growth temperatures in the range of 100 - 350°C.[78] Initially, a growth temperature of 300 °C was employed. Although this temperature was greater than the decomposition temperature of $[Ni\{(N^iPr_2)_2CNEt_2\}_2]$ (~ 160 °C), a higher temperature was used to ensure that the precursor kinetics were sufficient enough to generate film growth. At this early stage the possibility of CVD growth occurring was not an issue, as it was important to first examine the precursor

transportation into the reactor. Table 4.14 outlines the initial deposition conditions used at a substrate temperature of 300 °C. Depositions were performed with varying number of reaction cycles. However, upon XPS analysis of the substrates no NiO had been deposited, even upon increasing the number of reaction cycles. See Table 4.15 for a summary of all ALD depositions carried out using [Ni{(NiPr2)2CNEt2}2] and water.

	Time	**Bubbler temp (°C)**	**Purge flow (sccm)**	**$[Ni\{(N^iPr_2)_2CNEt_2\}_2]$ bubbler flow (sccm)**	**Water bubbler flow (sccm)**
$[Ni\{(N^iPr_2)_2CNEt_2\}_2]$ dose	2.5 sec	110	20	20	0
$[Ni\{(N^iPr_2)_2CNEt_2\}_2]$ purge	1 min	110	20	20	0
H_2O dose	2.0 sec	5	20	20	0
H_2O purge	3 min	5	20	20	0

Table 4.14 Initial reaction conditions used to deposit films via ALD of $[Ni\{(N^iPr_2)_2CNEt_2\}_2]$ and water at 300 °C

Variation of precursor dose and purge conditions

As $[Ni\{(N^iPr_2)_2CNEt_2\}_2]$ is a solid precursor at room temperature, it was possible that not enough gaseous molecules were being exposed into the reactor during the 2.5 second dose cycles. In order to overcome this problem, the $[Ni\{(N^iPr_2)_2CNEt_2\}_2]$ dose time was increased from 2.5 seconds to 5 seconds and then to 1 minute (samples 4.6a, b, c, Table 4.15). The bubbler temperatures and growth temperature remained unchanged to those described above (water bubbler 5 °C, $[Ni\{(N^iPr_2)_2CNEt_2\}_2]$ bubbler 110 °C, growth temperature 300 °C). However, after repeating the depositions, no NiO deposition occurred.

Variation of growth temperature

It was unusual that no film deposition occurred at a growth temperature of 300 °C, even though this was well above the $[Ni\{(N^iPr_2)_2CNEt_2\}_2]$ decomposition temperature. It was possible that the growth temperature may have actually been too high, in that the precursor was decomposing as soon as it entered the reaction chamber; before it even reached the substrate. The growth temperature was therefore reduced to 200 °C (samples 4.6d, e, f, Table 4.15) and then to 140 °C (samples 4.6g, 4.6h, Table 4.15) and depositions were repeated, but no film deposition occurred.

With growth temperatures of 200 °C and 140 °C, the gas flow rates for the purge line and the $[Ni\{(N^iPr_2)_2CNEt_2\}_2]$ bubbler assist were increased from 20 - 140 sccm, as it was not known how effectively or efficiently the precursor was moving through the reactor. Higher flow rates (samples 4.6f, h, Table 4.15) were employed in case the precursor was not so volatile and therefore required a greater gas assist through the bubbler to assist its movement into the reactor. The $[Ni\{(N^iPr_2)_2CNEt_2\}_2]$ dose time was also increased from 1 minute to 5 minutes to increase the prospect of the precursor saturating the substrate surface. However, implementation of all these conditions resulted in no NiO deposition.

To check if growth could be achieved via thermal decomposition of $[Ni\{(N^iPr_2)_2CNEt_2\}_2]$, the substrate temperature was raised to 450 °C and depositions were repeated with various precursor dose times and gas flow rates (samples 4.6i, j, Table 4.15) but no film deposition was observed, as confirmed by XPS. At these higher temperatures there should be sufficient thermal energy for $[Ni\{(N^iPr_2)_2CNEt_2\}_2]$ to thermally decompose onto the substrate. Temperatures of up to 350 °C have been used to deposit metal guanidinates elsewhere (although not nickel guanidinates).[78] It may be possible that the precursor decomposes in the gas phase rather than on the substrate, which has been reported before.[45]

Sample ID	$[Ni\{(N^iPr_2)_2CNEt_2\}_2]$ dose	$[Ni\{(N^iPr_2)_2CNEt_2\}_2]$ purge	H_2O dose	H_2O purge	Ni Bubbler gas assist	Growth temp (°C)	Result
4.6a	2.5 sec	1 min	2 sec	3 min	20 sccm	300	No film
4.6b	5 sec	1 min	2 sec	3 min	20 sccm	300	No film
4.6c	1 min	1 min	4 sec	3 min	20 sccm	300	No film
4.6d	1 min	1 min	2 sec	3 min	20 sccm	200	No film
4.6e	1 min	1 min	2 sec	3 min	70 sccm	200	No film
4.6f	1 min	1 min	2 sec	3 min	140 sccm	200	No film
4.6g	5 min	1 min	2 sec	3 min	20 sccm	140	No film
4.6h	1 min	1 min	2 sec	3 min	120 sccm	140	No film
4.6i	1 min	1 min	2 sec	3 min	20 sccm	450	No film
4.6j	5 min	1 min	2 sec	3 min	20 sccm	450	No film

Table 4.15 Summary of ALD reactions using $[Ni\{(N^iPr_2)_2CNEt_2\}_2]$ and water. The $[Ni\{(N^iPr_2)_2CNEt_2\}_2]$ bubbler temperature was maintained at 110 °C. Reaction cycles were varied between 300 - 1000 cycles

CVD of [Ni{(N^iPr_2)$_2$CNEt$_2$}$_2$]

The bubbler was filled with approximately 0.5 g of [Ni{(N^iPr_2)$_2$CNEt$_2$}$_2$] and two 1000 cycle ALD depositions were performed at a substrate temperature of 400 °C using a 1 minute [Ni{(N^iPr_2)$_2$CNEt$_2$}$_2$] dose time. This resulted in no film formation.

Subsequently, the contents of the bubbler were inspected and it was found that the entire precursor had been depleted. It can therefore be concluded that the precursor was clearly being transported out of the bubbler during the ALD depositions, indicating that the precursor was suitably volatile and could be transported into the reactor.

In order to see whether [Ni{(N^iPr_2)$_2$CNEt$_2$}$_2$] could be deposited onto the substrate, depositions were performed in "CVD mode". The bubbler temperature was maintained at 110 °C, but the substrate temperature was raised to 450 °C. Table 4.16 outlines the depositions performed in CVD mode.

Sample ID	**Purge flow (sccm)**	**[Ni{(N^iPr_2)$_2$CNEt$_2$}$_2$] bubbler flow (sccm)**	**Deposition time (hrs)**	**Growth temp (°C)**	**Result**
4.6k	20	20	24	375	Film at inlet
4.6l	20	20	24	450	Brown film
4.6m	20	20	89	450	Brown film
4.6n	120	120	24	450	Brown film

Table 4.16 Reaction conditions used to deposit [Ni{(N^iPr_2)$_2$CNEt$_2$}$_2$] in CVD mode at 375 °C and 450 °C

The results show that $[Ni\{(N^iPr_2)_2CNEt_2\}_2]$ was successfully deposited onto the substrate via CVD. However, XRD showed that the deposited films were NiO, rather than the expected Ni_3N (Figure 4.31), with the (200) reflection the most intense. As $[Ni\{(N^iPr_2)_2CNEt_2\}_2]$ does not contain any oxygen atoms, it was apparent that NiO films had formed due to oxidisation of the precursor in the reactor. It is possible that this may have been the result of a small leak within the system somewhere (even though the pressure of the reactor was reasonably low). Alternatively, there may have been some residual water molecules inside the reactor which may have readily reacted with the precursor. It is important to note that pure Ni_3N films (as well as other late transition metal nitrides) are notoriously difficult to deposit by CVD techniques at temperatures below 500 °C. These processes usually utilise metal chlorides and either N_2, H_2 or NH_3 which results in high chlorine contamination which weakens the film properties.[9]

Metal guanidinate complexes have commonly been used in thin film deposition methods to form carbonitrides.[58,56] Carbonitrides are notoriously difficult to deposit, but LPCVD (low pressure chemical vapour deposition) has been employed to deposit zirconium and titanium carbonitrides, where the deposition process has to be done quickly (in around 1 hour) to prevent the formation of unwanted oxides. Subsequently, in the reported literature no metal oxides were detected on the substrate by XRD or XPS. In contrast, the CVD depositions performed in this work (Table 4.16) had a much longer deposition time (at least 24 hours), so any residual water molecules present would have had time to react with the $[Ni\{(N^iPr_2)_2CNEt_2\}_2]$ precursor to form NiO. However, it is encouraging that $[Ni\{(N^iPr_2)_2CNEt_2\}_2]$ was suitably volatile and could easily be transported into the reactor. The fact that CVD depositions at 450 °C worked but ALD depositions at 450 °C did not work, advocates that $[Ni\{(N^iPr_2)_2CNEt_2\}_2]$ was insufficiently sensitive with water to react in an ALD scheme under the reaction conditions used.

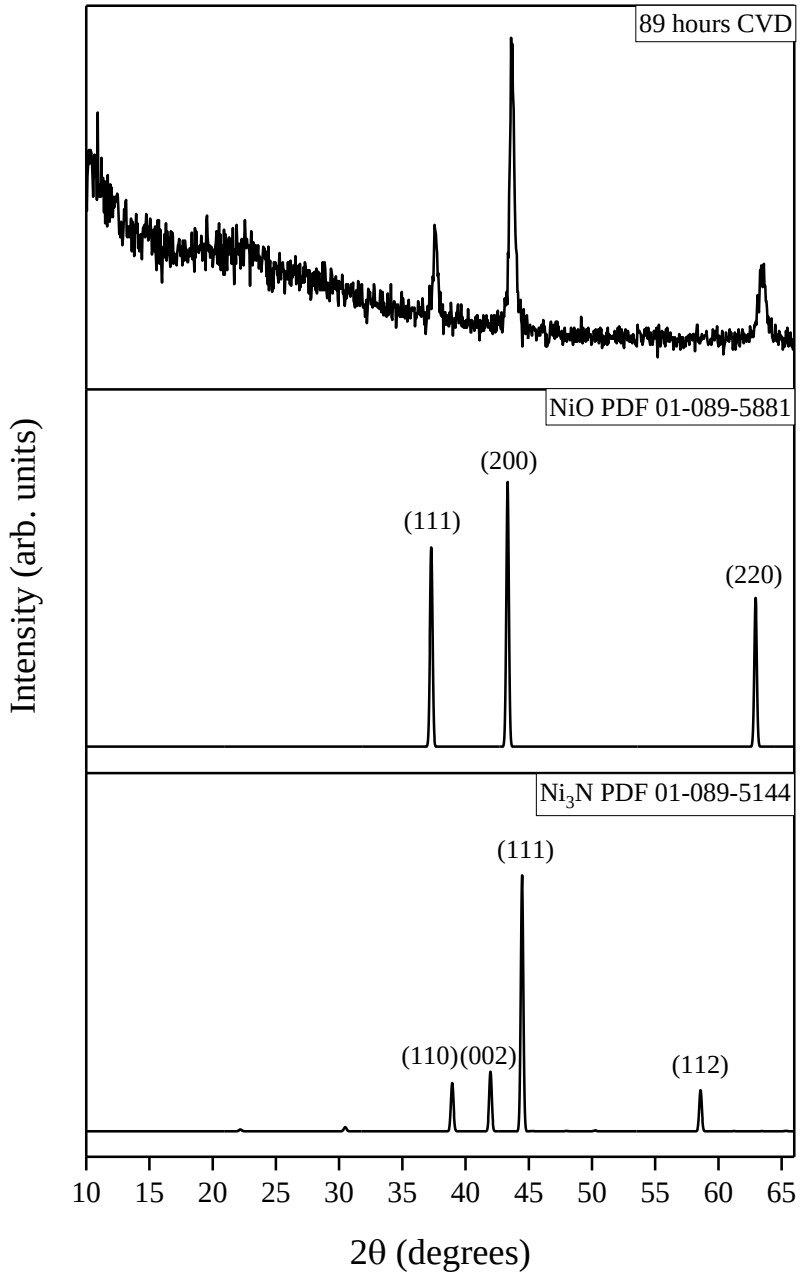

Figure 4.31 XRD patterns for films deposited by CVD of $[Ni\{(N^iPr_2)_2CNEt_2\}_2]$ at 450 °C. Typical NiO and Ni_3N reference patterns included (PDF 01-089-5881 and PDF 01-089-5144 respectively)

Pulsed-CVD of [Ni{(N^iPr_2)$_2$CNEt$_2$}$_2$]

As CVD of [Ni{(N^iPr_2)$_2$CNEt$_2$}$_2$] resulted in the deposition of NiO, pulsed-CVD was carried out to see if the precursor could still be deposited. As described in section 4.3.3.3.2, pulsed-CVD involved dosing [Ni{(N^iPr_2)$_2$CNEt$_2$}$_2$] for 2.5 seconds or 1 minute, followed by a 3 minute gas purge, which was repeated for 300 cycles. The [Ni{(N^iPr_2)$_2$CNEt$_2$}$_2$] bubbler temperature was maintained at 110 °C and the substrate temperature was 450 °C. Under these conditions, deposition was taken closer to those conditions used for ALD in chapter 3 (2.5 second TTIP dose time used) and theoretically, dosing the precursor into the reactor in this way should still result in NiO deposition. Depositions carried out under pulsed-CVD conditions are outlined in Table 4.17.

	Time	**Purge flow (sccm)**	**[Ni{(N^iPr_2)$_2$CNEt$_2$}$_2$] bubbler flow (sccm)**	**Growth temp (°C)**
[Ni{(N^iPr_2)$_2$CNEt$_2$}$_2$] dose	2.5 sec/ 1 min	120	120	450
purge	3 min	120	120	450

Table 4.17 Reaction conditions used to deposit [Ni{(N^iPr_2)$_2$CNEt$_2$}$_2$] in pulsed-CVD mode for 300 cycles at 450 °C

Pulsed-CVD with a 1 minute [Ni{(N^iPr_2)$_2$CNEt$_2$}$_2$] dose time resulted in no NiO film growth. When the dose time was reduced to 2.5 seconds, in order to bring the conditions closer to those used for ALD of TiO_2 (see chapter 3) there was still no NiO film deposited.

The fact that CVD of [Ni{(N^iPr_2)$_2$CNEt$_2$}$_2$] works, but pulsed-CVD did not work suggests that there were issues with the vapour pressure of [Ni{(N^iPr_2)$_2$CNEt$_2$}$_2$]. Vapour in the bubbler often depletes during dosing and recovers during purges, so it is somewhat surprising that pulsed-CVD experiments resulted in no film deposition, but 'normal' CVD did. However, the overall dose times used for CVD and pulsed-CVD experiments were not like-for-like, so it was likely that a significantly less amount of precursor was dosed into the reactor during pulsed-CVD.

It is evident that vapour transport of the precursor was occurring as 'normal' CVD resulted in NiO film deposition. However it may be that during pulsed-CVD mode, the vapour pressure of the precursor was not restored sufficiently during the purges and therefore during the dose steps minimal precursor was exposed into the reactor. Liquid precursors provide constant vapour pressure as the material is depleted,[78] but this may not be the case for solid precursors.

The TGA of $[Ni\{(N^iPr_2)_2CNEt_2\}_2]$ (Figure 4.15) shows that its volatility is slightly lower than that of $[Ni(dmamp)_2]$ (Figure 4.14), which may be why no film deposition occurs during the pulsed-CVD experiments for $[Ni\{(N^iPr_2)_2CNEt_2\}_2]$ but was observed with $[Ni(dmamp)_2]$. In order to overcome this issue, the volatility of $[Ni\{(N^iPr_2)_2CNEt_2\}_2]$ could be increased by raising the temperature of the bubbler, but then this would consequently cause the precursor to thermally decompose.

4.3.3.4.3 Summary

Atomic layer deposition of NiO thin films using $[Ni\{(N^iPr_2)_2CNEt_2\}_2]$ and water as precursors was shown to be unsuccessful. The $[Ni\{(N^iPr_2)_2CNEt_2\}_2]$ bubbler was maintained at a temperature of 110 °C as TGA/DSC showed that the onset of precursor vaporisation occurred at 110 °C, with complete decomposition at ~ 340 °C.

Although the precursor dose/purge times and gas flow rates could be easily manipulated, this had no effect on the deposition outcome. Variation of the growth temperature in the range of 140 - 450 °C also had no effect on the film growth. This was unusual because at high temperatures (> 160 °C), the growth temperature was greater than the decomposition temperature of $[Ni\{(N^iPr_2)_2CNEt_2\}_2]$ so it was expected that the precursor would thermally decompose onto the substrate to form Ni_3N via CVD. The bubbler content was examined before and after the ALD depositions and it was evident that the precursor was being depleted during the depositions. XPS confirmed that NiO had not been deposited on the substrates.

CVD of [Ni{(N^iPr_2)$_2$CNEt_2}$_2$] was conducted to clarify whether the precursor was suitably volatile and could be easily transported into the reactor. The results confirm that NiO was deposited on the substrate at a growth temperature of 450 °C, as determined by XRD. The fact that NiO was the deposited material rather than the expected Ni_3N implied that there could be residual water molecules within the reactor which were readily reacting with the precursor. The long deposition times may be the root cause of this. The fact that CVD depositions at 450 °C worked but ALD depositions at 450 °C did not work, advocates that [Ni{(N^iPr_2)$_2$CNEt_2}$_2$] was insufficiently sensitive with water to react in an ALD scheme under the test conditions and reactor design used.

Pulsed-CVD experiments with various [Ni{(N^iPr_2)$_2$CNEt_2}$_2$] dose times resulted in no film deposition at 450 °C. The fact that CVD experiments worked but pulsed-CVD experiments did not work suggested that there may have been issues with the volatility of [Ni{(N^iPr_2)$_2$CNEt_2}$_2$], as well as with the reactor. Although the use of [Ni{(N^iPr_2)$_2$CNEt_2}$_2$] was not suitable for ALD application in this case, this does not rule out its use as a potential CVD precursor. As a novel precursor, its chemical/physical properties may provide advances over other commonly used precursors for use in different CVD processes, for example LPCVD. If [Ni{(N^iPr_2)$_2$CNEt_2}$_2$] can be used to deposit metal nitride films (which are notoriously difficult to deposit) then this could provide a significant breakthrough to future of metal nitride film deposition. Even if the precursor is not suitable for nitride CVD, it could still be good as a CVD precursor for oxides by deliberately introducing an oxygen co reactant.

4.4 Overall Conclusions

Atomic layer deposition (ALD) of *p*-type NiO thin films has been attempted using four different nickel precursors. Nickel(II) bis(2,2,6,6-tetramethyl-3,5-heptanedionate), [Ni(thd)$_2$]; Bis(cyclopentadienyl)nickel(II), [Ni(Cp)$_2$]; [Ni(dmamp)$_2$], (dmamp = 2-dimethylamino-2-methyl-1-propanolate) and nickel guanidinate, [Ni{(N^{i}Pr$_2$)$_2$CNEt$_2$}$_2$]. [Ni(thd)$_2$], [Ni(dmamp)$_2$] and [Ni{(N^{i}Pr$_2$)$_2$CNEt$_2$}$_2$] were synthesised in reasonable yields, where the structures were characterised using ^{1}H NMR, ^{13}C{^{1}H} NMR, mass spectrometry, elemental analysis, thermogravimetric analysis and X-ray crystallography.

ALD of NiO thin films using [Ni(thd)$_2$] and water as precursors was shown to be unsuccessful. Variation of the precursor vapour pressure, gas flow rates and growth temperature had no effect on the deposition outcome. However, it was discovered that a large excess of water was required in order to achieve complete saturation of the substrate surface due to low reactivity of the adsorbed nickel species towards water. XPS analysis showed predominantly Ni metal on the film surfaces, with small amounts of NiO. The results suggest that [Ni(thd)$_2$] reacted with the hydroxyl groups on the substrate surface, but the surface adsorbed nickel species were inactive towards water. Therefore NiO growth could not be initiated. It has been suggested that ALD of [Ni(thd)$_2$] and water to grow NiO was unsuccessful due issues with the reaction conditions used and the reactor design itself.

ALD of NiO thin films using [Ni(Cp)$_2$] and water as precursors was shown to be unsuccessful. Variation of the precursor vapour pressure and gas flow rates at a growth temperature of 165 °C had no effect on the deposition outcome. Increasing the growth temperature to 300 - 350 °C resulted in the deposition of thin grey films which were characterised using AFM, XRD and XPS. AFM showed that the films had variable surface roughness with film thickness, which made it difficult to determine what the growth mechanism was. XPS confirmed the presence of Ni^{2+} on the substrate surfaces in the form of Ni(OH)$_2$ rather than NiO. This suggested that growth was not occurring under ‘true’ ALD conditions. The surface roughness of the films was relatively high; suggesting that films were porous with no defined structural growth. SEM analysis revealed no further information about the

morphology of the films. Annealing of the films removed all traces of Ni^{2+} on the substrate surface, emphasising that the films were not stable.

ALD of $[Ni(Cp)_2]$ and water to grow NiO was shown to be unsuccessful, even though there are reports in the literature suggesting that NiO can be grown by ALD using this precursor combination (although most reports have utilised O_3, O_2 or H_2 as the co-reactant). It has been suggested that the precursor dose and purge times may not have been optimised in order to form completely saturated layers. The surface-adsorbed Ni species may not have been very reactive towards water under the conditions used and the reactor design used. Additionally, there may have been problems with the precursor delivery into the reactor and also holdups of water in the system. Conduction of CVD experiments would help confirm if this was an issue.

ALD of NiO thin films using $[Ni(dmamp)_2]$ and water as precursors was shown to be unsuccessful. Variation of the precursor dose/purge times, gas flow rates and substrate materials had no effect on the deposition outcome. Small amounts of Ni^0 and Ni^{2+} were detected by XPS on the substrate surfaces after raising the substrate temperature to 450 °C. The oxidised nickel species (NiO or $Ni(OH)_2$) was formed due to precursor decomposition. CVD of $[Ni(dmamp)_2]$ lead to the deposition of NiO, as confirmed by XRD. Pulsed-CVD of $[Ni(dmamp)_2]$ produced NiO films for a 1 minute dose time, but no deposition was observed for a 2.5 second dose time. The results suggest that during a 2.5 second dose time, an insufficient amount of precursor was released in to the reaction chamber to be able to saturate the substrate surface. Although $[Ni(dmamp)_2]$ appears to be a volatile enough precursor for ALD, under the reaction conditions used and reactor design used, the precursor appeared to be insufficiently reactive towards water to be able to produce NiO films via this technique.

ALD of NiO thin films using $[Ni\{(N^iPr_2)_2CNEt_2\}_2]$ and water as precursors was shown to be unsuccessful. Variation of the precursor dose/purge times, gas flow rates and growth temperature had no effect on the deposition outcome. CVD of $[Ni\{(N^iPr_2)_2CNEt_2\}_2]$ lead to the deposition of NiO rather than Ni_3N, as confirmed by XRD. The fact that NiO was the deposited material rather than the expected Ni_3N implied that there could be residual water molecules within the reactor which were readily reacting with the precursor, which was not helped by the long deposition times. Pulsed-CVD of $[Ni\{(N^iPr_2)_2CNEt_2\}_2]$ resulted in no film deposition. As CVD experiments worked but pulsed-CVD experiments did not work suggested that there may have been issues with the volatility of $[Ni\{(N^iPr_2)_2CNEt_2\}_2]$. Although the use of $[Ni\{(N^iPr_2)_2CNEt_2\}_2]$ was not suitable for ALD application in this case, this does not rule out its use as a potential CVD precursor. As a novel precursor, its chemical/physical properties may provide advances over other commonly used precursors for use in different CVD processes. Even if the precursor is not suitable for nitride CVD, it could still be good as a CVD precursor for oxides by deliberately introducing an oxygen co reactant.

As ALD of the novel precursors $[Ni(dmamp)_2]$ and $[Ni\{(N^iPr_2)_2CNEt_2\}_2]$ was unsuccessful, it was decided to further investigate the use of $[Ni(dmamp)_2]$ as a CVD precursor.

Chapter 5

CVD of nickel oxide thin films

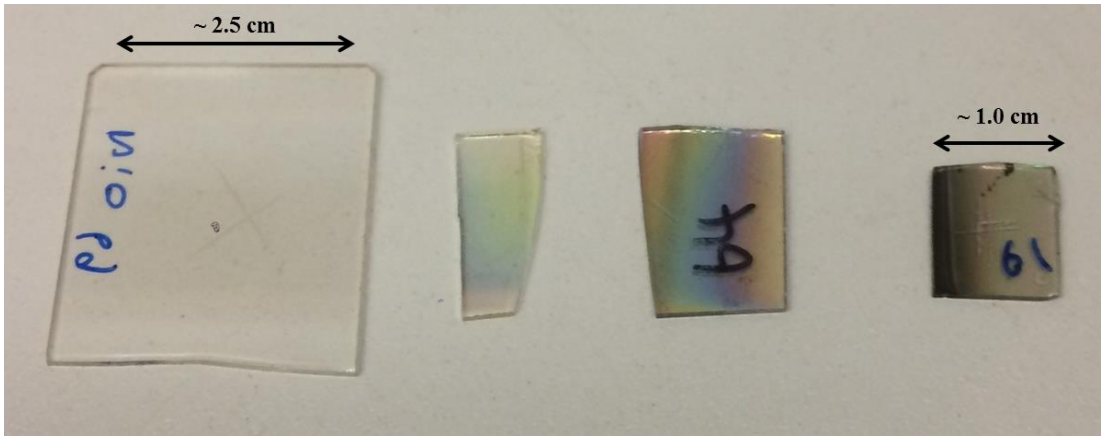

Chapter 5 CVD of nickel oxide thin films

5.1 Introduction

This chapter describes the chemical vapour deposition (CVD) of *p*-type nickel oxide (NiO) thin films. Depositions were performed using the novel precursor [Ni(dmamp)$_2$], (dmamp = 2-dimethylamino-2-methyl-1-propanolate) which was previously used in chapter 4 in attempt to deposit NiO via atomic layer deposition (ALD); the synthesis of which is outlined in chapter 4. The nickel guanidinate precursor [Ni{(N^{i}Pr$_2$)$_2$CNEt$_2$}$_2$] whose synthesis is also described in chapter 4, was not investigated any further for its use as a CVD precursor. Although it was capable of depositing NiO by CVD, this was not the expected material for this precursor (Ni_3N) as it does not contain any source of oxygen. This suggested that [Ni{(N^{i}Pr$_2$)$_2$CNEt$_2$}$_2$] may have been readily reacting with residual water molecules within the reactor, which implied that it was an unsuitable precursor to be utilised in long CVD deposition processes.

The use of [Ni(dmamp)$_2$] to deposit NiO via ALD with water as the co-reactant failed due to issues with both precursor volatility and poor reactivity with water. In chapter 4 it was briefly shown that that this precursor was capable of depositing NiO films via CVD, therefore its application as a potential CVD precursor was investigated further in this chapter. The films were analysed using various techniques to determine film quality and conformality.

5.2 Experimental

CVD experiments were carried out using [Ni(dmamp)$_2$], (dmamp = 2-dimethylamino-2-methyl-1-propanolate). Pureshield argon (99.998%) obtained from BOC, was used as the inert carrier gas. Quartz glass slides (obtained from Wuxi Crystal and Optical Instrument Company Limited) were used as the substrate materials. Prior to deposition, substrates were cut into ~ 4.0 cm x 2.5 cm pieces, cleaned using iso-propanol (Sigma Aldrich, 99.5%) and air dried before loading into the reactor. Whilst the substrate holder was being heated to the required temperature, the reactor was pumped down under vacuum to achieve a base pressure of ~ 4 x 10^{-2} mbar. Gas flows were then turned on, where the running pressure was recorded. As described in chapter 2, [Ni(dmamp)$_2$] was introduced into the reaction chamber by bubbling the carrier gas into the bubbler to assist the transportation of vaporised precursor molecules. To prevent the precursor condensing or reacting in the pipework, the bubbler outlet line was held at a temperature higher than the bubbler temperature but lower than the substrate temperature.

CVD experiments were achieved by simply opening the inlet and outlet valves of the bubbler and continuously dosing [Ni(dmamp)$_2$] into the reactor under a constant gas flow for a certain amount of time. The bubbler temperature was maintained at a temperature lower than the decomposition temperature of the precursor, but the substrate temperature was raised to a temperature higher than the decomposition temperature of the precursor to ensure that the precursor decomposed onto the substrate. Throughout these experiments, the reaction parameters investigated (but not limited to) included; deposition time and growth temperature.

With this method of CVD only one precursor was introduced into the reactor where it decomposes and absorbs onto the substrate surface to form a metal oxide film. This is different to other conventional CVD methods where usually multiple gaseous precursors are introduced into the reactor, which undergo gas phase reactions to form intermediate species.[10] It is these species which then absorb onto the substrate surface to form a metal oxide film.

5.3 Results and Discussion

5.3.1 CVD of [Ni(dmamp)$_2$]

5.3.1.1 [Ni(dmamp)$_2$] precursor for CVD

The novel precursor [Ni(dmamp)$_2$], (dmamp = 2-dimethylamino-2-methyl-1-propanolate) is a brown solid which was synthesised in house as described in chapter 4 (section 4.2.3.2). The TGA/DSC (Figure 4.14 chapter 4) shows that the onset of precursor vaporisation occurred at around 80 °C and previous experiments showed that at this temperature the vapour pressure was high enough to generate sufficient gas transport of the precursor into the reactor. The TGA shows that complete precursor decomposition occurred at ~ 240 °C, which is comparable to the data reported in the literature for similar [Ni(dmamp)$_2$]-type structures. ^{1}H NMR analysis of the precursor after being heated at 80 °C for long periods of time showed no signs of decomposition. Therefore, in order to ensure that the precursor decomposed onto the substrate surface growth temperatures of at least 250 °C were employed.

There are several publications outlining the use of similar [Ni(dmamp)$_2$]-type structures for use in MOCVD[45] (metal organic chemical vapour deposition) and CVD[76] applications to deposit NiO thin films. Although solids at room temperature, nickel dialkylamino alkoxide complexes ([Ni(dmamp)$_2$], [Ni(emamp)$_2$], and [Ni(deamp)$_2$]) are volatile and thermally stable. As described earlier in section 4.3.1.2, the [Ni(dmamp)$_2$] synthesised and utilised in this work was a novel precursor in that the 2 methyl groups on the dmamp ligand were positioned on a different carbon atom to those structures reported in the literature.[70] The slightly increased steric hindrance about the nickel centre thus resulted in a higher decomposition temperature compared to those structures reported in the literature, indicating a more thermally stable complex. Therefore higher growth temperatures may be utilised and its potential use extended across various applications.

5.3.1.2 CVD of [Ni(dmamp)$_2$] at various temperatures

As [Ni(dmamp)$_2$] is a solid at room temperature, it was therefore sublimed at 80 °C within the bubbler in order to generate sufficient gaseous molecules to be dosed into the reactor. In order to determine the optimum growth temperature for the NiO films, CVD experiments were performed for 24 hours and 66 hours at growth temperatures of 250 - 400 °C (Figure 5.1). Note: film thicknesses were measured by ellipsometry.

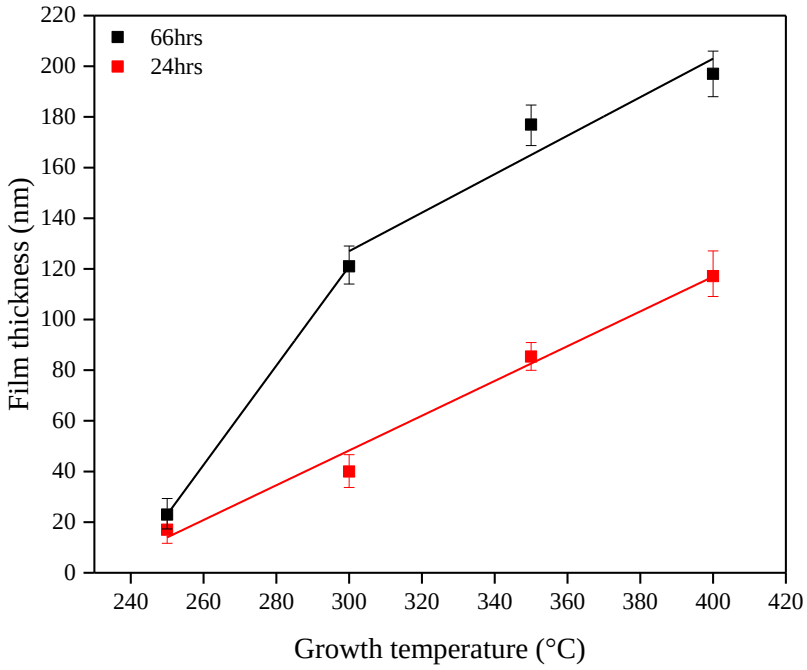

Figure 5.1 Temperature dependence on the film thickness of NiO films deposited by CVD of [Ni(dmamp)$_2$]

Figure 5.1 shows a relatively linear relationship of increasing film thickness with deposition temperature. Under these CVD conditions, the growth rate could be more easily controlled as compared to conventional CVD methods.

The refractive indices (*n*) of the deposited films were obtained by ellipsometry at a wavelength of 632.8 nm using a two phase Tauc-Lorentz dispersion function model with incorporation of a Bruggeman diffusion layer to account for the surface roughness of the films (Table 5.1). The angles of incident used to obtain such values

were 60°, 65°, 70° and 75°; which are close to the Brewster angle for NiO, which is ~76 - 80°.[160,161,162] The most accurate ellipsometry measurements are achieved at a polarising angle (also known as the Brewster angle) for which an unpolarised plane wave is reflected as a linearly-polarised plane wave.[120] At this angle, the ratio of reflection coefficients for *p* and *s* polarised light (*rp, rs*) is maximised and therefore the measurement sensitivity is at its maximum also.[76] The refractive index values for the NiO films are in line with those reported in the literature, which range from 2.3 to 2.9 depending on the deposition temperature.[156,163]

Deposition time (hours)	**Growth temp (°C)**	**Film thickness (nm)**	***n* @ 632.8 nm**
24	250	17	1.5
24	300	40	2.3
24	350	85	2.6
24	400	117	1.8
66	250	23	1.9
66	300	121	2.2
66	350	177	2.7
66	400	197	2.0

Table 5.1 Film thickness and refractive index values of NiO films deposited by CVD of $[Ni(dmamp)_2]$ at various temperatures

For the films deposited for 66 hours, there is a significant increase in the film thickness from 23 nm to 121 nm for films deposited at 250 °C and 300 °C respectively. The decomposition temperature of $[Ni(dmamp)_2]$ is ~ 240 °C, so at a growth temperature of 250 °C it is believed that only partial precursor decomposition occurs. At 300 °C however the growth temperature is substantially higher than the decomposition temperature, so complete precursor decomposition occurs resulting in a much thicker film.

For the films deposited at 250 - 350 °C the refractive index increases with film thickness, which suggests the density and crystallinity of the films increases. However for films deposited at 400 °C the value of *n* decreases. This can be attributed to a decrease in the crystallinity with increasing thickness from 85 nm to 117 nm and 177 to 197 nm for 24 hour and 66 hour deposited films, respectively. Similar behaviour has been reported by Lu *et al.*, where a decrease of 0.2 in the refractive index of NiO films was observed in the photon energy region from 1.2 to 3.3 eV when samples were annealed at temperatures above 500 °C.[156] The decrease in refractive index may be attributed to a change in film homogeneity or composition as the deposition temperature increases.

Films deposited at a growth temperature of 400 °C appeared non-uniform in thickness, with the inlet end of the substrate thicker than the outlet end of the substrate. It is likely that this is because as the precursor enters the reactor and is exposed to such high temperatures, it immediately decomposes and deposits onto the front end of the substrate. For films deposited for 24 hours, reduction of the growth temperature from 400 °C to 300 °C resulted in much more uniform thin films (Figure 5.2).

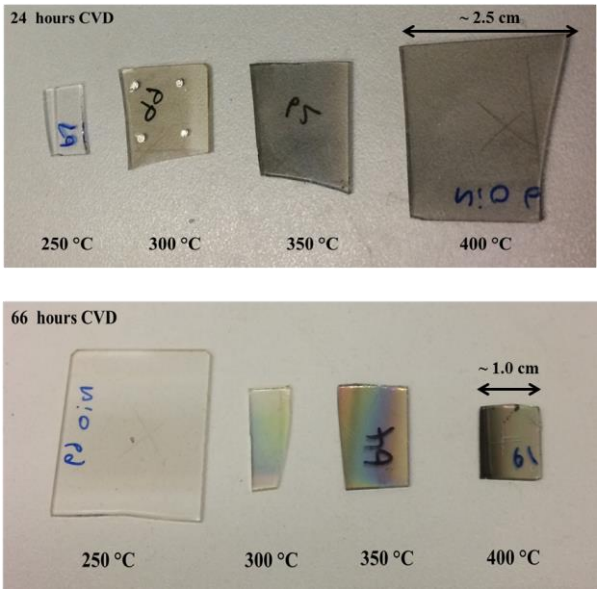

Figure 5.2 NiO films deposited by CVD of [Ni(dmamp)$_2$] at various substrate temperatures for 24 hours and 66 hours

5.3.1.3 Characterisation of films

The surface morphology of the NiO films deposited by CVD was studied using non-contact mode atomic force microscopy (AFM). Films deposited at 250 °C and 300°C showed good thickness uniformity across the substrate, whereas films deposited at 350 °C and 400 °C were less uniform in thickness.

The AFM images in Figure 5.3 show that as the growth temperature increases, the surface roughness of the NiO films also increases. It was observable that initially film growth occurs via small growth sites, which then lead to nucleation and surface chemical reactions leading to NiO film formation.[31] Like with ALD growth, the nucleation sites grow together which then coalesce to form a dense film. Some larger particulates were observed on the film surface as the deposition temperature exceeds 300 °C; however the surface roughness remained reasonably low at 9 nm and 12 nm for the 66 hour films deposited at 350 °C and 400 °C respectively. The presence of larger particulates and the increase in refractive index suggests that the films become more crystalline as the growth temperature and hence film thickness increases. The root mean square (RMS) roughness values measured for these films are shown in Table 5.2.

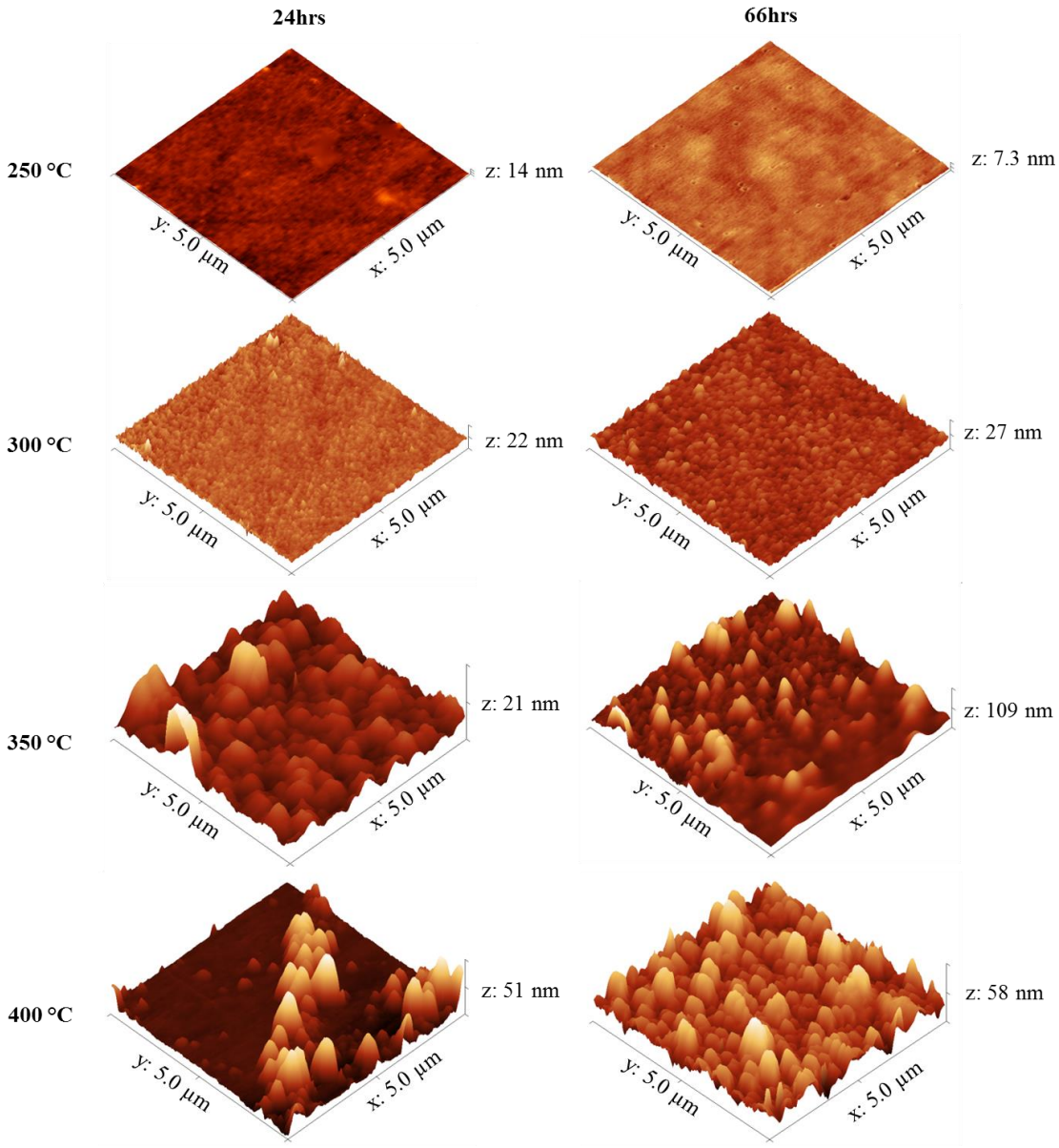

Figure 5.3 AFM images of NiO films deposited by CVD of [Ni(dmamp)$_2$] at different substrate temperatures. Images set to a physical scale factor of 30 in the z axis

Deposition time (hours)	Growth temp (°C)	Film thickness (nm)	RMS (nm)
24	250	17	1
24	300	40	3
24	350	85	5
24	400	117	7
66	250	23	2
66	300	121	8
66	350	177	9
66	400	197	12

Table 5.2 Film thickness and roughness measurements of NiO films deposited by CVD of [Ni(dmamp)$_2$] at various temperatures

Figure 5.4 shows the X-ray diffraction (XRD) measurements for films deposited for 66 hours at different temperatures. The XRD patterns show that films deposited at 250 °C (~ 23 nm) appear amorphous, with the NiO (200) peak only just becoming visible. It is likely that this is because the films are too thin to produce significant diffraction, which is consistent with the appearance of a broad background peak attributed to breakthrough to the glass substrate. For films deposited at 300 °C and above, NiO peaks become visible, with the (200) reflection the most intense (NiO PDF reference number 01-089-5881). As the growth temperature increases the intensity of the NiO peaks increases, with the relative peak intensity ratio between the (111), (200) and (220) reflections becoming smaller. This suggests a preferred orientation of growth along the (200) plane. The relative ratio of the three main XRD peaks does not correlate with the powder reference pattern because it is likely that the deposited films are not 'pure' NiO and will probably contain some impurities (e.g. carbon) due to the way in which the films were deposited by CVD. These impurities may therefore affect the preferred orientation of growth for the polycrystalline material.

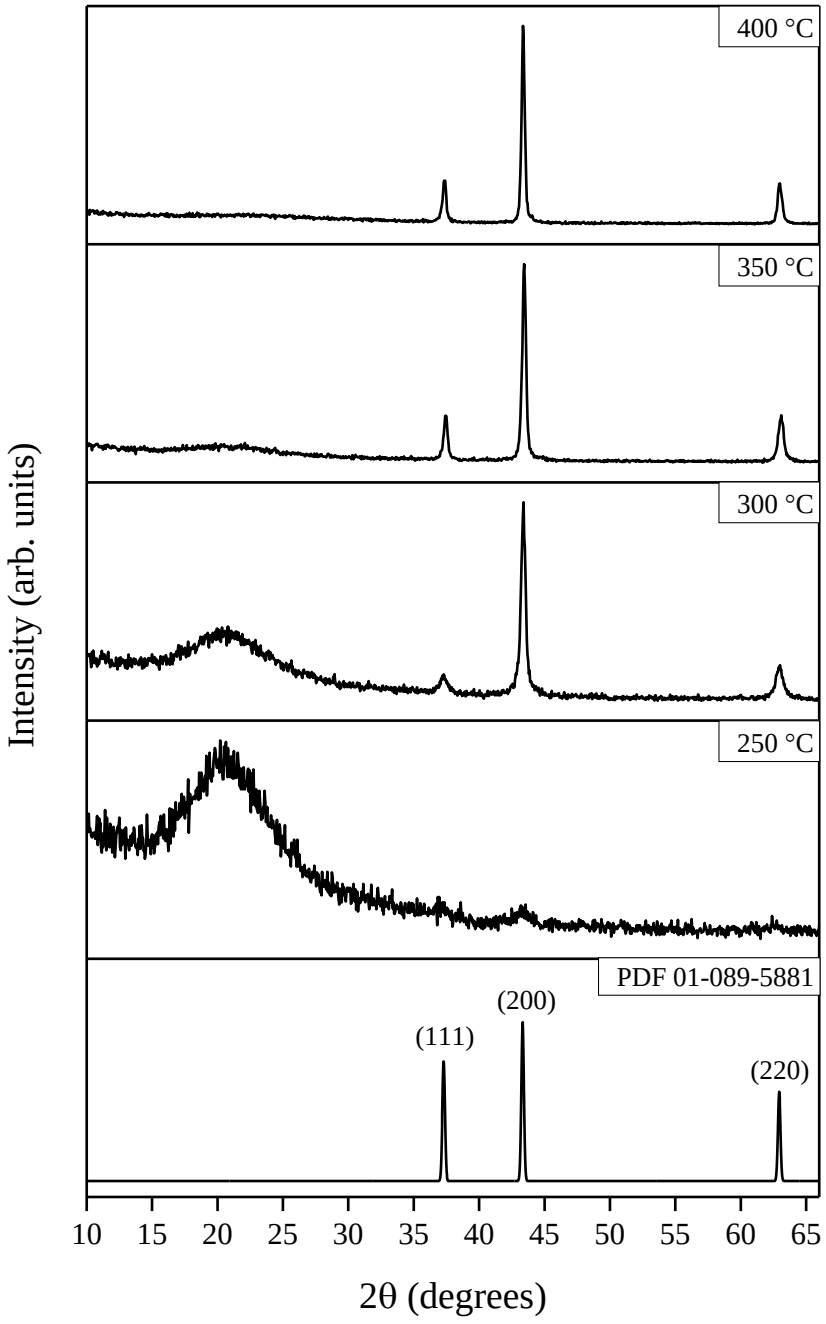

Figure 5.4 Typical XRD patterns for NiO films deposited by CVD of [Ni(dmamp)$_2$] for 66 hours at various temperatures. Typical NiO reference pattern included [PDF 01-089-5881]

Together with the weakness of the diffraction pattern and the AFM images, it can be suggested that films deposited at low growth temperatures (250 °C) consisted of mixtures of amorphous and NiO phases, where the fraction of NiO phase increased with increasing growth temperature. This is consistent with the findings from ellipsometry where the measured refractive indices increased with film thickness.

Utilisation of the Scherrer equation allows an approximate calculation of the mean crystallite size for these NiO films. This was calculated by measuring the broadening of the X-ray reflections from the (200) crystallographic plane. If the crystallite sizes are small, this creates a broadening of the diffraction pattern maxima by an amount which is inversely proportional to the crystallite size.[124] Through measurement of this additional peak broadening, the crystallite size can be approximately measured using equation 3.3 as outlined in chapter 3 (section 3.2.3). Table 5.3 shows the approximate crystallite sizes calculated for NiO films deposited by CVD for 66 hours at different temperatures.

Deposition temp (°C)	Film thickness (nm)	Approximate crystallite size (nm)	Approximate layers of crystallites
250	23	6	4
300	121	22	5
350	177	30	6
400	197	40	5

Table 5.3 Approximate crystallite sizes of NiO films deposited via CVD of [Ni(dmamp)$_2$] for 66 hours at different substrate temperatures

Comparison of the relative values gives an indication of the film crystallinity and structure. Here, it is advocated that films deposited at 250 °C consist of crystallite sizes of approximately 6 nm, which equates to around 4 layers of separated crystallites for a 23 nm thick film. As the growth temperature is increased, the approximate crystallite size increases, but the estimated number of layers of crystallites remains approximately the same. These results support the XRD data in Figure 5.4, which shows that the film crystallinity increases with film thickness.

NiO is notoriously a poor material for Raman scattering, so no NiO peaks were detected using this this technique.

To determine the elemental composition and electronic state of the elements within the NiO films, X-ray photoelectron spectroscopy (XPS) was performed. The data reveals the presence of Ni and O elements on the film surface with minimal contaminants present, as shown by the survey spectrum in Figure 5.5.

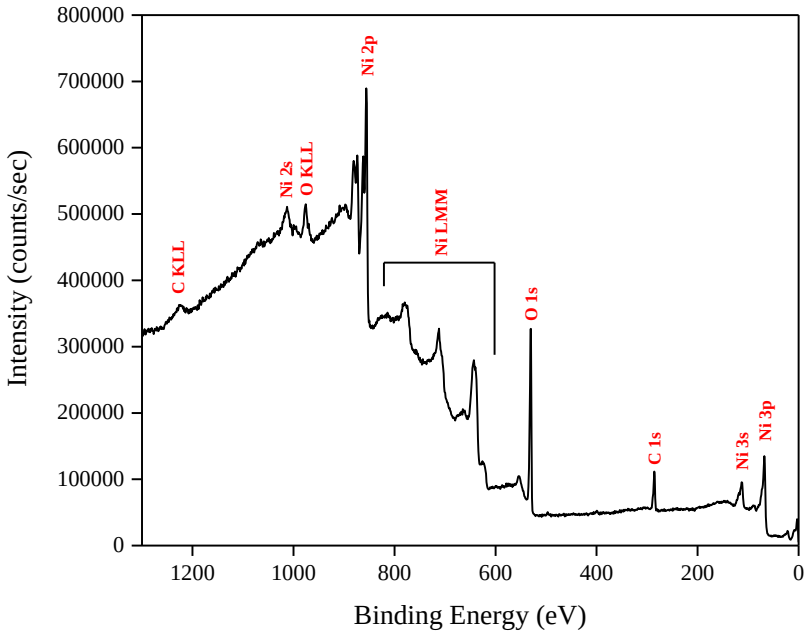

Figure 5.5 Typical XPS survey spectrum of NiO films deposited by CVD of [Ni(dmamp)$_2$] at 300 °C

High resolution surface scans (Figure 5.6a) of the Ni2p peak confirm the presence of Ni^{2+}, with $2p_{3/2}$ and $2p_{1/2}$ peak binding energies of 855.4 eV and 873.2 eV respectively, with a peak separation of 17.8 eV. These values are within ± 0.2 eV of literature values.[45,138] Characteristic satellite peaks for the $2p_{3/2}$ and $2p_{1/2}$ peaks were observed at 861.8 ± 0.2 eV and 880.2 ± 0.2 eV respectively. The prominent satellite shoulder 1.8 eV above the Ni$2p_{3/2}$ principal peak is unique to NiO.[154]

De-convolution of the O1s peak reveals 2 peaks. The two peaks at higher binding energy, 532.8 ± 0.2 eV and 531.4 ± 0.2 eV can be attributed to surface bound carbon and surface adsorbed water, respectively. The peak with the lowest binding energy (529.6 ± 0.2 eV) is attributed to the O1s core peak of O^{2-} bound to Ni^{2+} (Figure 5.6b). Again, these peaks are consistent with literature values for these peak environments.

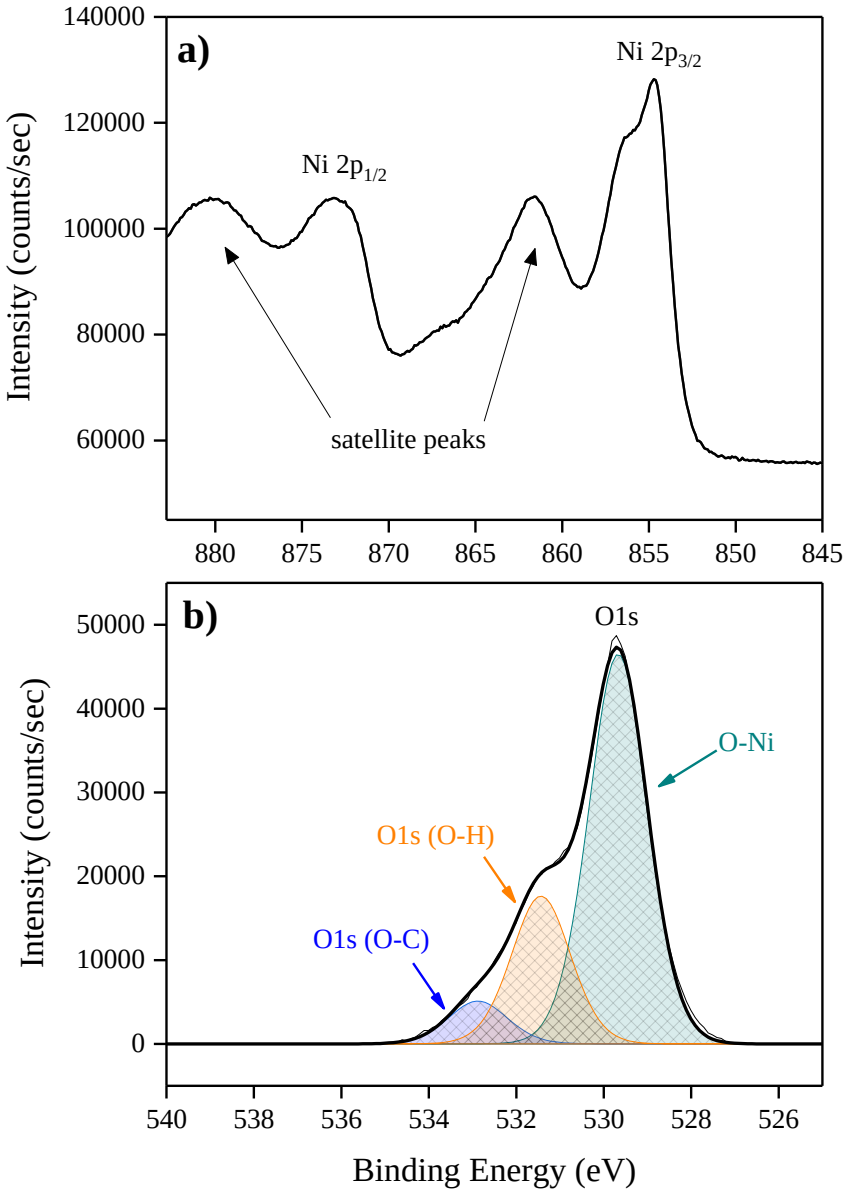

Figure 5.6 Typical high resolution surface XPS spectra of a) Ni2p peak and b) de-convoluted O1s peak for NiO films. Peaks fitted with FWHM value of 1.6 eV

As the area of the Ni2p and O1s peaks in the XPS spectrum are proportional to the amount of element present, the Ni:O elemental ratio was calculated using equation 3.4 (chapter 3). The relative sensitivity factors used were 0.66 for the O1s peak and 4.5 for the Ni2p peak (NIST X-ray photoelectron spectroscopy standard reference database). The elemental ratio of Ni:O was ~ 1:1.5 indicating that the films were oxygen rich, which was not surprising since the films were deposited via thermal decomposition of the precursor.

Figure 5.7 shows a high resolution surface scan of the $Ni2p_{3/2}$ peak. The principal core peak of Ni^{2+} (red peak) was observed at a binding energy of 855.4 ± 0.2 eV, with satellite peaks 6.1 eV (green peak) and 9.0 eV (purple peak) above the principal peak, which can be attributed to multi-electron excitation.[154] The prominent satellite shoulder 1.8 eV above the $Ni2p_{3/2}$ principal peak (blue peak) is unique to NiO. It has the same shape and FWHM (3.2 eV) as the principal peak.

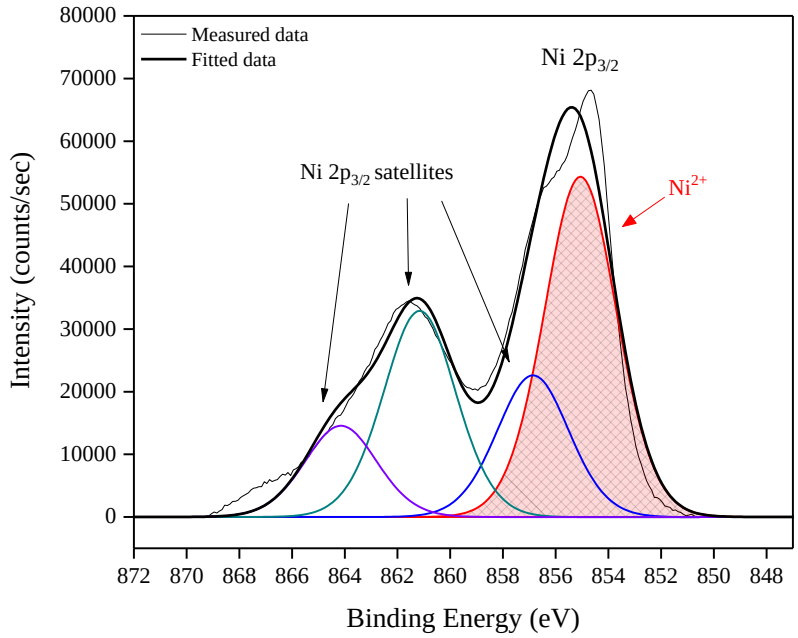

Figure 5.7 High resolution surface scan of $Ni2p_{3/2}$ peak with 3 observable satellite intensities fit by broad peaks (FWHM 3.2 eV) with binding energies at 1.8, 6.1 and 9.0 eV above the principal peak at 855.4 eV

An argon ion etching gun was used to penetrate into the film (100 second etch time), allowing depth profile analysis. Upon etching, it was observed that the Ni^{2+} species was reduced to Ni^{0} metal, which is not uncommon during the etching process (Figure 5.8). The Ni^{0} peak binding energy was 852.5 ± 0.2 eV which was consistent with values reported in the literature for nickel metal.[154] The Ni^{2+} and Ni^{0} peaks were both fitted using a FWHM of 2.0 eV. The prominent satellite shoulder above the $Ni2p_{3/2}$ principal peak was observed at 1.9 ± 0.2 eV – a slight shift in binding energy as compared to the surface scan.

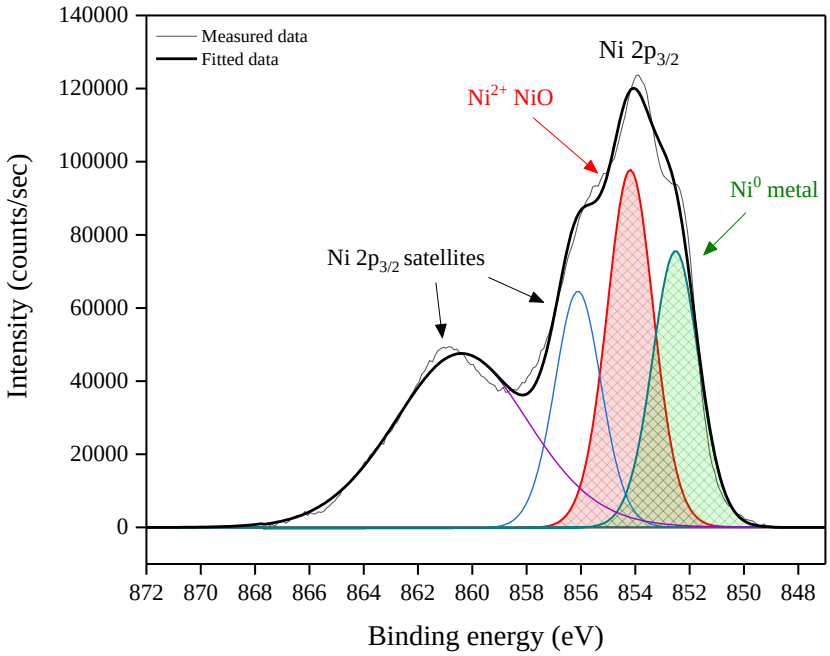

Figure 5.8 High resolution scan of the $Ni2p_{3/2}$ peak for NiO films sputtered for 100 seconds. Ni^{2+} and Ni^{0} peaks were fitted (FWHM 2.0 eV) with binding energies of 854.2 and 852.5 ± 0.2 eV respectively

5.3.2 CVD of [Ni(dmamp)$_2$] at 300 °C

As the films deposited at a growth temperature of 300 °C appeared most uniform in film thickness, the relationship between deposition time and NiO film thickness was investigated. Although it was not expected to achieve a similar linear relationship between deposition time and film thickness as obtained for the TiO_2 films (chapter 3), the relationship here for the CVD films was encouraging (Figure 5.9). The results suggest that under these CVD growth conditions, the film thickness can be controlled relatively easily. Note: film thicknesses measured by ellipsometry.

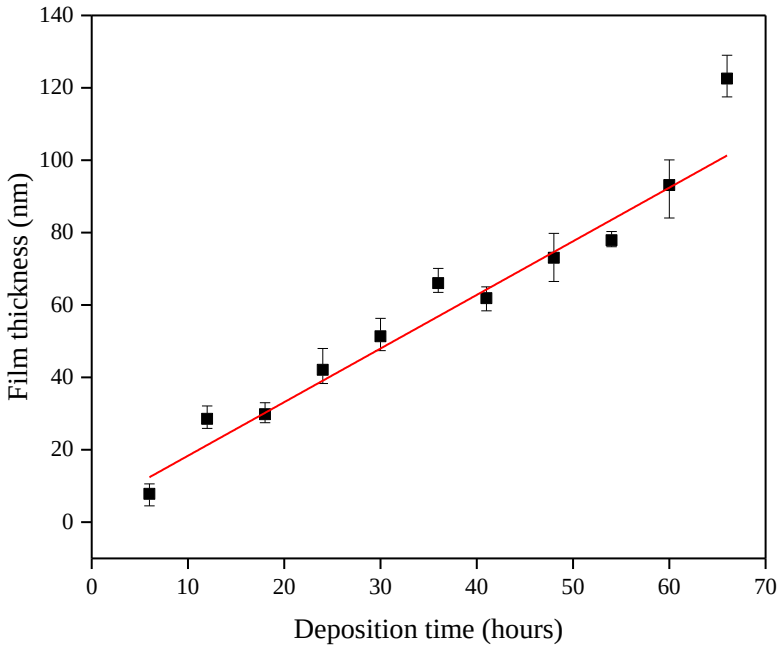

Figure 5.9 Relationship between deposition time and film thickness for NiO films deposited by CVD of [Ni(dmamp)$_2$] at a growth temperature of 300 °C

Figure 5.10 shows that as the CVD deposition time was reduced to below 12 hours, the relationship between deposition time and film thickness was a little more varied.

Due to the short deposition times, the amount of precursor deposited onto the substrate could have been variable which meant that some areas of the substrate may have been less dense than other areas. Additionally, this may just as likely be due to intrinsic error in the measurements.

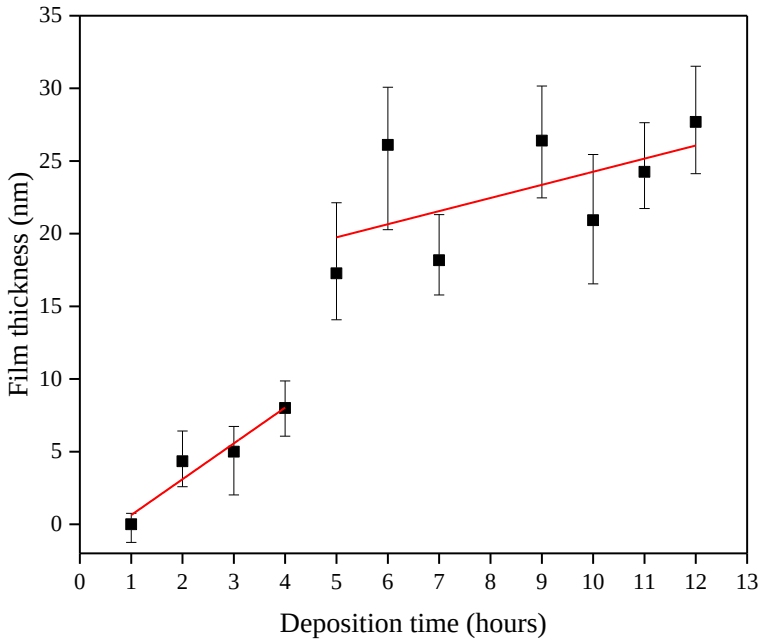

Figure 5.10 Relationship between deposition time and film thickness for ultra-thin NiO films deposited by CVD of [Ni(dmamp)$_2$] at a growth temperature of 300 °C

5.3.2.1 Characterisation of films

The surface morphology of the NiO films deposited by CVD was studied using non-contact mode atomic force microscopy (AFM). The AFM images in Figure 5.11 show that as the deposition time (and hence film thickness) increases, the surface roughness of the NiO films also increases. Likewise for the films described earlier in section 5.3.1.3, it was observed that film growth occurred via small growth sites, which then lead to nucleation and surface chemical reactions leading to NiO film formation. The nucleation sites grow together which then coalesce to form a dense film. Some larger particulates were observed on the film surface as the film thickness approached 73 nm (48 hours deposition). This resulted in a sharp increase in the

surface roughness of the films; from 9 nm to 22 nm RMS (root mean square) roughness for films deposited for 30 hours and 66 hours respectively. The presence of larger particulates suggests that the films become more crystalline with increasing film thickness. The root mean square (RMS) roughness values measured for these films are shown in Table 5.4.

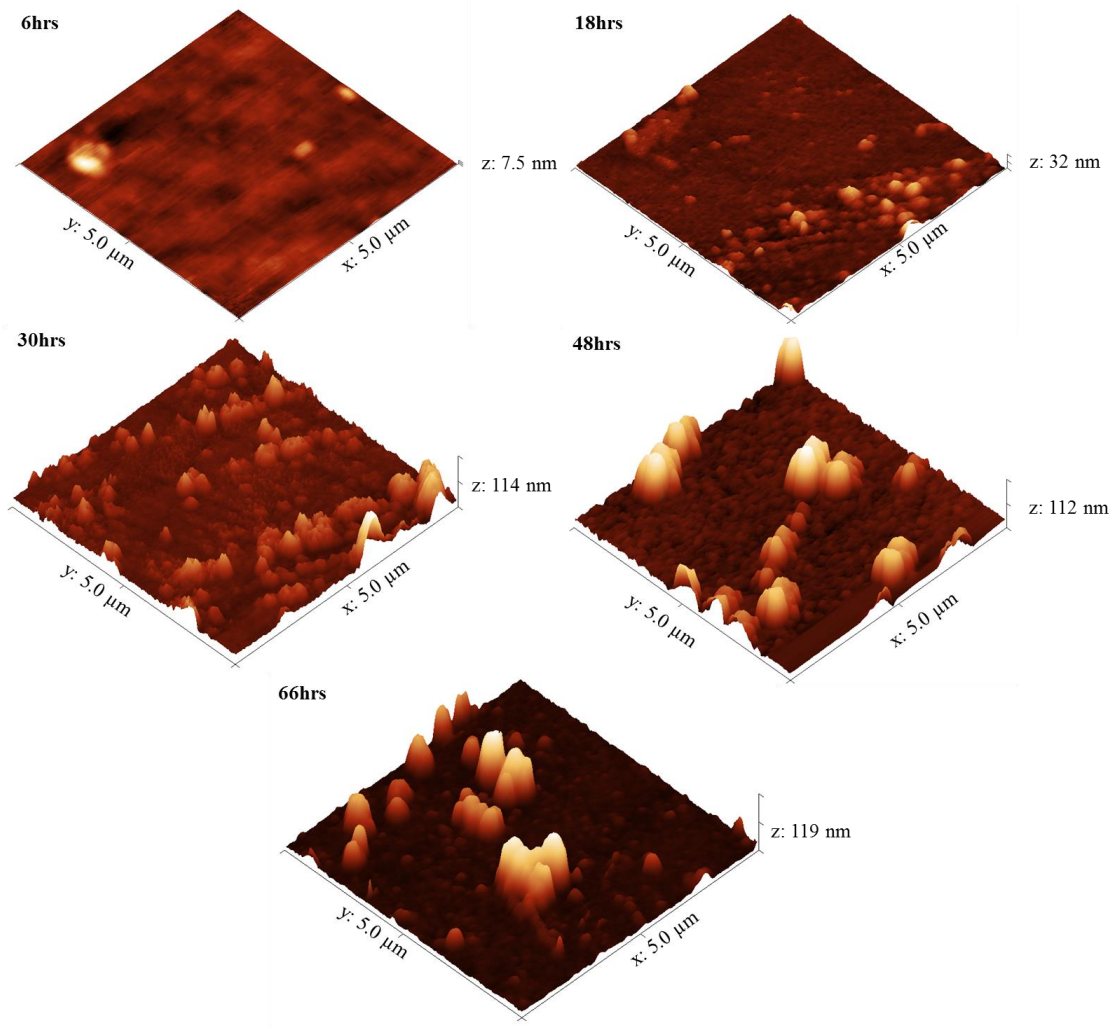

Figure 5.11 AFM images of NiO films deposited by CVD of [Ni(dmamp)$_2$] at 300 °C for various times. Images set to a physical scale factor of 10 in the z axis

Deposition time (hours)	Film thickness (nm)	RMS (nm)
6	5	1
18	29	2
30	50	9
48	73	15
66	121	22

Table 5.4 Film thickness and roughness measurements of NiO films deposited by CVD of $[Ni(dmamp)_2]$ at 300 °C for various times

Figure 5.12 shows the X-ray diffraction (XRD) measurements for films deposited at 300 °C for various lengths of time. The XRD patterns show that a 6 hour CVD film (~ 5 nm) appears amorphous. It is likely that this is because the films are too thin to produce significant diffraction, which is consistent with the appearance of a broad background peak attributed to breakthrough to the glass substrate. For films deposited by CVD for 18 hours of longer (> 29 nm), NiO peaks become visible, with the (200) reflection the most intense (NiO PDF reference number 01-089-5881). As the film thickness increases (i.e. longer deposition time) the intensity of the NiO peaks increases, with the relative peak intensity ratio between the (111), (200) and (220) reflections becoming smaller. This suggests that the film crystallinity increases with film thickness.

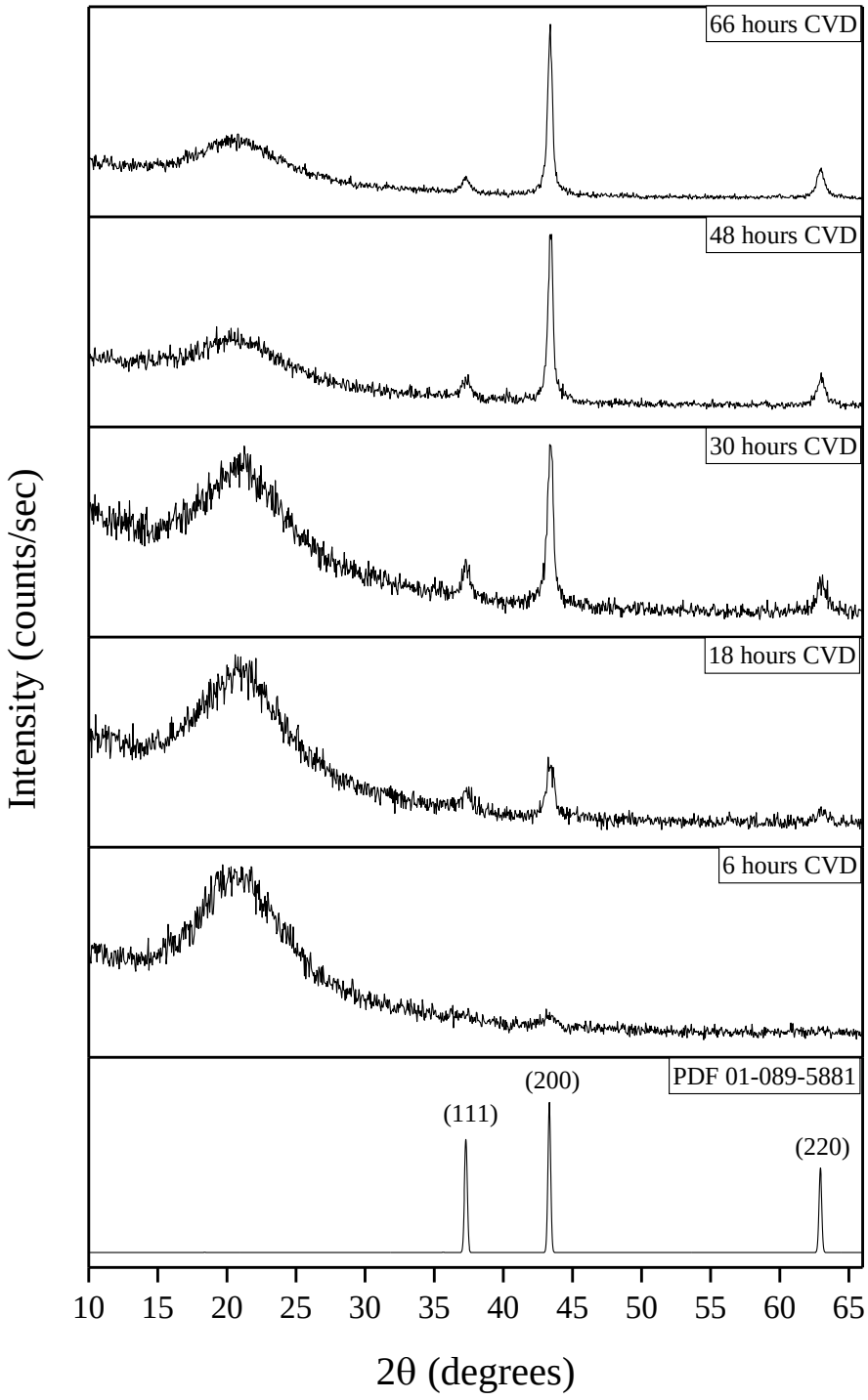

Figure 5.12 Typical XRD patterns for NiO films deposited by CVD of [Ni(dmamp)$_2$] at 300 °C for various times. NiO reference pattern included [PDF 01-089-5881]

Scherrer equation calculations of the approximate crystallite sizes of the NiO films and thus the approximate number of layers of crystallites are outlined in Table 5.5. Comparison of the relative values gives an indication of the film crystallinity and structure. Here, is it proposed that a 6 hour CVD NiO film (~ 5 nm thick) consists of approximately 7 nm crystallites, which suggests that the film is composed of a single layer of separated crystallites, as the crystallite size is similar to the measured film thickness. As the deposition time and hence film thickness increases, the approximate crystallite size also increases. The calculations suggest that the approximate number of crystallite layers increases too, which supports the XRD data in Figure 5.12, which shows that the film crystallinity increases with film thickness.

Deposition time (hours)	Film thickness (nm)	Approximate crystallite size (nm)	Approximate layers of crystallites
6	5	7	1
18	29	13	2
30	50	17	3
48	73	21	3
66	121	22	6

Table 5.5 Approximate crystallite sizes and number of layers of crystallites for NiO films deposited by CVD of [Ni(dmamp)$_2$] at 300 °C at different thicknesses'

NiO is notoriously a poor material for Raman scattering. However a NiO peak was observed for films deposited at ~ 200 nm and above. Figure 5.13 shows a dominant NiO peak at 500 cm^{-1}. Other characteristic peaks for NiO[164] which are normally observed at ~ 825 cm^{-1} and ~ 1100 cm^{-1} were not detected in these films. For films deposited at thicknesses below 200 nm, the Raman spectra were very close to that of the bare substrate, so no NiO peaks were detected.

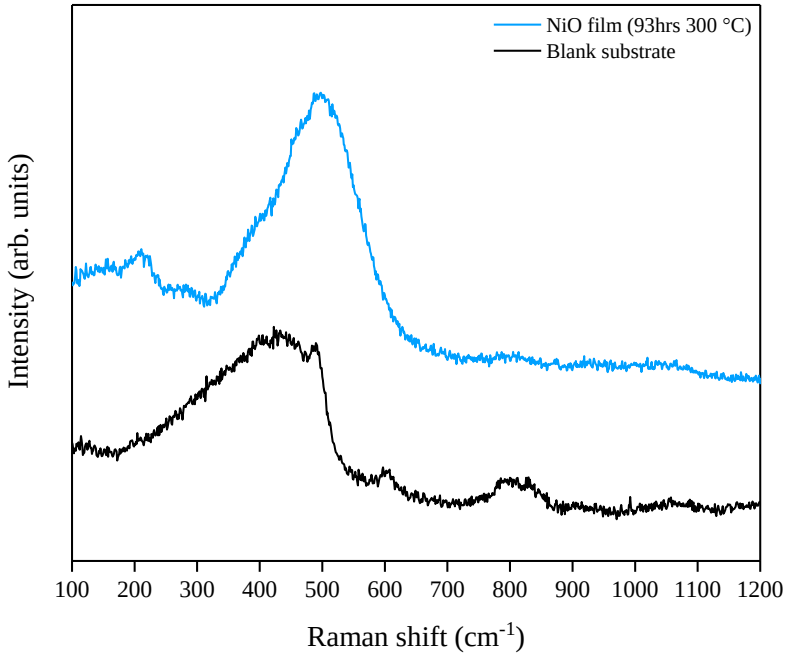

Figure 5.13 Typical Raman spectrum of NiO films deposited by CVD of [Ni(dmamp)$_2$] at thicknesses > 200 nm

XPS analysis of the films deposited at 300 °C with varying deposition times was comparable to the results described earlier in section 5.3.1.3; Ni and O elements were detected on the substrate surface, where high resolution scans of the Ni2p peak confirmed the presence of Ni^{2+} in the form of NiO.

5.4 Overall Conclusions

NiO thin films have been deposited by CVD of [Ni(dmamp)$_2$] at substrate temperatures in the range of 250 - 400 °C, where films with the highest conformality and uniformity tended to be those deposited at 300 °C. NiO films were deposited at 300 °C for between 1 hour and 66 hours, where the film thickness increased relatively linearly with both temperature and deposition time.

AFM and XRD analysis suggest that the film density and crystallinity increased with film thickness, which was supported by an increase in the refractive indices of the films deposited at 250 - 350 °C. However at higher growth temperatures (400 °C) films appeared non-uniform and the refractive index decreased, which suggested that the film crystallinity had decreased due to a possible change in film composition and less uniformity in thickness.

Together with the XRD patterns and the AFM images, it can be suggested that films deposited at low growth temperatures/thicknesses consisted of mixtures of amorphous and NiO phases; where growth occurred via nucleation sites which grow together and coalesce to form a dense film.

XPS analysis confirmed the presence of Ni^{2+} on the film surfaces with $2p_{3/2}$ and $2p_{1/2}$ peak binding energies consistent with those reported in the literature. A prominent satellite shoulder 1.8 eV above the principal $2p_{3/2}$ peak was observed which is unique to NiO.

The reactor design meant that the nickel precursor could be introduced into the reactor slowly and in a more controlled manner; meaning that films could be deposited with a higher control over the film thickness as compared to other conventional CVD methods. The results presented in this chapter demonstrate that the novel precursor [Ni(dmamp)$_2$] is a suitable precursor for use in CVD applications and provides a higher volatility over [Ni(Cp)$_2$], which is commonly used as a precursor for the deposition of NiO films. The slight increase in steric hindrance about the nickel centre increases its decomposition temperature which widens its use across a larger range of deposition temperatures.

Chapter 6
Gas Sensor Testing

Chapter 6 Gas Sensor Testing

6.1 Introduction

This chapter describes the gas sensor testing of TiO_2 thin films which were deposited by atomic layer deposition (ALD) onto standard alumina gas sensor substrates. The resistance of the films was then measured at various temperatures in the presence of CO, CH_4, NO_2, NH_3 and SO_2 gases to determine the responsivity of the sensors towards these gases.

As ALD allows atomic level control of the film growth (in the order of nanometers), this allows the fabrication of materials with defined thickness in the order of the Debye length, thus making it an ideal tool for exploring the fundamental gas sensing properties of these materials. The Debye length is a key measurement which defines the enhancement of a gas sensor response with reducing film thickness.[90] It effectively characterises the size of the space-charge region next to the film surface in which the free carrier concentration may be affected by surface adsorbed gas species. The sensitivity of gas sensing materials should be highly dependent on the film thickness, especially when the film thickness is at the order of the Debye length.

The gas sensing properties of TiO_2 have already been widely studied, including TiO_2 films deposited by ALD.[93,94] However there is still little knowledge about the effect of TiO_2 film thickness at the order of the Debye length on the sensing properties. Sysoev *et al.* reported the Debye length for TiO_2 to be ~10 nm at 250 °C.[91] In 2008, Du and George published work on the use of ALD to explore the gas sensing properties of *n*-type SnO_2 films for CO.[90] They determined that optimum gas sensitivity was achieved at a film thickness of 3 nm, which correlated with the Debye length for SnO_2 under the test conditions. Apart from this work there has been little research on the effect of metal oxide film thickness on the gas sensitivity and selectivity.

It is also worth noting that most previous reported studies on ALD of gas sensing materials have used bespoke gas sensor substrates, instead of the more traditional ceramic sensors. As the gas sensor substrate feature design is important for nano-

scaled gas sensing materials, the use of non-standard designs in this work therefore makes it difficult to directly compare these results with published work.

6.2 Experimental

6.2.1 TiO_2 deposition conditions

TiO_2 thin films were deposited by ALD onto standard alumina gas sensor platforms (from The University of Warwick) using titanium tetraisopropoxide [$Ti(O^iPr)_4$] (TTIP), and distilled water at a deposition temperature of 200 °C.

Pureshield argon (99.998%) obtained from BOC, was used as the inert carrier gas. Small pieces of quartz glass (obtained from Wuxi Crystal and Optical Instrument Company Limited) were also placed inside the reactor in order to provide a sample on which to perform standard film characterisation techniques. The alumina gas sensor platforms were used as obtained and the small pieces of quartz glass were cleaned using iso-propanol (Sigma Aldrich, 99.5%) and air dried prior to loading into the reactor. Whilst the substrate holder was being heated to 200 °C, the reactor was pumped down under vacuum to achieve a base pressure of ~ 4 x 10^{-2} mbar. Gas flows were then turned on, where the running pressure was recorded (~ 2.5 mbar). As described in chapter 3, titanium isopropoxide was held at a temperature of 25 °C and was introduced into the reaction chamber by bubbling the carrier gas into the bubbler to assist the transportation of vaporised precursor molecules. Water was held at a temperature of 5 °C and was introduced into the reaction chamber by means of its own vapour pressure, without any bubbling systems.

6.2.2 Gas Sensor Testing

The standard alumina gas sensors (2.5 x 2.5 mm in size, and 0.550 mm thick) were composed of gold detection electrodes and platinum heater tracks (Figure 6.1).

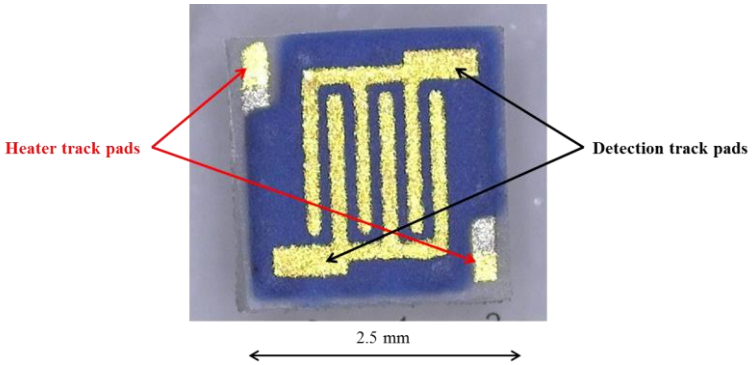

Figure 6.1 Standard alumina gas sensor substrate

The detection electrodes were exposed to air while the heater tracks were embedded within a layer of glassy ceramic insulating material, excluding pads for the subsequent attachment of wires (Figure 6.2).

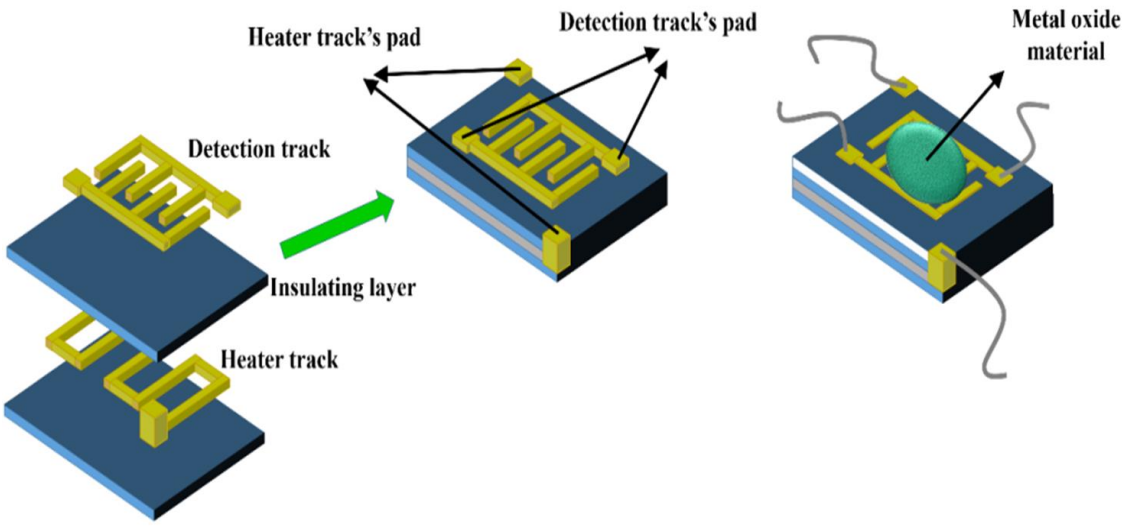

Figure 6.2 Structure of alumina sensor. The shadow masks used for deposition were tungsten foils 100 µm thick with 2000 µm diameter holes

After deposition of TiO_2, the gas sensor substrates were then welded onto a TO-39 housing using platinum wires (Figure 6.3).

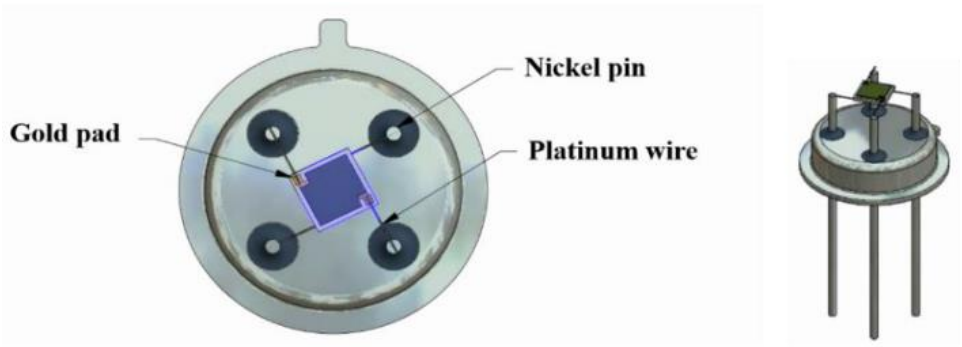

Figure 6.3 TiO_2 gas sensor substrate welded onto a TO-39 housing using platinum wires

The operating temperature during the gas sensor testing was varied between ambient and 480 °C, where the associated power consumption at 480 °C was 1.5 W. In order to maintain a constant operating temperature during the gas sensor testing, the heater calibration of the TiO_2 coated sensor substrates was performed using a digital pyrometer from LumaSense IN 5-L plus.

The entire gas sensor testing on the TiO_2-coated substrates was conducted at the National Institute of Materials Physics in Bucharest, Romania. The experimental gas sensing setup consisted of a fully computer controlled Gas Mixing System (GMS), PTFE sensor chamber designed for TO-39 samples, power supply, Keithley 6517A-Electrometer and Keithley 2000-Multimeter (Figure 6.4). The GMS had eleven channels provided with high purity (5.0) certified test gases from cylinders. Each gas port was electronically controlled by a Bronkhorst mass flow controller and two electrovalves. The first two channels were dedicated for carrier gas with controlled relative humidity (RH) in the range of 0 - 80 %. In order to avoid outgassing, the gas channel interconnections were made of PTFE and stainless-steel with Kalrez seals. The required test gas concentrations were acquired by controlling the flow ratio between the carrier gas and the target gas.

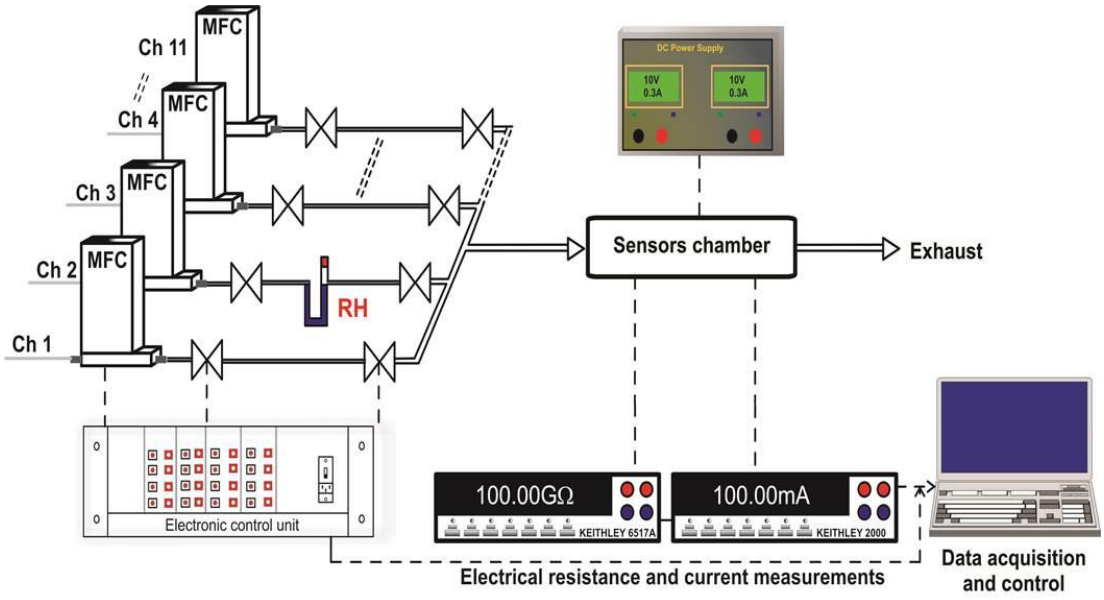

Figure 6.4 Experimental setup used for gas sensing performance evaluation. Real time acquisition of electrical resistance and current data

The concentrations of the target gases used were: CO (50, 70, 100 ppm); CH_4 (500, 1000, 1500, 2000 and 2500 ppm); NO_2 (3, 5, 7 ppm); NH_3 (50, 70, 100, 150, 200 ppm) and SO_2 (5, 10, 20 ppm), dosed in: 0, 10, 30 and 50% RH. The length of each gas pulse was set to 15 minutes while the dedicated recovery time was set to 30 minutes. The flow through the system was kept constant at 200 sccm.

6.3 Results and Discussion

6.3.1 Analysis of TiO_2 films

The reaction conditions used to deposit TiO_2 were the same as those reported in chapter 3 and are outlined in Table 6.1. A growth rate of ~ 0.35 - 0.5 Å/cycle was achieved (as measured by filmetrics), which is comparable to the growth rate achieved using similar TiO_2 systems.[19,117] As described in chapter 3, complete monolayers of TiO_2 (~ 3.92 Å) were not formed during each reaction cycle due to steric hindrance of the bulky $[Ti(O^iPr)_4]$ molecules. Following an induction period, the film thickness increased with the number of reaction cycles in a relatively linear fashion (Figure 6.5).

	Time	Purge flow (sccm)	TTIP bubbler flow (sccm)	Water bubbler flow (sccm)	Growth temp (°C)
TTIP dose	2.5 sec	100	100	0	200
TTIP purge	1 min	100	100	0	200
H_2O dose	2.0 sec	100	100	0	200
H_2O purge	3 min	100	100	0	200

Table 6.1 Conditions used to deposit TiO_2 films via ALD of TTIP and water onto standard alumina gas sensor platforms

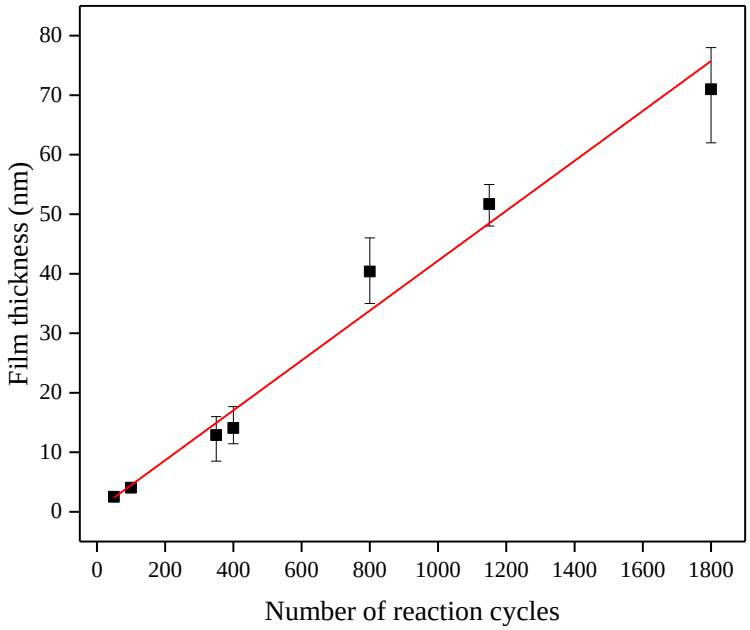

Figure 6.5 Increase in TiO_2 film thickness and growth rate with number of reaction cycles. Thickness measured on small piece of quartz glass placed inside reactor along with alumina gas sensor substrates

Likewise for the TiO_2 films deposited by ALD as described in chapter 3, these films were also characterised using AFM (Figure 6.6) and XRD (Figure 6.7), with similar results. Film characterisation was performed on small pieces of quartz glass which were placed inside the reactor along with the alumina gas sensor substrates during the deposition process.

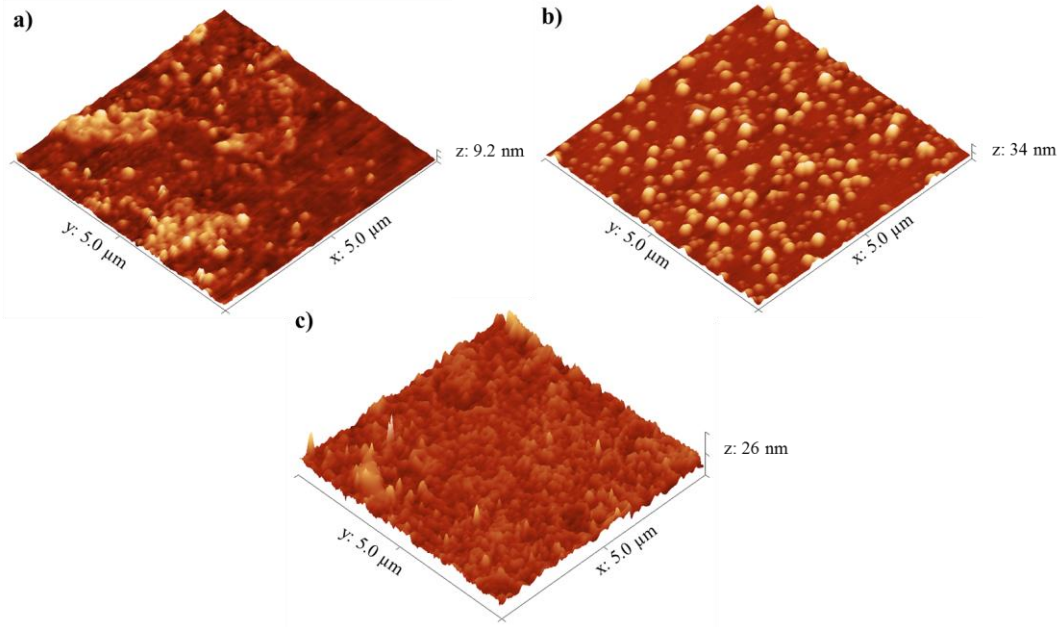

Figure 6.6 AFM images of a) 10 nm, b) 50 nm and c) 70 nm TiO_2 films deposited by ALD of TTIP and water at 200 °C. Images set to a physical scale factor of 30 in the z axis

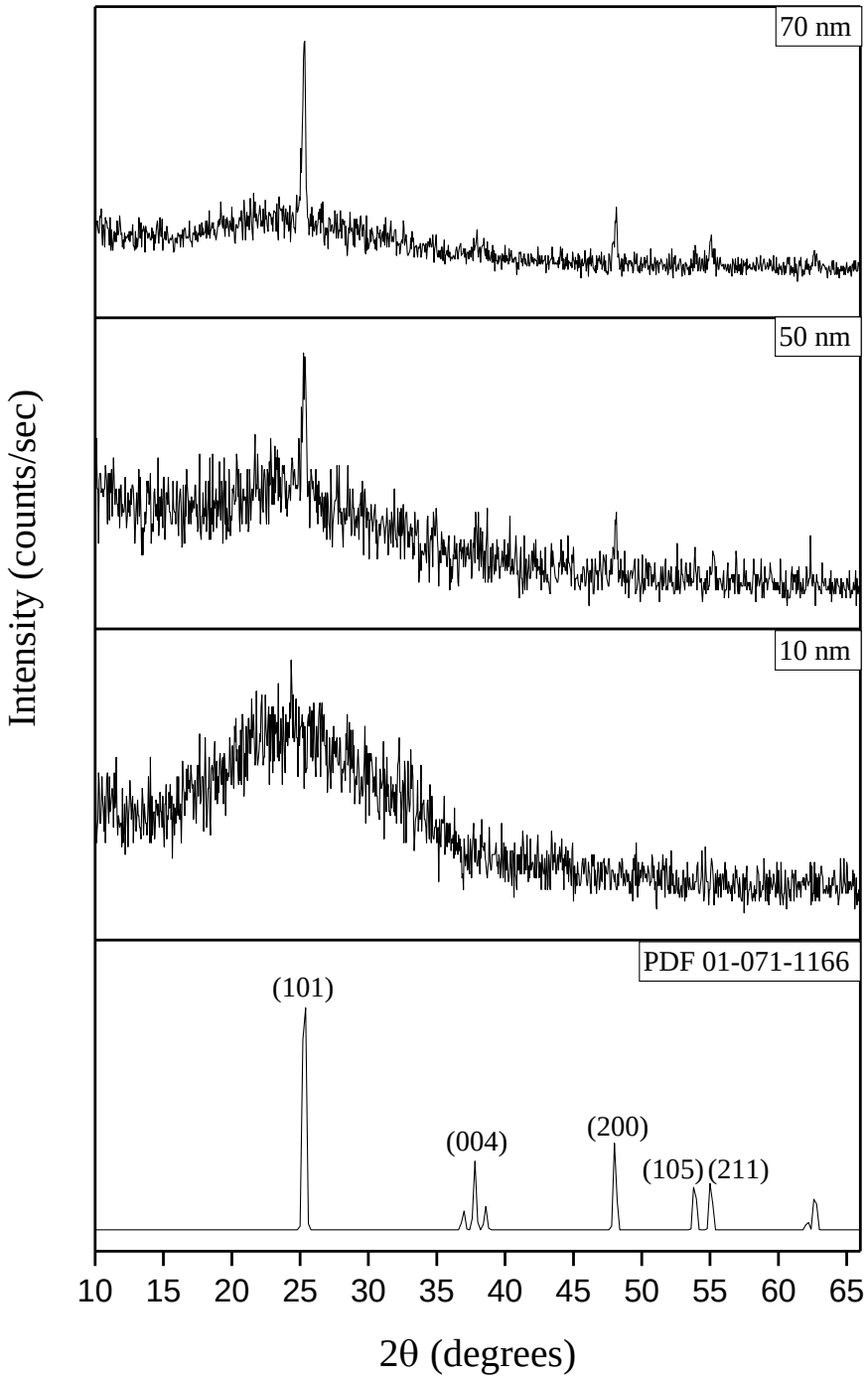

Figure 6.7 Typical XRD patterns for 10nm, 50 nm and 70 nm TiO_2 films deposited by ALD of TTIP and water at 200 °C. Typical anatase reference pattern included

6.3.2 Gas Sensing Results

A selection of the TiO_2-coated gas sensor substrates were exposed to various concentrations of CO, CH_4, NO_2, NH_3 and SO_2 under dry air (0% relative humidity) in order to evaluate their sensitivities. Unfortunately only two samples could be evaluated: the 10 nm and 50 nm TiO_2 films. The wiring contacts on the other films were broken either during transportation of the sensors or during the testing procedure. The electrical resistance and current through each of the films was measured at operating temperatures of 350 °C (Figure 6.8) and 480 °C (Figure 6.9). From Figure 6.8, it is observable that only CH_4 and NH_3 induced measurable changes; either in the electrical resistance (black line) or in the electrical current passing though the heater (blue line). Upon exposure of CO, NO_2 and SO_2 to the sensor substrates, the recorded changes in the electrical resistance were less than 10%, with a sensor signal S ~ 1.1. Therefore only CH_4 and NH_3 gases were chosen for the remainder of the gas sensing investigations since there were no possible cross-sensing effects with the other tested gases.

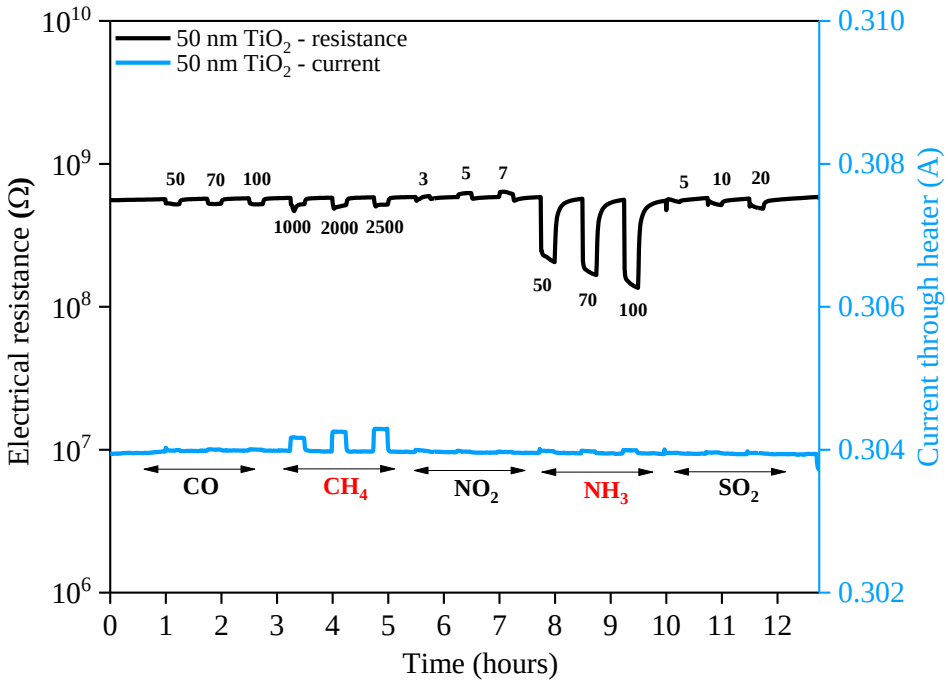

Figure 6.8 Electrical resistance and current response of 50 nm TiO_2-coated gas sensor substrates exposed to different concentrations of CO, CH_4, NO_2, NH_3 and SO_2 under 0% relative humidity at 350°C. Sensors were exposed to 50, 70, 100 ppm CO; 1000, 2000, 2500 ppm CH_4; 3, 5, 7 ppm NO_2; 50, 70, 100 ppm NH_3 and 5, 10, 20 ppm SO_2

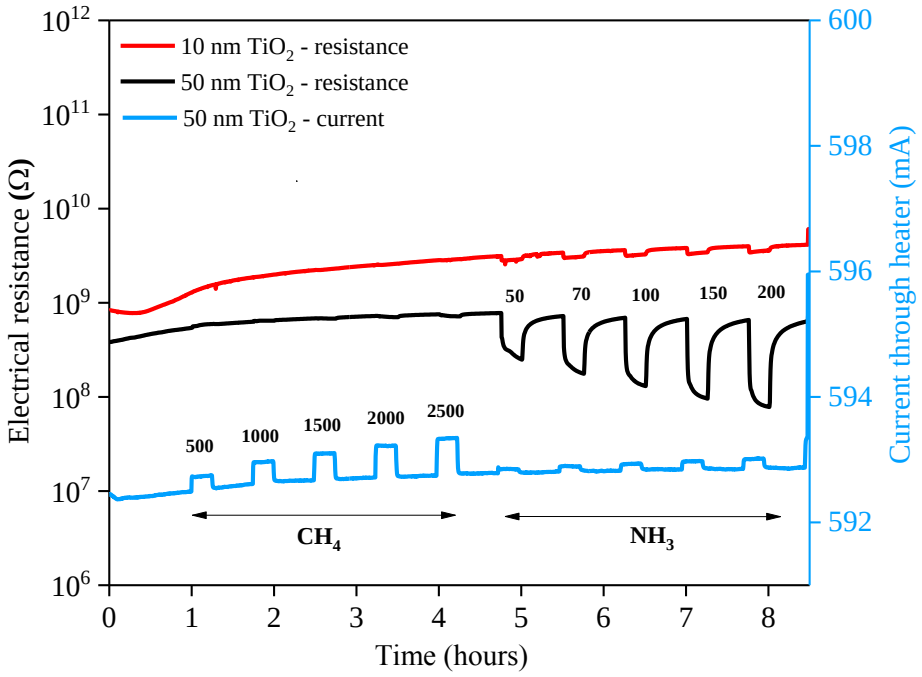

Figure 6.9 Electrical resistance and current response of 10 nm and 50 nm TiO_2-coated gas sensor substrates exposed to different concentrations of CH_4 and NH_3 under 0% relative humidity at 480 °C. Sensors were exposed to 500, 1000, 1500, 2000, 2500 ppm CH_4 and 50, 70, 100, 150 and 200 ppm NH_3

At both operating temperatures a decrease in the electrical resistance was observed in response to NH_3 (in the range of 50 - 200 ppm) for the 50 nm TiO_2 film; where the electrical resistance change was greater with increasing NH_3 gas concentration. NH_3 is a reducing gas. It reacts with the surface O_2 species on the TiO_2 film surface. The loss of surface O_2 species therefore generates O vacancies which subsequently ionise and add electron charge carriers back into the bulk of the film.[90] The increase in electron charge carriers therefore lowers the resistance of the film, which is what was observed. For the 10 nm TiO_2-coated sensor (red line Figure 6.9), no electrical resistance changes were observed in response to CH_4 or NH_3 due to the high baseline resistivity of the film. Very small electrical resistance changes were observed for the film in response to CH_4 (in the range of 500 - 2500 ppm). An explanation of this is described later on.

At higher operating temperatures, the resistance of the films decreased which is a common behaviour for most semiconducting metal oxide materials. The adsorption of gases to the film surface is also enhanced at higher temperatures, which can result in faster responses and recovery times.[165] It has previously been reported that TiO_2 requires high operating temperatures to accomplish in-field gas sensing demands.[166] The pattern of responses of the electrical resistance towards CH_4 and NH_3 indicate typical *n*-type semiconducting like behaviour,[167,168] where the TiO_2 film thickness plays a dominant role within the conduction mechanism. No measurable gas responses were achieved for CH_4 or NH_3 at operating temperatures below 350 °C.

Effect of relative humidity on the gas sensitivity

Figure 6.10 shows the effect of increasing the relative humidity (RH) from 0% to 50% on the gas response. At higher humidity, the baseline resistance of the TiO_2 films is slightly higher. It was observed that for the 50 nm TiO_2 film, the sensor resistance and response to CH_4 and NH_3 gases was reduced at higher humidity. It is assumed that water molecules dissociate on the TiO_2 surface to produce hydroxyl species which are capable of acting as electron donors. This therefore decreases the density of the chemisorbed atomic oxygen species.[169] Again, no electrical response was measured for the 10 nm TiO_2 film due to its high resistance.

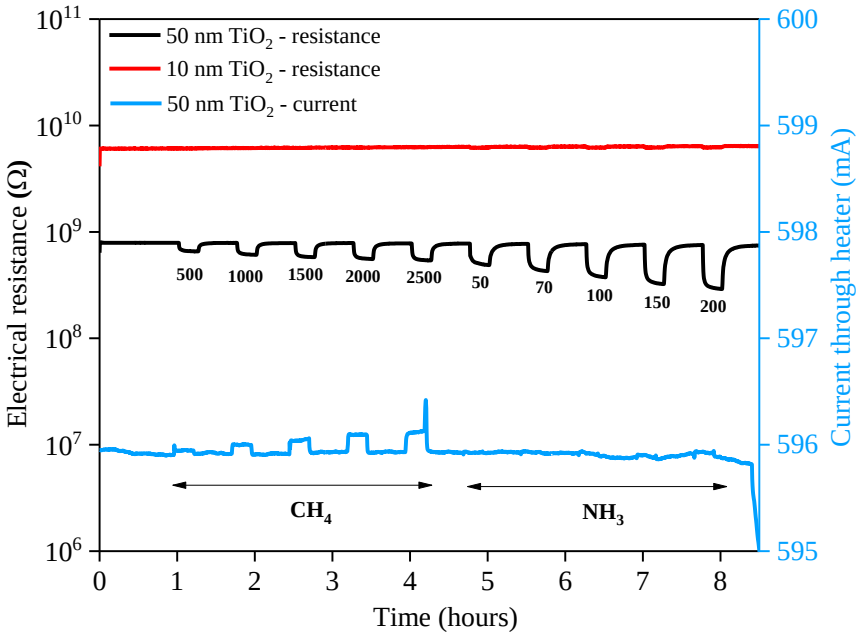

Figure 6.10 Electrical resistance and current response of 10 nm and 50 nm TiO_2-coated gas sensor substrates exposed to different concentrations of CH_4 and NH_3 under 50% relative humidity at 480 °C. Sensors were exposed to 500, 1000, 1500, 2000, 2500 ppm CH_4 and 50, 70, 100, 150, 200 ppm NH_3

The effect of relative humidity on the gas sensor signal has also been demonstrated. Figure 6.11 shows the relationship between the NH_3 concentration on the sensor signal at various relative humidity's for the 50 nm TiO_2 film at an operating temperature of 480 °C. The sensor signal was calculated using equation 6.1, were R_{air} is the baseline resistance and R_{NH3} is the resistance measured when the films were exposed to NH_3 gas.

$$S = \frac{Rair}{RNH3} \qquad (6.1)$$

The sensor signal dependence on NH_3 concentration (in the range of 50 - 200 ppm) at 0% relative humidity (black line) closely resembles that previously reported in the literature.[170] The results show that as the NH_3 concentration increases, the sensor signal increases linearly, which is as expected. However, as the relative humidity increases in the range of 0 - 50%, the NH_3 sensitivity and hence the sensor signal decreases. As mentioned earlier, it is thought that this may be related to competition

between NH_3 and OH^- species for the same pre-adsorbed oxygen species on the TiO_2 film surface.[171]

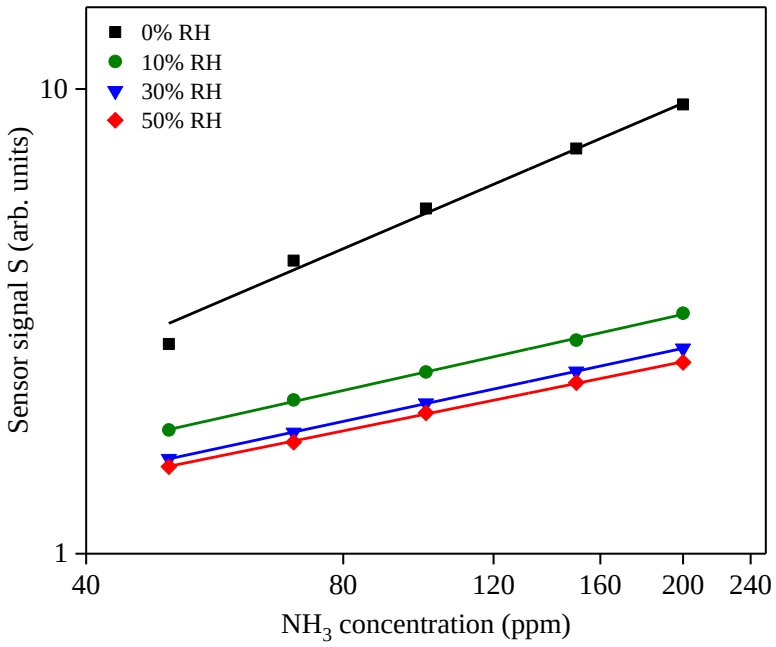

Figure 6.11 Logarithmic plot of sensor signal dependence of 50 nm TiO_2-coated sensor with respect to the NH_3 concentration at various relative humidity's at an operating temperature of 480 °C

Literature reports suggest that gas sensors based on metal oxide semiconducting materials exhibit a decrease in electrical resistance in the presence of CH_4. Kohl[172] has reported that there are two reaction pathways which might be possible in order to explain the CH_4 gas surface interaction. The first involves the reaction with the surface ionosorbed oxygen, whereas the second one takes into account the interaction with the lattice oxygen.

However as shown in Figure 6.8 and Figure 6.9, minimal electrical resistance changes (ΔR) were observed for the 50 nm film in response to CH_4 (in the range of 500 - 2500 ppm). Yet a change in the current through the heater ($\Delta I = I_{CH4} - I_{air}$) was detected with respect to CH_4 concentration, which varied from dozens to hundreds of microamperes.

The increase in the electrical current passing through the heater during CH_4 exposure can be translated into a decrease in the electrical resistance. These results are in good agreement with Heilig *et al*.[173]

When the sensors were exposed to CH_4 gas, the changes in electrical resistance were less than 10%, with a slightly decreasing behaviour. These weak interactions may be explained by the low reaction ability of the TiO_2 sensors when operated at 350 °C due to the high structure symmetry and high decomposing properties of CH_4 hydrocarbon gas. Reports by Sun *et al*[174] and Khol[172] suggest that the reducing role (that is the ability to reduce the coverage with the surface ionosorbed oxygen species) of CH_4 can be expressed by the following gas-surface interaction pathway (equation 6.2):

$$CH_4 + 4O^- \rightarrow CO_2 + 2H_2O + 4e^- \qquad (6.2)$$

By simultaneously measuring the electrical resistance and current passing through the heater, it can be proposed that the majority of CH_4 decomposes onto the heating element leading to the formation of CH^{3+} and CH^{2+} species.[174]

Since the combustion process requires a certain amount of energy, this directly translates into a temperature variation of the gas sensor substrate.[173] Consequently, as energy is consumed in the combustion process the overall temperature of the sensor decreases upon CH_4 exposure, which leads to a subsequent increase in power consumption and hence an increase in the current. Therefore through measurement of the electrical resistance and current changes through the heater, it is possible to highlight the selective-sensitivity of the TiO_2 gas sensors to CH_4 and NH_3 test gases.

Figure 6.12 shows the effect of relative humidity on the electrical current changes (ΔI) for the 50 nm TiO_2-coated sensor with respect to the CH_4 concentration.

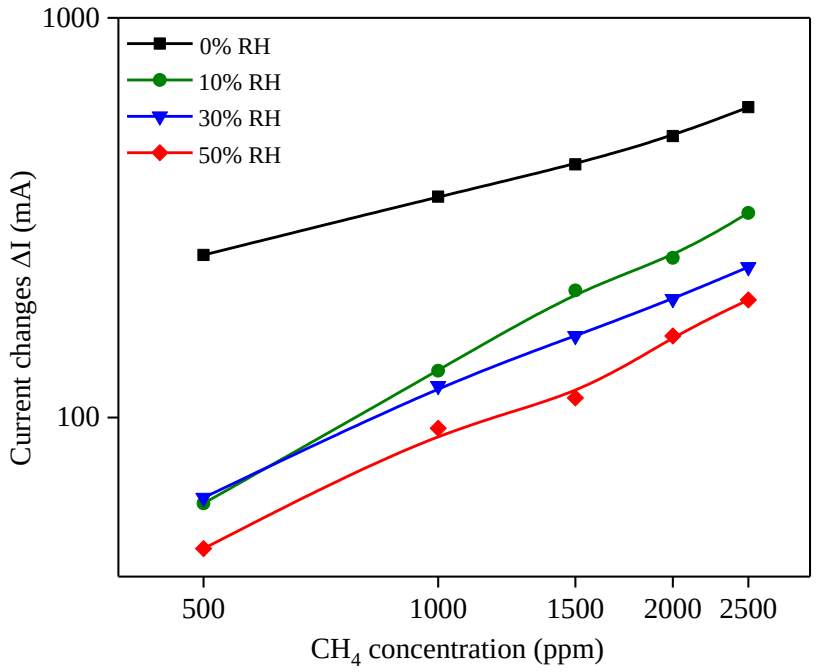

Figure 6.12 Logarithmic plot of the electrical current changes (ΔI) of the 50 nm TiO_2-coated sensor with respect to the CH_4 concentration at various relative humidity's at an operating temperature of 480°C

Evidently, the TiO_2 film thickness plays an important role within the conduction mechanism. Charge carrier concentrations were not able to be experimentally measured due to the high resistance of the films. Charge carrier concentrations for TiO_2 reported in the literature are in the range of 10^{22} to 10^{26} m^{-3}.[175] Figure 6.13 correlates an estimation of the variation of the Debye length as a function of the charge carrier concentration (using the reported literature values).

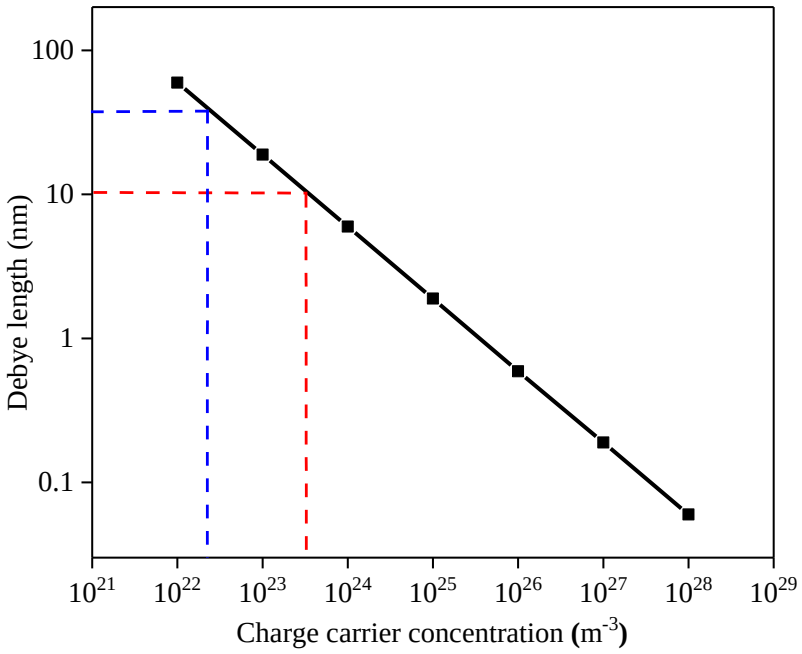

Figure 6.13 Estimation of the Debye length dependence on the charge carrier concentration. Red lines are related to the 10 nm TiO_2 film whereas blue lines are related to the 50 nm TiO_2 film

The Debye length (L_d) was calculated using equation 6.3, where T is the operating temperature of the TiO_2-coated gas sensor substrates which was set to 753.15 K (480°C) and ε is the relative permittivity, or dielectric constant which was set to 18.9.[176] ε_0 is the permittivity of free space, k_B is the Boltzmann constant, e is the elementary charge and n_0 is the charge carrier concentration.[91]

$$L_d = \sqrt{\varepsilon\varepsilon_0 k_B T / e^2 n_0} \qquad (6.3)$$

As the 10 nm and 50 nm TiO_2 films are quite resistive, it is reasonable to assume that the charge carrier concentration is ~ 10^{22} m^{-3}, which is at the lower end of the reported literature values for the charge carrier concentration of TiO_2. A high resistance means that there are less charge carriers within the film. It is therefore likely that the Debye length is within the range of film thicknesses studied i.e. between 10 - 50 nm.

The value of the Debye length for TiO_2 has been reported at ~ 10 - 11 nm.[91,94] It is therefore surprising that the 10 nm TiO_2 film has such low sensitivity towards CH_4 and NH_3, as it is close to the expected value for the Debye length. As electrical conduction must take place parallel to the substrate, the 10 nm thick film can be described as being "fully depleted" as the ratio between the Debye length and the film thickness is so small. Therefore the lack of sensitivity could be related to the screening effect exhibited by the Debye length.

6.4 Overall Conclusions

TiO_2 thin films were deposited onto standard alumina gas sensor substrates by ALD of titanium(IV) isopropoxide and water at 200 °C, with thicknesses in the range of the expected Debye length. The TiO_2-coated sensor substrates were exposed to various concentrations of CO, CH_4, NO_2, NH_3 and SO_2 to evaluate their gas sensitivities at operating temperatures of 350 °C and 480 °C at 0% relative humidity. Electrical resistance changes were only observed for the 50 nm TiO_2-coated sensors in response to NH_3 and CH_4 test gases. No response was observed for the 10 nm film due to its high resistivity.

Small electrical resistance changes were observed for the 50 nm TiO_2 film in response to CH_4 (in the range of 500 - 2500 ppm). In addition, this resulted in a change in the current through the heater, which can be ascribed to the decomposition of CH_4 onto the heating element. The overall temperature of the sensor decreased upon CH_4 exposure, which lead to a subsequent increase in power consumption and hence an increase in the current.

The effect of relative humidity on the gas sensitivity and sensor signal has also been demonstrated. It was observed that for the 50 nm TiO_2 film, the change in sensor resistance and response to CH_4 and NH_3 was reduced at higher humidity. It is suggested that this may be due to competition between NH_3 and OH^- species for the same pre-adsorbed oxygen species on the TiO_2 film surface.

The results show that the TiO_2 film thickness played a dominant role within the conduction mechanism and the pattern of response for the electrical resistance towards CH_4 and NH_3 exposure indicated typical *n*-type semiconducting behaviour. The sensitivity varied with TiO_2 film thickness, but the 10 nm film whose thickness was most consistent with reported literature values of the Debye length for TiO_2 was the not the most sensitive. This lack of sensitivity may be ascribed to screening effects induced by a fully depleted layer.

Chapter 7

Conclusions and future perspectives

Chapter 7 Conclusions and future perspectives

7.1 Overall Conclusions

This thesis has examined the use of atomic layer deposition (ALD) and chemical vapour deposition (CVD) to form semiconducting metal oxide thin films for gas sensing applications. ALD is a unique gas-phase thin film deposition technique which involves the sequential, alternative dosing of chemical precursors onto a substrate surface. ALD growth proceeds via a series of self-limiting reactions to form materials with high conformality and uniformity in thickness. As the film thickness depends solely on the number of reaction cycles, this enables materials to be deposited with defined thickness (in the order of nanometers) which makes ALD an ideal tool for exploring the fundamental gas sensing properties of these materials.

TiO_2 is a highly versatile material and its films have been employed across many applications including photocatalysis, anti-reflective coatings, electrochromic displays, gate oxide dielectrics and gas sensors. ALD has been used to deposit *n*-type TiO_2 thin films using two ALD reactors which have been designed and constructed in house specifically for this project. TiO_2 films were deposited from titanium(IV) isopropoxide and water precursors at a temperature of 200 °C, where the growth rate varied from 0.2 - 0.6 Å/cycle. Through manipulation of the precursor vapour pressures, dose/purge times, gas flow rates and temperatures, the optimum growth conditions for TiO_2 have been established, where film growth has been shown to proceed in a self-limiting and complementary manner. XRD, XPS and Raman techniques confirmed that the films were composed of anatase phase, where anatase peaks only became visible when the film thickness exceeded ~ 40 nm. AFM measurements have shown that the surface roughness of the films increased with film thickness which suggests that film growth occurs via stable nucleation sites which then grow and coalesce to form a continuous film. This has been supported by ellipsometry data which shows an increase in the refractive index with film thickness, indicating an increase in film density and hence crystallinity. XPS analysis confirmed Ti^{4+} oxidation state on the film surfaces with the core level Ti2p binding energies in line with those reported in the literature.

The second stage of the project demonstrated the deposition of *p*-type NiO thin films by ALD and CVD techniques. NiO films are becoming increasing more studied due to their wide range of properties (excellent chemical stability and high resistivity) which makes them attractive for various applications (e.g. catalysts, electrochromic devices, magnetic memories, gas sensors). A limitation to the ALD reactor is that it is only capable of using water as the co-reactant precursor, meaning that the choice of nickel precursor was highly important. Consequently, four nickel precursors were investigated: Nickel(II) bis(2,2,6,6-tetramethyl-3,5-heptanedionate), $[Ni(thd)_2]$; nickel cyclopentadienyl, $[Ni(Cp)_2]$; $[Ni(dmamp)_2]$, (dmamp = 2-dimethylamino-2-methyl-1-propanolate) and Nickel guanidinate, $[Ni\{(N^iPr_2)_2CNEt_2\}_2]$, where the latter two were novel precursors synthesised specifically for the purpose of this project. Complexes were analysed using $^1H/^{13}C$ NMR, mass spectrometry, elemental analysis and single crystal X-ray crystallography.

ALD of $[Ni(thd)_2]$ and water to deposit NiO films was shown to be unsuccessful. Manipulation of the precursor vapour pressure, gas flow rates, growth temperature and introduction of a piranha substrate cleaning protocol was found to have no impact on the film growth. It was discovered that a large excess of water was required in order to achieve complete saturation of the substrate surface due to low reactivity of the adsorbed nickel species towards water. XPS analysis however, confirmed the majority of the nickel species on the film surfaces was nickel metal, with only small amounts of NiO detected. As ALD of $[Ni(thd)_2]$ and water has been successfully reported in the literature, it is likely that the depositions outlined in this work were not successful at depositing NiO due to issues with the reactor design. Although the decomposition profile of the synthesised $[Ni(thd)_2]$ was similar to that reported in the literature, it may be that the reactor was not optimised to dose the solid $[Ni(thd)_2]$ precursor under the conditions tested.

ALD of [$Ni(Cp)_2$] and water to deposit NiO films was shown to be unsuccessful at a substrate temperature of 165 °C, which is the growth temperature employed in the literature for such systems. It is believed that a growth temperature of 165 °C is below the "ALD process window", where there was insufficient thermal energy to initiate the growth kinetics. However, increasing the growth temperature in the range of 300 - 350 °C (which are temperatures within or close to the "ALD process window"; where there is sufficient energy for chemical reactions to occur) resulted in the deposition of grey coloured films. AFM measurements appeared to show no significant relationship between the surface roughness and film thickness, so it was not clear what growth mechanism was occurring. XPS analysis confirmed the presence of Ni^{2+} species on the film surfaces, but this was in the form of $Ni(OH)_2$ rather than NiO. Post-deposition annealing of the films completely removed all traces of Ni^{2+} which emphasised that the films were unstable and may be composed of the more unstable structure of α-$Ni(OH)_2$.

It is therefore likely that there were problems with the precursor delivery and also holdups of water in the system. One way to investigate whether the delivery of [$Ni(Cp)_2$] into the reactor was a problem would be to conduct CVD experiments at a higher substrate temperature. With controlled dosing of the precursor at a higher temperature, this should result in precursor decomposition onto the substrate to form NiO. If this could be achieved then this would rule out any issues with precursor delivery into the reactor. In addition, most reports showing ALD of NiO from [$Ni(Cp)_2$] have utilised either O_3, O_2 or H_2 as the co-reactant, so it may be that [$Ni(Cp)_2$] was not particularly reactive with water under the reaction conditions used.

The novel precursor [Ni(dmamp)$_2$] was synthesised following adaptations from two different literature reports, where the [Ni(dmamp)$_2$] synthesised in this work had a slight increase in steric hindrance about the nickel centre. Although the temperature range of decomposition for this novel precursor was comparable to those reported in the literature for similar [Ni(dmamp)$_2$]-type structures, it is believed that the novel precursor has a higher thermal stability as its end decomposition temperature is greater (240 °C compared to 174 °C in literature). Therefore higher growth temperatures may be utilised and its potential use extended across various thin film applications.

ALD of [Ni(dmamp)$_2$] and water to deposit NiO was also shown to be unsuccessful at substrate temperatures in the range of 120 - 250 °C. Manipulation of the precursor dose/purge times, gas flow rates and substrate material had no effect on the deposition outcome. Pulsed-CVD experiments were performed to see whether [Ni(dmamp)$_2$] could still be deposited under conditions used closer to those used in ALD. One minute pulsed-CVD experiments resulted in NiO deposition, whereas 2.5 second pulsed-CVD did not. These results suggest that during a 2.5 second dose time, an insufficient amount of precursor was released in to the reaction chamber to be able to saturate the substrate surface. It is well known that the volatility of solid precursors decreases as the precursor is depleted.

CVD of [Ni(dmamp)$_2$] was performed at substrate temperatures of 250 – 400 °C to form NiO films, as confirmed by XPS. The films with the highest conformality and uniformity tended to be those deposited at 300 °C. These films showed a relatively linear relationship between deposition time/substrate temperature and film thickness. The fact that CVD depositions at 400 °C worked but ALD depositions at 400 °C did not work, advocates that [Ni(dmamp)$_2$] was insufficiently sensitive with water to react in an ALD scheme under the reaction conditions used and the reactor design used.

The novel precursor [Ni{(N^iPr_2)$_2$CNEt_2}$_2$] was synthesised following adaptations of the synthesis of copper bis-guanidinate complexes. The novel complex should possess ideal properties for use as an ALD precursor in that it has relatively non-bulky ligands which should prevent steric hindrance around the nickel centre and therefore increase the volatility of the complex. The chelating effect of the guanidinate ligands is also expected to enhance the thermal and chemical stability of the nickel metal complex.

The properties of the novel [Ni{(N^iPr_2)$_2$CNEt_2}$_2$] precursor cannot be directly compared to other nickel guanidinate complexes reported in the literature as the structures are very different and often consist of large, bulky ligands. However, the decomposition profile shows that the volatility of the novel precursor [Ni{(N^iPr_2)$_2$CNEt_2}$_2$] is on par with the synthesised [Ni(dmamp)$_2$], but is more volatile than [Ni(thd)$_2$], as well as [Ni(Cp)$_2$] as reported in the literature. [Ni{(N^iPr_2)$_2$CNEt_2}$_2$] is however less thermally stabile due to the larger percentage of residual mass remaining after decomposition. The decomposition profile of the novel [Ni{(N^iPr_2)$_2$CNEt_2}$_2$] precursor is also comparable to those reported in the literature for simialr nickel amidinate complexes and copper guanidinate complexes. This potentially gives huge scope for the use of [Ni{(N^iPr_2)$_2$CNEt_2}$_2$] as a precursor for use in ALD applications over some of the other nickel precursors widely used.

However ALD of [Ni{(N^iPr_2)$_2$CNEt_2}$_2$] and water to deposit NiO films was unsuccessful at substrate temperatures in the range of 140 - 450 °C. Manipulation of the precursor dose/purge times and gas flow rates had no effect on the deposition outcome. The decomposition temperature of [Ni{(N^iPr_2)$_2$CNEt_2}$_2$] was experimentally measured by TGA as 340 °C, so it was unusual that no film growth occurred at this temperature through precursor decomposition. Ni_3N was expected to form via CVD-like methods, but no Ni species were detected on the substrates by XPS.

CVD of $[Ni\{(N^iPr_2)_2CNEt_2\}_2]$, conducted at a higher temperature of 450 °C revealed the deposition of NiO, rather than the expected Ni_3N. The results imply that there could have been residual water molecules within the reactor which were reacting with the nickel precursor. Alternatively, the long deposition times may be the root cause of this. Pulsed-CVD experiments with $[Ni\{(N^iPr_2)_2CNEt_2\}_2]$ resulted in no film deposition at 450 °C. Vapour in the bubbler often depletes during dosing and recovers during purges, so it is somewhat surprising that pulsed-CVD experiments resulted in no film deposition, but 'normal' CVD did. However, the overall dose times used for CVD and pulsed-CVD experiments were not like-for-like, so it was likely that a significantly less amount of precursor was dosed into the reactor during pulsed-CVD experiments. It is evident that vapour transport of the precursor was occurring as 'normal' CVD resulted in NiO film deposition. However it may be that during pulsed-CVD mode, the vapour pressure of the precursor was not restored sufficiently during the purges and therefore during the dose steps minimal precursor was exposed into the reactor. Liquid precursors provide constant vapour pressure as the material is depleted, but this may not be the case for solid precursors.

The fact that CVD experiments worked but pulsed-CVD experiments did not work suggested that there were issues with the volatility of $[Ni\{(N^iPr_2)_2CNEt_2\}_2]$, as compared to $[Ni(dmamp)_2]$. Although the use of $[Ni\{(N^iPr_2)_2CNEt_2\}_2]$ was not suitable for ALD application in this case, this does not rule out its use as a potential CVD precursor. While the precursor purity could be responsible, it is much more likely to be a reactor issue. As a novel precursor, its chemical/physical properties may provide advances over other commonly used precursors for use in different CVD processes, for example LPCVD. If $[Ni\{(N^iPr_2)_2CNEt_2\}_2]$ can be used to deposit pure metal nitride films; which are notoriously difficult to deposit by CVD techniques at temperatures below 500 °C, then this could provide a significant breakthrough to future of metal nitride film deposition. Even if the precursor is not suitable for nitride CVD, it could still be good as a CVD precursor for oxides by deliberately introducing an oxygen co reactant.

The third stage of the project was to investigate the gas sensitivity and selectivity of *n*-type TiO_2 films deposited by ALD onto alumina gas sensor substrates. Although the gas sensing properties of TiO_2 have been widely studied, there is still little knowledge about the effect of TiO_2 film thickness at the order of the Debye length on the sensing properties. The TiO_2-coated sensor substrates were exposed to various concentrations of CO, CH_4, NO_2, NH_3 and SO_2 to evaluate their gas sensitivities at operating temperatures of 350 °C and 480 °C at 0, 10, 30 and 50% relative humidity. Electrical resistance changes were only observed for the 50 nm TiO_2-coated sensors in response to NH_3 and CH_4 test gases. Small electrical resistance changes were observed in response to CH_4, which was accompanied by an increase in the current through the heater. This was attributed to the decomposition of CH_4 onto the sensor surfaces. No sensor response was observed for the 10 nm film for any of the test gases due to its high resistivity.

An increase in humidity reduced the sensor performance due to competition between the test gas and OH^- species for the same pre-adsorbed oxygen species on the TiO_2 film surface. The gas sensitivity varied with TiO_2 film thickness, but the 10 nm film whose thickness was most consistent with reported literature values of the Debye length for TiO_2 was the not the most sensitive. This lack of sensitivity may be ascribed to screening effects induced by a fully depleted layer.

7.2 Future Perspectives

To build upon the results and conclusions presented in this work, the reactor design could be modified slightly to try and achieve NiO deposition by ALD of the nickel precursors described. For example, it is possible that ALD was not successful due to over saturation of water. The solenoid valves utilised on the reactor were limited to a minimum dose time of 2 seconds, meaning that a lot of water will have been dosed into the reactor in that short time. In order to reduce the level of water saturation, alternative solenoid valves should be sought to overcome this problem (i.e. to dose 10 - 20 milliseconds). Alternatively, the use of different co-reactants could be explored. Alcohols for example are less volatile than water and hence may help overcome some the problems previously encountered. The reactor design should also be configured as to reduce the lengths of pipework and hence minimise the chances of blockages or hold-ups occurring.

The effects of adding dopants into the films could also be investigated to see how the dopants influence the film properties and the gas sensing performance of the films. Furthermore, TiO_2/NiO *n/p*-heterojunctions could be generated using the synthesised nickel precursors and thus investigate these films as potential gas sensing materials.

Additionally, an alternative method of introducing the metal precursor into the reactor may be an option. Installation of a liquid injection system (Figure 7.1) may help overcome some of the many problems encountered when trying to dose solid nickel precursors into the reactor. The technology is particularly useful for low vapour pressure precursors or poorly thermally stable precursors. A liquid injection system would involve dissolving the metal precursor in an organic solvent which is normally held at room temperature. The vaporiser is then heated and then the carrier gas is delivered into the vaporiser with the precursor solution. The amount of precursor solution delivered to the vaporiser is only what is required for the precursor dose into the reactor.

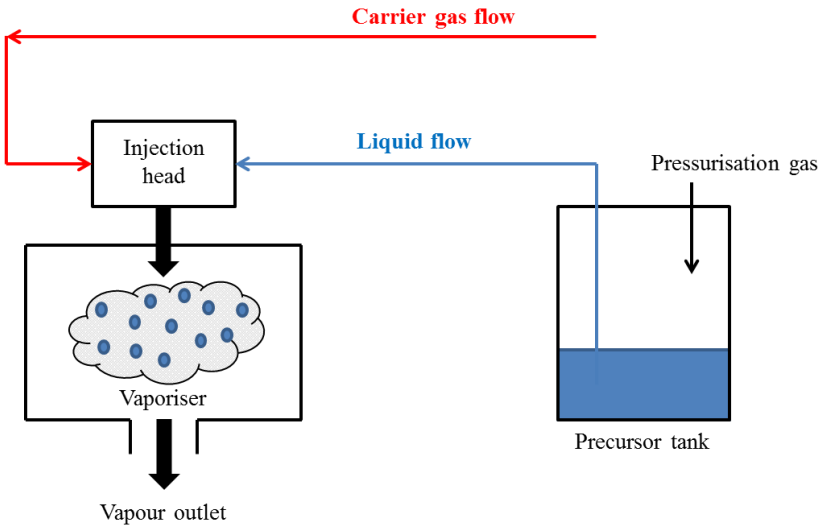

Figure 7.1 Schematic of direct liquid injection system

Further nickel guanidinate precursors could be investigated by variation of the substituents on the carbodiimide ligand and through using different lithiated salts. This way, a library of complexes could be synthesised and through decomposition studies, the most volatile complexes could be screened for their use as ALD precursors with water. To our knowledge there are currently no reported studies on the use of nickel guanidinates or amidinates to deposit nickel oxide films by ALD. If successful, the NiO films could then be tested for their gas sensitivity and selectivity in order to determine the film thickness which results in the optimum sensor response.

There are other nickel compounds which could be investigated as potential precursors for ALD with water. A fine example would be nickel amidinate precursors, $[Ni(R\text{-}Me\text{-}amd)_2]_x$ (x = 1, R = ^{t}Bu; x = 2, R = ^{i}Pr, Et).[177] The R group can be tuned so that the groups are bulky enough to limit oligomerisation and increase the volatility of the precursor. Bis(N,N'-di-tert-butylacetamidinato)nickel(II) has a reasonably high vapour pressure and is reported to be air and moisture sensitive which makes it an ideal precursor for ALD with water as the co-reactant. As these types of precursors do not contain any metal-carbon bonds, the amount of carbon impurities in the resulting films is minimal.

In addition, the metal-nitrogen bond strengths are weaker as compared to metal-chlorine or metal-oxygen bonds, which mean that deposition of amidinates can be performed at relatively lower temperatures.[177] There are some reports in the literature of amidinates being used for ALD; N,N'-diisopropylacetamidinato-copper(I), $[Cu(^{i}Pr\text{-}amd)]_2$[178] and N,N'-di-sec-butylacetamidinato-copper(I) $[Cu(^{s}Bu\text{-}amd)]_2$[179] have both been reported to react with hydrogen to deposit copper metal by ALD. Gordon has reported the pulsed-CVD of the ruthenium amidinate, $[Ru^{II}\{(N^{t}Bu)_2CMe\}(CO)]_2$ to deposit ruthenium metal, and direct liquid injection CVD (DLI-CVD) of the nickel amidinate, $[Ni^{II}\{[(N^{t}Bu)CMe\}]_2$ and NH_3 to deposit nickel nitride films.[57.139] Amidinato complexes of Al, Ga and In have also been reported for use in CVD to deposit the respective nitride films.[57]

With regards to the gas sensing experiments, NiO films deposited either by ALD or CVD should be investigated and evaluated for their gas sensitivity and selectivity against a range of test gases. ALD or CVD of *p*-type copper(I) oxide films could be explored. The $[Cu(thd)_2]$ precursor has been used to deposit Cu_2O by ALD with water as the co-reactant, so this would be a good place to start. If unsuccessful, alternative copper precursors could be examined, e.g. $[Cu(acac)_2]$, $[Cu(hfac)_2]$, $[Cu(dmamp)_2]$, $[Cu(^{s}Bu\text{-}amd)]_2$ and $[Cu(^{i}Pr\text{-}amd)]_2$. If Cu_2O films can be deposited then they could be subsequently tested for their gas sensitivity and selectivity.

References

1. Wang C, Yin L, Zhang L, Xiang D, Gao R. Metal oxide gas sensors: Sensitivity and influencing factors. *Sensors*. 2010; 10(3), 2088-2106.
2. Bharathi J.J, Pappayee N. Titanium dioxide (TiO_2) thin film based gas sensors. *J Chem Pharm Sci*. 2014, (4), 59-61.
3. Kim H-J, Lee J-H. Highly sensitive and selective gas sensors using p-type oxide semiconductors: Overview. *Sensors Actuators B Chem*. 2014, (192), 607-627.
4. Phanichphant S. Semiconductor Metal Oxides as Hydrogen Gas Sensors. *Procedia Eng*. 2014, (87), 795-802.
5. Woo H.S, Na C, Lee J.H. Design of Highly Selective Gas Sensors via Physicochemical Modification of Oxide Nanowires: Overview. *Sensors*. 2016, 16(10), 1531.
6. Neri G. First Fifty Years of Chemoresistive Gas Sensors. *Chemosensors*. 2015, 3(1), 1-20.
7. Puurunen R.L. A Short History of Atomic Layer Deposition: Tuomo Suntola's Atomic Layer Epitaxy. *Chem Rev*. 2014, 20, 332-344.
8. George S.M. Atomic layer deposition: An overview. *Chem Rev*. 2010, 110, 111-131.
9. Leskelä M, Ritala M. Atomic Layer Epitaxy in Deposition of Various Oxide and Nitride Thin Films. *J Phys IV*. 1995, 5, C5-937.
10. Sneh O, Clark-Phelps R.B, Londergan A.R, Winkler J, Seidel T.E. Thin film atomic layer deposition equipment for semiconductor processing. *Thin Solid Films*. 2002, 402, 248-261.
11. Leskelä M, Ritala M. Atomic layer deposition (ALD): From precursors to thin film structures. *Thin Solid Films*. 2002, 409, 138-146.
12. Leskelä M, Ritala M. Atomic Layer Deposition Chemistry: Recent Developments and Future Challenges. *Angew Chem. Int Ed*. 2003, 42, 5548-5554.
13. Miikkulainen V, Leskelä M, Ritala M, Puurunen R.L. Crystallinity of inorganic films grown by atomic layer deposition: Overview and general trends. *J Appl Phys*. 2013, 113.
14. Moore G.E. Cramming more components onto integrated circuits, Reprinted from Electronics. *Electronics*. 1965, 38(2), 33-35.
15. Hoefflinger B. ITRS: The International Technology Roadmap for Semiconductors. *Chips 2020 A Guid to Futur Nanoelectron*. 2012, 161-174.
16. Ritala M, Leskelä M, Dekker J, Mutsaers C, Soininen P.J, Skarp J. Perfectly Conformal TiN and Al_2O_3 Films Deposited by Atomic Layer Deposition. *Chem Vap Depos*. 1999, 5(1), 7-9.

17. Lubitz M, Phillip A, Medina I.V, Antic A, Rosin J.T, Fahlman B.D. Cost-Effective Systems for Atomic Layer Deposition. *J Chem Educ*. 2014, 91, 1022-1027.

18. Lim B.S, Rahtu A, Gordon R.G. Atomic layer deposition of transition metals. *Nat Mater*. 2003, 2(November), 749-754.

19. Ritala M, Leskelä M, Niinisto L, Haussalo P, Niinist L. Titanium Isopropoxide as a Precursor in Atomic Layer Epitaxy of Titanium Dioxide Thin Films. *Chem Mater*. 1993, 5(8), 1174-1181.

20. Elam J.W, Xiong G, Han C.Y, et al. Atomic layer deposition for the conformal coating of nanoporous materials. *J Nanomater*. 2006, 2006, 1-5.

21. Kim H. Atomic layer deposition of metal and nitride thin films: Current research efforts and applications for semiconductor device processing. *J Vac Sci Technol B Microelectron Nanom Struct*. 2003, 21(2003), 2231.

22. Reinke M, Kuzminykh Y, Hoffmann P. Surface Reaction Kinetics of Titanium Isopropoxide and Water in Atomic Layer Deposition. *J Phys Chem C*. 2016, 120(8), 4337-4344.

23. Moshe H, Mastai Y. Atomic Layer Deposition on Self-Assembled-Monolayers, *Materials Science - Advanced Topics* (Yitzhak Mastai, ed.), 1974.

24. Bernal Ramos K, Saly M.J, Chabal Y.J. Precursor design and reaction mechanisms for the atomic layer deposition of metal films. *Coord Chem Rev*. 2013, 257(23-24), 3271-3281.

25. Suntola T. Atomic layer epitaxy. *Thin Solid Films*. 1992, 216(1), 84-89.

26. Johnson R.W, Hultqvist A, Bent S.F. A brief review of atomic layer deposition: From fundamentals to applications. *Mater Today*. 2014, 17(5), 236-246.

27. Ritala M, Leskelä M, Zirconium dioxide thin films deposited by ALE using zirconium tetrachloride as precursor. *Appl Surf Sci*. 1994, 75(1), 333-340.

28. Johansson P, Lahtinen K, Kuusipalo J, Kääriäinen T, Maydannik P, Cameron D. Atomic Layer Deposition Process for Barrier Applications of Flexible Packaging. *2010 Place Conf*. 2010.

29. Creighton J.R, Ho P. Chapter 1 Introduction to Chemical Vapor Deposition (CVD). *Chem Vap Depos*. 2001, 1-13.

30. Choy K.L. Chemical vapour deposition of coatings. *Prog Mater Sci*. 2003, 48(2), 57-170.

31. Jones A.C, Hitchman M.L. Overview of Chemical Vapour Deposition. *Chem Vap Depos Precursors, Process Appl*. 2009, 1-36.

32. Lu J, Elam J.W, Stair P.C. Atomic layer deposition - Sequential self-limiting surface reactions for advanced catalyst "bottom-up" synthesis. *Surf Sci Rep*. 2016, 71(2), 410-472.

33. Emslie D.J.H, Chadha P, Price J.S. Metal ALD and pulsed CVD: Fundamental

reactions and links with solution chemistry. *Coord Chem Rev*. 2013, 257(23-24), 3282-3296.

34. Ohring M. *The Materials Sciene of Thin Films*. Academic Press Limited; 1992.

35. Hämäläinen J, Ritala M, Leskelä M. Atomic layer deposition of noble metals and their oxides. *Chem Mater*. 2014, 26, 786-801.

36. Devi A. "Old chemistries" for new applications: Perspectives for development of precursors for MOCVD and ALD applications. *Coord Chem Rev*. 2013, 257(23-24), 3332-3384.

37. Gordon P.G, Kurek A, Barry S.T. Trends in Copper Precursor Development for CVD and ALD Applications. *ECS J Solid State Sci Technol*. 2015, 4(1), N3188-N3197.

38. Hatanpää T, Ritala M, Leskelä M. Precursors as enablers of ALD technology: Contributions from university of helsinki. *Coord Chem Rev*. 2013, 257(23-24), 3297-3322.

39. Werndrup P, Gohil S, Kessler V.G, Kritikos M, Hubert-pfalzgraf L.G. Synthesis, characterization and molecular structures of homo- and heterometallic nickel (II) aminoalkoxides $Ni(\eta^2\text{-}OR^N)_2$ and $Ni(Ni_{0.25}Cu_{0.75})_2(\mu_3\text{-}OH)(\mu\text{-}OAc)(\eta^1\text{-}OAc)_2(\mu,\eta^2\text{-}OR^N)_2(\eta^2\text{-}R^NOH)(R^N=CHMeCH_2NMe_2)$. *Polyhedron*. 2001, 20, 2163-2169.

40. Ritala M. Atomic Layer Deposition of Oxide Thin Films with Metal Alkoxides as Oxygen Sources. *Science (80)*. 2000, 288(April), 319-321.

41. Aarik J, Aidla A, Uustare T, Ritala M, Leskelä M. Titanium isopropoxide as a precursor for atomic layer deposition: characterization of titanium dioxide growth process. *Appl Surf Sci*. 2000, 161(3-4), 385-395.

42. Wilhoit R. Vapor Pressures of Some Aluminum, Alkoxides. *J Phys Chem*. 1957, 61(1810), 4-6.

43. Yoo S.H, Choi H, Kim H.S, et al. Synthesis and characterization of Nickel(II) aminoalkoxides: Application to molecular precursors for MOCVD of Ni thin films. *Eur J Inorg Chem*. 2011, (11), 1833-1839.

44. Antony Premkumar P, Toeller M, Adelmann C, et al. NiO Thin Films Synthesized by Atomic Layer Deposition using $Ni(dmamb)_2$ and Ozone as Precursors. *Chem Vap Depos*. 2012, 18(1-3), 61-69.

45. Min K-C, Kim M, You Y-H, et al. NiO thin films by MOCVD of $Ni(dmamb)_2$ and their resistance switching phenomena. *Surf Coatings Technol*. 2007, 201(22-23), 9252-9255.

46. Matero R, Ritala M, Leskelä M, Sajavaara T, Jones A.C and Roberts J.L. Evaluation of New Aminoalkoxide Precursors for Atomic Layer Deposition. Growth of Zirconium Dioxide Thin Films and Reaction Mechanism Studies. *Chem Mater,*. 2004, 16(26), 5630–5636.

47. Lindahl E, Ottosson M, Carlsson J-O. Atomic Layer Deposition of NiO by the $Ni(thd)_2/H_2O$ Precursor Combination. *Chem Vap Depos*. 2009, 15(7-9), 186-

191.

48. Wächtler T. Thin Films of Copper Oxide and Copper Grown by Atomic Layer Deposition for Applications in Metallization Systems of Microelectronic Devices. *PhD Thesis*. 2009, 245.

49. Utriainen M, Kröger-Laukkanen M, Niinistö L. Studies of NiO thin film formation by atomic layer epitaxy. *Mater Sci Eng B*. 1998, 54(1-2), 98-103.

50. Alnes M.E, Monakhov E, Fjellvag H, Nilsen O. Atomic Layer Deposition of Copper Oxide using Copper(II) Acetylacetonate and Ozone. *Chem Vap Depos*. 2012, 18(4-6), 173-178.

51. AzoNano, Applications of Metal Cyclopentadienyl CVD/ALD Precursors. *AzoNano*. 2013, 1-9.

52. Lindahl E. Thin Film Synthesis of Nickel Containing Compounds. *Int J Math*. 1994, 5(2), 201-212.

53. Chae J, Park H-S, Kang S. Atomic Layer Deposition of Nickel by the Reduction of Preformed Nickel Oxide. *Electrochem Solid-State Lett*. 2002, 5(6), C64.

54. Lu HL, Scarel G, Li XL, Fanciulli M. Thin MnO and NiO films grown using atomic layer deposition from ethylcyclopentadienyl type of precursors. *J Cryst Growth*. 2008;310(24):5464-5468.

55. Kim D.H, Sim J.K, Lee J, et al. Carbon dioxide reforming of methane over mesoporous Ni/SiO_2. *Fuel*. 2013, 112, 111-116.

56. Carmalt C.J, Newport A.C, O'Neill S.A, Parkin I.P, White A.J.P, Williams D.J. Synthesis of titanium(IV) guanidinate complexes and the formation of titanium carbonitride via low-pressure chemical vapor deposition. *Inorg Chem*. 2005, 44(3), 615-619.

57. Barry S.T. Amidinates, guanidinates and iminopyrrolidinates: Understanding precursor thermolysis to design a better ligand. *Coord Chem Rev*. 2013, 257(23-24), 3192-3201.

58. Potts S.E, Carmalt C.J, Blackmail C.S, Abou-Chahine F, Pugh D, Davies H.O. Synthesis of zirconium guanidinate complexes and the formation of zirconium carbonitride via low pressure CVD. *Organometallics*. 2009, 28(6), 1838-1844.

59. Whitehorne T.J.J, Coyle J.P, Mahmood A, Monillas W.H, Yap G.P.A, Barry S.T. Group 11 amidinates and guanidinates: Potential precursors for vapour deposition. *Eur J Inorg Chem*. 2011, (21), 3240-3247.

60. Zaera F. Mechanisms of surface reactions in thin solid film chemical deposition processes. *Coord Chem Rev*. 2013, 257(23-24), 3177-3191.

61. Ritala M, Kukli K, Rahtu A, et al. Atomic layer deposition of oxide thin films with metal alkoxides as oxygen sources. *Science*. 2000, 288(5464), 319-321.

62. M. Schuisky, J. Aarik, K. Kukli, A. Aidla, J. Lu A.H. No Title. In: *AVS Topical Conference on Atomic Layer Deposition; 2001; Monterey, Calif.*; 2001.

63. Aarik J, Aidla A, Uustare T, Kukli K. Atomic layer deposition of TiO_2 thin films from TiI_4 and H_2O. *Appl Surf Sci*. 2002, 193, 277-286.

64. Aarik J, Aidla A, Sammelselg V, Uustare T, Ritala M, Leskelä M. Characterization of titanium dioxide atomic layer growth from titanium ethoxide and water. *Thin Solid Films*. 2000, 370(1), 163-172.

65. Aarik J, Aidla A, Kiisler A, Uustare T. Effect of crystal structure on optical properties of TiO_2 films grown by atomic layer deposition. *Thin Solid Films*. 1997, 305, 270-273.

66. Aarik J, Aidla A, Uustare T, Sammelselg V. Morphology and structure of TiO_2 thin films grown by atomic layer deposition. *J Cryst Growth*. 1995, 148(3), 268-275.

67. Pore V, Rahtu A, Leskelä M, Ritala M, Sajavaara T, Keinonen J. Atomic layer deposition of photocatalytic TiO_2 thin films from titanium tetramethoxide and water. *Chem Vap Depos*. 2004, 10(3), 143-148.

68. Gowthami V, Meenakshi M, Perumal P, Sivakumar R, Sanjeeviraja C. Optical dispersion characterization of NiO thin films prepared by nebulized spray technique. *ChemTech Res*. 2014, 6(13), 5196-5202.

69. Lu H.L, Scarel G, Wiemer C, et al. Atomic Layer Deposition of NiO Films on Si(100) Using Cyclopentadienyl-Type Compounds and Ozone as Precursors. *J Electrochem Soc*. 2008, 155(10), H807.

70. Chung T.M, Lee S.S, Cho W, et al. Volatile nickel aminoalkoxide complexes as liquid precursors for non-volatile memory device of NiO films by ALD. *Bull Korean Chem Soc*. 2011, 32(3), 783-784.

71. Lindahl E, Lu J, Ottosson M, Carlsson J-O. Epitaxial NiO (100) and NiO (111) films grown by atomic layer deposition. *J Cryst Growth*. 2009, 311(16), 4082-4088.

72. Becht M, Gallus J, Hunziker M, Atamny F, Dahmen K-H. Nickel Thin Films Grown by MOCVD Using Ni(dmg)2 as Precursor. *Le J Phys IV*. 1995, 5(C5), C5-465-C5-472.

73. Korošec R.C, Bukovec P. Sol-gel prepared NiO thin films for electrochromic applications. *Acta Chim Slov*. 2006, 53(2), 136-147.

74. Kim W-H, Lee H-B-R, Heo K, et al. Atomic Layer Deposition of Ni Thin Films and Application to Area-Selective Deposition. *J Electrochem Soc*. 2011, 158(1), D1-D5.

75. Yang T.S, Cho W, Kim M, et al. Atomic layer deposition of nickel oxide films using $[Ni(dmamp)_2]$ and water. *J Vac Sci Technol A Vacuum, Surfaces, Film*. 2005, 23(4), 1238.

76. Sharma V. Evaluation of novel metalorganic precursors for atomic layer deposition of nickel-based thin films. 1988.

77. Daub M, Knez M, Goesele U, Nielsch K. Ferromagnetic nanotubes by atomic layer deposition in anodic alumina membranes. *J Appl Phys*. 2007, 101(November 2015), 1-4.

78. Kurek A, Gordon P.G, Karle S, Devi A, Barry S.T. Recent Advances Using Guanidinate Ligands for CVD and ALD Applications. *Aust J Chem*. 2013, 989-996.

79. Niinistö L, Ritala M, Leskelä M. Synthesis of oxide thin films and overlayers by atomic layer epitaxy for advanced applications. *Mater Sci Eng B*. 1996, 41(1), 23-29.

80. Ponraj J.S, Attolini G, Bosi M. Review on Atomic Layer Deposition and Applications of Oxide Thin Films. *Crit Rev Solid State Mater Sci*. 2013, 38(3), 203-233.

81. Hotovy I, Huran J, Spiess L, Hascik S, Rehacek V. Preparation of nickel oxide thin films for gas sensors applications. *Sensors Actuators, B Chem*. 1999, 57(1-3), 147-152.

82. Van Delft J.A, Garcia-Alonso D, Kessels W.M.M. Atomic layer deposition for photovoltaics: applications and prospects for solar cell manufacturing. *Semicond Sci Technol*. 2012, 27(7), 74002.

83. Fine G.F, Cavanagh L.M, Afonja A, Binions R. Metal oxide semi-conductor gas sensors in environmental monitoring. *Sensors*. 2010, 10(6), 5469-5502.

84. Sun Y-F, Liu S-B, Meng F-L, et al. Metal Oxide Nanostructures and Their Gas Sensing Properties: A Review. *Sensors*. 2012, 12(3), 2610-2631.

85. Iftimie N, Luca D, Lacomi F, Girtan M, Mardare D. Gas sensing materials based on TiO_2 thin films. *J Vac Sci Technol B Microelectron Nanom Struct*. 2009, 27(1), 538.

86. Marichy C, Pinna N. Atomic Layer Deposition to Materials for Gas Sensing Applications. *Adv Mater Interfaces*. 2016, 3(21).

87. Shokry Hassan H, Kashyout A.B, Morsi I, Nasser A.A.A, Ali I. Synthesis, characterization and fabrication of gas sensor devices using ZnO and ZnO:In nanomaterials. *Beni-Suef Univ J Basic Appl Sci*. 2014, 3(3), 216-221.

88. Yamazoe N. New approaches for improving semiconductor gas sensors. *Sensors Actuators B Chem*. 1991, 5(1-4), 7-19.

89. Bruno L, Pijolat C, Lalauze R. Tin dioxide thin-film gas sensor prepared by chemical vapour deposition. *Sensors Actuators B Chem*. 1994, 18(1), 195-199.

90. Du X, George S.M. Thickness dependence of sensor response for CO gas sensing by tin oxide films grown using atomic layer deposition. *Sensors Actuators, B Chem*. 2008, 135(1), 152-160.

91. Sysoev V.V, Button B.K, Wepsiec K, Dmitriev S, Kolmakov A. Toward the nanoscopic “electronic nose”: Hydrogen vs carbon monoxide discrimination with an array of individual metal oxide nano- and mesowire sensors. *Nano Lett*. 2006, 6(8), 1584-1588.

92. Hastir A, Kohli N, Singh R.C. Comparative study on gas sensing properties of rare earth (Tb, Dy and Er) doped ZnO sensor. *J Phys Chem Solids*. 2017, 105(February), 23-34.

93. Boyadjiev S, Georgieva V, Vergov L, Baji Z, Gáber F, Szilágyi IM. Gas

sensing properties of very thin TiO_2 films prepared by atomic layer deposition (ALD). *J Phys Conf Ser*. 2014, 559, 12013.

94. Marichy C, Donato N, Latino M, et al. Gas sensing properties and p-type response of ALD TiO_2 coated carbon nanotubes. *Nanotechnology*. 2015, 26(2), 24004.

95. Karunagaran B, Uthirakumar P, Chung S.J, Velumani S, Suh E-K. TiO_2 thin film gas sensor for monitoring ammonia. *Mater Charact*. 2007, 58(8-9), 680-684.

96. Bittencourt C, Felten A, Espinosa E.H, et al. WO_3 films modified with functionalised multi-wall carbon nanotubes: Morphological, compositional and gas response studies. *Sensors Actuators, B Chem*. 2006, 115(1), 33-41.

97. Pol- U, Rumelt R.P, Costa O. Semiconductor Technology. *Vacuum*. 2003.

98. Shankar P, Bosco J, Rayappan B. Gas sensing mechanism of metal oxides : The role of ambient atmosphere , type of semiconductor and gases - A review ScienceJet. *Sci Jet*. 2015, 4(January 2015), 126.

99. Zhou X, Lee S, Xu Z, Yoon J. Recent Progress on the Development of Chemosensors for Gases. *Chem Rev*. 2015, 115(15), 7944-8000.

100. Liu Y, Li G, Mi R, Deng C, Gao P. An environment-benign method for the synthesis of p-NiO/n-ZnO heterostructure with excellent performance for gas sensing and photocatalysis. *Sensors Actuators, B Chem*. 2014, 191(February), 537-544.

101. Liu X, Cheng S, Liu H, Hu S, Zhang D, Ning H. A Survey on Gas Sensing Technology. *Sensors*. 2012, 12(7), 9635-9665.

102. Filmetrics. Advanced thin film measurement systems. 2012, 2-12.

103. Filmetrics. Thin-Film Analyzer. 2015.

104. Budai J, Farkas B, Horváth Z.L, Geretovszky Z. On determining the optical properties and layer structure from spectroscopic ellipsometric data using automated artifact minimization method. *Thin Solid Films*. 2014, 567, 14-19.

105. Wilson M. Integrated Electrical and Optical Characterization of Large Area Thin Film Photovoltaic Materials. 2011, 474-478.

106. Miller J.D. Effect of roughness as determined by atomic force microscopy on the wetting properties of PTFE thin films Effect of Roughness as Determined by Atomic Force Microscopy on the Wetting Properties of PTFE Thin. 1996, 36(August 2015).

107. Chang S-L. Thin-film characterization by grazing incidence X-ray diffraction and multiple beam interference. *J Phys Chem Solids*. 2001, 62(9-10), 1765-1775.

108. Hull A.W. A New Method of Chemical Analysis. *J Am Chem Soc*. 1919, 41(8), 1168-1175.

109. Staveley L.A.K. *The Characterization of Chemical Purity: Organic Compounds*. Elsevier; 2013.

110. Chauhan A.P.S. Coke Resistant Coating Technology for Applications in Ethylene Pyrolysis Heaters. *PhD Thesis*, 2004.

111. Goldstein J, Newbury D.E, Echlin P, Joy D.C, Romig Jr. A.D, Lyman C.E, Charles Fiori EL. Scanning Electron Microscopy and X-Ray Microanalysis: A Text for Biologists, Materials Scientists, and Geologists. *Science (80-)*. 2012.

112. Agilent Technologies Ltd. CrysAlis PRO. 2014.

113. Burla M.C, Caliandro R, Camalli M, et al. IL MILIONE: A suite of computer programs for crystal structure solution of proteins. *J Appl Crystallogr*. 2007, 40(3), 609-613.

114. Sheldrick G.M. A short history of SHELX. *Acta Crystallogr Sect A Found Crystallogr*. 2007, 64(1), 112-122.

115. Dolomanov O.V, Bourhis L.J, Gildea R.J, Howard J.A.K, Puschmann H. OLEX2: A complete structure solution, refinement and analysis program. *J Appl Crystallogr*. 2009, 42(2), 339-341.

116. Filatova E.S, Nizardb H, Semyannikova P.P, Sysoeva S.V, Trubina S.V, Morozovaa N.B, Zherikovaa K.V. Thermal Properties of Some Volatile Titanium(IV) Precursors. *ECS Trans*. 2009, 5(8), 557-560.

117. Matero R, Rahtu A, Ritala M, Leskelä M, Sajavaara T. Effect of water dose on the atomic layer deposition rate of oxide thin films. *Thin Solid Films*. 2000, 368(1), 1-7.

118. Diebold U. The surface science of titanium dioxide. *Surf Sci Rep*. 2003, 48, 53-229.

119. Kischkat J, Peters S, Gruska B, et al. Mid-infrared optical properties of thin films of aluminum oxide, titanium dioxide, silicon dioxide, aluminum nitride, and silicon nitride. *Appl Opt*. 2012, 51(28), 6789.

120. Lakhtalda A. Would Brewster recognize today's Brewster angle? *Opt News*. 1989, (June), 14-18.

121. Sammelselg V. TiO_2 thin films by atomic layer deposition: a case of uneven growth at low temperature. *Appl Surf Sci*. 1998, 134, 78-86.

122. Hanaor D.H, Sorrell C.C. Review of the anatase to rutile phase transformation. *J Mater Sci*. 2011, 46(4), 855-874.

123. Matero R, Rahtu A, Ritala M, Leskela M, Sajavaara T. Effect of water dose on the atomic layer deposition rate of oxide thin films. *Thin Solid Films*. 2000, 368, 1.

124. Langford J.I, Wilson A.J.C. Scherrer after sixty years: A survey and some new results in the determination of crystallite size. *J Appl Crystallogr*. 1978, 11(2), 102-113.

125. Bukauskas V, Kaciulis S, Mezzi A, et al. Effect of substrate temperature on the arrangement of ultra-thin TiO_2 films grown by a dc-magnetron sputtering deposition. *Thin Solid Films*. 2015, 585(June), 5-12.

126. Kurtz R.L. Comparison of Ti2p Core-Level Peaks from TiO_2, Ti_2O_3, and Ti

Metal, by XPS. *Surf Sci Spectra*. 1998, 5(3), 179-181.

127. Fu Y, Du H, Zhang S, Huang W. XPS characterization of surface and interfacial structure of sputtered TiNi films on Si substrate. *Mater Sci Eng A*. 2005, 403(1-2), 25-31.

128. Rumaiz A.K, Ali B, Ceylan A, Boggs M, Beebe T, Ismat Shah S. Experimental studies on vacancy induced ferromagnetism in undoped TiO_2. *Solid State Commun*. 2007, 144(7-8), 334-338.

129. Mason R. Standard Enthalpies of Formation of Tris[bis(pentane-2,4-dionato)nickel-(II)] and Bis(2,2,6,6-tetramethylheptane-3,5-dionato)nickel(II) and an Estimation of Nickel-Oxygen Bond Energies. *JCS Dalt*. 1978, (11), 399-402.

130. Cotton F.A, Fackler J.P. Molecular Association and Electronic Structures of Nickel(II) Chelates. I. Complexes of Pentane-2,4-dione and Some 1,5-Di-substituted Derivatives . *J Am Chem Soc*. 1961, 83(13), 2818-2825.

131. Hubert-pfalzgraf L.G, Kesslerat V.G, Vaissermann J. Soluble Ni(II) alkoxides based on dimethylaminoisopropoxide ligands : molecular structure of $[Li(Pr^iOH)Ni(\eta^2\text{-}OR)_2Cl]_2$ and of *cis*-$NiCl_2(ROH)_2$(R=$CHMeCH_2NMe_2$). P*olyhedron*. 1997, 16(24), 4197-4203.

132. Knisley T.J, Kalutarage L.C, Winter C.H. Precursors and chemistry for the atomic layer deposition of metallic first row transition metal films. *Coord Chem Rev*. 2013, 257(23-24), 3222-3231.

133. Cotton F.A, Wise J.J. The Crystal and Molecular Structure of Bis(2,2,6,6-tetramethylheptane-3,5-dionato)nickel(II). *J Am Chem Soc*. 1965, 4(8), 3-9.

134. Coyle J.P, Monillas W.H, Yap G.P, Barry S.T. Synthesis and thermal chemistry of copper (I) guanidinates. *Inorg Chem*. 2008, 47(2), 683-689.

135. Tiow-Gan Ong , Glenn P.A. Yap, Richeson D.S. Formation of a Guanidinate-Supported Titanium Imido Complex: A Catalyst for Alkyne Hydroamination. *Organometallics*. 2002, 21, 2839–2841.

136. Ramos J.M, T. de M. Cruz M, C. Costa Jr. A, Versiane O, A. Tellez Soto C. Fourier transform infrared spectrum: Vibrational assignments using density functional theory and natural bond orbital analysis of the bis(guanidoacetate)nickel(II) complex. *ScienceAsia*. 2011, 37(3), 247.

137. Jones C, Schulten C, Fohlmeister L, et al. Bulky guanidinato nickel(I) complexes: Synthesis, characterization, isomerization, and reactivity studies. *Chem - A Eur J*. 2011, 17(4), 1294-1303.

138. Yang T.S, Cho W, Kim M, et al. Atomic layer deposition of nickel oxide films using $Ni(dmamp)_2$ and water, 2013, 1238, (2005).

139. Li Z, Gordon R.G, Pallem V, Li H, Shenai D.V. Direct-liquid-injection chemical vapor deposition of nickel nitride films and their reduction to nickel films. *Chem Mater*. 2010, 22(10), 3060-3066.

140. Siddiqi M.A, Siddiqui R.A, Atakan B. Thermal Stability, Vapor Pressures, and Diffusion Coefficients of Some Metal 2,2,6,6-Tetramethyl-3,5-heptandionate

[M(tmhd)n] Compounds. *J Chem Eng Data*. 2010, 55(6), 2149-2154.

141. Törndahl T, Ottosson M, Carlsson J-O. Growth of Copper(I) Nitride by ALD Using Copper(II) Hexafluoroacetylacetonate, Water, and Ammonia as Precursors. *J Electrochem Soc*. 2006, 153(3), C146.

142. Mansour A.N. Characterization of NiO by XPS. *Surf Sci Spectra*. 1994, 3(3), 231.

143. Matienzo J, Yin L.I, Grim S.O, Swartz W.E. X-ray photoelectron spectroscopy of nickel compounds. *Inorg Chem*. 1973, 12(12), 2762-2769.

144. Dufresne P, Payen E, Grimblot J, Bonnelle J.P. Study of Ni-Mo-y-Al,O, Catalysts by X-ray Photoelectron and Raman Spectroscopy. Comparison with Co-Mo-y-Al,O, Catalysts. *J Phys Chem*. 1981, 85(16), 2344-2351.

145. Lenglet M, D'Huysser A, Arsene J, Bonnelle J.P, Jorgensen C.K. XANES, X-ray photo-electron and optical spectra of divalent nickel at the crystallographic transition in $NiCr_2O_4$ and the $Ni_{1-x}Cu_xCr_2O_4$ system: correlation with the Jahn-Teller effect. *J Phys C Solid State Phys*. 1986, 19(17), L363-L368.

146. Sarr M, Bahlawane N, Arl D, Dossot M, McRae E, Lenoble D. Tailoring the properties of atomic layer deposited nickel and nickel carbide thin films via chain-length control of the alcohol reducing agents. *J Phys Chem C*. 2014, 118(40), 23385-23392.

147. Piranha Solution Information & Safety. :5-7. http://www.enma.umd.edu/LAMP/Sop/Piranha_SOP.htm.

148. Kang J-K, Rhee S-W. Metalorganic Chemical Vapor Deposition of Nickel Films from $Ni(C_5H_5)_2/H_2$. *J Mater Res*. 2000, 15(8), 1828-1833.

149. Siddiqui R.A. Experimental Investigations of Thermodynamic Properties of Organometallic Compounds (CVD). 2009.

150. Vieyra-Eusebio M.T, Rojas A. Vapor pressures and sublimation enthalpies of nickelocene and cobaltocene measured by thermogravimetry. *J Chem Eng Data*. 2011, 56(12), 5008-5018.

151. Mansour A.N, Melendres C.A. Characterization of α-$Ni(OH)_2$ by XPS. *Surf Sci Spectra*. 1994, 3(3), 255-262.

152. Grosvenor A.P, Biesinger M.C, Smart R.S.C, McIntyre N.S. New interpretations of XPS spectra of nickel metal and oxides. *Surf Sci*. 2006, 600(9), 1771-1779.

153. Frost, D.C, Ishitani A.M. X-ray photoelectron spectroscopy of copper compounds. *Mol Phys*. 1972, 24(4), 861-877.

154. McIntyre N.S, Cook M.G. X-ray photoelectron studies on some oxides and hydroxides of cobalt, nickel, and copper. *Anal Chem*. 1975, 47(13), 2208-2213.

155. Mansour A.N. Characterization of NiO by XPS. *Surf Sci Spectra*. 1994, 3(3), 231.

156. Lu H.L, Scarel G, Alia M, Fanciulli M, Ding S-J, Zhang D.W. Spectroscopic

ellipsometry study of thin NiO films grown on Si(100)by atomic layer deposition. *Appl Phys Lett*. 2008, 92, 1-3.

157. Knisley T.J. New precursors and chemistry for the growth of transition metal films by atomic layer deposition. *PhD Thesis*. 2012.

158. Ezema F, Ekwealor A, Osuji R. Optical properties of chemical bath deposited nickel oxide (NiO_x) thin films. *Superf Vacio*. 2008, 21(1), 6-10.

159. Willcocks A.M, Robinson T.P, Roche C, et al. Multinuclear copper(I) guanidinate complexes. *Inorg Chem*. 2012, 51(1), 246-257.

160. Johnson, P.B, Christy R.W. Optical constants of transition metals: Ti, V, Cr, Mn, Fe, Co, Ni, and Pd. *Phys Rev B*. 1974, 9(12), 5056-5070.

161. Ordal M.A, Bell R.J, Ralph W. Alexander, Long L.L. Optical properties of Au, Ni, and Pb at submillimeter wavelengths. *OSA Publ*. 1987, 26(4), 744-752.

162. Wolfgang S.M. Werner, Kathrin Glantschnig C. Optical Constants and Inelastic Electron-Scattering Data for 17 Elemental Metals. *J Phys Chem Ref Data*. 2009, 38(4), 1013-1092.

163. Park J-W, Choi K.N, Baek S.H, Chung K.S, Lee H. Optical Properties of NiO Thin Films Grown by Using Sputtering Deposition and Studied with Spectroscopic Ellipsometry. *J Korean Phys Soc*. 2008, 52(6), 1868.

164. De Los Santos Valladares L, Ionescu A, Holmes S, et al. Characterization of Ni thin films following thermal oxidation in air. *J Vac Sci Technol B, Nanotechnol Microelectron Mater Process Meas Phenom*. 2014, 32(5), 51808.

165. Bosco J, Rayappan B. Gas sensing mechanism of metal oxides: The role of ambient atmosphere, type of semiconductor and gases-A review. 2015, (January).

166. Galatsis K, Li Y.X, Wlodarski W, Comini E, Sberveglieri G. Comparison of single and binary oxide MoO_3, TiO_2 and WO_3 sol-gel gas sensors. *Sensors Actuators B*. 2002, 83, 276-280.

167. Jayatissa A.H, Samarasekara P, Kun G. Methane gas sensor application of cuprous oxide synthesized by thermal oxidation. *Phys Status Solidi*. 2009, 206(2), 332-337.

168. Batzill M, Diebold U. The surface and materials science of tin oxide. *Prog Surf Sci*. 2005, 79(2-4), 47-154.

169. Anisimov O.V, Maksimova N.K, Chernikov E.V, Sevastyanov E.Y, Sergeychenko N.V. The Effect of Humidity and Environment Temperature on Thin Film Pt/SnO_2 Gas Sensors. *Control Commun 2007 SIBCON '07 Sib Conf*. 2007.

170. Barsan N, Weimar UDO. Conduction Model of Metal Oxide Gas Sensors. *J Electroceramics*. 2001, 7, 143-167.

171. Patil S.J, Patil A.V, Dighavkar C.G, et al. Semiconductor metal oxide compounds based gas sensors: A literature review. *Front Mater Sci*. 2015, 9(1), 14-37.

172. Kohl D. Surface processes in the detection of reducing gases with SnO_2-based devices. *Sens Actuators*. 1989, 18, 71-113.

173. Heilig A, Barsan N, Weimar U, Göpel W. Selectivity enhancement of SnO_2 gas sensors: simultaneous monitoring of resistances and temperatures. *Sensors Actuators, B Chem*. 1999, 58(1-3), 302-309.

174. L. Sun, F. Qiu B.Q. Investigation of a new catalytic combustion-type CH_4 gas sensor with low power consumption. *Sens Actuators B*. 2000, 66, 289-292.

175. Tang H, Sanjinès R, Schmid P.E, Lévy F. Ellectrical and optical properties of TiO_2 anatase thin films. *J Appl Phys*. 1994, 75(4), 2042.

176. Wypych A, Bobowska I, Tracz M, et al. Dielectric properties and characterisation of titanium dioxide obtained by different chemistry methods. *J Nanomater*. 2014, 2014.

177. Lim B.S, Rahtu A, Park J.S, Gordon R.G. Synthesis and Characterization of Volatile, Thermally Stable, Reactive Transition Metal Amidinates. *Inorg Chem*. 2003, 42(24), 7951.

178. Li Z. Synthesis and Characterization of Copper (I) Amidinates as Precursors for Atomic Layer Deposition (ALD) of Copper Metal. 2005, 44(6), 2122-2128.

179. Li Z, Rahtu A, Gordon R.G. Atomic Layer Deposition of Ultrathin Copper Metal Films from a Liquid Copper(I) Amidinate Precursor. *J Electrochem Soc*. 2006, 153(11), C787.

Appendix

Appendix A – SEM of TiO_2 thin films

Figure A1: Scanning electron microscopy (SEM) images to show the surface morphology of TiO_2 thin films deposited by ALD of $[Ti(O^iPr)_4]$ and water with different number of cycles at 200 °C

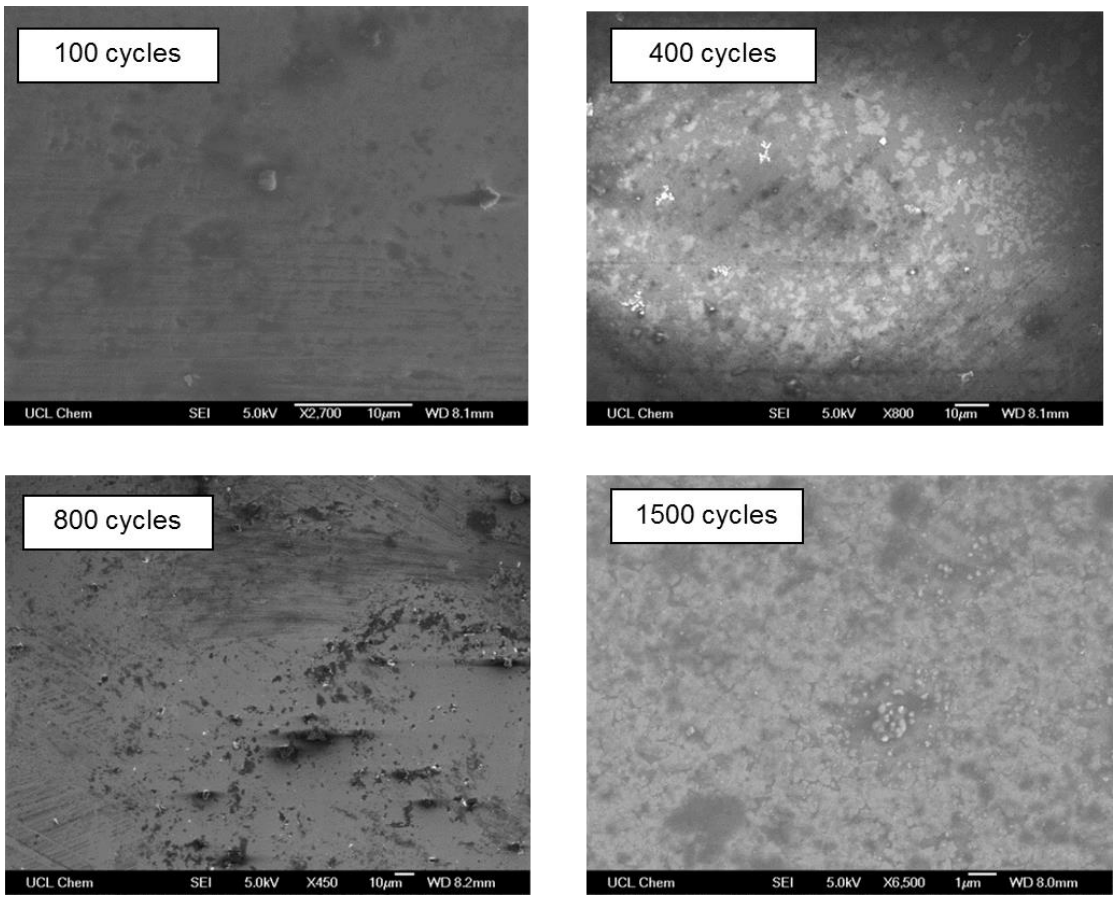

Appendix B – Mass Spectra of synthesised precursors

Figure B1: Mass Spectrum of complex (**4.1**), $[Ni(thd)_2]$. m/z: 425.21 $[M]^+$

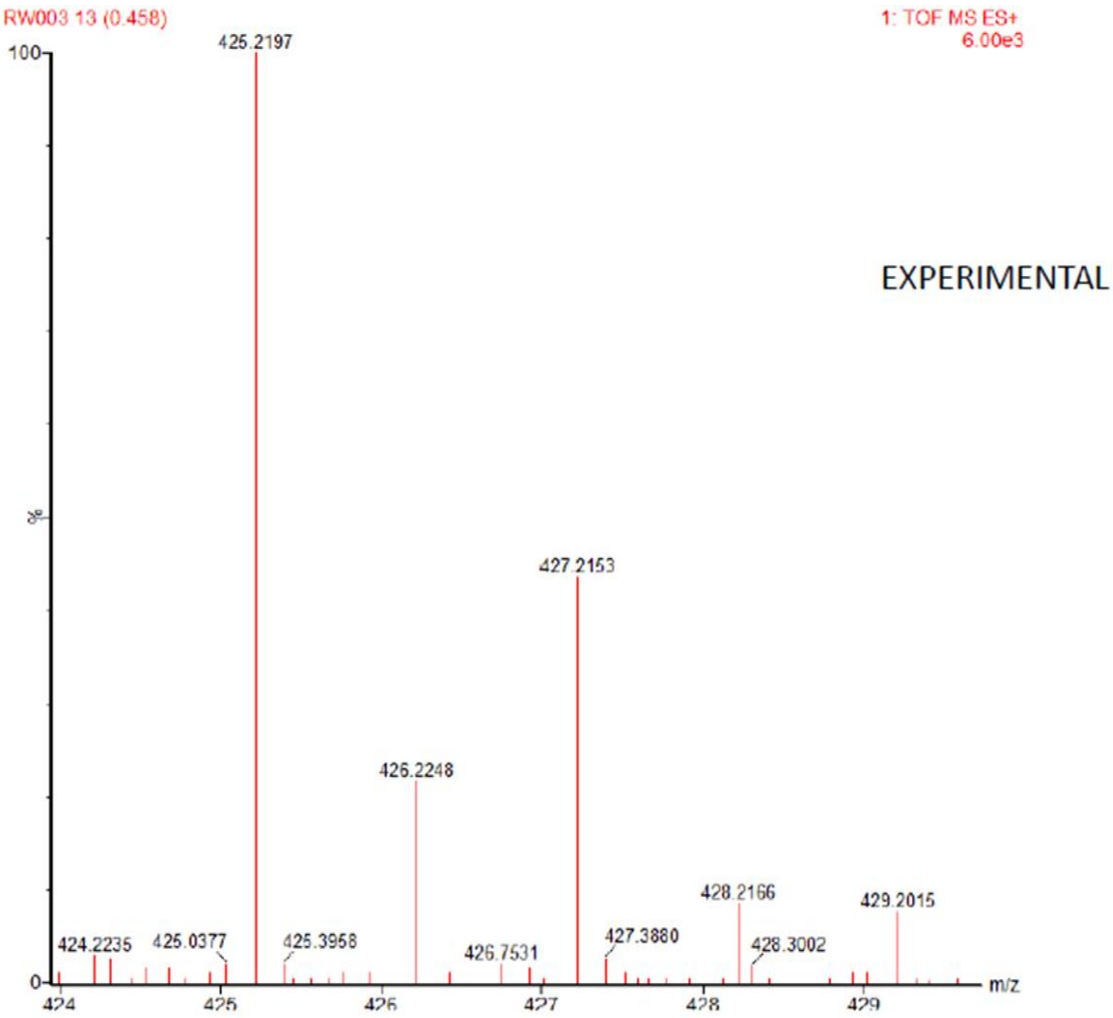

Figure B2: Mass Spectrum of complex (**4.2**), [Ni(dmamp)$_2$]. m/z: 291.2 $[M]^+$

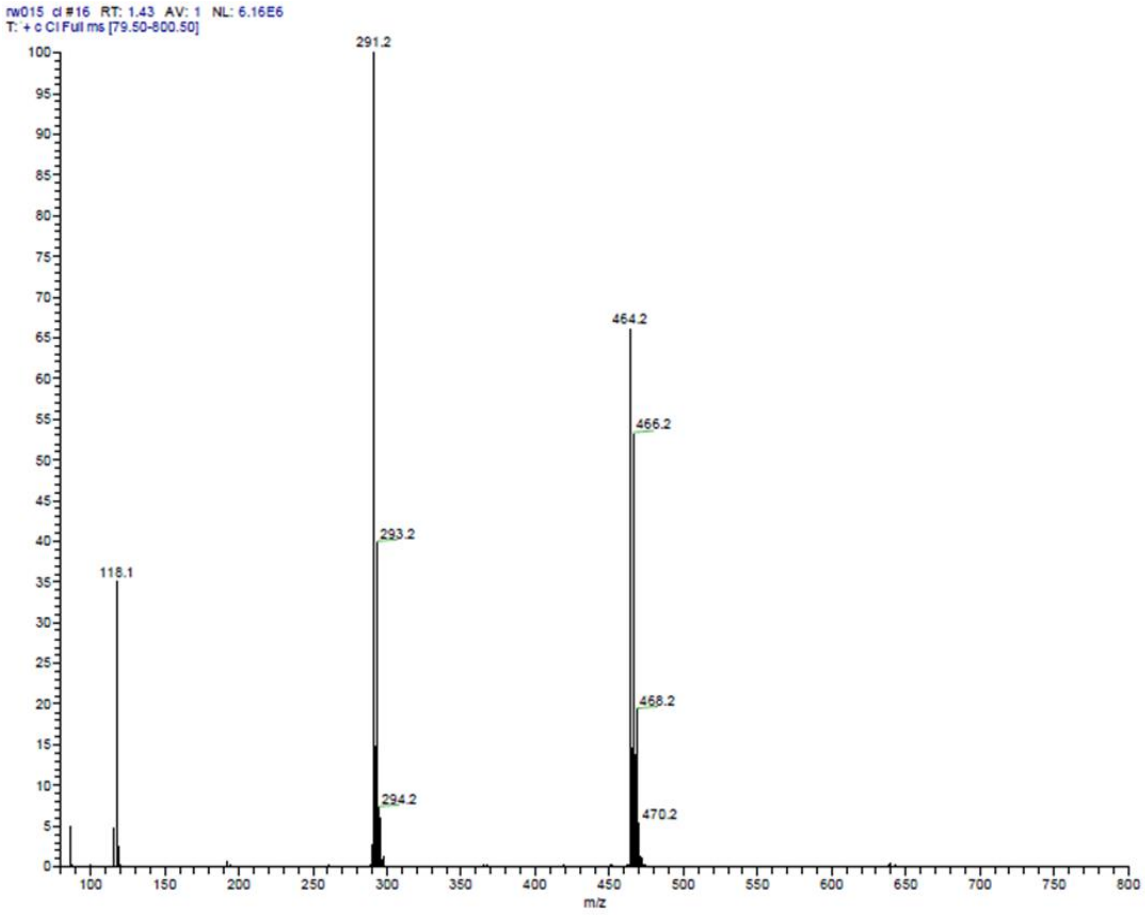

Figure B3: Mass Spectrum of complex (**4.3**), $[Ni\{(N^{i}Pr_2)_2CNEt_2\}_2]$. m/z: 489.00 $[M+CH_3OH+H]^+$

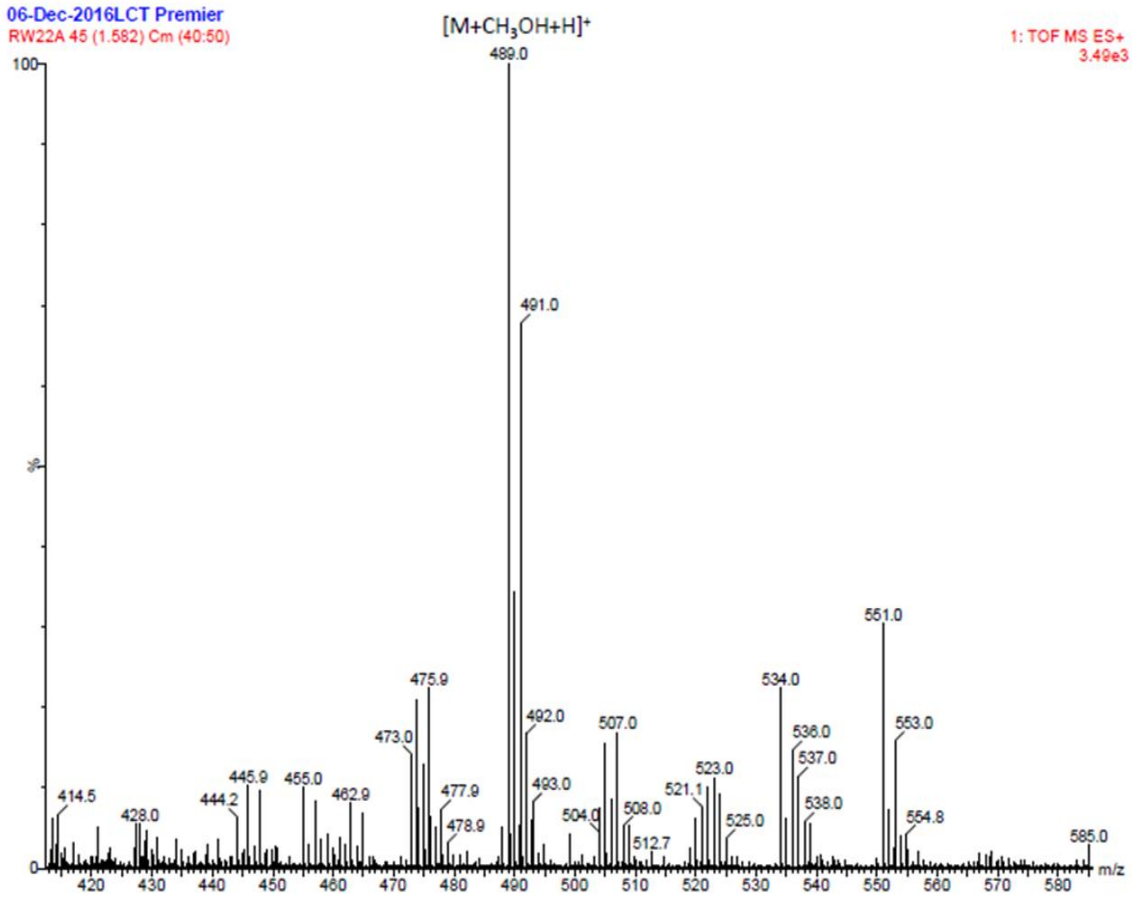

Appendix C – Crystal data for synthesised precursors

Table C1: Crystal data and structure refinement for compound **(4.2)** [$Ni(dmamp)_2$]

Identification code	Complex (**4.2**) [$Ni(dmamp)_2$]
Empirical formula	$C_6H_{14}NNi_{0.5}O$
Formula weight	145.54
Temperature/K	150.5(7)
Crystal system	orthorhombic
Space group	Pbca
a/Å	7.29116(10)
b/Å	10.68510(13)
c/Å	17.7933(2)
α/°	90
β/°	90
γ/°	90
Volume/$Å^3$	1386.22(3)
Z	8
$\rho_{calc}g/cm^3$	1.395
μ/mm^{-1}	1.965
F(000)	632.0
Crystal size/mm^3	0.09 × 0.07 × 0.05
Radiation	CuKα (λ = 1.54184)
2θ range for data collection/°	15.714 to 148.974
Index ranges	$-8 \leq h \leq 9$, $-13 \leq k \leq 13$, $-22 \leq l \leq 22$
Reflections collected	19533
Independent reflections	1412 [R_{int} = 0.0229, R_{sigma} = 0.0081]
Data/restraints/parameters	1412/0/91
Goodness-of-fit on F^2	1.096
Final R indexes [I>=2σ (I)]	R_1 = 0.0217, wR_2 = 0.0592
Final R indexes [all data]	R_1 = 0.0233, wR_2 = 0.0610
Largest diff. peak/hole / e $Å^{-3}$	0.36/-0.20

Table C2: Crystal data and structure refinement for complex (**4.3a**) **[**Ni(guanidinate)$_2$]

Identification code	Complex (**4.3a**) [Ni(guanidinate)$_2$]
Empirical formula	$C_{11}H_{24}N_3Ni_{0.5}$
Formula weight	227.69
Temperature/K	161(14)
Crystal system	orthorhombic
Space group	Pbcn
a/Å	10.61412(10)
b/Å	20.7302(2)
c/Å	12.10691(16)
α/°	90
β/°	90
γ/°	90
Volume/Å^3	2663.92(5)
Z	8
ρ_{calc}g/cm^3	1.135
μ/mm^{-1}	1.172
F(000)	1000.0
Crystal size/mm^3	0.15 × 0.12 × 0.05
Radiation	CuKα (λ = 1.54184)
2θ range for data collection/°	8.53 to 147.41
Index ranges	$-13 \leq h \leq 13$, $-25 \leq k \leq 25$, $-15 \leq l \leq 13$
Reflections collected	41302
Independent reflections	2675 [R_{int} = 0.0501, R_{sigma} = 0.0161]
Data/restraints/parameters	2675/0/140
Goodness-of-fit on F^2	1.087
Final R indexes [I>=2σ (I)]	R_1 = 0.0351, wR_2 = 0.0976
Final R indexes [all data]	R_1 = 0.0388, wR_2 = 0.1009
Largest diff. peak/hole / e Å^{-3}	0.27/-0.21

Table C3: Bond angles for complex (**4.3a**)

Atom – Atom – Atom	Angle (°)	Atom – Atom – Atom	Angle (°)
N(1) – Ni(1) – N(1)^1	68.73(6)	**C(2) – N(4) – C(11)**	120.61(8)
N(1)^1 – Ni(1) – C(1)	34.37(3)	**C(2) – N(4) – C(11)^1**	120.61(8)
N(1) – Ni(1) – C(1)	34.37(3)	**C(11) – N(4) – C(11)^1**	118.77(16)
N(1) – Ni(1) – C(2)	145.63(3)	**N(1)^1 – C(1) – Ni(1)**	55.42(8)
N(1)^1 – Ni(1) – C(2)	145.63(3)	**N(1) – C(1) – Ni(1)**	55.42(8)
N(2)^1 – Ni(1) – N(1)^1	111.16(5)	**N(1) – C(1) – N(1)^1**	110.83(16)
N(2) – Ni(1) – N(1)	111.16(5)	**N(1) – C(1) – N(3)**	124.58(8)
N(2) – Ni(1) – N(1)^1	176.23(4)	**N(1)^1 – C(1) – N(3)**	124.58(8)
N(2)^1 – Ni(1) – N(1)	176.23(5)	**N(3) – C(1) – Ni(1)**	180.0
N(2)^1 – Ni(1) – N(2)	69.22(6)	**N(2) – C(2) – Ni(1)**	55.67(8)
N(2)^1 – Ni(1) – C(1)	145.39(3)	**N(2)^1 – C(2) – Ni(1)**	55.67(8)
N(2) – Ni(1) – C(1)	145.39(3)	**N(2) – C(2) – N(2)^1**	111.34(16)
N(2) – Ni(1) – C(2)	34.61(3)	**N(2) – C(2) – N(4)**	124.33(8)
N(2)^1 – Ni(1) – C(2)	34.61(3)	**N(2)^1 – C(2) – N(4)**	124.33(8)
C(2) – Ni(1) – C(1)	180.0	**N(4) – C(2) – Ni(1)**	180.0
C(1) – N(1) – Ni(1)	90.22(8)	**N(2) – C(6) – C(8)**	111.86(11)
C(1) – N(1) –C(3)	121.28(11)	**N(2) – C(6) – C(7)**	110.38(11)
C(3) – N(1) – Ni(1)	137.51(9)	**C(7) – C(6) – C(8)**	111.45(12)
C(1) – N(3) – C(9)^1	120.72(7)	**N(3) – C(9) – C(10)**	112.66(11)
C(1) – N(3) – C(9)	120.72(7)	**N(1) – C(3) – C(4)**	111.51(11)
C(9)^1 – N(3) – C(9)	118.55(15)	**N(1) – C(3) – C(5)**	110.38(11)
C(2) – N(2) – Ni(1)	89.72(9)	**C(4) – C(3) – C(5)**	111.45(12)
C(2) – N(2) – C(6)	121.24(11)	**N(4) – C(11) – C(12)**	113.30(11)
C(6) – N(2) – Ni(1)	135.28(9)		

Table C4: Crystal data and structure refinement for complex (**4.3b**) [Ni(guanidinate)$_2$]

Identification code	Complex (**4.3b)** [Ni(guanidinate)$_2$]
Empirical formula	$C_{11}H_{24}N_3Ni_{0.5}$
Formula weight	227.69
Temperature/K	155(7)
Crystal system	triclinic
Space group	P-1
a/Å	8.8931(3)
b/Å	8.9707(3)
c/Å	9.4611(3)
α/°	63.244(3)
β/°	79.809(3)
γ/°	85.968(3)
Volume/Å^3	663.30(4)
Z	2
ρ_{calc}g/cm^3	1.140
μ/mm^{-1}	1.177
F(000)	250.0
Crystal size/mm^3	0.15 × 0.12 × 0.03
Radiation	CuKα (λ = 1.54184)
2θ range for data collection/°	10.614 to 134.998
Index ranges	$-10 \leq h \leq 10$, $-10 \leq k \leq 10$, $-11 \leq l \leq 11$
Reflections collected	9393
Independent reflections	2391 [R_{int} = 0.0461, R_{sigma} = 0.0352]
Data/restraints/parameters	2391/0/139
Goodness-of-fit on F^2	1.089
Final R indexes [I>=2σ (I)]	R_1 = 0.0562, wR_2 = 0.1521
Final R indexes [all data]	R_1 = 0.0579, wR_2 = 0.1539
Largest diff. peak/hole / e Å^{-3}	0.63/-0.76

Table C5: Bond angles for complex (**4.3b**)

Atom – Atom – Atom	Angle (°)	Atom – Atom – Atom	Angle (°)
N(1)^1 – Ni(1) – N(1)	180.0	**C(8) – N(1) – C(10)**	108.3(2)
N(1) – Ni(1) – C(1)	37.57(8)	**C(1) – N(2) – Ni(1)**	98.14(16)
N(1)^1 – Ni(1) – C(1)^1	37.57(8)	**C(1) – N(2) – C(2)**	122.8(3)
N(1)^1 – Ni(1) – C(1)	142.43(8)	**C(2) – N(2) – Ni(1)**	138.7(3)
N(1) – Ni(1) – C(1)^1	142.43(8)	**C(1) – N(3) – C(5)**	126.6(2)
N(2)^1 – Ni(1) – N(1)^1	69.93(9)	**N(1) – C(1) – Ni(1)**	52.18(11)
N(2)^1 – Ni(1) – N(1)	110.07(9)	**N(2) – C(1) – Ni(1)**	49.48(13)
N(2) – Ni(1) – N(1)	69.93(9)	**N(2) – C(1) – N(1)**	101.6(2)
N(2) – Ni(1) – N(1)^1	110.07(9)	**N(3) – C(1) – Ni(1)**	167.11(19)
N(2) – Ni(1) – N(2)^1	180.00(14)	**N(3) – C(1) – N(1)**	115.0(2)
N(2) – Ni(1) – C(1)	32.38(9)	**N(3) – C(1) – N(2)**	143.3(2)
N(2) – Ni(1) – C(1)^1	147.62(9)	**N(1) – C(10) – C(11)**	113.6(2)
N(2)^1 – Ni(1) – C(1)^1	32.38(9)	**N(1) – C(8) – C(9)**	113.5(2)
N(2)^1 – Ni(1) – C(1)	147.62(9)	**N(3) – C(5) – C(6)**	108.4(3)
C(1)^1 – Ni(1) – C(1)	180.0	**N(3) – C(5) – C(7)**	109.3(3)
C(1) – N(1) – Ni(1)	90.24(13)	**C(7) – C(5) – C(6)**	109.6(3)
C(10) – N(1) – Ni(1)	118.17(16)	**N(2) – C(2) – C(4)**	113.2(3)
C(10) – N(1) – C(1)	110.46(19)	**C(3) – C(2) – N(2)**	118.2(3)
C(8) – N(1) – Ni(1)	118.03(16)	**C(3) – C(2) – C(4)**	124.6(3)
C(8) – N(1) – C(1)	110.09(19)		

Table C6: Bond lengths for complexes (**4.3a**) and (**4.3b**)

Complex (4.3a)		**Complex (4.3b)**	
Atom - Atom	**Length (Å)**	**Atom - Atom**	**Length (Å)**
Ni(1) – N(1)	1.9368(11)	**Ni(1) – N(1)**	1.947(2)
Ni(1) – N(1)^{1}	1.9368(11)	**Ni(1) – N(1)^{1}**	1.947(2)
Ni(1) – N(2)	1.9348(11)	**Ni(1) – N(2)**	1.892(2)
Ni(1) – N(2)^{1}	1.9348(11)	**Ni(1) – N(2)^{1}**	1.892(2)
Ni(1) – C(1)	2.3525(18)	**Ni(1) – C(1)^{1}**	2.464(3)
Ni(1) – C(2)	2.3430(18)	**Ni(1) – C(1)**	2.464(3)
N(1) – C(1)	1.3279(15)	**N(1) – C(1)**	1.503(3)
N(1) – C(3)	1.4615(16)	**N(1) – C(10)**	1.492(3)
N(3) – C(1)	1.389(2)	**N(1) – C(8)**	1.491(3)
N(3) – C(9)	1.4550(14)	**N(2) – C(1)**	1.333(4)
N(3) – C(9)^{1}	1.4549(14)	**N(2) – C(2)**	1.468(4)
N(2) – C(2)	1.3307(15)	**N(3) – C(1)**	1.272(4)
N(2) – C(6)	1.4624(16)	**N(3) – C(5)**	1.453(3)
N(4) – C(2)	1.388(2)	**C(10) – C(11)**	1.504(4)
N(4) – C(11)	1.4533(15)	**C(8) – C(9)**	1.504(4)
N(4) – C(11)^{1}	1.4534(15)	**C(4) – C(2)**	1.480(4)
C(1) – N(1)^{1}	1.3279(15)	**C(5) – C(6)**	1.524(5)
C(2) – N(2)^{1}	1.3308(15)	**C(5) – C(7)**	1.520(5)
C(6) – C(8)	1.5257(18)	**C(2) – C(3)**	1.357(5)
C(6) – C(7)	1.524(2)		
C(9) – C(10)	1.511(2)		
C(3) – C(4)	1.5195(19)		
C(3) – C(5)	1.523(2)		
C(11) – C(12)	1.503(2)		

Publications

[1] D. Malarde, M. J. Powell, R. Quesada-Cabrera, **R. L. Wilson**, C. J. Carmalt, G. Sankar, I. P. Parkin, R. G. Palgrave, *ACS Omega*, 2017, 2, 1040-1046.

[2] M. J. Powell, D. B. Potter, **R. L. Wilson**, J. A. Darr, I. P. Parkin, C. J. Carmalt, *Materials & Design*, 2017, 129, 116-124.

[3] **R. L. Wilson**, C. E. Simion, C. S. Blackman, C. J. Carmalt, A. Stanoiu, F. Di Maggio, J. A. Covington, *Sensors*. Submitted.